SCUOLA DI DOTTTORATO
UNIVERSITÀ DEGLI STUDI DI MILANO-BICOCCA

Department of
Earth and Environmental Sciences

PhD program in Chemical, Geological, and Environmental Sciences

XXX Cycle

Geological Sciences Curriculum

# Numerical modelling of fluids related thermal anomalies

Volpi Giorgio

Number: 720974

Tutor: Prof. Crosta Giovanni Battista

Coordinator: Prof. Maria Luce Frezzotti

**ACADEMIC YEAR 2017/2018**

# Table of Contents

# List of Figures

# List of Tables

# Abstract

Among the renewable and sustainable energy sources, geothermal energy has been recognized as “the choice” to meet the future electricity demand, economically and environmentally speaking. Its ubiquitous occurrence and its low environmental impact in terms of $CO_2$ emissions, prompt present day governments toward a more efficient, large scale utilization of these energy sources. However, its utilization is still inconsistent with the enormous amount of energy available underneath the surface of the Earth.

The increasing threat of a worldwide energy crisis and the growing interest in geothermal systems require further development and application of advanced software and numerical modelling approaches to facilitate geothermal exploration and exploitation. These sophisticated, state-of-the-art tools provide crucial knowledge to characterize the thermal anomaly, as well as its connection with groundwater flow and heat transfer mechanisms, therefore limiting failures that may occur in subsurface and deep geothermal prospection. Due to the high costs of any geothermal related operation, a good knowledge of the explored site is required. In this regard, the present study is aimed to perform accurate three-dimensional simulations of three high to low-enthalpy type geothermal systems, for which no model was previously available.

The three selected sites are : i) the Bormio hydrothermal system and ii) the Castel Giorgio – Torre Alfina geothermal reservoir in Italy, and iii) the Tiberian Basin in the Jordan Rift valley, between Israel, Jordan and Syria. These study cases are characterized by substantial differences regarding both the geological setting and the active thermal regime, while they are pooled by the presence of fluids in the reservoir, which may be used for electricity generation or for other indirect types of application, such as the heating of spas.

The historical Italian thermal site of Bormio (Central Italian Alps) is a typical alpine low enthalpy geothermal site, whose waters are currently exploited by two thermal establishments. Thermal waters from ten springs are heated at a temperature of about 40°C in deep circulation systems and ascend vigorously from dolostones located close to the regional permeable Zebrù thrust. A hydrochemical characterization of the discharged thermal

waters has been performed to validate the assumptions formulated in the numerical model built with the finite element code Feflow®. Heat and fluid transport is explored taking into account the delayed effects of the last glaciation, which in the study area was recognized to end around 11,000–12,000 years ago. The full three-dimensional regional model (ca. 700 $km^2$) suggests a reactivation of the system following the end of the Last Glacial Maximum. Results correctly simulate the observed discharge rate of ca. 2400 l/min and the spring temperatures after ca. 13,000 years from deglaciation, and show a complete cooling of the aquifer within a period of approximately 50,000 years. Groundwater flow and temperature patterns suggest that thermal water flows through a deep system crossing both sedimentary and metamorphic lithotypes along a fracture network associated with the thrust system.

The Castel Giorgio - Torre Alfina geothermal field (Central Italy) is a promising, early explored and so far not exploited medium enthalpy reservoir. The involved fluids, pressurized water and gas, mainly $CO_2$, are hosted in a carbonate formation at temperatures ranging between 120-210 °C. Detailed hydro-geothermal data recognized a strong thermal anomaly associated with a vigorous convective regime, making that field suitable for electricity generation through geothermal methods. The three-dimensional reservoir-scale numerical model (ca. 293 $km^2$) has been developed, via the open source finite element code OpenGeoSys (OGS), to simulate the undisturbed natural geothermal field and investigate the impacts of the exploitation process. The commercial software Feflow® is also used as additional numerical constraint. The flow field displays multi-cellular convective patterns that cover the entire geothermal reservoir, and the resulting thermal plumes protrude vertically over 3 km at Darcy velocity of about $7*10^{-8}$ m/s. The analysis of the exploitation process demonstrates the sustainability of a geothermal doublet for the development of a 5 MW pilot plant. The buoyant circulation within the geothermal system allows the reservoir to sustain a 50 years production at a flow rate of 1050 t/h. The tested distance of 2 km, between the production and re-injection wells, is sufficient to prevent any thermal breakthrough within the estimated operational lifetime. OGS and Feflow® results are qualitatively very similar with only small differences in peak velocities and temperatures. The case study provides a thorough understanding of the Castel Giorgio – Torre Alfina purely convective reservoir, and valuable guidelines to the optimal reservoir management and sustainable utilization.

The last case study is the Tiberian Basin, located within in the Jordan Rift Valley at the border between Israel, Jordan and Syria. The selected area lies on the eastern side of the Lake Tiberias, the main freshwater resource of the entire Middle East. The sustainability of this resource is endangered by the occurrence of clusters of hot (temperatures in the range 20 – 60 °C) and salty springs, aligned along the lake shore and the Lower Yarmuk Gorge. This deep depression, which lies on the eastern margin of the lower Jordan Rift Valley, is supposed to act as the mixing zone of different flow paths responsible for the ascent of thermal waters. Moreover, the shallow heat anomaly, recognized in the northern Israel and Jordan territories, makes that field a potential site for production of electricity through geothermal methods, thus promoting the need of detailed numerical investigations. In this regard, the first regional three-dimensional model of the entire Tiberian Basin, ca. 565 $km^2$, has been developed with the commercial finite element software Feflow®. The model, accounting for major aquifers, aquicludes and deep-cutting faults, combines the knowledge from existing geological, hydrogeological and thermal surveys, as well as from previously numerical simulations. Available water levels for wells at different depths, allowed the correct calibration of the groundwater flow model. From a thermal point of view, results show that the discharge of thermal waters is tied to the coexistence of free convection in permeable units, and additional advective flow fields induced by topography gradients. Even though these simulations are not able to reproduce the correct temperature ranges for the thermal spring clusters, they provide reasonable explanation of groundwater flow behaviour associated to the anomalous geothermal gradient, and identify the mixed convection as the dominant heat flow process driving thermal waters below the Lower Yarmuk Gorge. Therefore, these first results can be considered as a valuable starting point for further numerical simulations aimed to a precise calibration of springs temperature values.

The understanding gained through this study about groundwater flow and heat transfer mechanisms in fluids related geothermal systems can be applied to other basins around the world in a wide variety of environments and not necessarily associated with convective heat flow. It improves also reservoirs knowledge for long term sustainable development in areas where an electricity generation exploitation project is planned or currently on-going.

# 1. INTRODUCTION

## 1.1 THE ENERGY PROBLEM and THE GEOTHERMAL ENERGY SOLUTION

From the beginning of the third millennium the world is facing the so-called "energy problem" (*Bundschuh, 2010*). This dilemma is based on two main assumptions: i) accessibility to water and energy in sufficient quantity and quality are essential for human development (*UNEP, 2009*), and ii) between 1999 and 2020 the world's energy consumption will rise by about 50%, due to the increase of population especially in rapid developing countries (*Energy Information Administration, 2001*). Therefore, if society will keep relying on the traditional fossil-based energies, in the very near future we will have limited oil supply coupled with increasing demand. This situation will lead to the raise of the oil prices together with global pollution and a severe environmental impact from continuous emissions of greenhouse gases (GHG, Fig. 1.1). Dealing with this serious energy problem is a primary task of the 21$^{st}$ century. It has recently entered public awareness that finding the supply to meet the increasing energy demand must also take into account the need to mitigate Earth climate change, thus satisfying the global needs in a "clean", sustainable way (*Fischedick et al., 2000; Change, 2007*). Recent studies clearly showed how the conventional sources of energy (i.e. oil, gas, coal and nuclear) will be depleted irretrievably within a few hundred years of human exploitation, since they restore over timescales inconsistent with present day economic system (*Kühn, 2004; Stober and Bucher, 2013*). At the same time, as the existing energy-related infrastructures are still designed for fossil fuels, the world will continue to heavily rely on hydrocarbon combustion in the medium-long term. Not only these conventional energies are the principal sources of air pollution and GHG (see Fig. 1.1 and Fig. 1.2), but also most countries require importing fossil fuels from politically volatile regions of the world (*Change, 2007; Solomon et al., 2007*). Therefore, we should not ignore its long-term impacts on environmental quality and political stability.

In the light of that, many governments are trying to reduce their dependence on traditional non-renewable energy sources and to encourage utilization of sustainable and renewable systems. Renewable describes a property of the energy source, whereas sustainable describes how the resource is exploited. A renewable energy source is characterized by reconditioning processes that are fast at human timescales. Sustainable resource means that the rate of

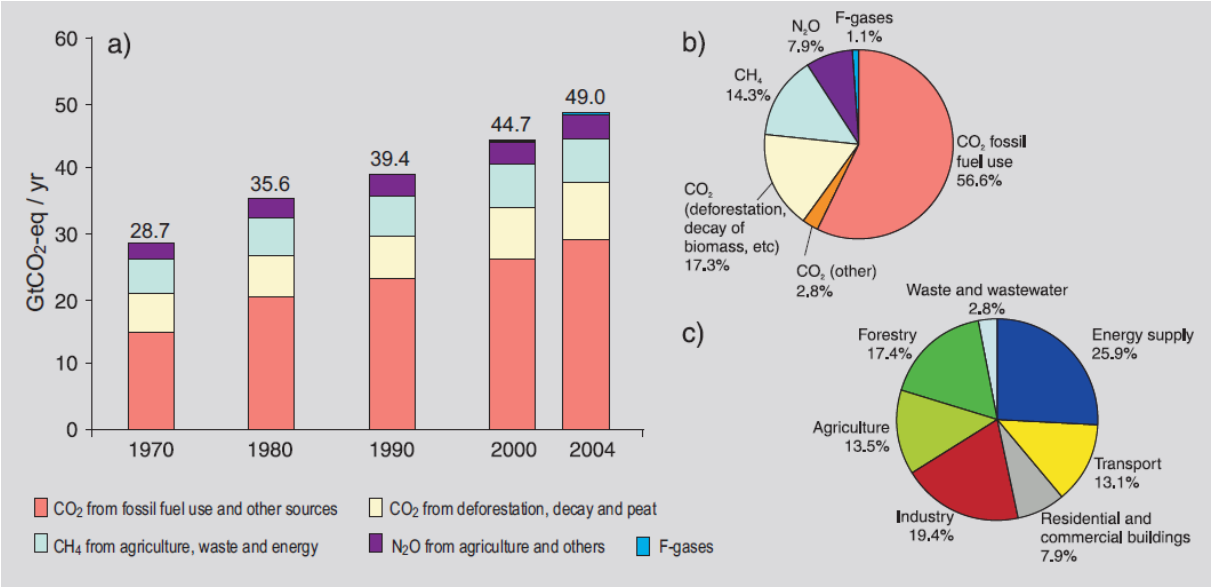


**Figure 1.1**: **(a)** Global annual emissions of anthropogenic GHGs from 1970 to 2004. **(b)** Share of different anthropogenic GHGs in total emissions in 2004 in terms of $CO_2$-eq. **(c)** Share of different sectors in total anthropogenic GHG emissions in 2004 in terms of $CO_2$-eq (from *Change, 2007*).

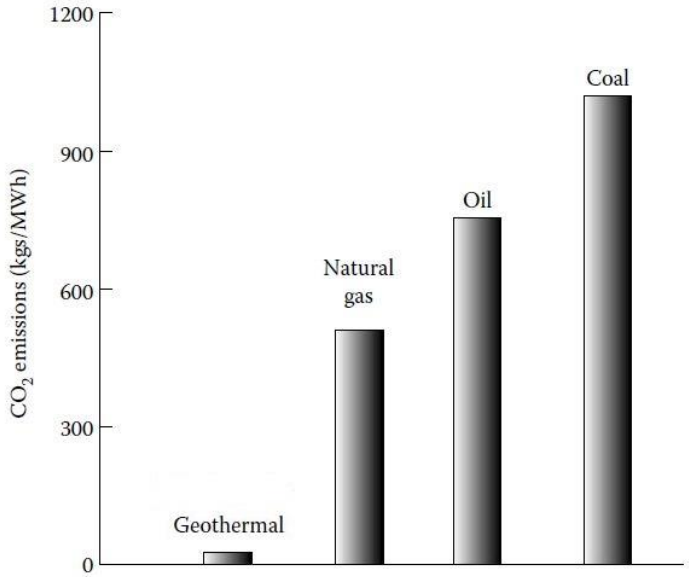


**Figure 1.2**: $CO_2$ emissions (in kg of $CO_2$/MWh) for different power generating technologies. Data from *Slack (2009).*

consumption is equal or smaller than the rate of the restoring processes (*Stober and Bucher, 2013*). These alternative energies include: geothermal, hydroelectric, wind and several forms of solar energy, such as bio-energy (bio-fuel), photovoltaic and solar-thermal energy. This needed radical energy change is a slow process, since the markets perceive renewable systems

as technically and financially risky, due to their high capital costs and to the applied technologies still in an optimization stage (*Baldwin, 2002*).

Geothermal energy is represented by the Earth heat losses emitted at the surface of the crust. Among alternative energy resources, it has the advantage to be almost ubiquitous and with very low environmental impact (Fig. 1.2; *Slack, 2009; Sonney, 2010; Al-Khoury, 2011*). Ascending hot magmatic rocks, the local thinning of the crust as well as natural radioactive decay of rock radiogenic isotopes are at the origin of geothermal anomalies around the world (*Romijn, 1985; Pruess, 2002*). *Cataldi et al. (1999)* present an extensive overview on the world's hydro-geothermal energy use since the Paleolithic era. Archeology proves that prehistoric humans used geothermal water from natural pools and hot springs for cooking, bathing and keeping themselves warm for more than 10,000 years. After the Second World War, technological advances leaded to the precise awareness that the energy potential of geothermal systems could provide electricity, heat and process heat for industries, with lower environmental impacts and higher economic competitiveness, compared with other forms of energy (*Kühn, 2004; Al-Khoury, 2011*).

It has been estimated that, considering a low range global-average temperature gradient of about 25°C/km, the heat stored in the upper few kilometres of the Earth's crust would be sufficient to supply the world's energy consumptions indefinitely (*Watson, 2013; Stober and Bucher, 2013; Bertani, 2005, 2016; Toth and Bobok, 2016*). The generation of an efficient hydraulic subsurface heat exchanger system is crucial for economic production of electricity and heat from geothermal systems (*Häring et al., 2008*). If the circulation of water through natural discontinuities is at too low flow rates, a hydraulic stimulation to improve the hydraulic properties of the naturally fractured hot rock mass is required (i.e. Enhanced Geothermal Systems or EGS). This is achieved by injecting fluid under high-pressure into a borehole (*Smith, 1983; Brown et al., 2012*). Terefore, although considered as an attractive environment-friendly energy source, these specific applications are currently limited due to induced seismicity (e.g. *Majer et al., 2007; Giardini, 2009*). The termination of the Basel EGS project, Switzerland (*Terakawa et al., 2012; Mignan et al., 2015*) and of the Soultz-sous-Forêts EGS project, France (e.g. *Charléty et al., 2007; Majer et al., 2007*) are two clear examples of the possible risks triggered by the operation of geothermal plants.

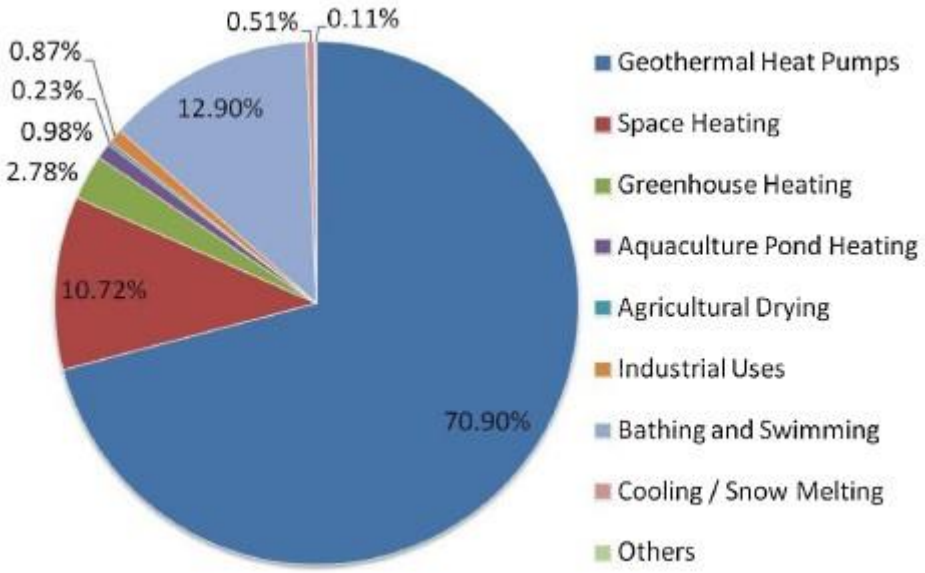


**Figure 1.3:** Categories of geothermal applications worldwide in 2015, distributed by percentage of the total installed capacity (from *Lund et al., 2016*).

Others minor issues related to this energy source, could be for example the minerals precipitation from the involved fluids in wells and pipelines, which may affects the exploitation of the reservoir and even contains dangerous radioactive material (*Caputo, 1999; Nicholson, 2012*).

Figure 1.3 shows the categories of geothermal application in 2015: electricity generation (i.e. direct use) is the most important form of utilization of medium-high temperature geothermal resources (*Lund et al., 2016; Kühn, 2004*). In countries having the greatest running geothermal capacities (i.e. USA, Philippines, Mexico, Italy, Indonesia, Japan, New Zealand, Iceland and countries of the Central America; see Table 1.1), these geothermal resources are linked to volcanic environment and to extremely high superficial heat flux anomalies (*Della Vedova et al., 2001, 2008; Sonney, 2010*). Medium to low temperature resources, usually not associated to volcanic or active tectonic environments, are suitable for many other types of application, like small district heating networks or for the heating of several spas (i.e. indirect use) (*Lund et al., 2016*). Therefore, direct or indirect use of the geothermal option has been recognized as the optimal choice, economically and environmentally speaking, to meet the future electricity demand and guarantee energy security and independence to both developing and developed countries (see Table 1.1; *Chandrasekharam and Bundschuh, 2002, 2008; Aaheim and Bundschuh, 2002; Bundschuh et al., 2002, 2007; Bundschuh and Coviello, 2002*).

**Table 1.1:** Worldwide geothermal power generation in early 2005 (from *Bertani, 2005a,b*).

| Country | Installed capacity ($MW_e$) | Running capacity ($MW_e$) | Annual energy produced (GWh/year) | Number of units | Percent of national energy |
|---|---|---|---|---|---|
| Australia | 0.2 | 0.1 | 0.5 | 1 | Negligible |
| Austria | 1.2 | 1.1 | 3.2 | 2 | Negligible |
| China | 28 | 19 | 96 | 13 | 30% of Tibet |
| Costa Rica | 163 | 163 | 1145 | 5 | 15 |
| El Salvador | 151 | 119 | 967 | 5 | 22 |
| Ethiopia | 7.3 | 7.3 | 0 | 2 | n/a |
| France (Guadeloupe) | 15 | 15 | 102 | 2 | 9 |
| Germany | 0.2 | 0.2 | 1.5 | 1 | Negligible |
| Guatemala | 33 | 29 | 212 | 8 | 3 |
| Iceland | 202 | 202 | 1483 | 19 | 17.2 |
| Indonesia | 797 | 838 | 6085 | 15 | 6.7 |
| Italy | 791 | 699 | 5340 | 32 | 1.9 |
| Japan | 535 | 530 | 3467 | 19 | 0.3 |
| Kenya | 129 | 129 | 1088 | 9 | 19.2 |
| Mexico | 953 | 953 | 6282 | 36 | 3.1 |
| New Zeland | 435 | 403 | 2774 | 33 | 7.1 |
| Nicaragua | 77 | 38 | 271 | 3 | 9.8 |
| Papua New Guinea (Lihir island) | 6 | 6 | 17 | 1 | n/a |
| Philippines | 1930 | 1838 | 9253 | 57 | 19.1 |
| Portugal (Sao Miguel island) | 16 | 13 | 90 | 5 | n/a |
| Russia | 79 | 79 | 85 | 11 | Negligible |
| Thailand | 0.3 | 0.3 | 1.8 | 1 | Negligible |
| Turkey | 20 | 18 | 105 | 1 | Negligible |
| USA | 2564 | 1935 | 17'917 | 209 | 0.5 |
| **Total** | **8933** | **8035** | **56'786** | **490** | |
| In 2009 | > 10'000 | | | | |

## 1.2 NUMERICAL MODELLING IN THE CONTEXT OF GEOTHERMAL RESOURCES

The highly diversified geological and hydrogeological environments, possibly hosting a geothermal resource, require to draw up a detailed exploration program before starting a geothermal exploitation plan. Different methods can be employed and combined together (e.g. geological, hydrogeological, geophysical, geochemical, isotopic and numerical investigations) targeting the characterization of the underlying thermal anomaly. The time and the financial resources availability are the two main factors limiting quality and quantity of investigations required to decipher the characteristics of the studied systems (*Al-Khoury, 2011*).

Over the last 50 years, due to the complex nature of the geothermal related scientific problems, the mathematical computer-based simulation method has found more and more applications in reservoir exploration and management. Various mathematical methods have been employed: analytical methods, analogue models and, most recently, numerical models

(*Bundschuh, 2010*). They have found applications at different stages of a geothermal project, for example in helping the understanding of reservoir behaviour, optimal reservoir management and sustainable utilization, or in planning of new investigations, well drilling and designing of exploitation steps aimed to the usage of geothermal energy. In addition, even if they require lot of data to provide reliable results, their cost is considerably lower when compared to any other exploration technique. This relatively recent development gradually changed the traditional geoscience from a description-dominated empirical discipline into a computer simulation-dominated scientific discipline (*Zhao et al., 2008*). The rapid improvement of computer technologies allows actual modelling of complex coupled subsurface processes, which was not possible a few years ago. Therefore, even if numerical modelling applied to geothermal systems is still not implemented to its optimal capacity, in the last years it has become a standard practice in the designing and in the management of the geothermal fields (*O'Sullivan, 2001; Blöcher et al., 2010*). Only in the last 20–25 years, various numerical models have been set up for more than 150 geothermal fields worldwide (*Antunez et al., 1990, 1994; O'Sullivan et al., 1990, 2001; Hanano 1992a, b; Axelsson and Bjornsson, 1993; Pham et al., 1993, 1996; Bertani and Cappetti, 1995; Antics, 1997; Della Vedova et al., 2008; Romagnoli et al., 2010; Fulignati et al., 2014*).

Mathematical models and associated numerical codes are helpful tools because: i) they can combine and verify several complex hypotheses and test them against observations; ii) they can test the most critical operation conditions, and iii) they have reliable ''prediction'' and ''retro-diction'' capacities. Indeed, they allow the quantitative estimation of future behaviours that are yet to be observed, as well as the estimation of processes that are no longer observed, but that were antecedent to the current phenomenon (*Bundschuh, 2010*).

Nowadays, many different types of numerical codes are available on the market, suitable for solving almost all the range of geothermal related problems depending on the needed level of complexity to be simulated. Advanced numerical models allow to define well's system design, fracture paths, extraction rates, temperature of injected and produced thermal waters, to interpret hydraulic tests or stimulation processes, and to predict reservoir behaviour during geothermal power production. Therefore, they are mandatory to optimize the productive capacity and the thermal breakthrough occurrence (*Stober and Bucher, 2013;*

*Li et al., 2016*). Moreover, mathematical modelling of a geothermal reservoir allows reconstructing not only the deep natural fluid circulation, but also the physical/chemical fluid characteristics. This can be of interest at geothermal sites where high temperatures and strong corrosion, caused by very acidic involved fluids, occur. In some cases, the fluids may react chemically with the hosting rocks, precipitating minerals that diminish reservoir permeability by pores and fractures obstruction (*Caputo, 1999*). These phenomena create a spatially variable pattern of mineralization and permeability, thus affecting the exploitation of the reservoir (*Caputo, 1999; Nicholson, 2012*).

The principal difficulty in establishing an accurate numerical model is due to the often very limited availability of spatial and chronological field data. Such lack of input data could be overcome by indirect estimation of needed values, for example through focused geophysical or geochemical surveys. Another obstacle to a reliable numerical modelling is that thermal and hydraulic parameters are often spatial-scale-dependent and time-dependent (*Sonney and Vuataz, 2009; Welch and Allen, 2014*). Therefore, a single constant value does not often adequately capture what we measure in the field or wish to predict numerically. Many different modelling approaches, described in Chapter 4, account for the acceptable degree of simplification from the complex real-world system to its virtual representation in the numerical models. In the light of that, a good understanding of the limitations of the data and modelling tools is vital for the numerical models intelligent application (*Bundschuh, 2010; Anderson et al. 2015*).

## 1.3 SELECTED SITES

Because of the growing interest in geothermal systems, further development of advanced software and numerical modelling approaches to facilitate geothermal exploration and exploitation is required.

Aiming to characterize the thermal anomaly, as well as its connection with groundwater flow and heat transfer mechanisms in high to low-enthalpy type geothermal systems, the present study will perform accurate three-dimensional simulations of three case studies, for which no model was previously available.

The three selected sites are: i) the Bormio hydrothermal system and ii) the Castel Giorgio – Torre Alfina geothermal reservoir in Italy, and iii) the Tiberian Basin in the Jordan Rift valley (between Israel, Jordan and Syria).

Herein, we summarize the main characteristics that make the selected sites suitable for our analyses. As regard the Bormio hydrothermal system, they are: 1) historical Italian thermal site not yet numerically investigated, 2) thermal waters exploited by two thermal establishments, 3) deep flow system from the basement in normal heat-flow conditions, 4) complex geological settings and hydraulic behaviour related to the regional Zebrù thrust and 5) availability of recent geochemical investigations, used to validate the assumptions formulated in the numerical model.

The Castel Giorgio - Torre Alfina site was selected for: 1) its extensive studies but unexploited medium enthalpy deep geothermal system, 2) no numerical investigation yet performed, 3) available data for model calibration and validation, 4) complex geological-structural settings, 5) recognized strong thermal anomaly and associated convective behaviour, 6) recently planned geothermal exploitation project.

Finally, the Tiberian Basin geothermal field was selected because of: 1) Tiberian Lake is the main freshwater resource of the entire Middle East, 2) hot and salty spring occurrence, 3) available data (i.e. borehole and chemical analysis on deep and superficial waters), 4) rock salt emplacement and strong thermal anomaly, 5) groundwater flow, heat and salinity coupled problem (mixed convection), 6) thermo-hydraulic behaviour related to complex fragile structures (i.e. fractures and faults networks), 7) published 2D simulations.

# 2. THESIS OUTLINE

The present thesis is structured as follows: the first part describes the generalities about geothermal energy, with focus on the different types of geothermal reservoirs, the thermal regimes responsible for the heat transfer mechanisms and typical reservoirs investigation techniques. In the second part, the procedure for the elaboration of a coupled groundwater-flow heat-transfer numerical model is developed. The other parts deal each with results obtained from investigations on each hydro-geothermal site: Bormio, Castel Giorgio - Torre Alfina and lastly the Tiberian Basin. For each case study, beside the regional and local geological and hydrogeological settings, also the hydrochemical investigations, when available, are described together with the applied numerical methods. The thesis ends with general conclusions, with the aim to analyse the work that has been done and suggesting possible future developments.

In detail, Chapter 3 frames first the origin of earth's heat surface evidences, representing the positive thermal anomalies underlying the geothermal reservoirs. The following section highlights the active heat-transfer mechanisms in rock/fluid systems providing the internal energy of all the geothermal reservoirs. The focus is on mechanisms playing an effective role in hydro-geothermal systems, namely conduction and convection, both free, forced and mixed (*Zhao et al., 2008; Bundschuh, 2010; Al-Khoury, 2011*). This chapter presents a classification of the geothermal systems as a combination of the work by Nicholson (1993), Pirajno (1992) and Heiken (1982). Geothermal reservoirs are subdivided between naturals or man-made sub-systems, following a classification based on their intrinsic hydraulic conditions, which are tied tightly to the active heat transfer mechanism (i.e. static or conductive systems and dynamic or convective systems). Both static and dynamic geothermal systems are further classified depending on reservoir temperature, with low and high temperatures strictly related to the hosting rock type (i.e. sediment hosted and magmatic hosted). It follows a short summary of the history of geothermal energy, from the first uses to the industrial explosion, including an overview of present day and short/long term forecasts in terms of worldwide geothermal installed capacity (*Cataldi, 1999; Bertani, 2013, 2016*). A short overview of the indirect/direct techniques (i.e. remote sensing techniques, field surveys as geological-hydrogeological studies, geochemical and geophysical surveys), used to identify a geothermal reservoir and to

estimate physical/chemical characteristics needed to construct a reliable numerical model (e.g. rocks and fluids parameters), is presented.

Chapter 4 is fully committed to the procedure of a coupled groundwater-flow heat-transfer numerical model elaboration. This provides a solid structure for an accurate mathematical representation of the complex reality associated to hydro-geothermal systems. Based on the work of *Kresic (2006)*, *Bundschuh (2010)* and *Anderson (2015)*, the processing of the large amount of information is subdivided in six steps: (1) definition of the model objectives, (2) development of the conceptual model, (3) numerical formulation of the conceptual model (i.e. mathematically defined boundary conditions and model properties, discretize model spatial extent, choice of an adequate software and mesh), (4) calibration and (5) validation of the numerical model, and (6) sensitivity analysis. All these steps will be thoroughly described, together with an overview of the main features of the codes adopted in the numerical simulations of the three selected study cases.

Chapter 5 is based on the papers of *Volpi et al. (2017*): "*Groundwater-driven temperature changes at thermal springs in response to recent glaciation: Bormio hydrothermal system, Central Italian Alps",* published on the Hydrogeology Journal; and of *Volpi et al. (2016*): "*Geochemical characterization of the Bormio hydrothermal system (central Italian Alps)",* on the Rendiconti Online Società Geologica Italiana. This case study analyses the thermal circulation and outflows of the Bormio area (Upper Valtellina Valley, Central Alps, Italy). Here, a hot spring system discharges water with temperatures in the 35-40 °C range from dolostones along the regional Zebrù thrust. This area represents a typical alpine low enthalpy geothermal system in normal heat-flow condition, where high temperatures result from the rapid upwelling of water from deep flow systems through permeable faults or subvertical strata (*Vuataz, 1983; Bianchetti et al., 1992; Sonney and Vuataz, 2009*). The aim is to build the first three-dimensional numerical model of heat and fluid transport in the Bormio area, using the commercial finite element software Feflow® (*Diersch, 2014*), to assess quantitatively the source area of hot waters and to investigate the behaviour of the system following the end of Last Glacial Maximum (LGM). The study tests the hypothesis that other thermal processes, such as heat convection, might occur within the faults of this hydrothermal system, as observed in other basins (*Evans and Raffensperger, 1992; Bodri and Rybach, 1998; Baietto et*

*al., 2008*). Moreover, the availability of recent geochemical investigations (*Volpi et al., 2016*), is used to validate the assumptions formulated in the numerical model. Besides providing a numerical framework to simulate complex fractured systems accounting for the interaction between superficial hydrography and regional groundwater levels, this example provides insights into the influence of glaciations on groundwater circulation that control the development of many low enthalpy geothermal systems, not necessarily associated with convective heat flow.

Chapter 6 is largely based on the paper of *Volpi et al. (2017)*: "*Modelling highly buoyant flows in the Castel Giorgio – Torre Alfina deep geothermal reservoir",* published on on Geofluids Journal. The Castel Giorgio - Torre Alfina geothermal field (CG-TA, northern Latium), is an example of an early explored and so far not exploited, medium enthalpy deep geothermal system (*Cataldi and Rendina, 1973; Buonasorte et al., 1988*). Detailed hydro-geothermal data, available for the selected area since early 70s, show that the CG-TA is a potential geothermal reservoir with medium thermal characteristics (120°C - 210°C) whose fluids (pressurized water and gas, mainly CO2) are hosted in a fractured carbonate formation (*Buonasorte et al., 1988, Barberi et al., 1994; Chiarabba et al., 1995; Chiodini et al., 1995; Doveri et al., 2010; Carapezza et al., 2015*). These features, coupled with observed strong convection phenomena (*Buonasorte et al., 1991*), make it suitable for future exploitation through a new generation 5 MWe geothermal pilot power plant. The aim consists in building a numerical model of the deep, medium-enthalpy CG-TA reservoir, through the finite element open-source simulator OpenGeoSys (*Kolditz et al., 2012*), and the commercial software Feflow® (*Diersch, 2014*) was also used as additional numerical constraint. Models were run to reproduce the highly convective undisturbed present-day natural state of the reservoir. These results, validated against the pressures and temperatures measured in geothermal wells, are used to investigate the feasibility of a geothermal power production configuration (i.e. injection and production wells). The simulations, besides sustaining the possible future exploitation of the field, improved the understanding of reservoir behaviour and the prediction of the long-term reservoir characteristics during geothermal power production. Such an understanding is critical to optimal reservoir management and sustainable utilization.

Chapter 7 refers to the Tiberian Basin located within in the Jordan Rift Valley (JRV) at the border between Israel, Jordan and Syria. The area is crossed by the Lower Yarmuk Gorge (LYG), which lies on the eastern margin of the lower JRV, separating the basalt-covered Golan Heights to the north from the carbonaceous Ajlun Plateau to the south. The LYG allows the outflow of the Yarmouk drainage basin and flow into the Jordan River, a few kilometres south of Lake Tiberias, the main freshwater resource of the Middle East. We hypothesize that the gorge acts as the mixing zone of two crossing flow pathways: N-S from the Hermon Mountains and from the Ajlun Plateau, and E-W from the Hauran Plateau. As a result, several spring cluster can be found within the gorge, posing a threat to the future sustainability of the lake freshwater resource. Thermal springs are characterized by widespread temperatures (20 – 60 °C) which indicate that, beside the complex regional flow, also ascending thermal waters control the hydrologic behaviour of the LYG. Previous simulations based on a conceptual 2D and simplified 3D models (*Magri et al., 2015, 2016*) showed that crossing flow paths result from the coexistence of convection, along NE-SW oriented faults or in permeable aquifers, and a regional flow induced by the N-S topographic gradient.

The aim of this study is the construction the first 3D hydrogeological model of the entire LYG including structural features based on actual logs and interpreted seismic lines from both Israeli and Jordanian territories (*Inbar et al., 2018*). The model, built with commercial finite element software Feflow® (*Diersch, 2014*), tests the occurrence of complex transboundary flow paths across faults as observed in the idealized 3D model from *Magri et al. (2016)*. Ten units from upper Eocene to the Permian basement, accounting for major aquifers, aquicludes and deep-cutting faults, have been considered. Model calibration was achieved through inverse procedure (PEST) against measured water levels at 22 wells referred to the two main aquifers characterizing in the area. The model reveals that two different mechanisms of basin-scale groundwater motion influence the transfer of heat: a topography-driven and a buoyancy-driven flow. Their occurrence is strongly conditioned by formation hydraulic properties controlling the location of discharge areas, while the anomalous spring temperatures are not necessarily linked to the presence of fault convection. Local permeability anisotropy due to aquifers folding or facies changes are features sufficient to control the rising of hot fluids.

# 3. THE GEOTHERMAL ENERGY

### 3.1 ORIGIN OF EARTH'S HEAT FLOW

Description and understanding of all diverse expressions of Earth's heat sources is mandatory to define thermal anomalies underlying present day geothermal reservoirs. The presence of a geothermal reservoir is conditioned by thermal regime in the surroundings, and thus by the thermal boundary conditions affecting the crust. Consequently, it is worth to understand and assess the whole range of thermal constraints on crustal rocks in order to figure out how different heat transfer mechanisms could lead to generation of such geothermal systems.

The average temperature at the Earth ground surface is 14 °C, at the core-mantle boundary the temperature is about 3,000 °C. The strong temperature difference between the surface and the interior is the primary driving force for the so-called heat flow. To balance this difference heat is continuously transported from the hot interior to the surface (Fig. 3.1; *Stober and Butcher, 2013*). The mean conductive heat flow measured near the Earth's surface is approximately 70 mW/m$^2$ (*Chapman and Pollack, 1975*). Correction for the effects of hydrothermal circulation in the oceanic crust increases to 87 mW/m$^2$ the mean global heat flux (*Pollack et al., 1993*). Integration of this value over the surface of the globe, leads to an Earth's heat loss of more than $10^{13}$ W. The sources of this heat are not yet completely resolved, cooling of an originally hot Earth, together with isotopic radioactive decay, are certainly the most significant contributions.

Earth's heat loss starts within its fluid core, which releases heat at the base of the mantle through distinct mechanisms: inner-core crystallization, secular cooling, chemical separation of the inner-core, and possibly radiogenic heat generation within the core itself (*Jaupart, Labrosse, and Mareschal, 2007*). Different authors calculate the values for the heat sources and heat losses in the Earth's core (*Labrosse, 2002; Roberts, Jones and Calderwood, 2003; Jaupart, Labrosse and Mareschal, 2007*). Total heat loss from the mantle is larger than heat input from the core and heat generation within it, the remaining heat content stands for mantle cooling through Earth's history (*Ledru and Frottier, 2010*). Therefore, from the core to the mantle, and from the mantle to the overlying crust, Earth's heat is dissipated continuously in the atmosphere. Globally, the range of observed variation in crustal heat flow is very wide, i.e. from 20 mW/m$^2$ to more than 500 mW/m$^2$ (*Davies, 2013*). The intensity of the heat flux depends, among other things, on the underlying lithology and on the variations of the mantle-

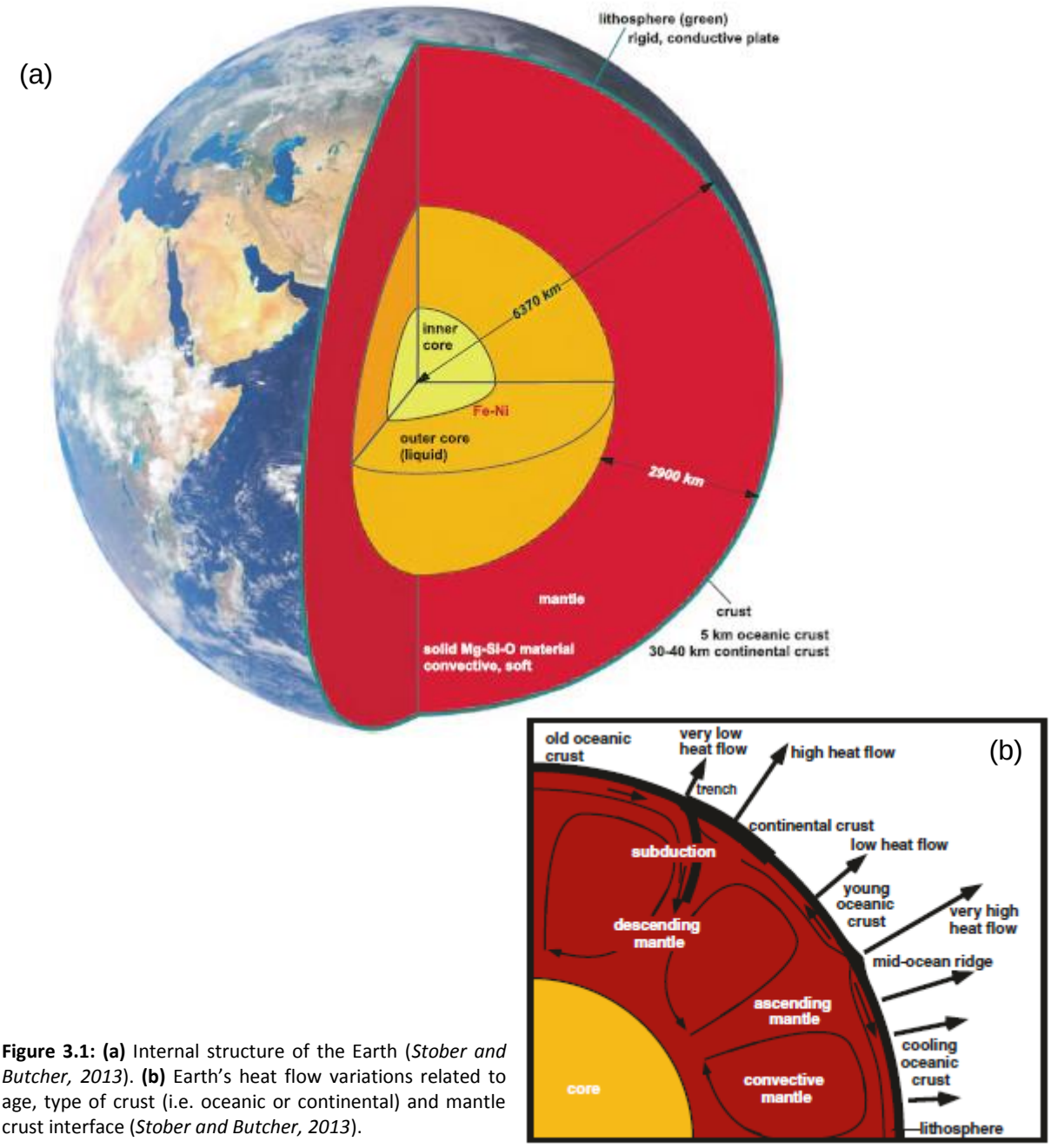


**Figure 3.1: (a)** Internal structure of the Earth (*Stober and Butcher, 2013*). **(b)** Earth's heat flow variations related to age, type of crust (i.e. oceanic or continental) and mantle crust interface (*Stober and Butcher, 2013*).

crust interface (Fig. 3.1b). On a global scale, there is a reasonably good correlation between the age of the Earth's crust and crustal heat flow (Fig. 3.2; *Ingebritsen et al., 1999*). This relation is much clearer in the oceanic crust than in the continental crust. Heat flow in the oceanic crust derives from its age, and thus distance from the mid-ocean ridge axes (*Sclater et al., 1980; Seton et al., 2012*). Oldest (ca. 200 Ma) oceanic crust is characterized by average heat flow values of about 50 mW/m$^2$, while very young crust, therefore near the mid-ocean ridges, is marked by a heat flow of over 300 mW/m$^2$ (Fig. 3.2b; *Pollack et al., 1993*). The age-

heat flow relation is much less defined on the continental crust, due to its enrichment in radioactive elements and its varied tectonic history (*Davies, 1980*). Nevertheless, on a global scale, it is still possible to establish a relationship between the timing of the most recent tectonic activity and associated heat flow (*Sclater et al., 1980*). Mean continental heat flow ranges from about 40 mW/m$^2$ on the stable cratons to about 70 mW/m$^2$ in active tectonic provinces (Fig. 3.2a; *Williams et Von Herzen, 1974; Jaupart et al., 2007*).

The measured surface heat flow density has several contributions. Only a small part of it is related to the heat flow from core and mantle as described above (about 30%). The remaining 70% derives by heat generated from the decay of radioactive elements in the crust, mostly in the continental "granitic" crust (*Stober and Butcher, 2013*).

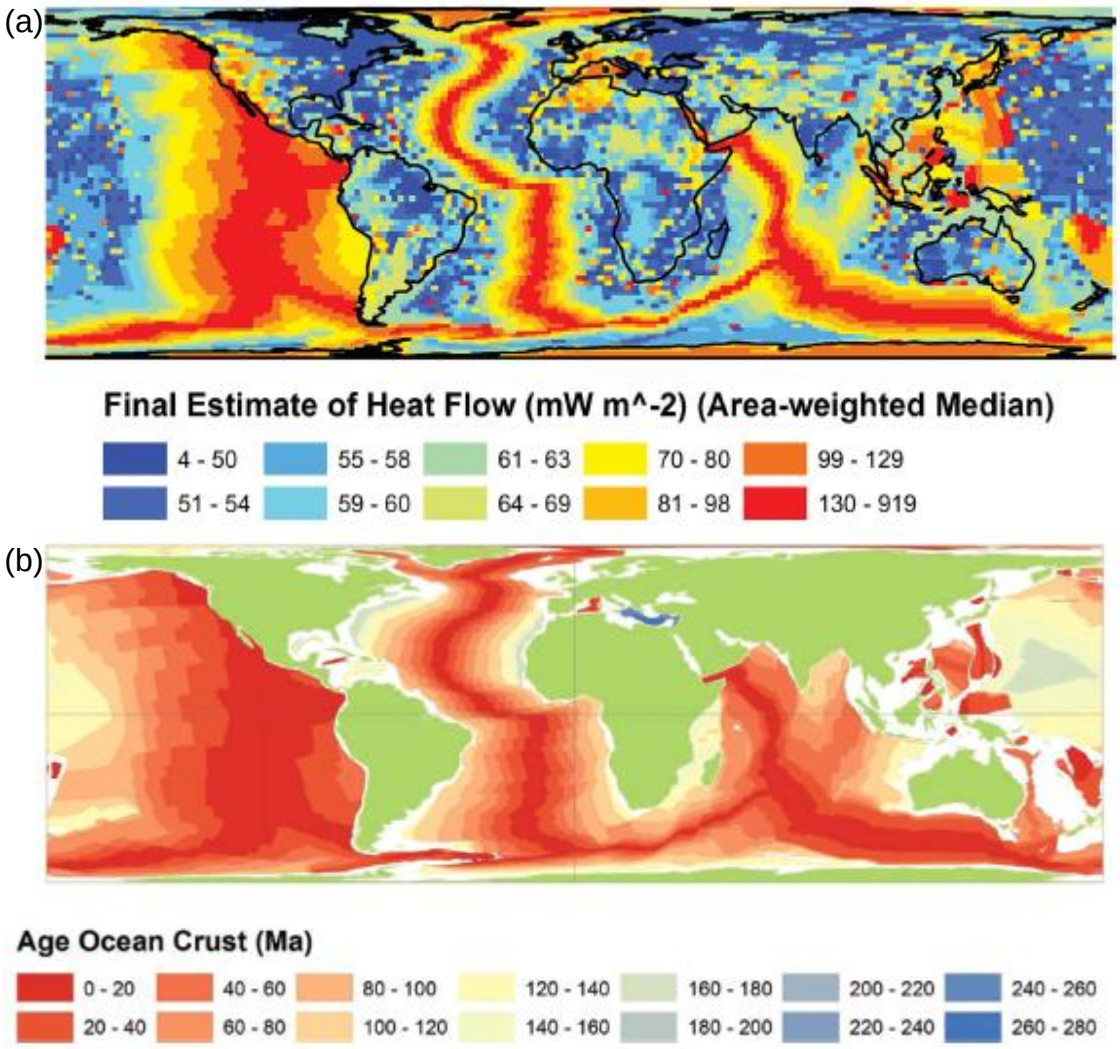


**Figure 3.2: (a)** Worldwide heat flow (mW/m$^2$) in continental and oceanic crust types (*Davies, 2013*). **(b)** Oceanic crust age (Ma) (*Seton et al., 2012*).

**Table 3.1:** Typical radiogenic heat production for selected rocks (*Kappelmeyer and Haenel, 1974; Rybach, 1976*).

| Rock type | Heat Production [$\mu J\ s^{-1}\ m^{-3}$] |
|---|---|
| Granite | 3.0 (<1–7) |
| Gabbro | 0.46 |
| Granodiorite | 1.5 (0.8–2.1) |
| Diorite | 1.1 |
| Gneiss | 4.0 (<1–7) |
| Amphibolite | 0.5 (0.1–1.5) |
| Serpentinite | 0.01 |
| Sandstone | 1.5 (0.2–2.3) |
| Shale | 1.8 |

All rocks contain a certain measurable amount of radioactive elements (Table 3.1). The energy generated by the decay of unstable nuclei is given off as ionizing radiation and then absorbed and transformed to heat (*Rybach, 1976*). The only significant contributions are Uranium ($^{238}U$, $^{235}U$), Thorium ($^{232}Th$) and Potassium ($^{40}K$) (*Kappelmeyer and Haenel, 1974*). Uranium and Thorium occur in accessory minerals, mainly zircon and monazite, in common rocks such as granite and gneiss, while Potassium is a major element in common rocks which are rich, for example, in K-feldspar and mica. Therefore, heat production of crustal rocks differs over a wide range because crust is a non-homogeneous shell: continental crust is typically thicker, granitic and rich in radioactive elements, whereas oceanic crust is thinner, basaltic and impoverished in radioactive elements (Table 3.1). A portion of these radioactive elements can be mobilized by water–rock interaction and dissolved in hydrothermal fluids. Therefore, some thermal waters may contain a considerable amount of radioactive components and be considered as radioactive (*Stober and Butcher, 2013*).

## 3.2 THERMAL REGIMES

Heat transport is the transfer of thermal energy from an object with high temperature to one with lower temperature (*Bundschuh, 2010; Diersch, 2014*). Heat transport in rock/fluid systems always originates from different temperatures existing between two regions and persists until they reach the same temperature, a state known as thermal equilibrium (*Al-Khoury, 2011*). The study of the heat transfer mechanisms in hydro-geothermal systems is

fundamental for understanding global geodynamics, as well as the basic porous rocks thermodynamic.

Generally, heat energy may be transferred through the following three mechanisms: i) conduction, which is the energy transferred by molecular vibration through a rock or fluid; ii) free or forced convection (i.e. natural convection, buoyancy/thermally-driven convection or gravity/pressure-driven convection), which is the energy transferred by the fluid in motion and occurs through both diffusion and advection, and iii) radiation, which is the energy transferred through electromagnetic waves (*Zhao et al., 2008; Bundschuh, 2010; Al-Khoury, 2011*). Heat transfer in physical systems often occurs as a combination of these three mechanisms, nevertheless in hydro-geothermal systems radiation plays no effective role, and therefore will not be treated in this work.

Between the above mentioned heat transfer mechanisms, the main active and permanent phenomenon at the scale of the continental crust is conduction. In conduction, heat moves through the material from a hotter to a cooler zone without material transport (i.e. fluid movement). This mechanism provides the internal energy of all the geothermal reservoirs worldwide, as it takes place within the impervious bedrock beneath them (permeability in the range $10^{-18}$ - $10^{-19}$ $m^2$). When it is the only process active in the system, conduction does not allow development of hydrothermal sources. The feasibility and intensity of such transfer is directly linked to the thermal properties of the rock, mainly the thermal conductivity, and to the heat flow (*Ledru and Frottier, 2010*). As continental crust is made by superposition of layers with different conductivity properties, originating a thermally heterogeneous shell, crustal conduction processes cannot be considered homogenous.

Heat convection is the second important heat transfer mechanism, associated with a fluid flow transporting heat in the direction of motion (*Al-Khoury, 2011*). We can distinguish between two mechanisms of convection: free convection (also known as natural convection, buoyancy- or thermally-driven convection) and forced convection (also named gravity- or pressure-driven convection, advection) (*Zhao et al., 1997, 1999a, 2001, 2008*).

In a free convection regime, temperature related variations in the fluid density induce dipping and raising of cold and hot fluids, respectively, under the effect of buoyancy forces. Free convection phenomena lead to anisotropic diffusion of heat since fluid circulates in form of

rolls and sharp inherent gradients may develop. The movement of hot fluids is controlled mainly by the intensity of the heat flux and by the permeability of the formations. Pure free convection systems are not so common in nature, typically they can be recognized in correspondence of mid-ocean ridges where strong temperature variations induce sea-water circulation, without involving a pressure gradient (*Anderson et al., 1979*). In principle, when fluid-saturated high permeability faults ($10^{-12}$ - $10^{-11}$ $m^2$) or porous sedimentary layers are subjected to normal geothermal gradients (25 °C/km or higher), free convection will spontaneously arise. Involved high permeability implies high Darcy velocities, therefore transfer of fluid and heat is fast, allowing the formation of convective cells confined along the fault planes or inside the permeable formations. When high heat flux is invoked, thermal perturbations are usually induced by intrusive igneous bodies (*Norton and Knight, 1977*). In their pioneering studies, *López and Smith (1995)* demonstrated that increasing of the heat flux allows the widening of the convective domain. The free convective regime is responsible for the formation of the hottest hydrothermal sources around the globe (*McKenna and Blackwell, 2004*).

In forced convection regime (gravity- or pressure-driven convection), heat is transported with the fluid that moves as result of a pressure gradient. Forced convection is a well-known phenomenon, observed at large and small basins throughout the world (*Toth, 1978; Deming et al., 1992; Musgrove and Banner, 1993; Person et al., 1996*). Pressure-driven flow arises from the uneven topography of a basin, as well as from pore fluid squeezed out of a sedimentary formation by the shortening of the upper crust (*Zhao et al., 2008*). This phenomenon, unlike the previously described free convection regime, is not confined to only very high permeability systems. Sedimentary basins and fault systems, with permeability values in the range of $10^{-17}$-$10^{-14}$ $m^2$ and $10^{-14}$-$10^{-11}$ $m^2$, respectively, may host a pressure-driven convection phenomenon. This thermal regime allows the development of hydrothermal sources with low to high discharged water temperatures, and widening of the convective domain was observed when increase in the height of the reliefs occurs (*López and Smith, 1995*).

In natural systems, free and forced convection usually coexist. Therefore, when thermally-driven convection interacts with regional gravity-driven flow, imposed for example by the topography of the basin, the resulting regime is referred as mixed convection. Mixed

convection is invoked as the main active process when shallow heat anomaly is coupled with permeable faults or fractures channeling the groundwater flow *(McKibbin and O'Sullivan, 1981; Raffensperger and Vlassopoulos, 1999; Magri et al., 2015*).

In a complex environment represented by a hydro-geothermal system, all the above mentioned heat transfer mechanisms may coexist. Onset of convection can be evaluated using the Rayleigh number representing the ratio of "buoyant" forces, that drive convective fluid flow, to the viscous forces inhibiting fluid movement (*Horton and Rogers, 1945; Lapwood, 1948*). The free convection threshold, based on a critical value ($4\pi^2$) of the Rayleigh number, is directly attained from classical theories about convective flow in porous media (*Nield, 1968; Bories and Combarnous, 1973; Caltagirone, 1975; Phillips, 1991; Zhao et al., 1997, 1998a, b, 1999a, b, 2000, 2001; Nield and Bejan, 2006*).

Several authors studied the driving mechanisms of both conductive and convective heat transfer processes, with the aim to establish a relation between the on-going thermal process and the geological setting, the presence of fragile or ductile structures and the occurrence of hydrothermal manifestations. For example, *Bjorlykke et al. (1988)* studied the onset of free convection in a heterogeneous system, concluding that even small (< 1 m) low-permeability layers could effectively split the system and inhibit free convection phenomena. *Muffler (1985)* and *Wood and Hewett (1982)* studied the free convection occurrence in a wide variety of sedimentary basins at regional scale. All these studies identified combinations of specific conditions which are suitable for the onset of free convention. Among them, there is a very high basal heat flux coupled with an unusually thick and permeable formation (*Bjorlykke et al., 1988, Raffensperger and Garven, 1995a, b*), or with the proximity of igneous intrusions (*Norton and Knight, 1977*) or of salt domes (*Hanor, 1987; Evans and Nunn, 1989*).

### 3.3 GEOTHERMAL FLUIDS

The fluid involved in the majority of the worldwide geothermal systems and constituting the heat carrier, can originate from: i) meteoric water*:* surface water permeating up to several kilometres from the ground surface, ii) formation/connate water: originally contained in the sediments and buried inside the hosting formations, iii) metamorphic water*:* resulting from

metamorphic reactions, and iv) juvenile water released from cooling magmas (*Nicholson, 2012*).

Contribution of these sources was debated till early 1960's, when several studies (*Craig, 1963; Ellis and Mahon, 1964, 1967; Mahon, 1967*) demonstrated that the geothermal fluids were dominantly meteoric with a very small percentage (5-10 %) of magmatic origin, and the solutes deriving from reactions between groundwater and hosting lithologies (i.e. rock-water interactions). Although the mixing with the magmatic brine is limited, this would significantly affect the chemistry of the final geothermal fluid. In fact, when small pulses of juvenile waters enter the geothermal convection cell, they are at temperatures of more than 400 °C and rich in Cl, $SO_2$ and $CO_2$, contributing the most to the fluid solute composition (*Nicholson, 2012*).

Following this scheme, geothermal fluids evolution starts from meteoric waters penetrating the crust and circulating to depths of more than 5-7 km. Deepening waters get heated, react with the host rocks, and then may start the upward migration by convection. At temperature of ca. 350 °C, deep waters are the primary geothermal chloride fluids containing 1,000 – 10,000 mg/kg of Cl. This soluble element is the first to be leached from the host rocks by water,

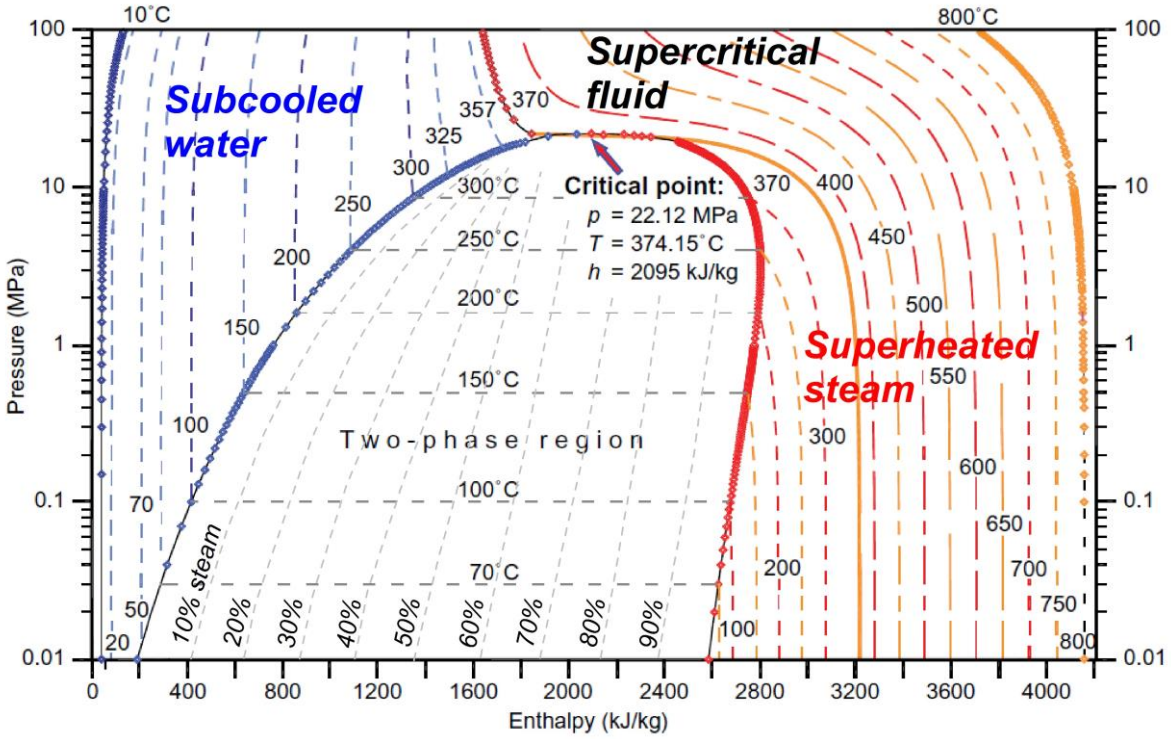


**Figure 3.3:** Pressure-enthalpy-temperature relationship for pure water under hydrostatic conditions, in the ranges: pressure $p \in [0.01, 100]$ MPa, temperature $T \in [0, 800]$ °C and enthalpy $h \in [0, 4200]$ kJ/kg. Modified after *Henley et al. (1984)*.

therefore all other types of geothermal fluids derive directly or indirectly from these chloride waters, following specific temperature-dependent reactions. When the chloride fluids leave the permeable horizon forming the reservoir and ascend to the surface, the hydrostatic pressure imposed upon them by the overlying water column will decrease. If the pressure drops down to a critical value, the dissolved gases and steam separate from the liquid phase (Fig. 3.3). This phase separation is named "boiling" and it is one of the most important process controlling the chemistry of geothermal fluids discharges. The residual chloride water can discharge at the surface in hot springs or travel laterally to finally emerge many kilometres from the upflow zone. The vapours, separated from the boiling zone, may migrate to the surface, independently from the liquid phase, and discharge as fumaroles or may condensate in the cooler ground to form steam-heated, acid sulphate and/or bicarbonate waters (*Nicholson, 1993*).

The relationship between boiling point and depth, described by *Haas (1971)*, is illustrated for pure water in Figure 3.3 as a pressure-enthalpy-temperature graph. As shown in this diagram, a combination of pressure, temperature and associated enthalpy value, defines the "critical point". This is the point at which the phase boundary between liquid and gas terminates, above this value distinct liquid and gas phases do not coexist. In pure water, the critical point occurs at around 374 °C and 22.12 MPa (see Fig. 3.3). As water approaches critical temperature, the properties of its gas and liquid phases converge, resulting in only one phase at the critical point: a homogeneous superheated steam. From the curves in Fig. 3.3 it is possible to define the maximum temperature a fluid can attain at any given pressure (or depth), as well as the depth at which a reservoir fluid at a given temperature will start boiling. From this depth, the two phase zone (steam + liquid) can extend upward toward the surface.

The boiling-point – depth relationship in Fig. 3.3 is for pure water under hydrostatic conditions, but this ideal condition rarely occurs in natural geothermal systems. *Grant et al. (1982)* and *Henley (1985)* demonstrated that hydrodynamic pressures, deriving from buoyancy effects, exist at depth in geothermal systems, and are about the 10 % of the above hydrostatic contribution. This means that higher temperatures can be found at shallower depths compared to the behaviour predicted by the curves in Fig. 3.3, and therefore the phase separation will occur at shallower depths too. On the other hand, for a fluid at a given

temperature, increases in salinity and gas content have opposite effects on the boiling-point – depth profile: increasing the salinity prevents the fluid boiling until shallower depths are attained, while increasing the gas content allows the fluid to boil at greater depths. *Sutton and McNabb (1977)* demonstrated that an increase in the salinity lowers the vapour pressure of water, thus raising the curves and preventing boiling. On the contrary, the presence of high percentage of gas in the fluid, increases the vapour pressure of water, due to the additional pressure of the dissolved gases, thus requiring greater confining pressure to prevent gases

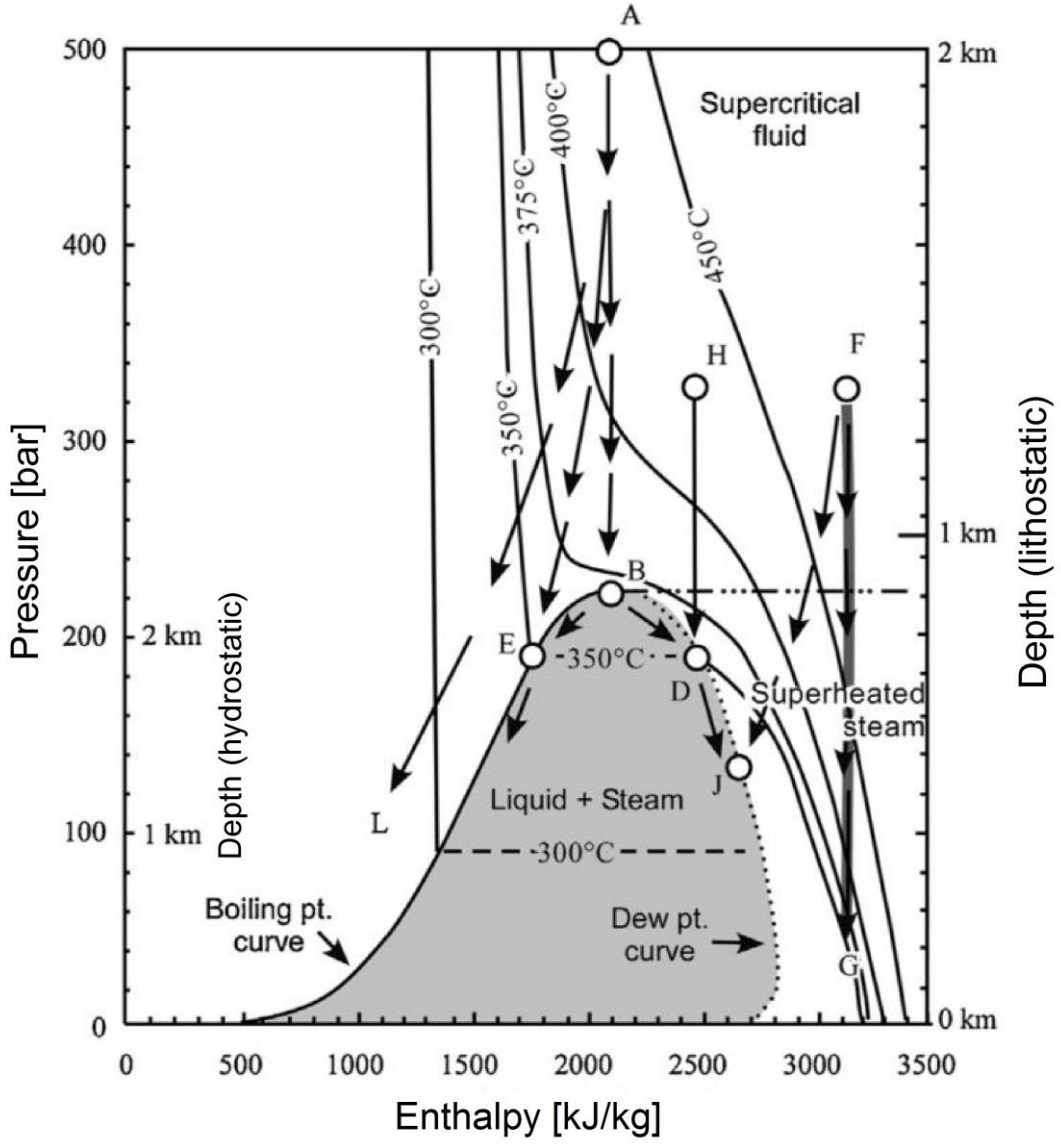


**Figure 3.4:** Pressure-enthalpy diagram for pure water showing selected temperature isotherms. The shaded area showing the conditions under which steam and liquid water co-exist is bounded on the left by the boiling point curve and to the right by the dew point curve. The arrows show adiabatic (vertical) and partly conductive (decreasing enthalpy with decreasing depth) different cooling paths of ascending fluids. See text for discussion. Modified after *Fournier (1999).*

loss from the solution. This means that the boiling zones in vapour-dominated systems (see Section 3.4) will appear at greater depths than for liquid-dominated systems (see Section 3.4), which follow the relationship for pure water as in Fig. 3.3. It is worth to point out that increasing the salinity has only a slight effect on the boiling profile, while relatively small increases in the gas content of the fluid significantly alter the boiling-depth relationship (*Nicholson, 1993*).

Figure 3.4 shows the pressure-enthalpy-depth for pure water, with various different cooling paths of ascending fluids (*Fournier, 1999*). The starting point (i.e. Point A in Fig. 3.4) is represented by a supercritical fluid at 500 bars (2 km lithostatic pressure) and a high enthalpy (2,000 kJ/kg). From this situation, the fluid can ascend along several Pressure-Temperature paths. If the fluid ascends without cooling (i.e. constant enthalpy), it can cross the critical point (Point B in Fig. 3.4), "boiling" occurs and it separates into liquid and vapour phase (Points E and D in Fig. 3.4, respectively). If the same starting fluid undergoes a conductive cooling during his ascent, it can reach shallower depths without phase separation (i.e. no "boiling" occurs, Point L in Fig. 3.4). This is typical in geothermal systems where the circulating fluids thermally interacts with the surrounding rocks, resulting global heat loss prevents phase separation. Point H in Fig. 3.4 is another starting point represented by a higher temperature supercritical fluid, as could happen in vapour-dominated geothermal systems. If this fluid ascends without heat loss, it can reach the two-phase boundary and therefore "boiling" occurs (Point D in Fig. 3.4). The last extreme example is the case of a superheated fluid (Point F in Fig. 3.4), for which the enthalpy decrease by conduction during the ascent is insufficient to allow phase separation and the fluid reaches the surface as superheated steam (Point G in Fig. 3.4).

### 3.4 GEOTHERMAL RESERVOIRS

Geothermal energy is a form of thermal energy generated within the high temperature portion of the Earth's crust, mantle and core. Quantitative expression of the terrestrial heat-flow is the geothermal gradient, that is the increase in temperature with depth in the Earth's crust. Down to depths accessible by drilling with modern technology, the average geothermal gradient is about 2.5-3 °C/100 m (*Kühn, 2004*). However, there are vast areas in which the

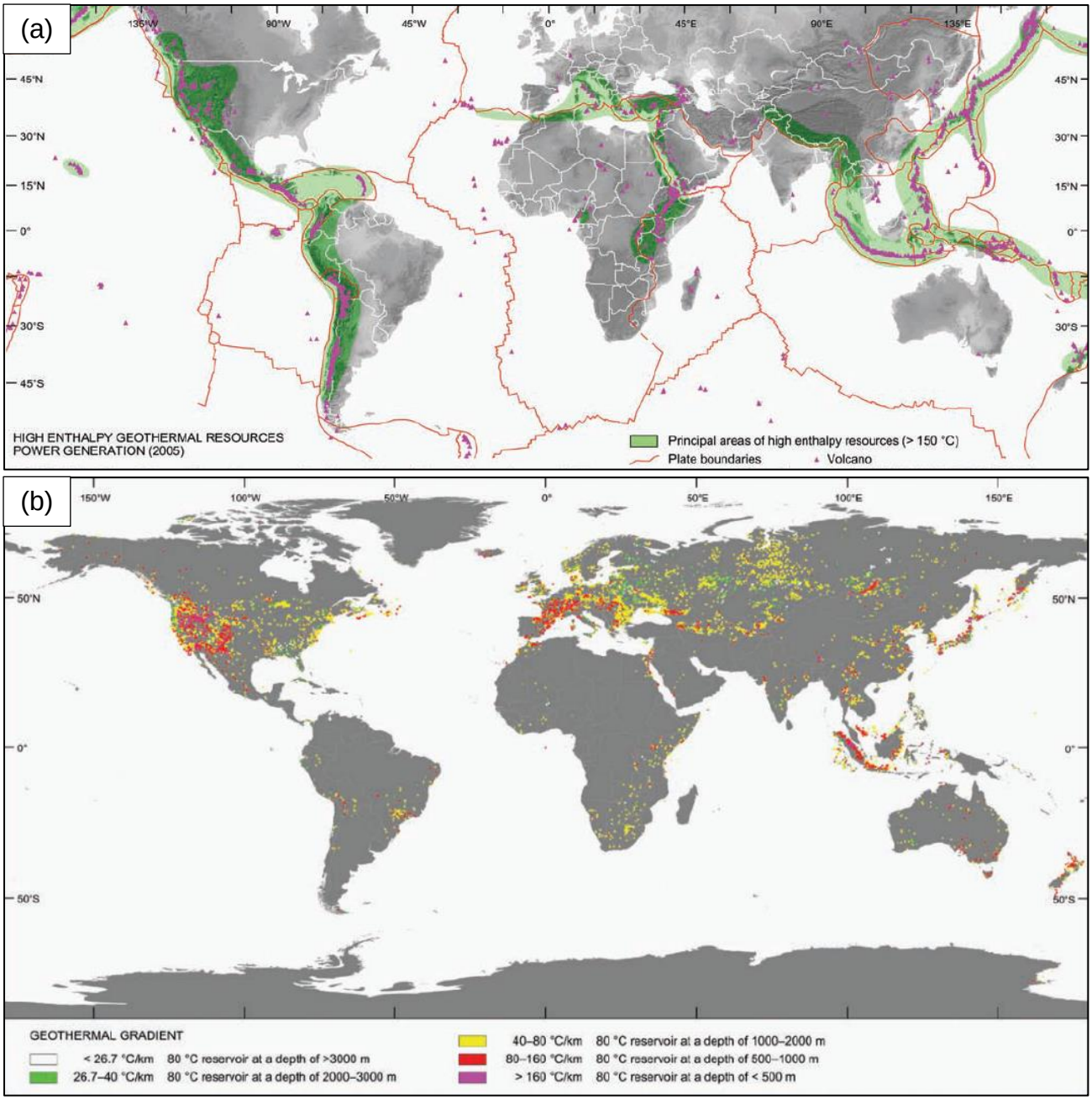


**Figure 3.5: (a)** Distribution of high- and low-enthalpy geothermal resources along plate boundaries and in active volcanic zones (*Chandrasekharam and Bundschuh, 2008*). **(b)** Geothermal gradient data and corresponding depths, where geothermal resources with a suitable temperature for power generation of minimum 80°C can be expected (*Chandrasekharam and Bundschuh, 2008*).

geothermal gradient is definitely lower or higher than this average value (e.g. 5-6 °C/100 m in active volcanic regions). In correspondence of these positive thermal anomalous areas (Fig. 3.5), geothermal fields have been initially recognized, by the help of surface manifestations such as geysers, fumaroles, or boiling mud-ponds (*Toth and Bobok, 2016*). Apart from active volcanic regions and regions around tectonic plate margins, promising geothermal fields can

be found in regions with normal geothermal gradients and coupled with a wide variety of geological settings (Fig. 3.5; *Kühn, 2004*). Such ubiquitous occurrence makes geothermal energy particularly interesting when speaking of Earth's renewable energy sources and sustainable future.

When not purely conductive, a geothermal field can be described schematically as a system of waters circulating laterally and vertically, at various temperatures and pressures, in the upper crust of the Earth and transferring heat from a heat source to a heat sink, usually the surface (*Hochstein, 1990*). In terrestrial geothermal systems the circulation of waters can reach depths of approximately 5 km, lasting from thousands up to millions of years (*Pirajno, 1992*). A typical geothermal system is made up of three main elements: i) a heat source, ii) a fluid, which is the heat carrier, and iii) a reservoir (*Giggenbach, 1997; Hayba and Ingebritsen, 1997; Dzikowski et al., 2016, Volpi et al., 2017*). Different heat sources have already been described in the previous Section 3.1. The geothermal (heat carrier) fluid is water, in the majority of cases of meteoric origin, in liquid or vapour phase depending on its temperature and pressure (see Fig. 3.3). Geothermal fluids can discharge at the surface in the form of geysers, fumaroles, boiling mud-ponds or hot springs. The reservoir is a volume of permeable rocks from which the field's internal energy content can be recovered through the use of native or man-injected reservoir circulating fluid (i.e. steam, hot water, or a mixture of both). At first sight, geothermal reservoirs could be subdivided in two classes: natural or man-made sub-systems (Fig. 3.6). From the classification of *Toth and Bobok (2016)*, a natural geothermal reservoir is an extended, porous and permeable formation saturated with hot water or steam, and characterized by both a sufficiently large heat supply and a reliable recharge mechanism. The most productive geothermal reservoirs are hosted in a fractured rock mass with high vertical permeability, allowing the onset of thermal convection phenomena. Thanks to new technologies, nowadays it is possible to create artificial reservoirs in Hot Dry Rocks (HDR o EGS; Fig. 3.6), which are characterized by a strong heating source from below, but no water nor pore/fracture-type permeability are present (*Hirschberg et al., 2014*). In this case, the fracture system is artificially induced by hydraulic fracturing, and then water is recirculated through a doublet system made by an injection and a production well. The injected water is

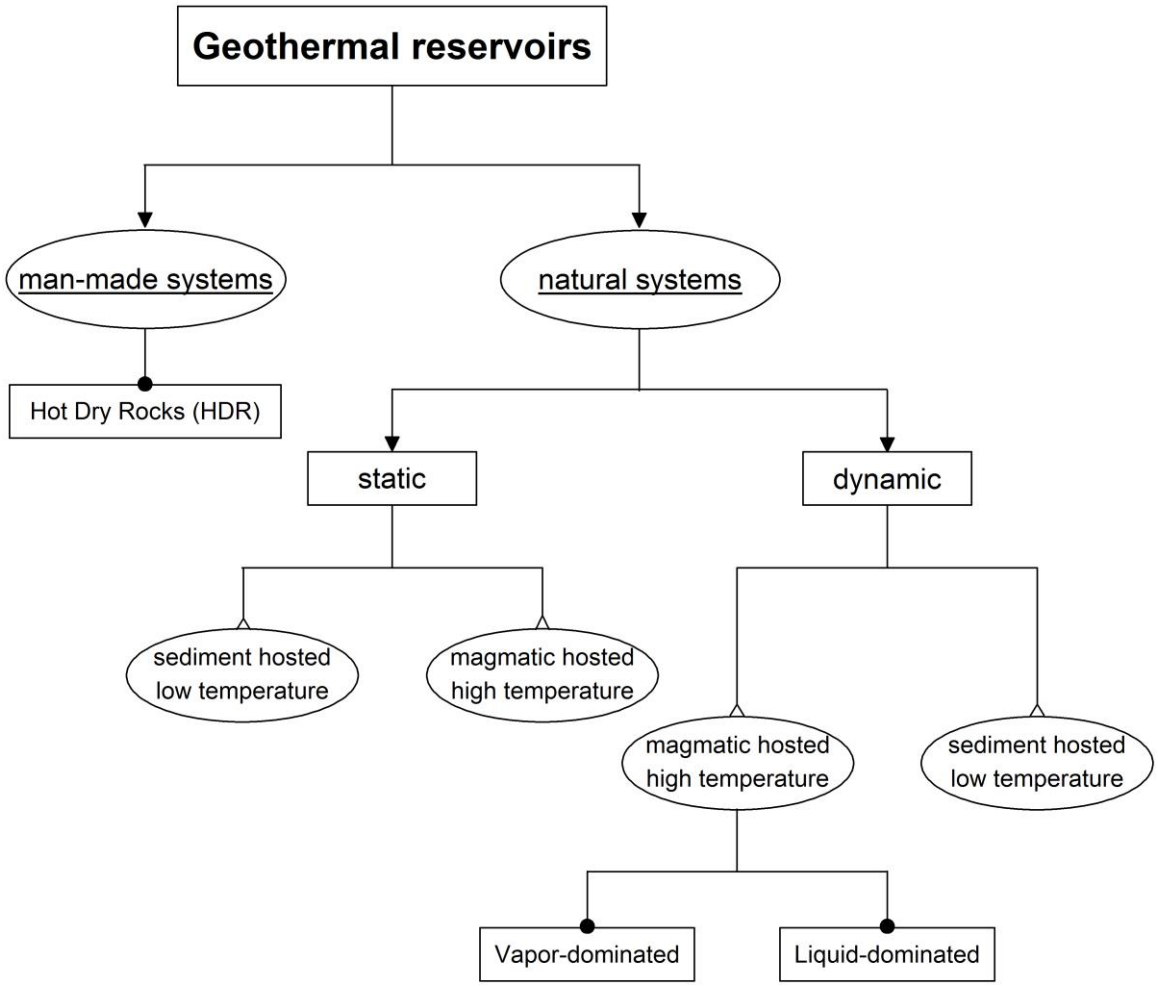


**Figure 3.6:** Classification of geothermal reservoirs, adapted and merged after *Nicholson (1993), Pirajno (1992)*, and *Heiken (1982).*

heated as it flows deep through the fracture system, and then delivered to the surface via the production well.

Beside this early stage classification proposed by *Toth and Bobok (2016)*, for the most part, geothermal reservoirs have been classified according to the dominant heat transfer mechanism occurring between the geothermal fluid and the reservoir rock through which it moves. In fact, whether the geothermal system is natural or man-made, heat transfer might occurs partly through conduction and partly through convection (free or forced), as the heat-bearing fluid flows up to the surface.

Nevertheless, a clear and unique classification of geothermal systems has not been accepted worldwide since geothermal systems occur in a variety of geological, physical, chemical and thermodynamic conditions, which are reflected in the fluid properties and its potential

applications. In the past, many authors proposed several classifications of geothermal systems and resources, based on different characteristics, mainly temperature, geological setting, mineral deposit or fluid type (*Muffler, 1979; Heiken, 1982; Pirajno, 1992; Nicholson, 1993; Sanyal et al., 2005; Moeck et al., 2014; Santilano et al., 2015*).

By merging the work of different authors, in the present study a classification of the geothermal systems is presented (Fig. 3.6) as a combination of contributions by *Nicholson (1993)*, *Pirajno (1992)* and *Heiken (1982)*. The geothermal reservoirs will be classified in the first stage based on their intrinsic hydraulic conditions, which are tied tightly to the active heat transfer mechanism. The geothermal reservoirs are primarily divided into dynamic and static systems (Fig. 3.6). A static geothermal reservoir does not involve fluid movement, therefore conductive heat-flow is only active. The average Earth's geothermal gradient of 30 °C/km results in a relatively moderate conductive heat flux of about 55.6 mW/m$^2$. Although such an environment is unsuitable for recoverable hydrothermal systems, the reservoir's internal energy can still be extracted by means of geothermal heat pumps (GSHP o GWHP; *Toth and Bobok*, *2016*). Dynamic geothermal systems arise where input of heat (usually magmatic heat) at depths of a few kilometres, sets deep groundwater in motion. Therefore, heat is transferred by convection. Since a high geothermal gradient is necessary to trigger thermal convection, magmatic intrusions represent the source of thermal energy to most of the Earth's high temperature (>150 °C) geothermal systems. However, few high-temperature systems occur also in areas of little or no apparent volcanic activity. This is the case of superficial or meteoric water deepening through faults or permeable strata in areas of above-average conductive heat flow (e.g. The Beowawe geysers, Nevada; *White, 1992*). Typical dynamic geothermal reservoir fluids are of meteoric origin but in some systems also deep fossil marine or other saline waters may be present (connate waters). Systems near the coast can be fed by both meteoric water and seawater (*Nicholson, 1993*).

Both the static and dynamic geothermal systems can be further divided depending on the temperature, with low temperature and high temperature reservoirs strictly related to the hosting rock type (i.e. sediment hosted and magmatic hosted; see Fig. 3.6).

Static low temperature or sediment hosted reservoirs are found in deep sedimentary basins where fluids are represented by waters trapped within the thick sedimentary sequences.

Usually to develop this kind of reservoir, a very low vertical permeability within the formations is needed, as a consequence waters remain trapped at depth until released tectonically or by drilling. These systems are also named low temperature reservoirs, because the involved fluids reach maximum temperatures around 70-150 °C at depths of 2-4 km due to conductive heat flow only. Low waters temperatures and formations permeability allow this sediment hosted geothermal system to be exploited only for direct energy use (e.g. through geothermal heat pumps) and not for power production. They are of greatest importance for countries with no strong positive thermal anomalies, where they remain the only geothermal resource currently under exploitation (e.g. North and Eastern Europe, *Kühn, 2004*). Static high temperature or magmatic hosted reservoirs are found in areas with shallow or deep-seated granitic bodies emplacement. In these cases, the magmatic intrusion is set at the boundary between hard and plastic rocks, crystallized at depths between 5 to 15 km, which normally do not vent at the surface (*Pirajno, 1992*). Above the intrusion, through the crystalline bedrock of good thermal conductivity but low permeability, a very intensive terrestrial heat-flow may develops. This system can be characterized by the presence of hydrothermal fluids, which are assumed to be generated entirely within the cooling magma body and remain confined in a closed system.

Dynamic high temperature or magmatic hosted reservoirs are the most common and exploited geothermal systems. They are found in areas with anomalous high geothermal gradient and rock temperatures of several hundred degrees Celsius at exploitable depths, i.e. between 1 and 3 km. These geothermal reservoirs are worldwide widespread and are characterized by an active time span ranging from $10^5$ to $10^6$ years (*Henley and Ellis, 1983*), which makes them particularly suitable for electricity production. The occurrence of dynamic, high temperature, magmatic hosted geothermal fields is always tectonically determined, indeed they are recognized in block faulting, grabens, rifting and collapsed caldera areas. These structures characterize active plate margins such as subduction zones (e.g. Pacific Rim), spreading ridges (e.g. Mid-Atlantic), rift zones (e.g. East Africa) and within orogenic belts (e.g. Mediterranean, Himalaya).

In the majority of the cases, the heat flow is provided by intrusive masses (Fig. 3.7), thus such high-temperature systems are termed volcanogenic. However, also non-volcanogenic or

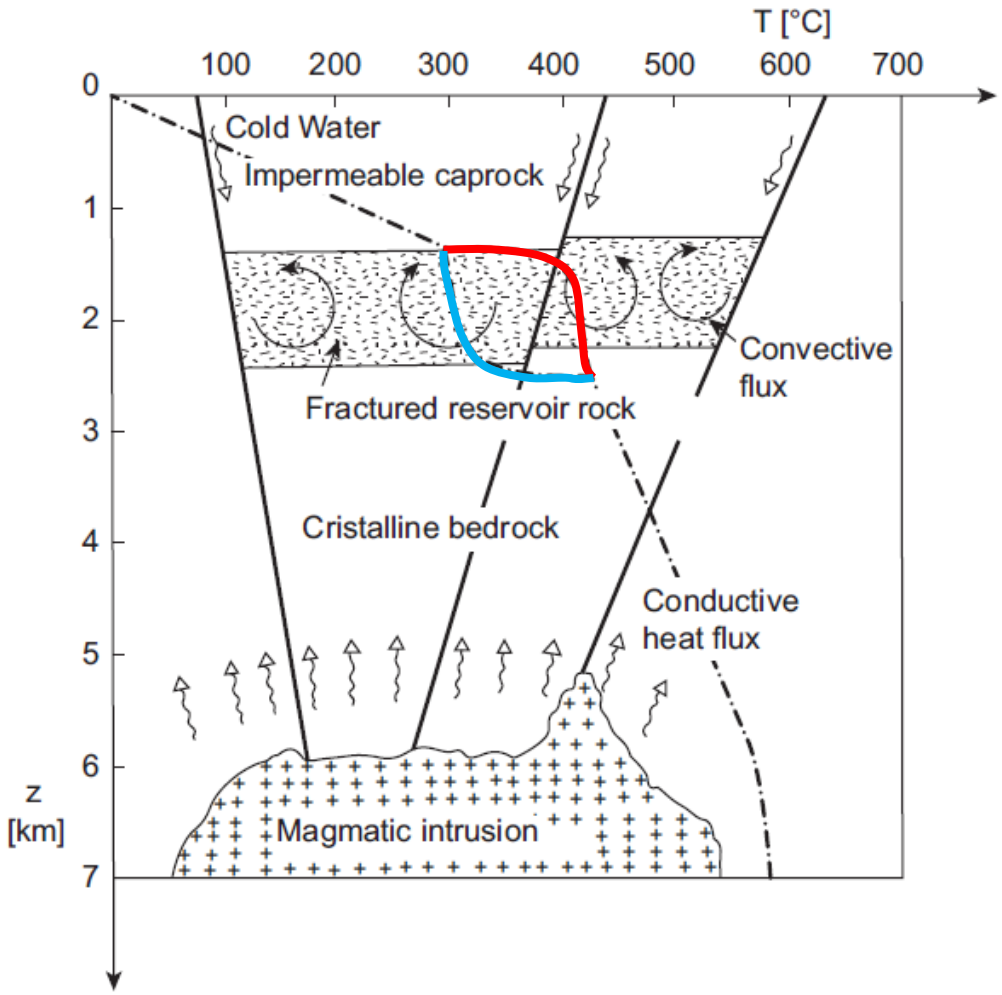


**Figure 3.7:** Schematic conceptual model of a dynamic, high-temperature geothermal system. Dashed line represents the geothermal gradient. Blue and red lines highlight the descending and ascending flows, respectively, whithin the convective cells developed in the fractured reservoir rock. Modified after *Toth and Bobok (2016).*

tectonic high-temperature systems may develop (e.g. in areas with tectonic uplift of hot basement rocks), even if they are less common (*Nicholson, 1993*). In the typical conceptual model of the volcanogenic geothermal field (Fig. 3.7), when magma did not reach to the surface, the intrusion remains at depth of 5-15 km triggering an intense heat-flow in the highly conductive crystalline bedrock above. A weak conductivity porous or fissured aquifer is emplaced over the bedrock. This layer cannot transfer the intense subsurface heat but the reservoir fluid allows for thermal convection. Further up, a low permeability rock layer, also called cap rock, may overlay the aquifer causing substantial overpressures in case of steam-producing reservoir (*Toth and Bobok, 2016*). Although a high heat-flow is present, a very low temperature gradient is recorded inside the aquifer due to the convective circulation. Here

the temperature change is very small and a thermal inversion can be observed; the temperature gradient is large between the top of the reservoir and the surface, and between the bottom of the reservoir and the magmatic intrusion (see Fig. 3.7).

The high temperature-magmatic hosted reservoirs can be further distinguished between vapour- and liquid-dominated system (Fig. 3.6). Vapour-dominated or dry-steam reservoirs

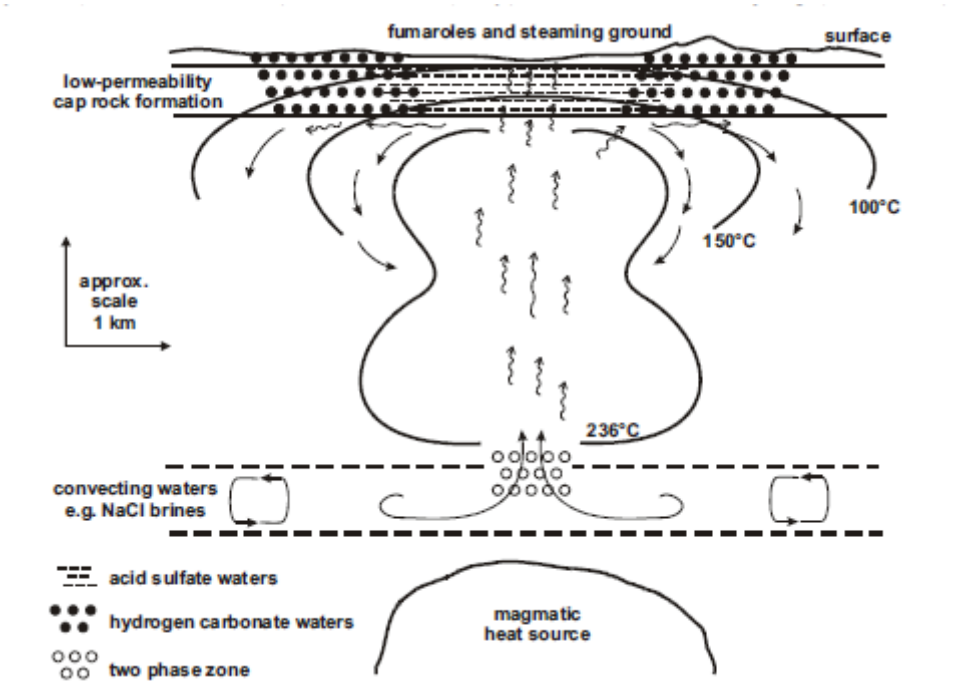


**Figure 3.8:** Conceptual model with characteristic features of vapour-dominated geothermal systems (*Nicholson, 1993*).

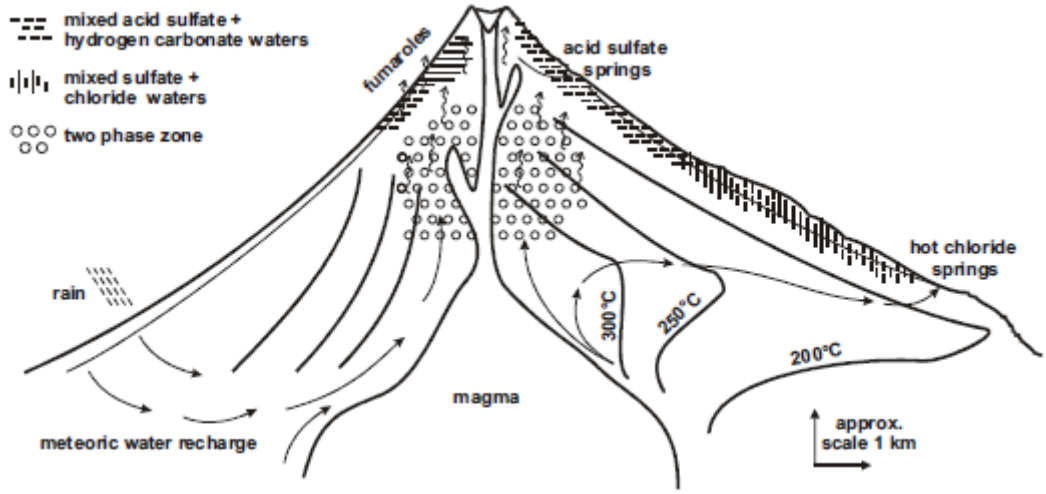


**Figure 3.9:** Conceptual model of liquid dominated geothermal systems in a high relief, typical of an andesitic volcanic terrain (*Henley and Ellis 1983*).

(Fig. 3.8) occur in areas that are tectonically active, but with no active volcanism, and characterized by peculiar surface expressions, such as fumaroles, steaming ground and acid-sulphate waters from hot springs (Fig. 3.8; *Nicholson, 1993*). The reservoir fractured rock matrix is filled with superheated steam at a relatively constant temperature of about 236 °C, which is the temperature of maximum enthalpy of saturated steam (see Fig. 3.3; *Haar et al., 1984*). The steam itself contains non-condensable gasses, but no hot water (*Toth and Bobok, 2016*). Due to the high temperatures, the vapour-dominated systems are extensively exploited, although the undisturbed states are poorly known since deep drillings often do not penetrate the vapour zone (*Kühn, 2004*). The lateral boundaries of this type of reservoir must be impermeable, or liquid water would flood sideways into the steam-filled region and collapse the superheated-steam reservoir. Convection in these systems is originated by the up flowing of the hot steam from the deepest portion of the reservoir, and by the lateral flowing along the base of the low-permeability cap-rock. Here the steam cools as it flows, and eventually condenses and recirculates into the deep reservoir (*Nicholson, 1993*). These high temperature systems are not very common, at present only three vapour-dominated site have been well characterised: The Geysers (California, USA), Larderello (Italy), and Kawah Kamojang (Indonesia).

Liquid-dominated reservoirs (Fig. 3.9) are more widespread than vapour-dominated systems, and they can be associated with high relief or low relief active volcanic environment. The deep geothermal fluid may appear at the surface, often close to the up-flow area, by fumaroles and steam heated aquifers. The actual formation temperatures are substantially lower than the saturation temperatures determined by the boiling curve (see Fig. 3.3), thus the water remains in liquid state in the reservoirs (*Toth and Bobok, 2016*). Examples of these systems are found in Indonesia, Taiwan, Japan, and the Philippines (*Nicholson, 1993*).

Dynamic low temperature or sediment hosted reservoirs (Fig. 3.10) are represented by deep groundwater systems that can occur in a variety of geological settings characterized by elevated or normal heat flow conditions. They are also called low-enthalpy geothermal systems and are widespread compared to the previously described high temperature reservoirs. They are found throughout Europe and Asia, and along some areas of Tertiary volcanism in the Pacific (*Nicholson, 1993*). The development of such low-temperature system

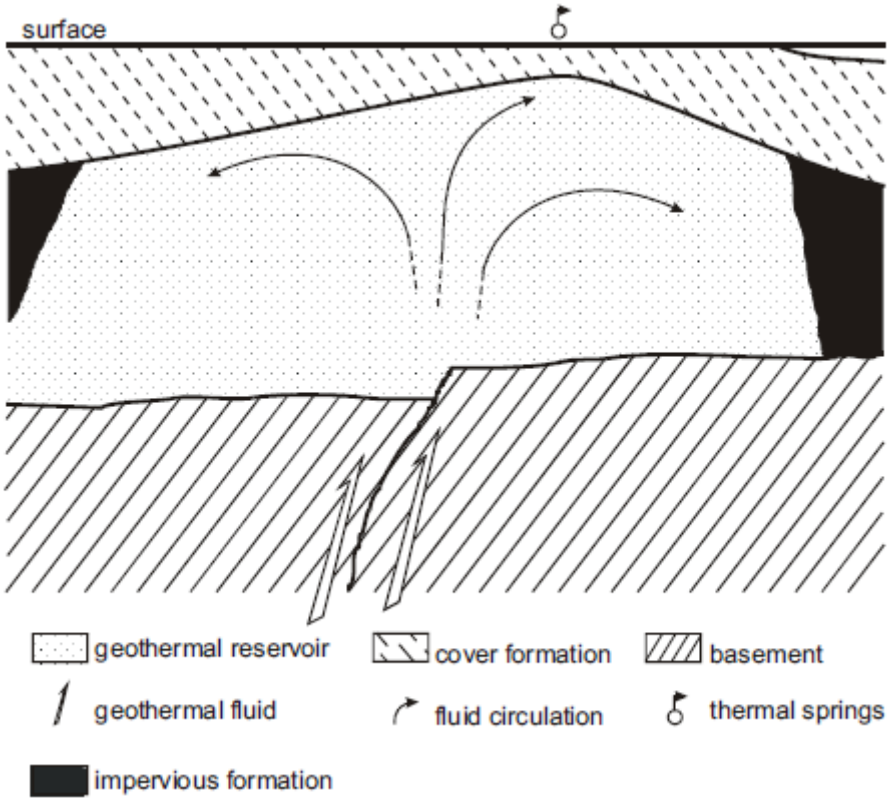


**Figure 3.10:** Conceptual model of groundwater circulation in a dynamic low temperature or sediment hosted system (*Kühn, 2004*).

is not related to specific volcanic or magmatic activity at depth, and therefore, given the varied origins of this type of system, no idealized model can be developed. These reservoirs are usually associated to natural deep flow systems mostly of meteoric water origin, circulating in areas where the complex geological setting is made by folded permeable strata, fault intersections and thrust faults, putting in contact various types of rocks (*Sonney, 2010, Volpi et al., 2017*). These deep flow systems are heated by the tectonic uplift of hotter rocks from depth, by residual heat from intruded plutons or by the local heat flux (*Albu et al., 1997*). According to *Bowen* (1989), dynamic low temperature, sediment hosted reservoirs are defined as convective geothermal systems with high porosity, high permeability, and with deep natural circulation of the heat carrier fluid (meteoric water).

Low-enthalpy geothermal systems usually discharge thermal waters through hot springs with temperatures around ≈ 30-65 °C. The geothermal water chemistry depends on the mineral composition of the hosting rocks and often on the relative contribution of the inherent formation water, the up-flowing geothermal water, and the recharging meteoric water (*Kühn,*

*2004*). The Alps mountain range, with a high concentration of geothermal sites known and exploited, is one of the areas in Europe where many deep circulation systems occur as thermal springs.

### 3.5 HYDROGEOTHERMAL ENERGY USE

For the early man the Earth's internal heat and hot springs had religious and mythical connotation meaning, they were the places of the God or endowed with divine powers (*Stober and Bucher, 2013*). *Cataldi (1999)* resumes the history of geothermal energy use, claiming from the non-written history that natural heat of volcanoes and other geothermal sources began to be used in the remote Paleolithic era. The most ancient data on the presence of people in geothermal areas only dates from 8,000 to 10,000 years ago. During that time, humans learned more about the different manifestations of terrestrial heat. The first uses were, of course, the most naturals and immediate: taking hot baths, cooking and practicing basic therapeutics. The period between human's first experiences with geothermal phenomena and the time when the simplest uses of the products of the Earth's heat were known, has been named the *Year Zero of Geothermics* (*Cataldi, 1999*). The uses of natural hot water for bathing, and the exploitation of hydrothermal products for a wide range of practical applications, extended to the boundaries of ancient Rome, achieving maximum use during the 3$^{rd}$ century A.D., the Roman Empire's apex (*Cataldi and Burgassi, 1999*). Besides the numerous private baths, installed in almost every villa and in many private buildings, there were over 1,000 public baths in Rome: about one for every 1,000 inhabitants (*Montanelli, 1969*). With the fall of Roman empire, in the 6$^{th}$ century, geothermal exploitation also declined throughout Southern Europe, this dark period lasted until the beginning of the second millennium (*Toth and Bobok, 2016*). There are evidences that geothermal resources were still being exploited around the world in the centuries that followed. For example in China, where about 2,000 years ago, bathing and treatment centres were erected at the hot springs Huaquingchi and Ziaotangshan near Beijing (*Ji-Yang, 1995*). *Cataldi et al. (1999)* collected all the Earth's geothermal heritage sites, showing that non only Romans and Chinese, but also Turkish (*Özgüler and Kasap, 1999*), Japanese (*Sekioka, 1999*), Russians (*Svalova, 1999*), Icelandic (*Fridleifson, 1999*), Frenches (*Gibert and Jaudin, 1999*), and Maori people in New Zealand

(*Severne, 1999*) have used geothermal resources, even if probably on a more limited scale and rudimental form.

On the global scale, the first advantages derived from geothermal resources have been mainly limited to the direct use of local Earth's surface manifestations (i.e. fumaroles, geysers, mud ponds and hot springs). Later on, with the opening of the second millennium, thanks to technical progress and to a better knowledge of the subsoil, many countries started to be attracted by the potentiality of geothermal energy and its use began to be industrial (*Le Lous, 2017*). *Allegrini et al. (1992)* identified three main periods of geothermal industrial exploitation: i) hydrothermal fluids as raw material, ii) hydrothermal fluids as source of thermal energy for the production cycle of boric acid, and iii) hydrothermal fluids as source for thermal energy and for electrical power production. The development of geothermal power generation, i.e. the second period of *Allegrini et al. (1992)* classification, is clearly associated with the Larderello area of Tuscany in central Italy (*Tiwari and Ghosal, 2005*).

From 1,000 A.D. a far-reaching cultural reawakening over all Italy led to relaunching many old enterprises and beginning many new ones. This occurred in all commercial and mining activities, including the exploitation of hydrothermal sources (*Burgassi, 1999*). In the Larderello region, in 1818, François de Larderel (1789-1858) made the history first commercial exploitation of the geothermal energy. Thanks to his efforts geothermal water was first used for boric acid production in 1827 (*Durand-Delga et al., 2001; Dickson and Fanelli, 2013*). Boric acid production was an Italian monopoly in Europe, and became a large-scale industry process in the middle of the 19$^{th}$ century (*Toth and Bobok, 2016*). In the twentieth century, following the increasing global energy needs and the growing interest in renewable energies, geothermal power generation took off, and Larderello site is once again the cradle of a bold invention (*Le Lous, 2017*). Indeed here, for the first time in the world, it was experimentally demonstrated the conversion of geothermal energy into electrical energy: on July 4$^{th}$, 1904, prince Ginori Conti (1865-1939), husband of a great-granddaughter of François de Larderel, symbolically lights five bulbs with a dry steam engine (Fig. 3.11; *Varet et al., 2004; Stober and Bucher, 2013*).

**Figure 3.11:** Lardarello 1904: The picture shows Principe Piero Ginori-Conti with his apparatus that converted geothermal to electrical energy for the first time in history. The installation had the power to light fife light bulbs (Photograph: *Unione Geotermica Italiana 2010*).

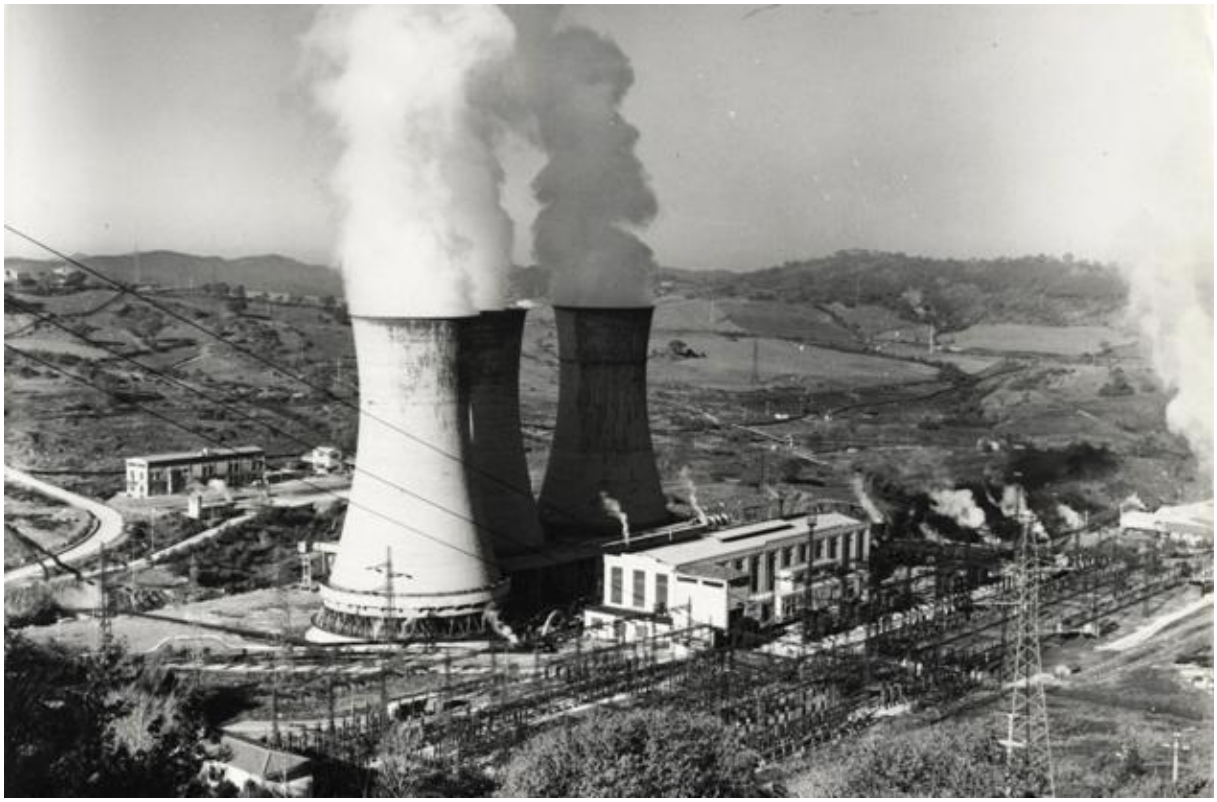

**Figure 3.12:** Geothermal power plant "Valle Secolo" in Larderello (120 MWe, 1991) (Photograph: *Unione Geotermica Italiana 2010*).

In 1913, the first geothermal power plant in the world was in operation with the name of "Larderello 1" (*Luzzini, 2012*). The industrial exploitation of geothermal energy for large scale electricity production would then develop more significantly, in fact by 1942, Larderello's installed geothermoelectric capacity reached 127,650 kWe (Fig. 3.12). Several countries soon followed Italy's example: in 1919 the first geothermal wells were drilled at Beppu field in Japan (*Allis and Yusa, 1989*) and, in 1921, several geothermal wells were drilled at the Geysers field, California (*Thomas, 1986*). Between the two World Wars, oil prospectors found huge geothermal reservoirs all over the world, usually by chance. In 1958, based on exploration data and after extensively mapping the variations in the Pannonian Basin's terrestrial heat flow, the Hungarian mining engineer Boldizsar composed the world's first regional heat flow map (*Boldizsar, 1964*). In the same year, a small geothermal power plant began operating in New Zealand, another started in 1959 in Mexico, and in the United States in 1960 (*Toth and Bobok, 2016*).

With current technologies, only high-temperature geothermal resources (>180 °C) are suitable to generate electricity through the production of steam, while medium to low temperature resources find a more local-scale application (e.g. urban district heating, fish farming, and greenhouse heating). We refer to the work of *Lindal (1973)* for an exhaustive classification of industrial and other applications of low to medium temperature geothermal energy systems.

At the beginning of the third millennium, the application of geothermal heat for direct utilization was reviewed by *Lund and Freeston (2001)* for 60 countries worldwide, among these 55 reported some form of geothermal direct utilization. The authors updated the previous survey carried out in 1995 (*Freeston 1999*). *Lund and Freeston (2001)* estimated the installed thermal power at the beginning of 2000 as 15,145 MWt, showing a strong positive trend compared to the 8,664 MWt registered in 1995. More recently, *Bertani (2016)* analysed the major activities carried out for geothermal electricity generation since the Word Geothermal Congress of 2010 (*WGC2010*). As in 2015, 78 countries reported direct utilization of geothermal energy, a significant increasing trend was observed from the 28 of 1995, to the 58 of 2000, and the 72 of 2005. In terms of installed capacity, this led to an increase of about 1,8 GW in the five year term 2010–2015 (about 17 %).

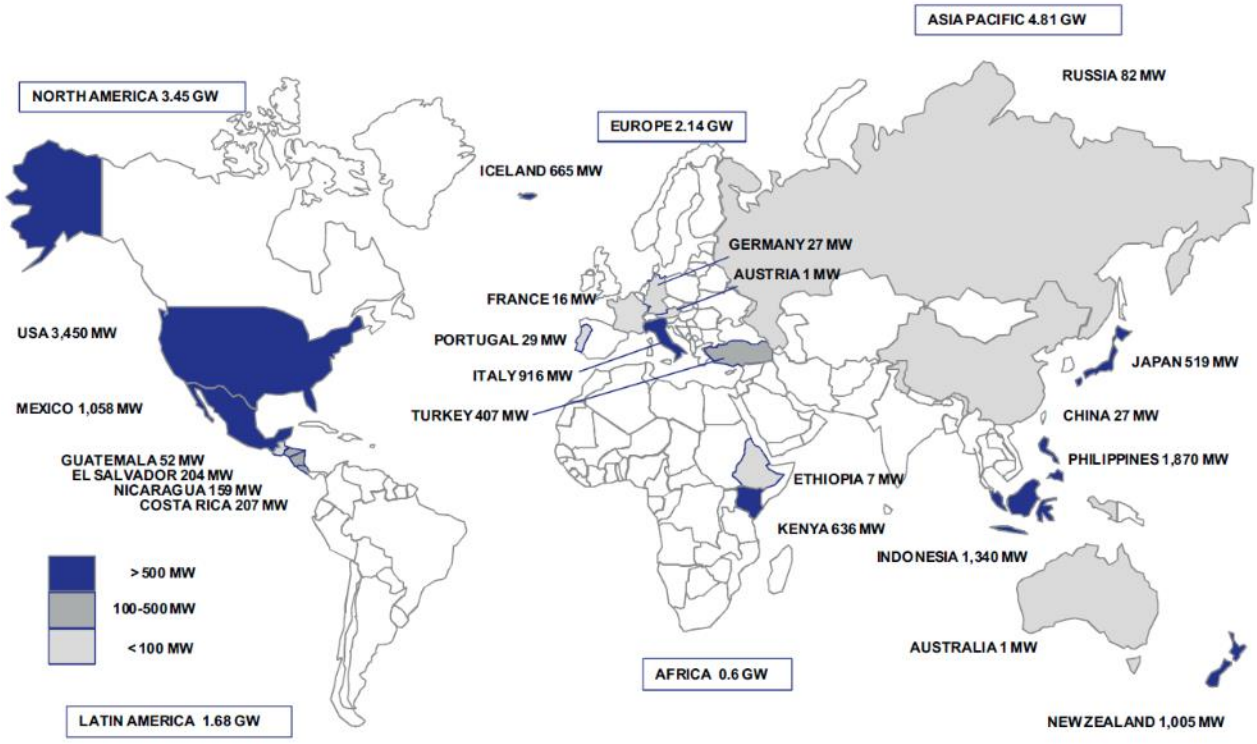


**Figure 3.13:** Worldwide Geothermal installed capacity in 2015 [12.6 GWe] (*Bertani, 2016*).

The calculated growing rate of 350 MW/year shows evident increment from the average value of about 200 MW/year recorded in the precedent 2000–2005 period (*Bertani, 2005a,b, 2006, 2007, 2010, 2012; Antics et al., 2013*). The top five countries for installed capacity in 2015 were USA, Philippines, Indonesia, Mexico and New Zealand, while Italy was only in 6$^{th}$ position (see Fig. 3.13; *Bertani, 2016*). The same author calculate the 2016 worldwide installed capacity value being around 12.7 GW and confirming the positive trend started in 2010. This was achieved mainly due to both, the increase in the medium-low temperature development projects through binary plants, and the strong combined effort in realizing all the economically viable projects worldwide. With an eye to the future, *Bertani (2013, 2016)* provides installed capacity short- and long-term forecasts, for 2020 and 2050 respectively. The predicted values are 21 GWe in 2020 and 140 GW in 2050, hoping on the transformation of all the paper-projects in real plants and considering the development of the promising EGS (Enhanced Geothermal System) fields. If this target will be reached, it would be possible to produce from geothermal sources up to the 8.3 % of total world electricity production, serving 17 % of world population. Moreover, 40 countries (located mostly in Africa, Central/South America, Pacific) could be 100 % geothermal supplied (*Bertani, 2016*).

### 3.6 RESERVOIR EXPLORATION TECHNIQUES

Geothermal systems occur in nature in a variety of geological, physical, chemical and thermodynamic conditions, this makes their identification not an easy task. Moreover, developing a geothermal exploitation plan requires a remarkable effort in both time and financial resources. For this reasons, a detailed characterization of the system coupled with an appropriate numerical modelling of the involved heat and fluid transfer processes, aiming to investigate the feasibility of a geothermal power production, is always strongly recommended (*Stober and Bucher, 2013; Li et al., 2016*).

As common practice, in the early exploration stage of the reservoir, the first applied techniques are the indirect investigation methods, due to their lower costs. They include remote sensing and a branch of field surveys techniques, such as geological-hydrogeological studies, geochemical and superficial geophysical surveys. These are useful preliminary methods to identify promising areas where later, more detailed and sophisticated exploration techniques (e.g. borehole geophysical tests, borehole injection tests and geothermal tracer tests), may confirm or not the presence of an exploitable hydro-geothermal system. Moreover, all these the reservoir exploration techniques allow to estimate geological and hydrogeological parameters needed to construct a reliable numerical model of the field, which chronologically represent the last step in a geothermal exploration and exploitation plan.

Remote sensing technologies include a wide variety of techniques (e.g. aerial photography, multi-spectral, and hyper-spectral satellite imagery) used to inspect, at different scale, Earth's surface and its characteristics (e.g. land cover, geological structures, temperatures). *Wolski (1998)* highlights the importance of defining surface characteristics related to groundwater movement and storage (i.e. land morphology, soils, faults, fractures, shear zones, recharge and discharge zones, vegetation, and drainage patterns) by using remote sensing images. Airborne investigations have obtained increased importance in the last few years for the investigation of geothermal reservoirs too. New technologies, such as the Forward Looking Infrared Radiometry (FLIR), allow to compile high-resolution temperature maps coupled with the geologic structures (Fig. 3.14; *Mongillo, 1992; Yourownpower, 2007; Haselwimmer et al.,*

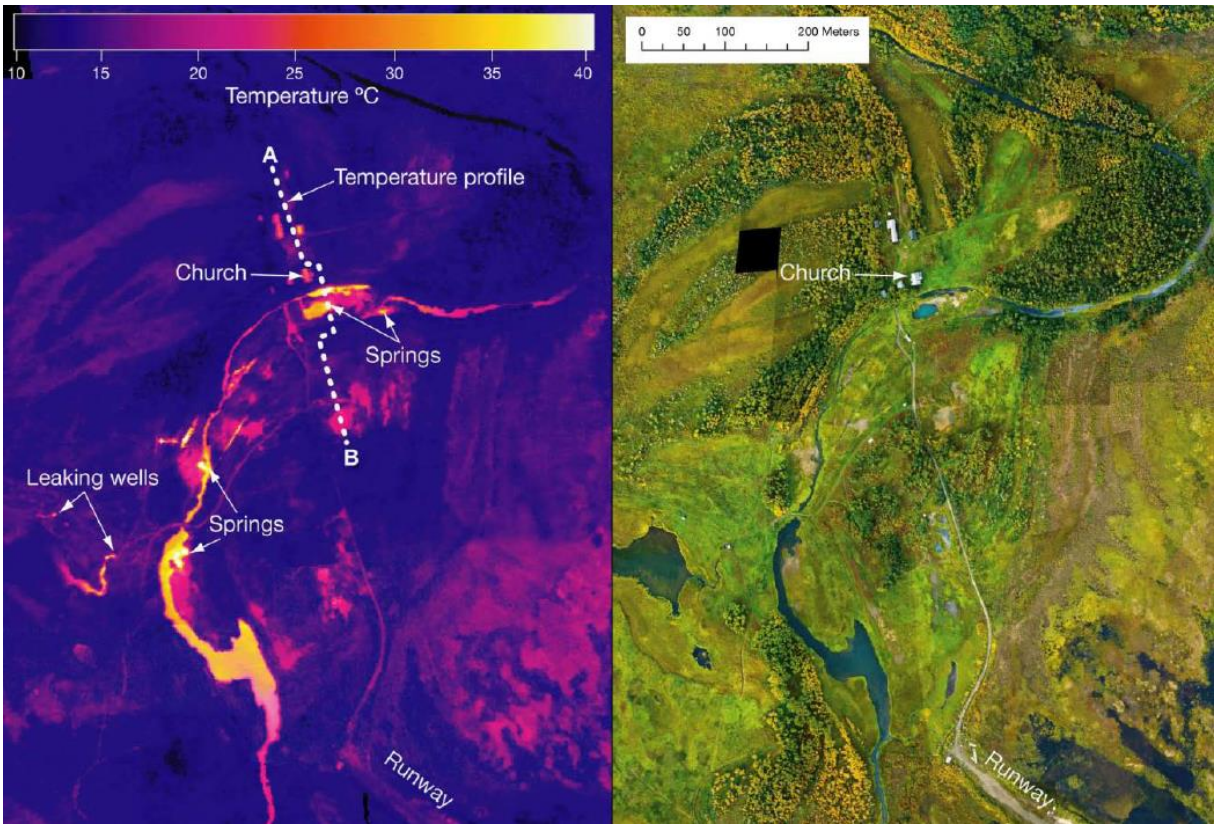


**Figure 3.14:** Example of application of Forward Looking Infrared Radiometry (FLIR) to the case study from Pilgrim Hot Springs, Alaska (*Haselwimmer et al., 2013*).

*2013*). Usually, big scale features are difficult to recognize from the surface, therefore remote sensing has become a fundamental tool to compile detailed regional geological maps, which include stratigraphic units and inner structures. These information are fundamental to recognize a possible geothermal reservoir, because fluid flow and discharges are structurally controlled in the majority of geothermal systems.

Field survey techniques group geological, hydrogeological, geophysical and geochemical survey methods, with both surface and subsurface application. They are cheap, efficient and widespread tools to assess particular properties of geothermal reservoirs. A thorough literature is available about this kind of surveys and their fields of application (*Weight and Sonderegger, 2001; Singhal and Gupta, 2010; Moore, 2011; Brassington, 2017*).

Geological and hydrogeological surface and subsurface studies (i.e. geomorphological investigations, groundwater vulnerability mapping, measurements of surface and groundwater levels, discharges of springs and rivers, rainfall, estimation of infiltration, and location of surface and groundwater divides) provide the geological maps of the area of

**Figure 3.15:** Fumaroles and boiling muds at the Namafjall Hverir geothermal field, Iceland.

interest and the identification of tectonic elements, such as active and inactive faults, fracture zones or caldera structures, and of geothermal surface manifestations, such as hot springs or fumaroles (Fig. 3.15). Therefore, they are mandatory for the identification of a promising geothermal field and for the selection of suitable sites for the production and injection wells.

Hydro-geochemical surveys represent another indirect exploration technique extensively applied in the early reservoir investigation stage. Hydrochemical data comprises physico-chemical parameters, major ions, inorganic minor elements, inorganic trace elements, isotopes and organic compounds (*Nicholson, 2012*). They provide useful data for planning more detailed explorations, and their costs are definitely lower compared to other techniques, as for example the geophysical surveys. Geochemical analyses can be applied to both the rocks and the involved fluids or gases (i.e. water, gas, soil-gas, mineralogical and rock surveys). Each different type of geothermal system has distinct characteristics, mainly reflected in the chemistry of its geothermal fluids (see Fig. 3.16). Therefore, these surveys are applied to determine whether the geothermal system is water- or vapour-dominated, to evaluate the expected composition and variability of the reservoir fluids, to obtain information on the

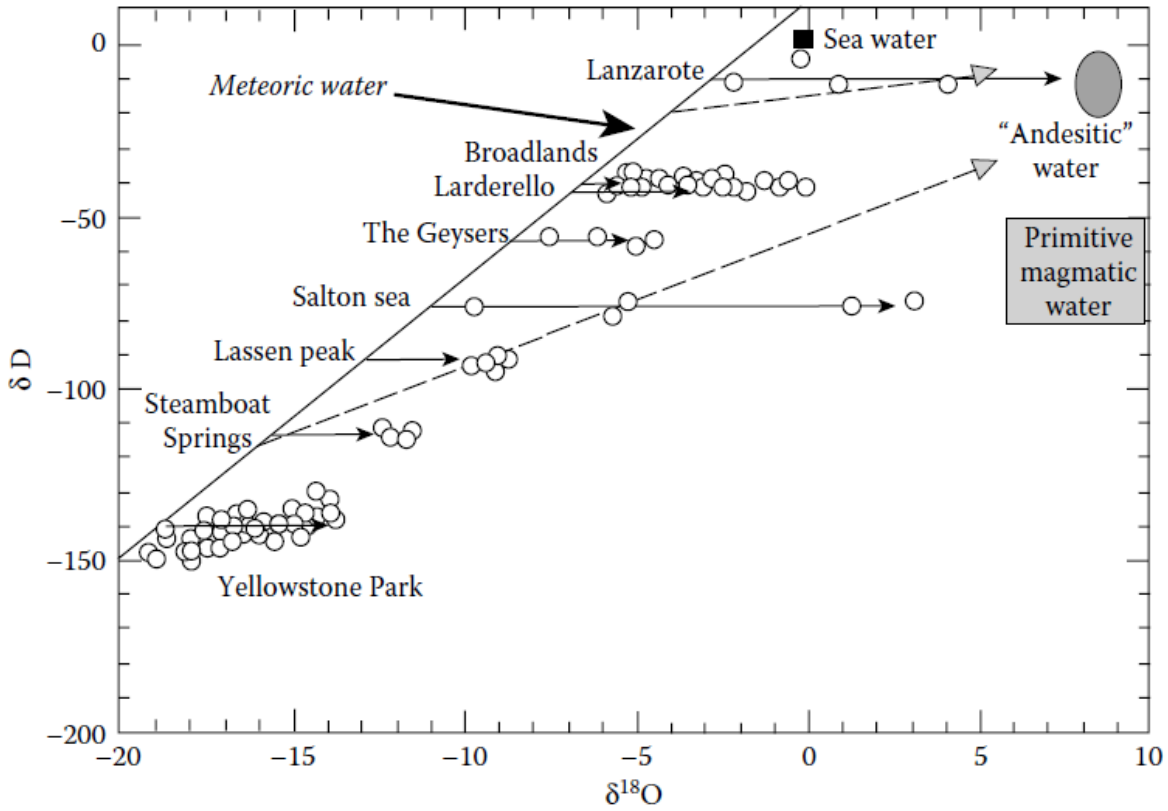


**Figure 3.16:** Isotopic imprint (δD and $\delta^{18}O$) for waters from geothermal areas. Modified from *Craig (1963, 1966), Truesdell and Hulston (1980)* and *Giggenbach (1992).*

sources of water and heat, to locate the recharge area and to estimate the respective recharge rate. These information are needed to simulate the response of the reservoir to exploitation and also to identify potential pollution, waste disposal and corrosion problems (*Pham et al., 2001; Kühn, 2004*). Geothermometers enable the temperature of the reservoir fluid to be estimated from the chemical composition of waters and gases. They are therefore valuable tools in the evaluation of new fields, and in monitoring the hydrology of systems on production (*Chandrasekharam and Bundschuh, 2008; Nicholson, 2012*).

Geophysical surveys can be used to provide, from the surface or from depth close to the surface, a three-dimensional map of subsurface structures (i.e. shape, size and depth of geological layers), as well as hydraulic properties and other characteristics of the geothermal reservoir (e.g. faults, fractures and temperatures). Geophysical methods and their application are described in detail in *Repsold et al. (1989)*, *Manzella (1999)*, and *Ernstson and Kirsch (2006)*. These methods can be divided into two groups: surface and borehole geophysics. Nevertheless, well logging equipment is generally unsuitable for the high temperatures

recorded in geothermal reservoirs. These measurements use electromagnetic fields or waves, acoustic waves, neutron scattering, gamma-ray radiation, nuclear magnetic resonance, infrared spectroscopy, and pressure and temperature sensors. There is no single technique adequate to define the structure and the properties of a whole reservoir and, in such complex systems, the interpretation of the data is often quite difficult (*Kühn, 2004; Santilano, 2017*).

Surface geophysical surveys include: electrical and electromagnetic methods, magnetic, seismic, gravimetric and thermal surveys (example of surface geophysical survey in Fig. 3.17). These last are fundamental as they allow the determination of the geothermal gradient and the terrestrial heat flow, which provide with good approximation the temperature of the geothermal reservoir units. While seismic, gravity, and magnetic methods can give information on the geometry of the deep structures of a geothermal reservoir (Fig. 3.17), they do not provide information about the presence of geothermal fluids in the considered field. As the presence of water decreases the electrical resistivity, only electrical and electromagnetic surveys allow the detection of geothermal fluids.

Once the result of all the above mentioned indirect surveys identified a promising geothermal field, exploratory wells are drilled and the second step in the reservoir exploration plan can began. A completely new branch of various tests, performed in such drillings, is now available

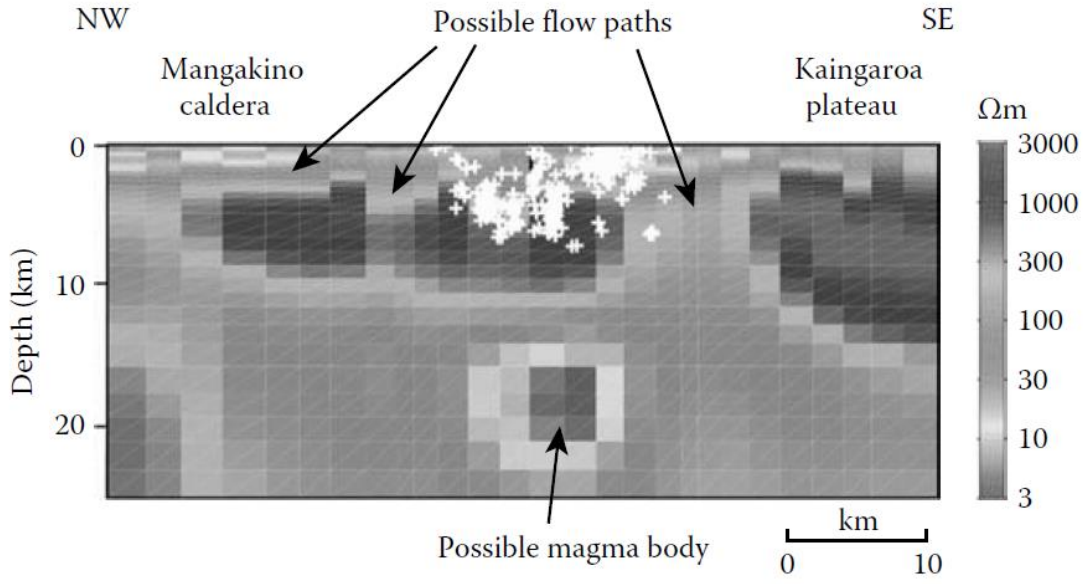


**Figure 3.17:** Example of magnetotelluric survey conducted in the Wairakei Valley, New Zealand. The low resistivity region at a depth of about 20 km is interpreted to be a magma body. The white crosses indicate sites of microseismic events. The locations of possible fluid flow paths at depths of less than 10 km are indicated by the arrows. Modified after *Heise et al. (2007).*

for a more detailed characterization of the different aspects of the system. These include borehole geophysical tests, steady state or transient injection tests and geothermal tracer tests. The last two are mainly used to characterize hydraulic properties of fractured rocks or of large scale fracture system, which may host the flow when the production wells are exploited. On the contrary, borehole geophysical methods allow to collect direct measured properties (e.g. stratigraphy, permeability, fluid characteristics and temperature distributions) to compare with the results from all the other indirect investigation techniques. Nevertheless, their application in geothermal reservoir exploration is limited due to high temperatures and strong corrosion caused by very acidic involved fluids.

# 4. HEAT TRANSPORT NUMERICAL MODEL

Nowadays numerical modelling is considered a reliable tool, which should be implemented for the improved integral management of geothermal resources (*Anderson et al., 2015*). Therefore, a step-by-step procedure for the setting up of an accurate and reliable heat-transfer numerical model is presented. A numerical model is a mathematical representation of a natural system (*Kresic, 2006*). Establishing a numerical model of a complex system, as the one associated to the geothermal reservoirs, requires the processing of a large amount of data regarding the domain area (e.g. geological setting, geometrical properties, hydraulic and thermal parameters, fluid properties, boundary conditions). All these data, collected in the conceptual model, describe the natural system without using numerical algorithms. The quality of the simulation results depends mostly on the preparation of such conceptual model, tied tightly to the knowledge of the geological situation, the hydrogeological and geochemical parameters and the initial and boundary values.

*Bundschuh (2010)* identified six different steps (Fig. 4.1) required for the development of an accurate numerical model simulating groundwater flow and heat transport mechanisms, namely:

(1) defining the objectives of the model;
(2) developing the conceptual model of the geothermal reservoir that includes all available geological, physical and chemical information relevant for framing the problem;
(3) numerical formulation of the conceptual model, that means translating all the information of the conceptual model into a set of mathematical expressions (i.e. boundary conditions and model properties), discretizing model spatial extent and choosing the adequate software and mesh;
(4) calibration of the numerical model, through optimization of the model parameters (numerical and physical) in order to obtain a good fit between simulated and measured field data;
(5) validation of the numerical model, to determine the degree to which a model is an accurate representation of the real system;
(6) sensitivity analysis, to determine the degree to which the most important parameters are affecting the behaviour of the system.

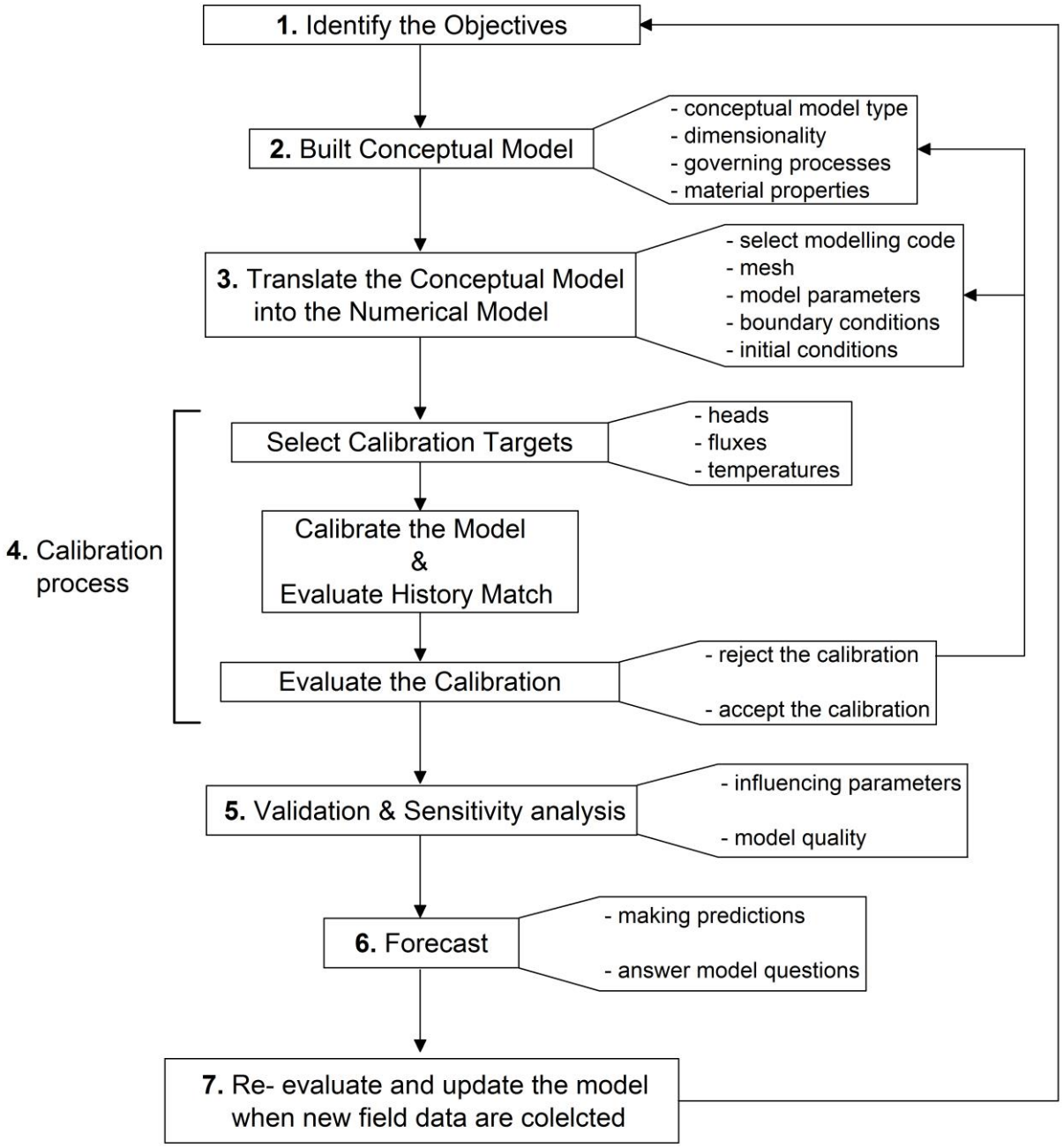


**Figure 4.1:** Workflow for groundwater and heat transfer modelling. As presented, the workflow assumes the objective of the model is a forecast but the workflow can be adapted for other modeling purposes, as described in the text. Although not shown in the figure, field data are critical for the workflow, especially conceptual model design and the calibration process.

For an optimal numerical elaboration of the geothermal problem, all these steps must be developed and solved with care. As mentioned above, the principal difficulty in establishing an accurate numerical model is due to the very limited availability of spatial and chronological field data. This leads to the formulation of assumptions based on incomplete information. Therefore, such necessary approximations, may affect the quality of the simulation and the possibility to precisely develop all the above mentioned steps.

## 4.1 DEFINING THE OBJECTIVE OF THE NUMERICAL MODEL

Defining the objective of the numerical model is a fundamental step, preceding the proper natural system simulation. Numerical models are used to both reconstruct processes which occurred in the past, and to forecast processes which will occur in the future (i.e. “prediction” and “retro-diction” capacities) in complex real subsurface systems, such as geothermal reservoirs. They can found their application at different stages of a geothermal project, helping the understanding of reservoir behaviour, optimal reservoir management and sustainable utilization, or planning of new investigations, well drilling and the designing of exploitation steps aimed to the usage of geothermal energy. The objectives of the simulation are strictly related to the type of the constructed simulation model. Due to the wide range of possible applications, the performed model can be very different, even for similar situations, depending on the specific characteristics of the problem and addressed questions. In any case, the accuracy and reliability of the answers from the simulation results depend on the level of knowledge available and on the complexity of the modelled system.

In his work, *Bundschuh (2010)* provides an updated overview on principal applications of numerical groundwater and heat transport models. This list deserves to be reviewed before starting up the construction of any fluid-flow or heat-transfer related numerical model.

## 4.2 THE CONCEPTUAL MODEL

An accurate conceptual model is the key for a reliable high-quality numerical simulation. It can be defined as a simplified and systematized high-level virtual representation of the geologic system, containing all the fundamentals assumptions, such as the governing processes related to groundwater and heat transfer, transport at the boundaries of the domain, dimensionality of the problem, hydrostratigraphy, flow directionality, material properties and heterogeneity patterns (Fig. 4.2; *Anderson et al., 2015*). Therefore, the idea behind the conceptual model is that it constitutes the best understanding of the processes that naturally occur in the aquifer

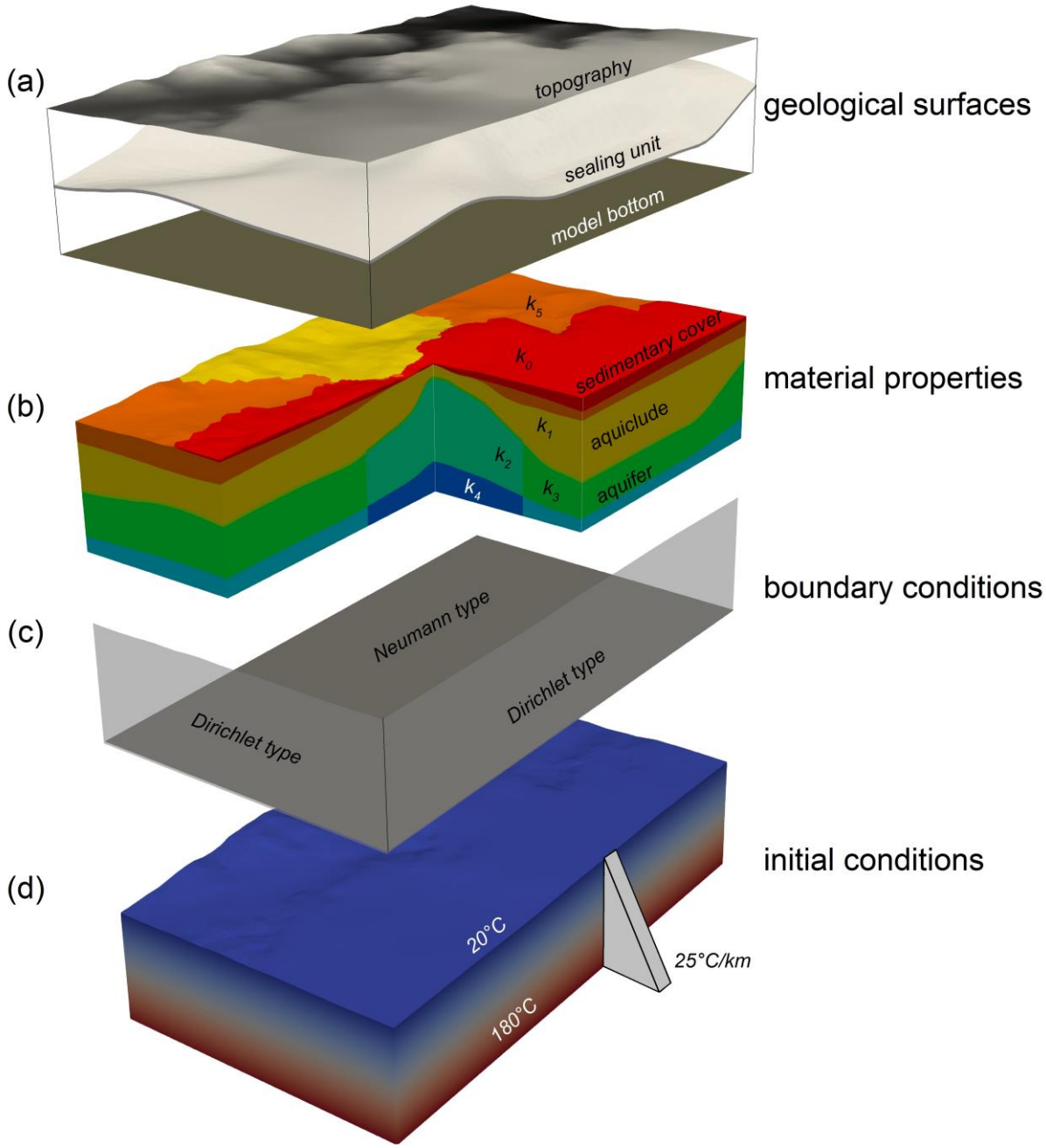


**Figure 4.2:** Construction of a regional groundwater and heat transport conceptual model. **(a)** Integration of all the surfaces defining the geological formations. **(b)** Assumptions about material properties and heterogeneities. **(c)** Definition of boundary conditions for both fluid and heat flow process. **(d)** Set up of model initial conditions for fluid and heat flow process. Modified after *Bundschuh (2010)* and *Anderson et al. (2015).*

or in the geothermal system. All the available field data, as well as the available time frame should also be taken into account, together with the determination of the adequate computer codes that will be used for the simulations.

If the conceptual model is not an accurate representation of the real-world system, the numerical model will make incorrect and/or meaningless predictions. An oversimplification

may results in inaccurate simulation results, while an under-simplification may leads to unreasonable demands for computer resources, and/or field data collection. After the preliminary simulations, the assumptions of the original conceptual model may be re-examined, changed, extended or improved. For this reason, working with only one conceptual model could not be sufficient, and different conceptual models need to be set up before a proper calibration is obtained. This is especially true if the real target systems are complex or if the initial field data are poor.

### 4.2.1 Conceptual model types

The acceptable degree of simplification, from the complex real-world system to its virtual representation in the mathematical and numerical models, is the main issue that must be solved by the conceptual model. The choice of a proper model is strictly related to the need of representing the essential points of interest and solving the tasks according to the defined objectives.

Generally for the conceptual model of a porous reservoir rock, the continuum approach is used (*Bear, 1972*). On the contrary, as numerical models of heat-transfer processes found applications mostly in problems associated to geothermal and petroleum reservoir exploration and exploitation, the applied conceptual approaches are about fractured rocks numerical implementations.

A variety of conceptual models have been developed according to different requirements for solving fluid and heat flow problems in fractured systems at different scales (see Fig. 4.3). In the following sections, we will give a short overview of the principal conceptual models used to describe fracture flow. For further details we refer to the works of *Bear et al. (1993)*, *National Research Council (1996)*, *Singhal and Gupta (1999)*, *Dietrich et al. (2005)* and *Krásný and Sharp (2007)*.

The equivalent porous medium *(EPM)* approach is the simplest conceptual model to describe fluid flow and heat transport in fractured porous media, describing the fractured bedrock as an homogenous region. Therefore, no distinction in hydraulic and thermal properties between the intact rock and the fracture is made, and permeability can be approximated by an equivalent permeability that considers the flow throughout the fracture and the porous-

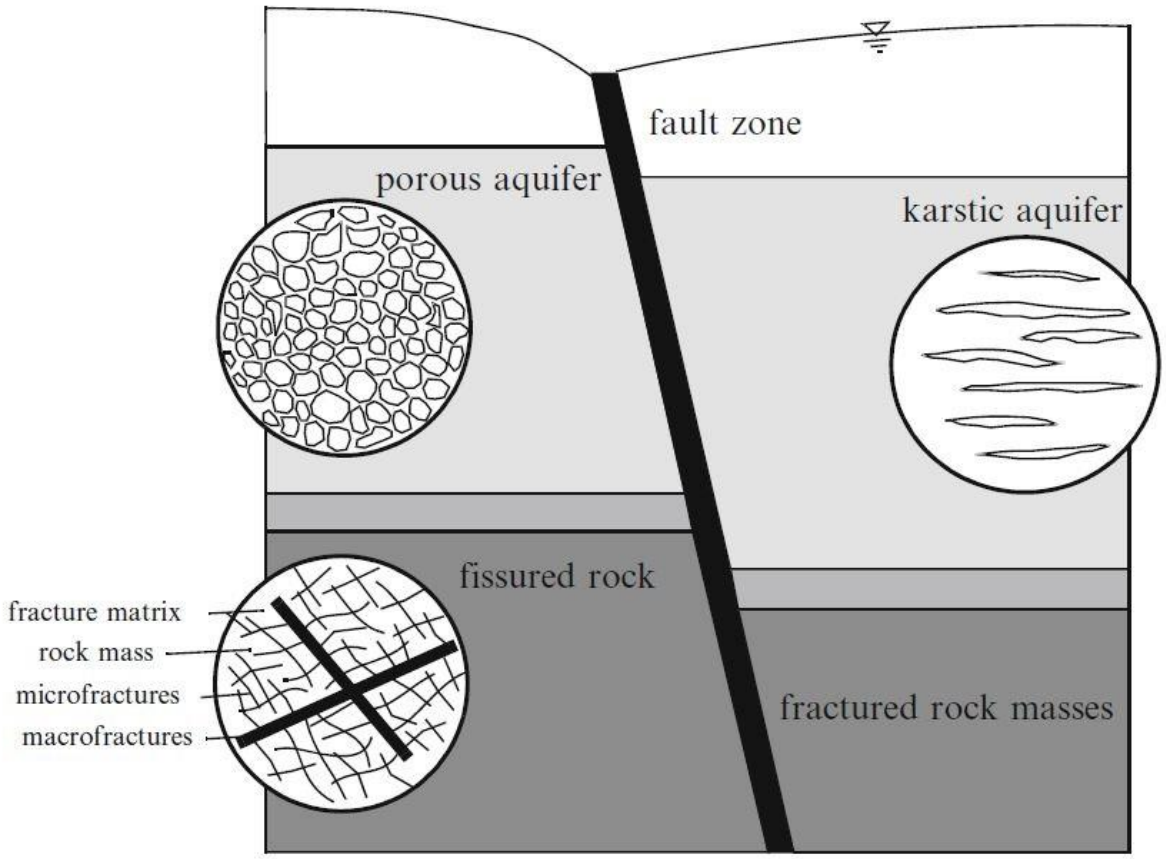


**Figure 4.3:** Representation of porous and fractured porous medium (*Diersch, 2014*).

media matrix. Due to its simplicity, this approach has been widely used for a description of regional flow systems in fractured rocks, but becomes unsuitable when fracture spacings are too large, flow velocities too high, or the permeability of the rock matrix too low (*Pruess et al., 1990a,b; Diersch, 2014*).

Dual and multiple continuum approaches (Fig. 4.4) are defintelt more powerful methods, where features and properties of fracture and rock matrix are represented as two separate interconnected domains. The unfractured rock masses (rock matrix) have a high storage and a low permeability (i.e. slow fluid flow), while fractures have a low storage capacity, but a high permeability (i.e. fast fluid flow) (*Diodato, 1994*). The use of multiple or dual continuum models, averaging the transient hydraulic behaviour of rock matrix and fractures, are appropriate for describing large fractured rock units. For these reasons, they can be considered the most widely used models to describe fractured groundwater, geothermal and petroleum systems. However, they often fail to describe local-scale features.

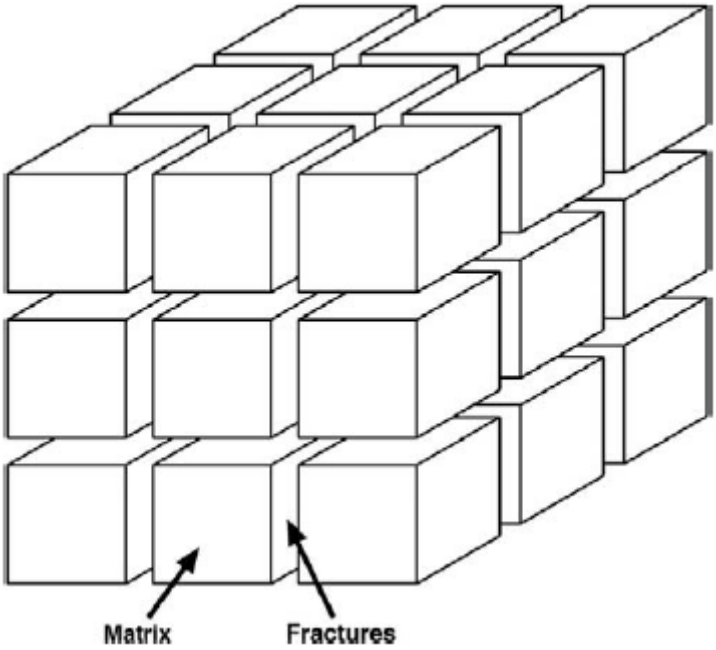


**Figure 4.4:** Schematic representation of the Dual Continuum Approach. Unfractured rock matrix and fractures are treated as two interconnected domains (*Grant, 1982*).

The explicit discrete-fracture approach has the significant advantage of incorporating fractures (or karst conduits) as explicit discrete elements, therefore allows the reliable representation of hydraulic head gradients and fluxes between fractures and rock matrix. On the other hand, it requires a great amount of information on all single fractures in the model domain (i.e. location, geometry, fracture matrix, hydraulic properties). This approach demands much more computational effort compared to the dual continuum method, and found useful application at fault zone, here represented as a single discrete fracture. In fact, data describing faults are more easily obtained than data describing smaller fractures, whose collection becomes especially difficult and time-consuming when the number is high and when fractures are not planar.

The discrete-fracture network *(DFN)* approach (Fig. 4.5) does not consider the porous medium (rock matrix), and all processes are confined within the fractures. The model describes fluid flow and heat transport coupling multiple dual-continuum models, where each fracture is treated as a continuous medium surrounded by an impervious matrix (see example in Fig. 4.5). Therefore, compared to the previously described models, the DFN approach significantly reduces the model complexity and the high computational resources needed for such

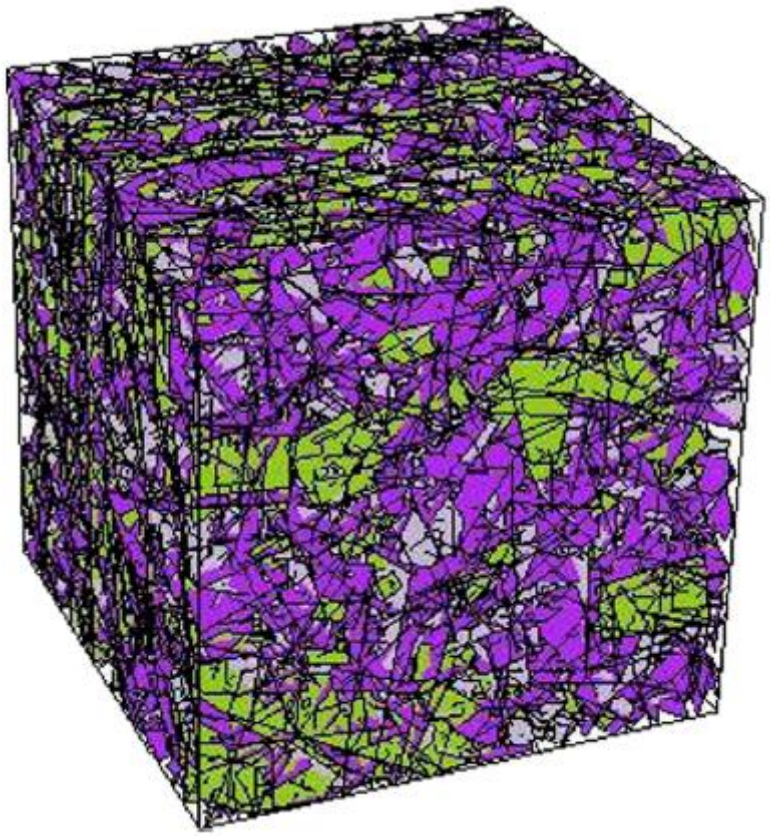

**Figure 4.5:** Example of a three-dimensional stochastic fracture network, generated within a 100m cube with a DFN approach (*Pan et al., 2010*).

sophisticated numerical simulations. The description of each single fracture in the model domain requires a huge volume of empirical data and may results in high computational effort. For this reason, a simplification of the fracture network (i.e. lines in 2-dimensional models or planes in 3-dimensional models) should always be considered.

As already mentioned, the chosen conceptual model must be the simplest possible but still allowing a reliable representation of the real-world system. All the previously described types of conceptual model applied to fractured aquifers, involve different degrees of simplification of the complex target addressed by this kind of models. Nevertheless, in many cases, room for a further level of simplification is possible, e.g. using 2-dimensional horizontal models to describe 3-dimensional groundwater flow and heat transport problems. This stratagem has significant advantages because it requires much less field data, less time, and fewer efforts in constructing the model, but it can be applied only under the assumption that groundwater flow is purely horizontal (i.e. flow horizontal velocities much larger than vertical velocities).

This situation is common when the horizontal extension of the aquifer or geothermal reservoir is much larger than the vertical extension.

### 4.2.2 Model boundaries types

Once the adequate conceptual model has been identified, hydrogeological constrains, internal and on model boundary, must be defined. They are the natural limits of regional groundwater flow and heat transport, such as large faults, zones of lithological changes, anticlinorium axes, large/small rivers, seashore, springs, drains and pumping/injection wells.

From a mathematical point of view, they are classified in three types: first order (Dirichlet type), second order (Neuman type) and third order (Cauchy type) boundaries, the last being a combination of the first two, and all these may be function of the time (*Kresic, 2006*).

First order or Dirichlet type boundaries are assigned to model portions where hydraulic head or temperature values are known. This situation is realized when rivers and lakes are in complete hydraulic contact with the groundwater body or at spring locations, modelled as points with fixed hydraulic head, corresponding to the topographic height of the spring outlet in the field. At first order boundaries, with prescribed hydraulic head or temperature, the assigned values are kept fixed or changed in a known way, during the simulation.

Second order or Neumann type boundaries are assigned to model margins which are characterized by a known flux, e.g. groundwater or heat flow. Contacts of the aquifer with impermeable rock units, groundwater flow lines diverging areas (e.g. at ridges) or basal heat flow in geothermal reservoir, are the most important applications of this type of boundary. Impervious boundaries are a special case within this group. Similarly to what is observed for the first order boundaries, the prescribed flux values can be fixed or evolved with time in a known way.

Third order or Cauchy type boundaries can be applied along rivers, lakes and lateral boundaries in order to account for surface-water/groundwater interaction. This kind of boundary condition, named also fluid-transfer boundary condition, applies a pre-defined reference head, as the value for the boundary condition, combined with a conductance parameter (transfer rate or leakage coefficient), set separately as a material property. Usually,

in the case of fluid flow models, the reference head is assumed equal to elevation and imposed where the water table intersects the topography.

Sources and sinks within the model area are inserted in the conceptual model following the above described boundary condition classes. They group the wide range of all steady and transient in- and out- fluxes of water, solutes, and heat, that may occur within the modelled area and on its inner boundaries. This group involves: groundwater recharge/discharge through pumping/injection wells, groundwater discharge at springs, areal groundwater recharge by rainfall or irrigation, groundwater recharge/discharge by infiltration/exfiltration from surface water bodies (rivers, lakes, canals), heat inputs, heat storage/withdrawal or solutes inputs/outputs.

### 4.2.3 Model parameters

Before switching from the conceptual model to the mathematical and numerical models, fluid and solid parameters must be determined. For a reliable simulation, they must be evaluated together with their spatial variations, homogeneity or heterogeneity, and isotropy or anisotropy in both horizontal and vertical directions. Spatial variation as well as heterogeneity can be considered by establishing zones with same uniform values (*Bear, 2012*). In the case of fractured aquifer, information on location, geometry, aperture, filling and hydraulic properties of the fractures need to be determined (*Bear et al., 1993; National Research Council, 1996; Singhal and Gupta, 1999; Krásný and Sharp, 2007*).

The techniques to collect hydrogeological parameter needed to construct the conceptual model of groundwater systems or geothermal reservoirs, are: (1) remote sensing, (2) field investigations and (3) laboratory tests and experiments. A detailed review of all these methods is outside of the scope of this thesis, and as these techniques are used also in the early exploration stage of the geothermal reservoir to evaluate the potentiality of the area, they have been already described in the previous section *3.6 Reservoir exploration techniques*.

It is important to point out that, since the values obtained through experimental methods are discrete measurements taken in a heterogeneous and often anisotropic medium, they do not represent the real distribution of the parameter. Therefore, the values determined from the three methods above, often do not correspond to the best values needed to construct and to

calibrate the model. The experimental evaluated parameters are used as starting values to restrict the value ranges that indeed can vary between many orders of magnitude (e.g. hydraulic or thermal conductivity). They need to be refined until a good match between observed and calculated values for parameters, such as hydraulic heads or discharge temperatures, is achieved. Several techniques can be adopted to adjust model parameters, including manual testing of reasonable values or inverse modelling technique, which, through an automatic calibration process, determine parameter's spatial distributions.

### 4.3 NUMERICAL FORMULATION OF THE CONCEPTUAL MODEL

Once the suitable conceptual model has been identified and all the information regarding parameters and boundary conditions have been included, it needs to be converted into a set of mathematical expressions. After that, the numerical model is constructed by discretizing these mathematical equations in space and in time.

Several numerical methods are used to solve differential equations and algorithms for modelling hydrogeological or geothermal problems. This thesis is not supposed to give a complete compilation of all modelling techniques, since this field of study is extremely wide and detailed mathematical derivations are described in by specialized literature. *Smith (1985)*, *Kinzelbach (1987)*, *Bear and Verruijt (1987)*, *Bear and Bachmat (1990)*, *Zienkiewicz and Taylor (1991, 2000)*, *Katsikadelis (2002)*, *Pruess (2006)*, *Fish and Belytschko (2007)*, contain full descriptions, including practical examples, of the different classical numerical methods. Nevertheless, all the numerical methods for the solution of flow/transport equations require the discretization of the model area or volume through the so-called *mesh*, defined as a network of intersecting lines embedded within the domain.

The region within the intersecting lines is called *element*, while the intersecting points are denoted as *nodes*. Elements in two dimensions can be of triangular, rectangular or polygonal shape, and in three dimensions of tetrahedral, quadrilateral or prismatic shape. Volumetric quantities such as temperature or pressure are defined at the centroids of the elements. Wells and drains should be located in centres of grid cells or at nodes of the mesh. For high accuracy, the mesh must be refined around important wells or in other areas where large gradients in hydraulic heads, temperature, concentration, or rock properties are observed.

Before running any numerical simulation, in order to avoid unrealistic values, a suitable distribution of hydraulic heads, and/or temperature must be set for the entire model as initial condition. These values should be as near as possible to the expected real values. This become more important when dealing with transient simulations, for this reason is common practice to use the results of the respective stationary model as a suitable initial condition.

### 4.3.1 Numerical model types

The selection of the code is a crucial step that must be evaluated with care before running the numerical simulations. The objectives, the questions to be solved and the nature and quantity of field data are the key-points to take into consideration when facing the choice of the numerical model code.

A large number of programs are already available and numerous new programs are under development, including commercial and open-source codes. Therefore it is impossible to provide a full description of all existing public and commercial modelling programs. Periodically, updated overview of the most used commercial and open-source modelling software can be found in the USGS (*United States Geological Survey*) and IGWMC (*International Groundwater Modelling Centre*) catalogues.

From a very general point of view, model types can be classified according to three criteria: (1) the numerical algorithms used for discretizing the mathematical equations, (2) their physical-chemical options, and (3) their dimensionality.

The first criterion deals with the techniques adopted by the software to substitute partial differential equations by a system of algebraic equations or by an ordinary differential equations that can be solved by means of different algorithms. This evolves in different numerical methods such as: the Finite Difference Method (FDM; *Smith, 1985*), the Finite Element Method (FEM; *Zienkiewicz and Taylor, 1991*), the Finite Volume Method (FVM; *Narasimhan and Witherspoon, 1976*) and the Boundary Element Method (BEM; *Cruse and Rizzo, 1975*).

The physical-chemical criterion indicates the aquifer properties that can be simulated with the selected code. This classification indicates (1) whether a system can be modelled as a porous or fractured aquifer, or a combination of both, (2) whether fluid density and viscosity show

dependency on temperature and/or salinity values or if they can be approximated by constant values, (3) whether the compressibility of the fluid and the solid structure must be considered or not, (4) whether the modelled processes include only groundwater flow or additionally transport of solutes and heat, and (5) whether flow and transport is in one or several phases of fluid (water, steam).

The last criterion is about how many dimensions can be handled by the selected software (i.e. 1, 2 or 3 dimensions). Most of the codes for groundwater flow, solute and/or heat transport modelling allow the construction of 1, 2 or 3-dimensional models, thus the choice is usually caused by the problem geometry and characteristics, time and financial resources, as well as data availability.

One-dimensional models are used to reproduce laboratory experiments and very small-scale cases in general (e.g. tracer test). Their results are suitable for initial assessment of a larger model or to define a field data collection campaign. The utilization of two-dimensional models is definitely more spread in thermal and fractured aquifer modelling, compared to the mono-dimensional case. They often approach the real problem with sufficient accuracy and moreover, are much easier to construct and require much less data compared to three-dimensional models. In this category, two types can be distinguished: two-dimensional horizontal models and two-dimensional vertical models.

Horizontal models are most useful for describing the regional groundwater flow if the vertical extension of the aquifer is much smaller compared to the horizontal extension of the model domain, and if only one principal aquifer is present. As fluid density must be considered as constant, these models are not frequently adopted for transport problems. On the other hand, a vertical model is mandatory when various aquifers are present, and therefore vertical flow components cannot be neglected. This is the case also when changes in hydraulic heads and aquifer properties along the horizontal direction are low, so that the model plane is parallel to groundwater flow lines.

The combination of horizontal and vertical two-dimensional models, can be a useful preliminary step for the full three-dimensional models. Clearly, three dimensional models are the most complex type and result in the more accurate representations of the real-world situation. They require a full understanding of the hydrogeological conditions of the model

domain and they must be developed especially if regional groundwater model, with multiple aquifers, need to be constructed, and in situations where the vertical groundwater flow component is significant or variable density flow is invoked.

### 4.3.2 Adopted numerical codes

The codes applied to model the three hydro-geothermal sites analysed in this thesis are: the commercial software Feflow® (*Diersch, 2014*) and the open-source simulator OpenGeoSys (*Kolditz et al., 2012*). In this section, they will be described accordingly to the three criteria presented above, together with a short overview of the main features that make them suitable for our analysis.

Regarding the first criterion, both codes respond to the finite element method (FEM), the most used numerical technique to solve approximately mathematical models expressed as partial differential equations. Finite element methods can be adapted to problems of great complexity and unusual geometry. They are an extremely powerful tool for the solution of important problems in heat transfer, fluid mechanics and mechanical systems (*Weisstein, 2002*).

About physical-chemical options that can be simulated with the selected codes, both Feflow® and OpenGeoSys can handle heat-transfer fractured aquifer simulations using the equivalent porous medium approach. Fluid density and viscosity can be set as temperature dependent values, and the compressibility of the fluid and of the solid structure are also considered.

Regarding the dimensionality, as most of the codes for groundwater flow, solute and/or heat transport modelling, Feflow® and OpenGeoSys can model 1, 2 or 3-dimensional problems.

**FEFLOW** is an advanced **F**inite **E**lement subsurface **FLOW** and transport modelling system under development since 1979 by the Institute for Water Resources Planning and Systems Research Inc. (*WASY GmbH*) of Berlin, Germany. The code supports an extensive list of functionalities (Fig. 4.6), including variably saturated flow, variable fluid density mass and heat

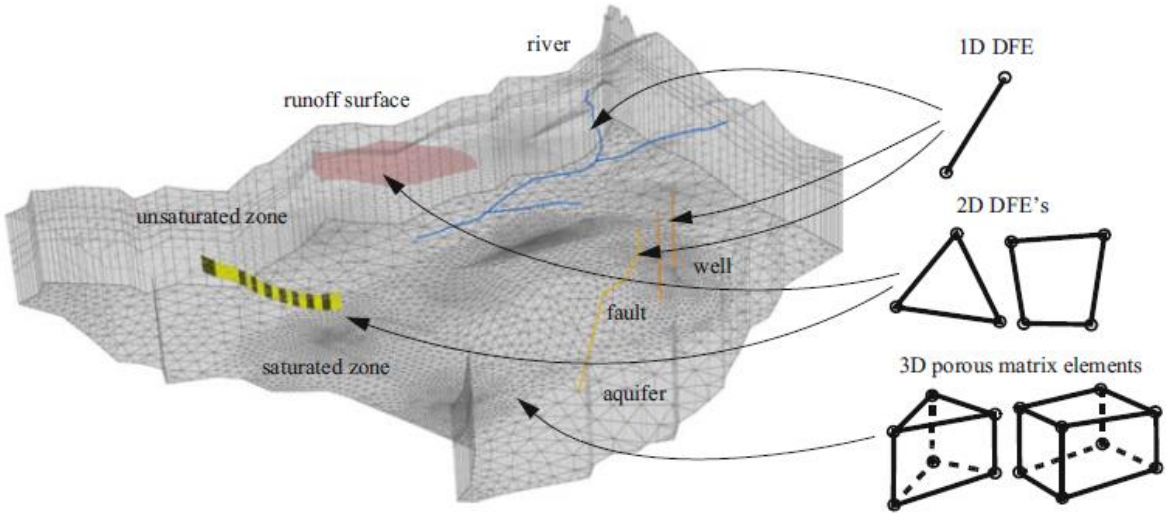


**Figure 4.6:** Schematization of a regional model developed with Feflow®. A combination of 1D and 2D discrete features is coupled with 3D volume discretization. 1D features are used to model rivers, channels and wells, while 2D features approximate infiltration or runoff surface, and fault systems. 3D elements, representing the basic discretization of the model domain, are used to identify the aquifer/aquiclude systems as well as the saturated/unsaturated zones (*Diersch, 2014*).

transport, and multispecies reactive transport. Since this modelling tool is known and popular in the field, is well documented in terms of both reviewed papers in the scientific literature and set of manuals. Feflow® supports multiple data import and export filters, it can also reads and reconstructs simulation files from SWS (Surface Water Modelling System) and GMS (Groundwater Modelling System). For spatial meshing and gridding, Feflow® can import a wide range of formats including AutoCAD DXF, ESRI shapefiles plus a variety of simple ASCII formats, and many bitmap formats for gridding and georeferencing operations.

**OpenGeoSys** code is an open-source flexible finite element simulator developed by the Helmholtz Centre for Environmental Research (UFZ) in Leipzig since the mid-eighties. The basic concept of OGS is to provide a flexible platform for solving multifield problems in porous and fractured media for applications in geoscience and hydrology.

OpenGeoSys includes a broad spectrum of interfaces for pre- and post-processing purposes, for example, for geometrical modelling, meshing, and visualization (Fig. 4.7). The idea behind OGS is to provide an open platform to the community, outfitted with professional software-engineering tools, such as platform-independent compiling. Already published comprehensive benchmark books have proven to be a valuable tool for cooperation between different developer teams, in terms of code comparison and validation purposes.

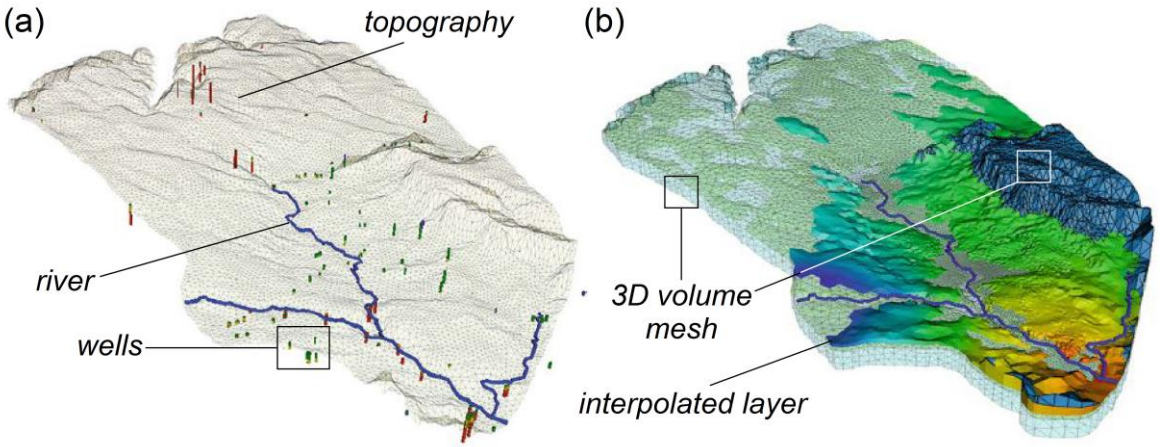


**Figure 4.7:** Schematization of a regional model developed with OpenGeoSys. **(a)** 3D surface model data including the 1D and 2D discrete features identifying topography, rivers and wells. **(b)** Subsurface 3D model with layers interpolated based on borehole data. Different information is displayed for each geological layer. Modified after *Sachse et al. (2015).*

## 4.4 CALIBRATION OF THE NUMERICAL MODEL

Once the suitable code has been selected and the conceptual model has been converted into the numerical model, the real simulation steps can began. It is common practice to run initial simulations in order to compare model results against benchmark numerical simulations or known field data, such as measured water levels or temperatures. These preliminary simulations are named model calibration and model validation, and are mandatory to verify if model is producing simulation results that suit to real-world conditions (*Anderson et al., 2015*). The calibration or parameter value estimation in a numerical groundwater flow and transport model is performed by varying the values of one or more of the model parameters and optimizing them, until agreement between simulation results and values measured in the field is obtained with acceptable precision (*Hill and Tiedemann, 2006*).

Depending on model type (e.g. flow, heat transport, hydro-thermal, hydro-thermo-chemical, hydro-thermo-chemo-mechanical, steady or transient), the number of parameters that must be estimated can vary considerably. Therefore, the calibration process can be performed manually by varying a specific parameter (trial-and-error method), or using automatic calibration tools provided by some of the existing modelling programs (e.g. UCODE or PEST; *Doherty, 1994; Poeter and Hill, 1999*). These automatic calibration tools, will run simulations in a batch mode through an inverse modelling routine, continuously adjusting input

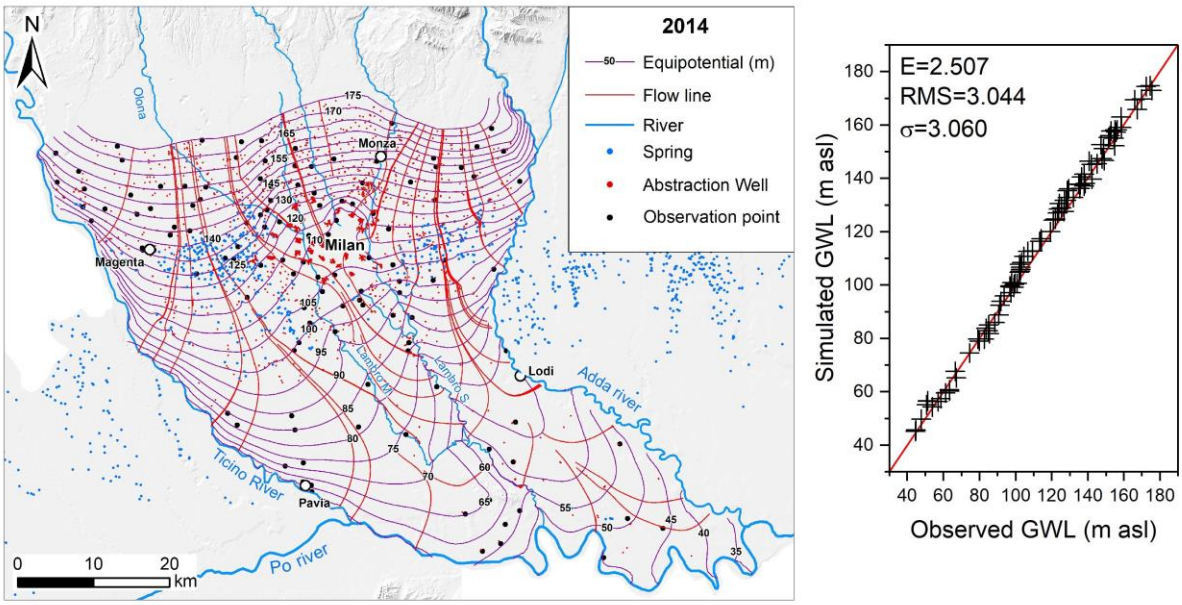


**Figure 4.8:** Example of calibration of the regional model of the Milan metropolitan area (Italy) from *De Caro et al. (2017).* Calibration process is achieved on a database of monitoring wells, on the right side the scatter plot from PEST software, plotting observed versus simulated groundwater levels. In red the 1:1 line, *E* is the *absolute error*, *RMS* is the *Root Mean Square error* and $\sigma$ is the *standard deviation*.

parameters until simulated and observed field data match within a specified tolerance range (see example in Fig. 4.8).

The calibration involves estimation of different parameters, i.e. hydraulic conductivity, groundwater recharge and boundary fluxes for stationary groundwater model, and additionally the storage coefficient for the transient ones. While for coupled groundwater flow and heat transport problems, firstly the pure groundwater flow parameters should be calibrated, then the transport ones, i.e. effective porosity and heat sources. The quality of the calibration, and therefore the accuracy of the model, is expressed by plotting observed versus simulated results. In these so-called scatter plots (Fig. 4.8), the closer the values fall on the 1:1 straight line, the better is the model performance.

## 4.5 MODEL VALIDATION AND SENSITIVITY ANALYSIS

Since different combinations of parameter values can lead to a calibrated model matching observed and simulated results, no unique solution of the parameter-estimation problem exists. Therefore, when accurate filed data are available, the calibrated model can be validated by history matching.

Through this process the model is tested for some period in the past to prove whether the simulation results reproduce well the known time series (i.e. aquifer responses to pumping tests, changes of flow conditions, hydraulic heads, solute concentrations, or temperatures). To perform this, an extensive time series is required, such that the model is calibrated on a first part of this time series, whereas the second part is used for validation (prediction mode). Once successfully validated the model, a sensitivity analysis can be accomplished. The sensitivity analysis is performed when an extensive set of field data is available, since it consists of changing parameters values and evaluate their influence on modelling results. The possible ranges in the parameters variation derive from prior knowledge of the behaviour of the parameter in the real world, thus they are linked to the uncertainty of the parameter observed in the field. The sensitivity analysis pinpoints the most influencing model variables (e.g. hydraulic conductivity, permeability, porosity, heat conductivity and capacity) so those variable which causes largest changes in the model results for a small change in their value.

### 4.6 MODEL USE AND MISUSE

Once all the previous steps are completed, the model is ready to simulate the real world system. However, even the most accurate models are a simplified description of the real field situation, including numerous simplifying approximations and assumptions. The quality and thus the reliability of predictions depends mainly on the detail and comprehensiveness of available information (e.g. permeability, porosity, characteristic curves, initial and boundary conditions). The needed discretization of space and time into finite-size intervals introduces inaccuracies, known as “space and time truncation errors,” which generally become smaller when discretization is refined (*Pruess, 2002*). The model domain boundaries are a source of uncertainties too, as their position and type may shift and change through time at the same location.

*Mercer and Faust (1981)* and *Mercer (1991)*, grouped into 4 classes all the possible error and misuses for numerical simulations: (1) not enough accurate or wrong conceptual model, (2) unsuitable modelling code, (3) improper model application, and (4) misinterpretation of model results.

The first group is the most spread source of error and of unreliable results. It is due not only to a wrong delimitation of the model domain area or to a wrong assumption regarding homogeneity, isotropy and hydraulic parameters of the aquifer, but also to an unsuitable selection of dimensionality. For this reason, different approaches have been developed to account for this issue. It is recommended to evaluate the conceptual model reliability in predictive results by performing simulations with the different models available and estimating the range of predictions obtained for the distinct models (*Medina and Carrera, 1996*).

The second group of errors occurs when the user forces simulation into a highly sophisticated code, even when the problem complexity does not require it or not enough data are available to support it.

The third class groups all the situations when improper input data are used, the mesh or grid size and the intervals of the time steps are not properly selected or when the chosen code is not compatible with the tested conceptual model. The model calibration step can also generate errors, if for example unsuitable calibration parameters or calibration periods are selected. These errors can lead to wrong results and incorrect interpretation of the modelling results.

# 5. THE BORMIO HYDROTHERMAL SYSTEM

The chapter is largely based on the published papers of *Volpi et al. (2017)*: *Groundwater-driven temperature changes at thermal springs in response to recent glaciation: Bormio hydrothermal system, Central Italian Alps,* on Hydrogeology Journal; and of *Volpi et al. (2016)*: *Geochemical characterization of the Bormio hydrothermal system (central Italian Alps),* on Rendiconti Online Società Geologica Italiana.

## 5.1 INTRODUCTION

Low-enthalpy geothermal systems are widespread in the European Alps compared to the high enthalpy fields. These reservoirs are usually associated to natural deep flow systems in normal heat-flow conditions and lead to the discharge of sub-thermal or thermal springs, with temperatures respectively 10–15 °C or higher. In Switzerland more than 82 geothermal sites and 203 hot springs and boreholes are known and exploited (*Vuataz, 1983; Sonney and Vuataz, 2007, 2008*). Italian alpine and Apennine regions are also rich in thermal springs, which have been used for bathing since Roman times (*Minissale, 1991*).

Generally, a classic hydrothermal system is formed by three components: a heat source, a thermal pathway, and a fluid, which in 90 % of continental systems is of meteoric origin (*Giggenbach, 1997; Hayba and Ingebritsen, 1997; Dzikowski et al., 2016*). In non-magmatic continental hydrothermal systems, the heat source may be a high geothermal gradient and/or significant heat flow anomaly (>150 mW/m$^2$) (*Rybach et al., 1987; Sonney and Vuataz, 2008*). In many alpine hydrothermal sites, thermal water occurrences could be related to the weathered and fractured zone between crystalline basement and sedimentary cover. In such settings, high temperature is not necessarily associated with a heat flow anomaly but results from the rapid upwelling of water from deep flow systems through permeable faults or subvertical strata (*Vuataz, 1983; Bianchetti et al., 1992; Sonney and Vuataz, 2008*). Many studies have been performed to better understand water circulation in mountainous terrains (*Toth, 1963; Forster and Smith, 1988; Gleeson and Manning, 2008; Welch and Allen, 2012, 2014*), and to model coupled heat and fluid transport processes driving deep fluids from the reservoir to the springs or wells (*Mercer and Faust, 1979; López and Smith, 1995, 1996; Gallino, 2007; Thiébaud, 2008; Sonney and Vuataz, 2009; Sonney, 2010; Dzikowski et al., 2016*).

The complex geometry and hydraulic behaviour of individual or multiple faults and thrust systems strongly affect the patterns and rate of fluid and thermal flow (*Yeamans, 1983; Sibson, 1987; Henley and Adams, 1992; Barton et al., 1995, Hickman et al., 1995; Benoit, 1999*). Firstly, in an indirect way, faults can connect units with strongly different hydraulic conductivity, thus forcing water to upwell along the contact zone and to flow through the more permeable unit. Secondly, in a direct way, the shearing of rocks along the fault plane can lead to damage zones of high or low hydraulic conductivity, channelling or preventing hot water flows, depending on the geological setting, the host rocks, the state of stress and the temporal evolution of the fault zone (*Smith et al., 1990; Scholz and Anders, 1994; López and Smith, 1996*). Quantitative assessment of thermal flow systems requires an accurate conceptual model of the fault zone structure coupled to data regarding the thermo-hydraulic properties of the aquifers (e.g. hydraulic conductivity, porosity, storativity, thermal conductivity of solid and fluid) (*Evans et al., 1997; Barton et al., 1995; Caine et al., 1996; Parry, 1998; Sibson, 2001; Baietto et al., 2008*). However, in the majority of hydrothermal systems, these parameters are difficult to assess because of their spatial and temporal variability and the scarcity of direct measurements (*Smith, 1980; Sibson, 1994*).

Results of chemical and isotopic analyses are often used to highlight the characteristics of deep flow system, such as the study of mixing processes, water-rock interaction, mean elevation of the recharge zone, reservoir temperature and groundwater residence time (*Hem, 1985; Drever, 1997; Langmuir, 1997; Mazor, 2003; Appelo and Postma, 2004; Nicholson, 2012*). The chemical composition and the concentration of dissolved species allows deciphering the geological origin of the host rocks. While hydrochemical parameters act as natural tracers to gain insight into the origin of water and the pathways along which it has migrated. Geothermometers constitute one of the most important geochemical tool for the exploration and development of geothermal resources (*Arnórsson, 2000; Sonney and Vuataz, 2010*). Many different chemical and isotopic reactions provides geochemical thermometers to estimate reservoir temperature (*Fournier, 1981*).

The thermal behaviour of alpine groundwater systems has evolved over time in relation to main paleoclimatic events. Quaternary glaciations have influenced thermal systems in temperate regions up to the present day (*Maréchal et al., 1999; Kohl et al., 2001; Gallino et*

*al., 2009; Thiébaud et al., 2010; Dzikowski et al., 2016*). Alpine glaciers extended down to elevations lower than 1,000 m a.s.l., whereas the present lower limit averages 4,000 m a.s.l. (*Bini et al., 2009, Scotti et al., 2014*). It is widely accepted that glaciations significantly reduced or completely blocked aquifer inflows and outflows due to continuous permafrost conditions and the deposition of compacted and impermeable subglacial tills on both valley bottom and flanks (*Chapron, 1999; Thièbaud et al., 2010*).

This study refers to the thermal outflow of the Bormio area (Fig. 5.1), located in the Upper Valtellina Valley (Central Alps, Italy), where a hot spring system emerges along the regional Zebrù thrust with temperatures in the range 35 - 40 °C. The observed topographic difference between recharge and emergence area (Bormio springs are located at 1300 m a.s.l. and adjoining summits reach 3905 m a.s.l. at Mount Ortles), suggests that discharge of hot fluids is primarily due to topographically-driven advective flow. However, the structures controlling infiltration and deep circulation of meteoric and snowmelt water into the thermal system, as well as the nature of their circulation patterns, remain largely unknown.

Aiming to gain new insights into the flow patterns of water and the interactions between groundwater and surface water, a hydrochemical characterization of the discharged waters have been performed. Water samples were collected during four campaigns in different seasons (June 2012, October 2012, May 2013 and September 2013) and analyzed for major ions and stable isotopes. Geothermometers analysis has been performed to estimate reservoir temperature. The seasonal variations in water temperature, electric conductivity and discharge rates were also examined.

The aim of this study is to build the first numerical model of heat and fluid transport in the Bormio area, to assess quantitatively the source area of hot waters and to investigate the behaviour of the system following the end of Last Glacial Maximum (LGM). Moreover, the study also tests the hypothesis that other thermal processes, such as heat convection, might occur within the faults of this hydrothermal systems, as observed in other basins (*Evans and Raffensperger, 1992; Bodri and Rybach, 1998; Baietto et al., 2008*).

The chapter is structured as follows. First, the geological and hydrogeological settings of the model domain are presented, with particular emphasis on the thermal outflow area. In the following the description of the performed hydrochemical characterization of the discharged

waters is reported. Then, the numerical framework used to simulate coupled thermo-hydraulic processes is illustrated. Finally, the analyses and relative results are presented and discussed.

## 5.2 GEOLOGICAL AND HYDROGEOLOGICAL SETTINGS

### 5.2.1 Geological setting

The Bormio area (Fig. 5.1a) is located within the Penninic and Austro-Alpine sectors of the Alps, and consists of a complex sequence of sedimentary, volcanic and mainly metamorphic rocks of Paleozoic and Mesozoic age (*Vuataz, 1983; Froitzheim et al., 2008*). Alpine orogeny severely deformed these rocks, resulting in large and complicated overthrusts. A thorough description of the tectonic and metamorphic settings of this area is reported in *Conti (1994)* and *Froitzheim et al. (1996, 1997)*. The geological units of the area belong to five main nappes (Quattervals, Ortles, Campo, S-Charl and Umbrail-Chavalatsch), and the major regional structures are the Trupchun-Braulio thrust and the Zebrù thrust (Fig. 5.1a and Fig. 5.1c). This last separates the Campo Nappe to the south (low/medium metamorphic unit, phyllites and micaschists) from the overlying Ortles sedimentary cover to the north (Triassic carbonate unit, Dolomia Principale) (*Conti, 1994; Pena Reyes et al., 2015*).

The Zebrù thrust is characterized by thick mylonitic/cataclastic layers at the contact between younger sedimentary permeable rocks (above) and older less-permeable metamorphic rocks (*Berra, 1994*).

The geomorphological setting of the area is strongly influenced by Quaternary glaciations. The beginning of widespread deglaciation after LGM in the European Alps (*Ivy-Ochs et al., 2006, 2008; Hormes et al., 2008*) was commonly fixed between 19,000 and 16,000 years BP. However, $^{10}$Be (beryllium) exposure age calculations, performed on two moraine boulders belonging to LGM (Viola Valley, 15 km WSW of Bormio village) revealed an age of 11,000-

12,000 years (*Hormes et al., 2008*). Therefore, this timing is assumed as the beginning of the LGM deglaciation in the area and it is used for the analysis of the model results.

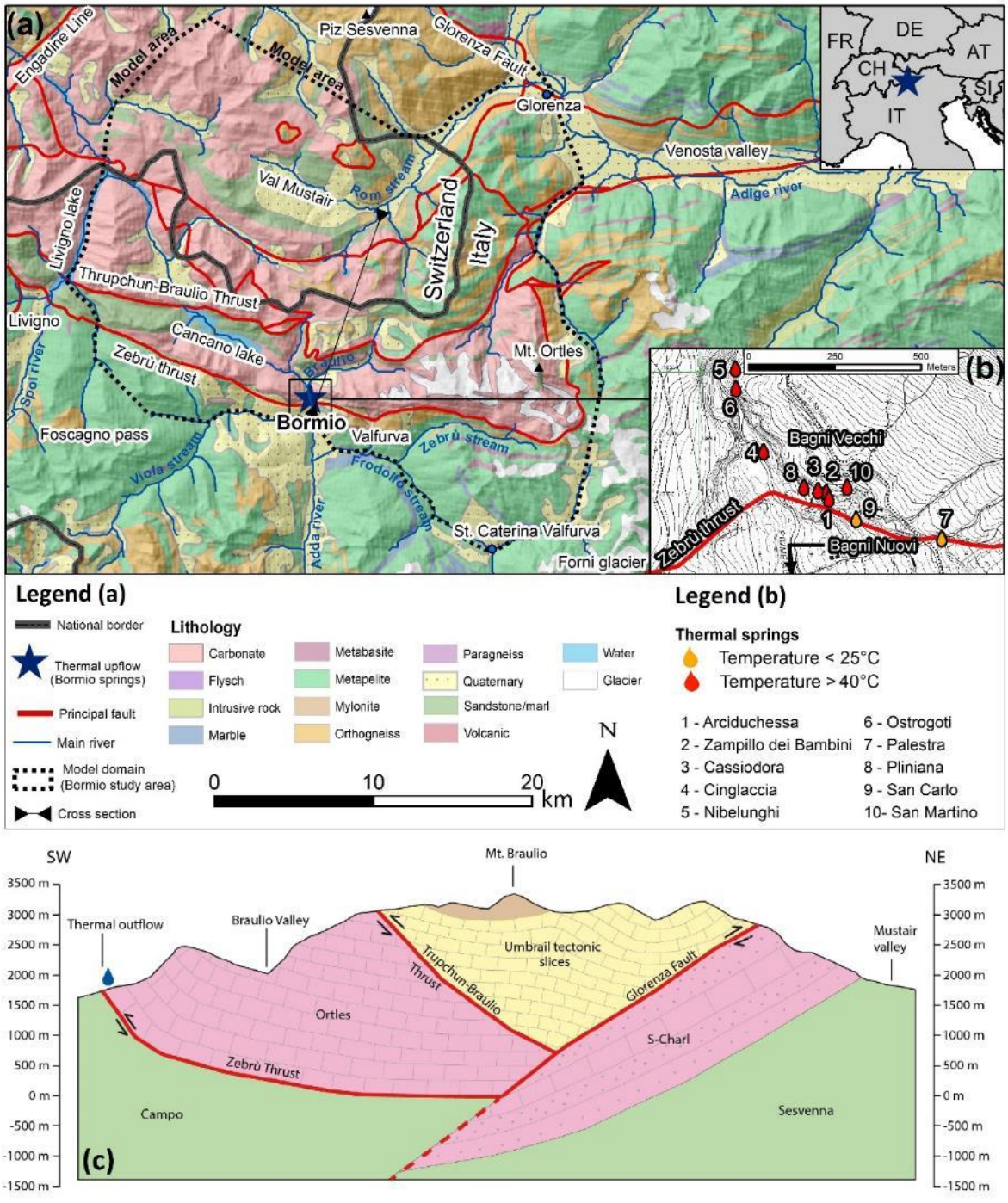


**Figure 5. 1 : (a)** Geological settings of Upper Valtellina Valley, with main tectonic structures (red line), lithological units and thermal springs location in the "Bormio study area". Lithology derives from Italian CARG (Foglio 024.BORMIO. Servizio geologico d'Italia, scale 1:50,000, 2009) and from 1:500,000 Geological map of Switzerland (Geologische Karte der Schweiz, 2005). **(b)** Location of the thermal springs in the "Bagni Vecchi" area. Spring names are reported in the legend (see also Table 1). (c) Cross section (along the track represented in a) illustrating the geological structure of the area with major faults and kinematics. [IT = Italy, CH = Switzerland, FR = France, DE = Germany, AT = Austria, SI = Slovenia]

### 5.2.2 Hydrogeological setting

The area includes three main watersheds (Spol, Adda and Adige rivers) and three big artificial lakes for hydropower energy generation (Cancano, San Giacomo di Fraele and Livigno lakes). The primary aquifers in this region are represented by the sedimentary units (Triassic carbonate unit, Dolomia Principale) and the underlying fractured zones primarily associated with major regional thrusts and faults (Zebrù and Trupchun-Braulio thrusts, Glorenza fault). Annual precipitation ranges between 790 and 1490 mm as measured since 1881 at Bormio meteorological station (*Servizio Idrografico e Mareografico Nazionale, Consorzio dell'Adda, ARPA Lombardia, Database OLL – Regione Lombardia D.G.S.P.U., Scotti et al., 2016*). A groundwater recharge of 400 mm/year (i.e. 40% of mean annual precipitation) is obtained by analysing the baseflow from the available discharge records (*Swiss Federal Office of Environment, FOEN 2017*) of the Rom stream (Val Mustair, Fig. 5.1a) which drains about 35% of the study area. This value is consistent with infiltration rates, ranging between 200 and 800 mm/year, computed for alpine environments with similar mean annual precipitation (*Maréchal, 1998; Gallino, 2007; Baietto et al., 2008; Thiébaud, 2008*). Most of this recharge exits as seepage to streams and cold/hot springs.

Most of the aquifers in the area present hydraulic conductivities controlled by epikarst development and by fracture systems generated from unloading and weathering processes during the Alpine orogeny (*Pena Reyes et al., 2015*). Field observations and Lugeon permeability tests carried out along the foundation of the Cancano-S.Giacomo di Fraele dam (Fig. 5.1a), indicate a superficial epikarstic and strongly fractured rock mass with hydraulic conductivities ranging between $1.5\times10^{-6}$ and $5\times10^{-7}$ m/s (*Clerici and Sfratato, 2008*).

### 5.2.3 Thermal springs

The ten geothermal springs of Bormio (Fig. 5.1b), described in the first century A.D. by the naturalist "Pliny the Elder" on his *Naturalis Historia*, are currently exploited by two thermal establishments: the older named Bagni Vecchi (1450 m a.s.l.), built since Roman colonization of the Valtellina valley, and a more recent one, the Bagni Nuovi (1334 m a.s.l.) exploited since 1820 A.D. Hot waters are directly collected, mainly from Cassiodora spring, in the Bagni Vecchi area; the discharge is piped each night to the Bagni Nuovi spa, while water of Cinglaccia spring is piped to the public swimming pool in Bormio. At present, water flowing from other springs

(Nibelunghi, Ostrogoti, Pliniana, Arciduchessa, San Carlo, Palestra and Zampillo dei Bambini) is unexploited due to low or discontinuous discharge (see Table 5.1). All ten thermal outflows are concentrated into a narrow zone with a vertical extent of about 200 meters and a horizontal extension of 500 meters. Such spatial distribution is controlled by WNW-ESE and NNW-SSE trending fractures directly related to the Zebrù thrust (*Conti, 1994, Froitzheim et al., 1996*). Outflow temperatures range between 18 °C and 43 °C, while mean spring discharge rates vary over several orders of magnitude, from 1 l/min (San Carlo spring) to 1200 l/min (Cinglaccia spring), for a total average discharge of about 2400 l/min (see Table 5.1).

**Table 5.1:** Bormio thermal spring water characteristics. The reference number is as in Fig. 5.1b.

| # | Spring Name | Elevation [m a.s.l.] | Temperature [°C] | Discharge rate [l/min] |
|---|---|---|---|---|
| 1 | Arciduchessa | 1406 | 36-39 | 400 |
| 2 | Zampillo dei Bambini | 1395 | 35-38 | 150 |
| 3 | Cassiodora | 1414 | 39-43 | 250 |
| 4 | Cinglaccia | 1280 | 37 | 1200 |
| 5 | Nibelunghi | 1330 | 35-37 | 40 |
| 6 | Ostrogoti | 1340 | 34-35 | 30 |
| 7 | Palestra | 1420 | 18-19 | 4 |
| 8 | Pliniana | 1340 | 36-38 | 100 |
| 9 | San Carlo | 1370 | 18-19 | 4 |
| 10 | San Martino | 1421 | 39-40 | 250 |

## 5.3 GEOCHEMICAL ANALYSES

### 5.3.1 Methods

Annual data of water quality for the thermal springs were made available by the Bagni di Bormio Spa Resort and from the Regional Health Agency (ASL) for the period 1999 to 2011. Data organized in a database have been interpreted through GIS and Aquachem® (*Calmbach, 1997*) modelling tools. Additional season samplings were performed on June 2012, October

2012, May 2013, and September 2013. Moreover, available continuous daily measurements were used to compare the seasonal variations in water temperature, electric conductivity and discharge. Determination of main cations (Ca, Mg, K, Na, Fe, As, $SiO_2$) was carried out through a ICP-MS Plasma, while anions (Cl, $SO_4$, $NO_3$) were analysed by a ion chromatographer. Therefore, cations were analysed twice and discrepancies lower than 5% were observed (*Pena Reyes et al., 2015*). The alkalinity (expressed as mg/L of $CaCO_3$) was calculated by titration, according to *Harris (2010)*; the ionic balance for the samples was less than 5%. In addition isotopic analyses ($^2H$, tritium and $^{18}O$) for six thermal and one cold water samples were performed by laser spectroscopy in order to estimate the age and the recharge altitude, both useful to define the general circulation in the hydrothermal circuit.

### 5.3.2 Cations and Anions analyses

The dominant water type is Ca-Mg-$SO_4$, with some variations towards the Ca-Mg-$HCO_3$ type, probably due to mixing with superficial waters. This reflects the dolomitic and carbonatic composition of the host rocks, almost entirely forming the Ortles and Umbrail-Chavalatsch Nappes. From Schoeller's diagram of the Cassiodora spring, minimal historical variations, during the years 1999 – 2011, in the water facies from Ca-Mg-$SO_4$ to Ca-$SO_4$-$HCO_3$, support a geochemical stability within the thermal source (Fig. 5.2a). High concentration of $SO_4$ could originate from water circulation in metamorphic rocks belonging to Campo Nappe, such as phyllites and micaschists. Moreover, contact between thermal waters and rocks belonging to the Campo Nappe is suggested by the detection of dissolved Fe, Sb and As (*Pena Reyes et al., 2015*). Elevated concentration in Fe, from pyrite and chalcopyrite mineralizations, can cause reddish concretions (deposits) at spring outcrops as observed at the San Carlo and Palestra springs. Here, mixing warm waters with shallow, cold and oxygen-rich waters probably causes an oversaturation in Fe oxides, with resulting deposition.

Most of the thermal springs are located very close to the Mg vertex of the Giggenbach's diagram (e.g. Cassiodora spring in Fig. 5.2b). This suggests a dominant sulphate water type typical of deep thermal waters, high-temperature processes and few connections with superficial waters.

Slight changes in the water chemistry are observed in the Piper's diagram (Fig. 5.2c), where data from Cassiodora spring during years 1999 – 2011 are plotted. Water type plots at top the

diamonds, suggesting a high Calcium, Magnesium and Sulphates composition. This diagram also reveals extremely small concentrations of chlorine (usually <0.3 mg/L; *Pena Reyes et al., 2015*). In conclusion, major ions geochemical analyses show that the composition of the waters is quite homogeneous, with the exception of the Palestra and San Carlo springs, which are enriched in iron and colder (mean temperature of about 18 °C – Table 5.1) due to stronger dilution by surface water. Moreover, they also confirm that the highly mineralized Bormio thermal discharges originate from deep circulation of meteoric and snowmelt waters through both sedimentary and metamorphic rocks.

### 5.3.3 Seasonal variations

The seasonal behaviour of thermal springs was analysed using geochemical data, temperature, discharge and electrical conductivity, of the constantly monitored Cassiodora spring (elevation: 1380 m a.s.l. - average discharge: 250 l/min). Concentrations in main cations and anions of Cassiodora spring remained stable, with only minor oscillations during the last 10 years, supporting the idea of medium-term stable conditions inside thermal reservoir (*Vuataz, 1983*).

Analysis of data from multi-parametric probes, located at the Cassiodora spring in 2011 and 2012 (Fig. 5.2d), shows some seasonal oscillations, particularly in spring when snowmelt abruptly feeds superficial watersheds at higher elevations. Shallow cold water mixes with thermal deep end-member during the upflow resulting in temperatures 4-5°C lower than winter mean, when shallow systems are supposed to be frozen. In response to cold-water inflow, discharge reaches the annual maximum.

The influence of intense precipitation on thermal spring regime occurs with an average time lag of 3-4 days from the meteoric events.

### 5.3.4 Geothermometers

Geothermometers are used to estimate subsurface or aquifer temperatures from geochemical properties of water. A basic assumption in using these instruments is that temperature-dependent chemical or isotopic equilibria prevail in the source reservoir. The

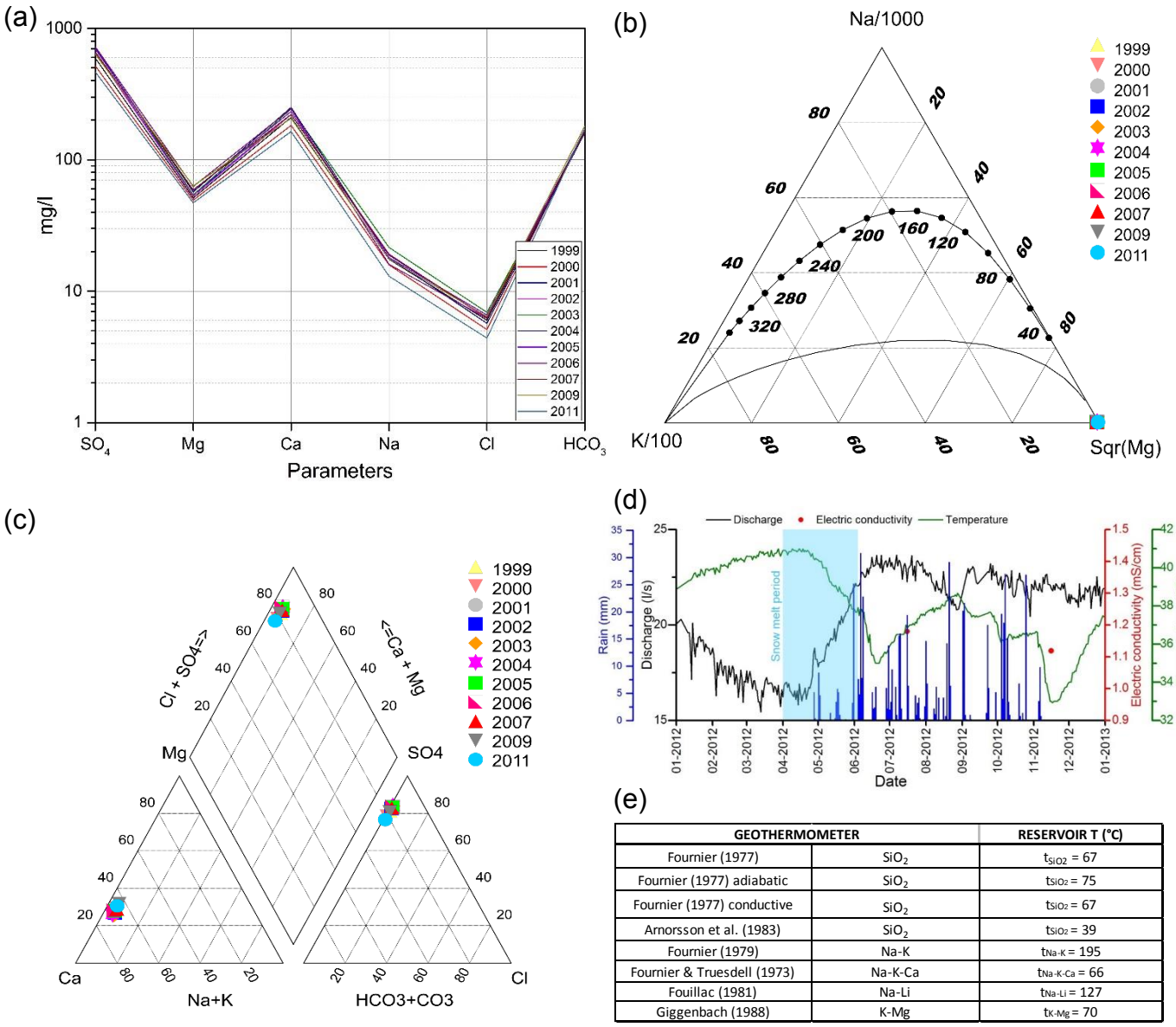


(e)

| GEOTHERMOMETER | | RESERVOIR T (°C) |
|---|---|---|
| Fournier (1977) | $SiO_2$ | $t_{SiO2}$ = 67 |
| Fournier (1977) adiabatic | $SiO_2$ | $t_{SiO2}$ = 75 |
| Fournier (1977) conductive | $SiO_2$ | $t_{SiO2}$ = 67 |
| Arnorsson et al. (1983) | $SiO_2$ | $t_{SiO2}$ = 39 |
| Fournier (1979) | Na-K | $t_{Na-K}$ = 195 |
| Fournier & Truesdell (1973) | Na-K-Ca | $t_{Na-K-Ca}$ = 66 |
| Fouillac (1981) | Na-Li | $t_{Na-Li}$ = 127 |
| Giggenbach (1988) | K-Mg | $t_{K-Mg}$ = 70 |

**Figure 5. 2:** Geochemical analyses: **(a)** Schoeller diagram for Cassiodora spring from 1999 to 2011; **(b)** Giggenbach triangle for the Cassiodora spring from 1999 to 2011; **(c)** Piper diagram for Cassiodora spring from 1999 to 2011; **(d)** discharge, temperature, electric conductivity (EC) and rain for the Cassiodora spring in 2012; **(e)** results of geothermometers analyses with calculated reservoir temperature.

most important water geothermometers are based on silica (quartz and chalcedony), Na/K and (Na-K)/Ca ratios. For the analysis of Bormio thermal waters, we used a winter sample, in which dilution due to mixing with shallow groundwater is supposed to be negligible.

Using the Fournier's $SiO_2$ geothermometer (*Fournier, 1977*) for adiabatic and conductive flow, temperatures around 67-75°C were obtained for the thermal reservoir (Fig. 5.2e), which are consistent with the observed conditions at the thermal springs, particularly Cassiodora, Pliniana and Cinglaccia. Due to the high Ca concentrations, a correction has been necessary to account for dissolution of dolomitic rocks. According to *Fournier's (1977)* $SiO_2$

geothermometer for Na-K-Ca-Mg, temperatures of 51-69°C were obtained for the Pliniana, Cassiodora and Cinglaccia springs.

The Giggenbach's geothermometer (recommended between 0°C and 250°C) is particularly useful when Na and Ca are not in equilibrium between rock and fluid (*Giggenbach, 1988*). The obtained results indicate temperatures between 53 °C and 69°C.

### 5.3.5 Isotopic data

Isotopic analyses were carried out for six thermal and one cold (Bocche d'Adda) springs scattered across the research area, on samples collected on January 2012 and July 2012, when also tritium ($^3H$) was analysed. The relationship between $\delta^2H$ and $\delta^{18}O$ for the analysed springs is plotted in Fig. 5.3a. The global meteoric water line (GMWL) ($\delta^2H = 8.0\ \delta^{18}O + 10$) (*IAEA, 2005*), and the North Italian local meteoric water line LWL ($\delta^2H = 7.7094\ \delta^{18}O + 9.4034$) (*Longinelli and Selmo, 2003*) are also shown. It can be observed that the sampled springs fall slightly above or mainly below the GMWL. Springs in the upper right corner of Fig. 5.3a indicate waters enriched with heavier isotopes, probably recharged from precipitation occurring at lower elevations, while springs located on opposite corner of Fig. 5.3a show lighter isotopic contents, indicating a probable recharge from higher elevations (*Pena Reyes et al., 2015*). Comparing January 2012 and June 2012 samples for Pliniana thermal spring, it is possible to observe an increase of $\delta^2H$ and a slight decrease of $\delta^{18}O$ in winter with respect to summer. This could indicate the presence of mixing between superficial water within the thermal springs during summer. Based on the function of recharge elevation with $\delta^{18}O$ found in *Pena Reyes et al. (2015),* we observe that the recharge elevations of thermal springs are higher than 2000 m a.s.l. indicating recharge from areas located in Switzerland or in the Trafoi valley (South Tyrol, Italy). The only exception is Palestra spring, where a strong mixing with cold water is observed, thus altering the isotopic composition, as we can see from Fig. 5.3b.

Tritium was used to reveal the age of spring water through comparison with a reference tritium atmospheric time curve (*IAEA, 2005*). The Pliniana and Cassiodora thermal springs show the smallest values of tritium Units, 3.9 and 2.3, respectively. These correspond to the longer circulation time between 5 and 10 years (*Pena Reyes et al., 2015*). Such long residence time is inconsistent with a deep karstic system, whereas supports the hypothesis of a

superficial epikarstic and strongly fractured rock mass, accordingly to the field observations and Lugeon permeability tests previously mentioned.

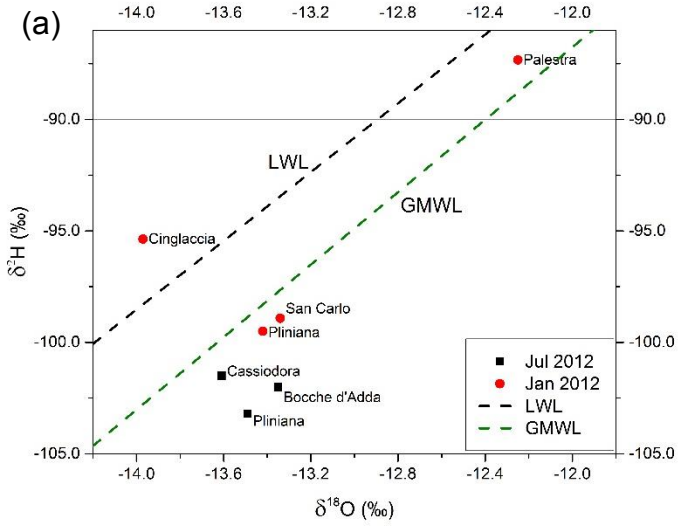


(b)

| Spring | Date | $\delta^{18}O$ (‰) (V-SMOW) | $\delta^{2}H$ (‰) (V-SMOW) | $\Delta^{3}H$ (T.U.) | Spring elevation (m asl) | Calculated recharge elevation (m asl) |
|---|---|---|---|---|---|---|
| Pliniana | Jul 2012 | -13.49 | -103.2 | 2.3 | 1340 | 2122 |
| Cassiodora | Jul 2012 | -13.61 | -101.5 | 3.9 | 1414 | 2185 |
| Bocche D'Adda | Jul 2012 | -13.35 | -102.0 | 6.5 | 1510 | 2052 |
| Pliniana | Jan 2012 | -13.42 | -99.50 | - | 1340 | 2027 |
| San Carlo | Jan 2012 | -13.34 | -98.92 | - | 1370 | 1997 |
| Palestra | Jan 2012 | -12.25 | -87.33 | - | 1420 | 1582 |
| Cinglaccia | Jan 2012 | -13.97 | -95.36 | - | 1280 | 2236 |

**Figure 5. 3:** Isotopic analyses: **(a)** dual isotope plot for spring water samples taken in January 2012 (red dots) and July 2012 (black dots). LWL (local meteoric water line for North Italy), GMWL (global meteoric water line); **(b)** results of isotopic analyses and calculated recharge elevation for seven thermal springs sampled on January and July 2012.

## 5.4 CONCEPTUAL MODEL

The model spatial extent is of extreme relevance in the reconstruction of deep circulation systems. An overly restricted scenario hampers a complete representation of groundwater flow and heat exchange processes, whereas a very large one results in excessive computational loading and more complex and uncertain geological reconstruction. Due to the

large extent of the supposed contributing area and its intrinsic geological complexity, a review of the existing literature on the study area was performed (*Pozzi, 1990; Berra, 1994; Froitzheim et al., 1997, Geologische Karte der Schweiz, 2005; Foglio CARG 1:50,000 N. 024, 2009*). Based on regional structural studies (*Conti, 1994; Froitzheim et al., 1996*), the model was extended north of Bormio to include entirely the S-Charl Nappe, where a transition between Triassic sedimentary cover and metamorphic basement occurs (Fig. 5.1a and Fig. 5.1c). This results in a very large regional groundwater flow and heat transport model covering about 700 $km^2$ and embracing the Livigno lake, Piz Sesvenna, Val Mustair, M.te Ortles, Forni glacier and St. Caterina Valfurva (Fig. 5.1a). Elevations range from the M.te Ortles summit (3905 m a.s.l.) to the municipality of Glorenza (850 m a.s.l.). As a common practice, limits of the model match with valley bottom, principal rivers and mountain watersheds, thus allowing an easier attribution of hydraulic boundary conditions.

The geological model was based on several deep geological cross sections from *Eugster (1971)*, *Pozzi (1965)* and *Conti (1994)*. By reconstructing a fence diagram connecting the neighbouring sections, interpolated surfaces were created. Major attention was devoted to representing the Zebrù thrust and the Glorenza fault at the contact between sedimentary cover and metamorphic basement. The base of the model is located at –4,500 m a.s.l., and the upper limit is defined by topography derived from a 40 x 40 meter DEM, resulting in a maximum thickness of about 8.5 kilometres (see Fig. 5.4). The lower limit of the Zebru' thrust damage zone is located approximately at +500 m a.s.l. forming the top surface of the metamorphic basement. As a result, the structural model includes a 5 km thick quasi-impervious unit (i.e. metamorphic basement) below the central portion of the model (cross section in Figure 5.4). This unit acts as a buffer for applying thermal boundary conditions at the bottom of the model. The highly fractured rock-mass of the deformation band, associated with the Zebrù thrust - Glorenza fault system, is assumed to constitute a preferred path for deep groundwater circulation as well as a conduit for rapid ascent in Bormio thermal area. This has been described in other geothermal systems of the Alps (e.g. *Vuataz, 1983; Rybach, 1995; Perello et al., 2001; Pastorelli et al., 1999; Baietto et al., 2008*). The dolostone/carbonate rock mass is refined by subdividing it into two different discrete zones (Fig. 5.4): (i) a superficial unit, often

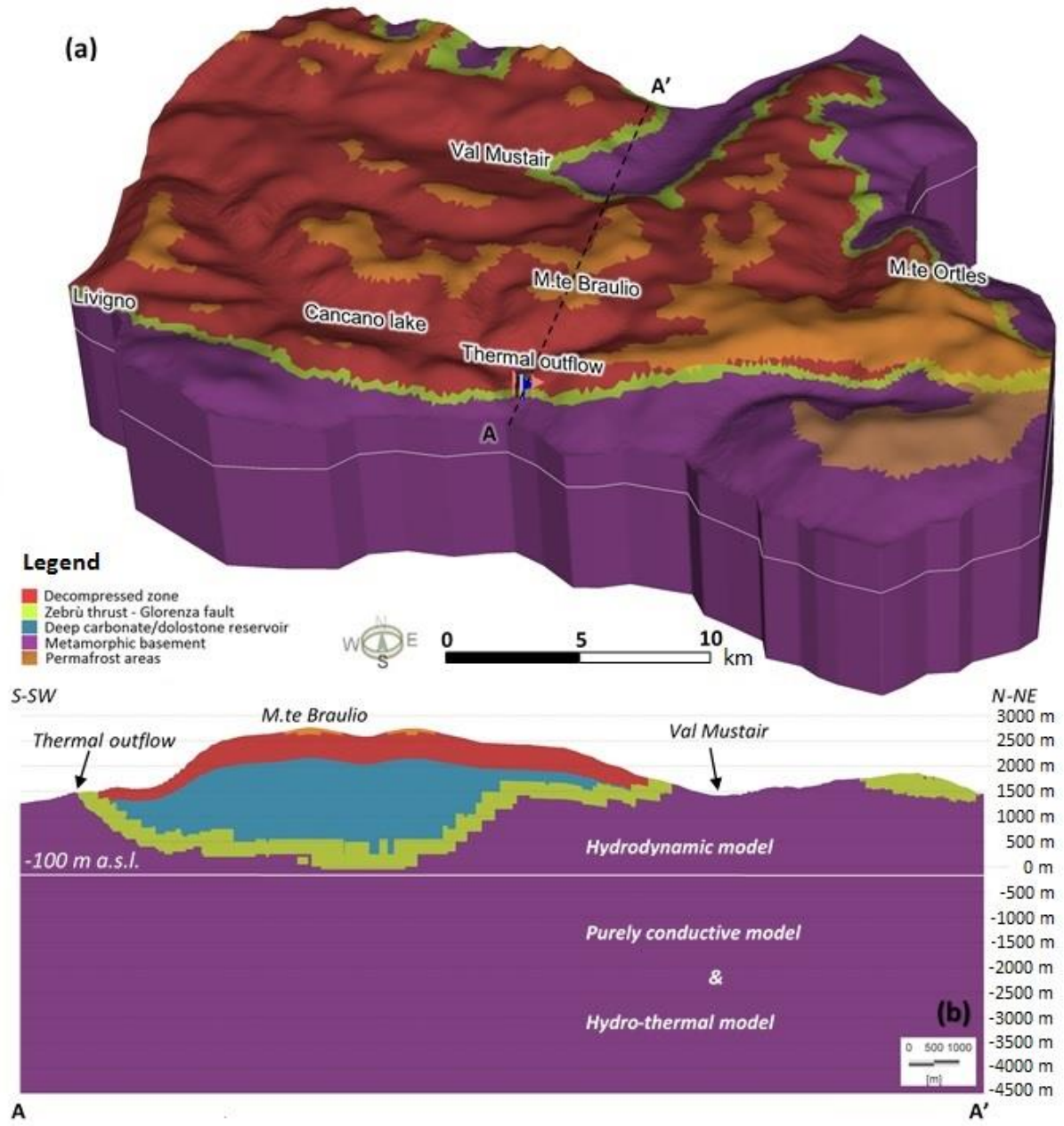


**Figure 5.4: (a)** Three-dimensional geological conceptual model showing the internal subdivision according to the four main hydrogeological units and the present day permafrost areas (orange). Recharge in the uplands is limited below the permafrost limit at 2650 m a.s.l. **(b)** Cross section A-A' passing through the thermal outflow area. The hydrogeological units include: the low-permeability metamorphic basement (purple); the high-permeability Zebrù thrust – Glorenza fault damage zone (light green); the low-permeability dolostone/carbonate rocks (blue); the highly permeable, fractured and epikarstic zone (red). The white line (-100 m a.s.l.) marks the base of the pure hydrodynamic model. For the conductive and the coupled hydro-thermal models the computational domain is extended down to -4,500 m a.s.l.

referred as the decompressed zone (*Jamier, 1975; Raven, 1977; Cruchet, 1985*), which represents the more permeable layers due to weathering processes, intense fracturing and epikarstic characteristics, and (ii) a deeper unit with lower permeability simulating the underlying non karstic, unweathered and less fractured sedimentary rocks (*Ofterdinger, 2001; Welch and Allen, 2014*).

In summary, the conceptual model consists of four hydrogeological units: (1) a superficial decompressed zone, with a medium thickness around 400 meters and representing the epikarstic aquifer where the infiltration from meteoric waters occurs; (2) a lower less-fractured non-karstic isotropic rock mass; (3) a high-permeability 100-m thick damage zone associated with the regional Zebru' thrust – Glorenza fault system and (4) the low-permeability metamorphic basement (Fig. 5.4).

## 5.5 NUMERICAL MODELLING

### 5.5.1 Numerical formulation of the conceptual model

A three-dimensional thermo-hydraulic model was built to simulate the deep and complex regional groundwater flow system. The commercial Feflow® groundwater finite-element simulator (*Diersch, 2014*) was used to solve the differential equations governing density-driven flows. The mathematical and numerical formulation of the problem can be found in *Diersch (2014)*.

Feflow® solves the following set of governing equations in saturated porous media:

Fluid mass conservation: $$S\frac{\partial \varphi}{\partial \mathrm{t}} + \mathrm{div}(\mathbf{q}) = 0 \qquad (\mathrm{Eq.}\,1)$$

Darcy's law: $$\mathbf{q} = -\mathbf{K}\left(\mathrm{grad}(\varphi) + \frac{\rho_\mathrm{f}-\rho_\mathrm{0f}}{\rho_\mathrm{0f}}\mathbf{u}\right) \qquad (\mathrm{Eq.}\,2)$$

Energy balance equation:

$$\frac{\partial}{\partial t}\{[\varphi\rho_\mathrm{f}c_\mathrm{f} + (1-\varphi)\rho_\mathrm{s}c_\mathrm{s}]T\} + \mathrm{div}(\rho_\mathrm{f}c_\mathrm{f}T\mathbf{q}) - \mathrm{div}[\lambda\mathrm{grad}(T)] = 0 \qquad (\mathrm{Eq.}\,3)$$

In the equation of fluid mass conservation (*Eq. 1*), *S* is the specific storage, *φ* is the hydraulic head and **q** is the Darcy velocity defining the specific discharge of the fluid.

In the Darcy's law (*Eq. 2*) **K** is the hydraulic conductivity tensor, **u** the gravitational unit vector and $\frac{\rho_\mathrm{f}-\rho_\mathrm{0f}}{\rho_\mathrm{0f}}\mathbf{u}$ is the buoyancy force induced by density variation ($\rho_\mathrm{0f}$ is the reference value of the fluid density $\rho_\mathrm{f}$).

In the energy balance equation for the fluid and the porous medium (*Eq. 3*), $c_\mathrm{f}$ and $c_\mathrm{s}$ denote the heat capacity of the fluid and the solid, respectively, *T* is the temperature and *λ* is the thermal conductivity of the saturated porous medium.

The flow and transport equations (*Eq. 2* and *3*) are non-linear and strongly coupled since temperature controls the hydraulic conductivity tensor **K**, the fluid density and dynamic viscosity, as expressed by the following constitutive and phenomenological relation:

$$\mathbf{K} = \frac{\mathbf{k}\rho_{0\mathrm{f}}g}{\mu_{\mathrm{f}}(C,T)} \qquad (\mathrm{Eq.}\,4)$$

In *Eq. 4*, **K** is the hydraulic conductivity tensor, **k** is the permeability tensor, *g* is the gravitational acceleration and $\mu_{\mathrm{f}}(C,T)$ takes into account the fluid viscosity effects due to temperature and concentration variations.

Feflow® fully implements an extended Equation of State (EOS) in order to reproduce a variable fluid density and viscosity for a wide range of temperature (0 ≤ *T* ≤ 350 °C) and pressure ($p_{sat}$ ≤ *p* ≤ 100 MPa).

The EOS (Equation Of State) for the fluid density is written as:

$$\rho_{\mathrm{f}} = \rho_{0\mathrm{f}}\left[1 - \bar{\beta}(T,p)(T - T_0) + \bar{\gamma}(T,p)(p - p_0)\right] \qquad (\mathrm{Eq.}\,5)$$

The fluid density in the single liquid phase is expressed in terms of reference values for density, temperature and pressure ($\rho_0, T_0$ and $p_0$). $\bar{\beta}(T,p)$ is the coefficient of thermal expansion and $\bar{\gamma}(T,p)$ is the coefficient of compressibility. The polynomial expressions used to fit the coefficients in a wide range of temperature (0 ≤ *T* ≤ 350 °C) and pressure ($p_{sat}$ ≤ *p* ≤ 100 MPa) are given in Magri et al. (2009) and ensure an accurate estimate of fluid density and viscosity as a function of pressure and temperature.

The fluid viscosity is calculated with the following function as shown in *WASY-GmbH (2002)*.

$$\frac{\mu(T)}{\mu(T_0)} = \frac{1 + 0.70603 \times \varsigma_{\mathrm{T_0}} - 0.04832 \times \varsigma_{\mathrm{T_0}}^3}{1 + 0.70603 \times \varsigma - 0.04823 \times \varsigma^3}\ ;\ \varsigma = \frac{T - 150}{100}\ ;\ \varsigma_{\mathrm{T_0}} = \frac{T_0 - 150}{100} \qquad (\mathrm{Eq.}\,6)$$

This allows for modelling heat transfer in hydrothermal reservoirs where high temperatures and pressures occur.

### 5.5.2 Modelling approach

Based on the conceptual configuration presented above, two numerical models were built to investigate the different processes involved in the area. In the pure hydrodynamic flow model (no heat transport), the bottom is set at an elevation of -100 m a.s.l. within the metamorphic basement (maximum thickness of ca. 4 km; Fig. 5.4). The coupled thermo-hydraulic model,

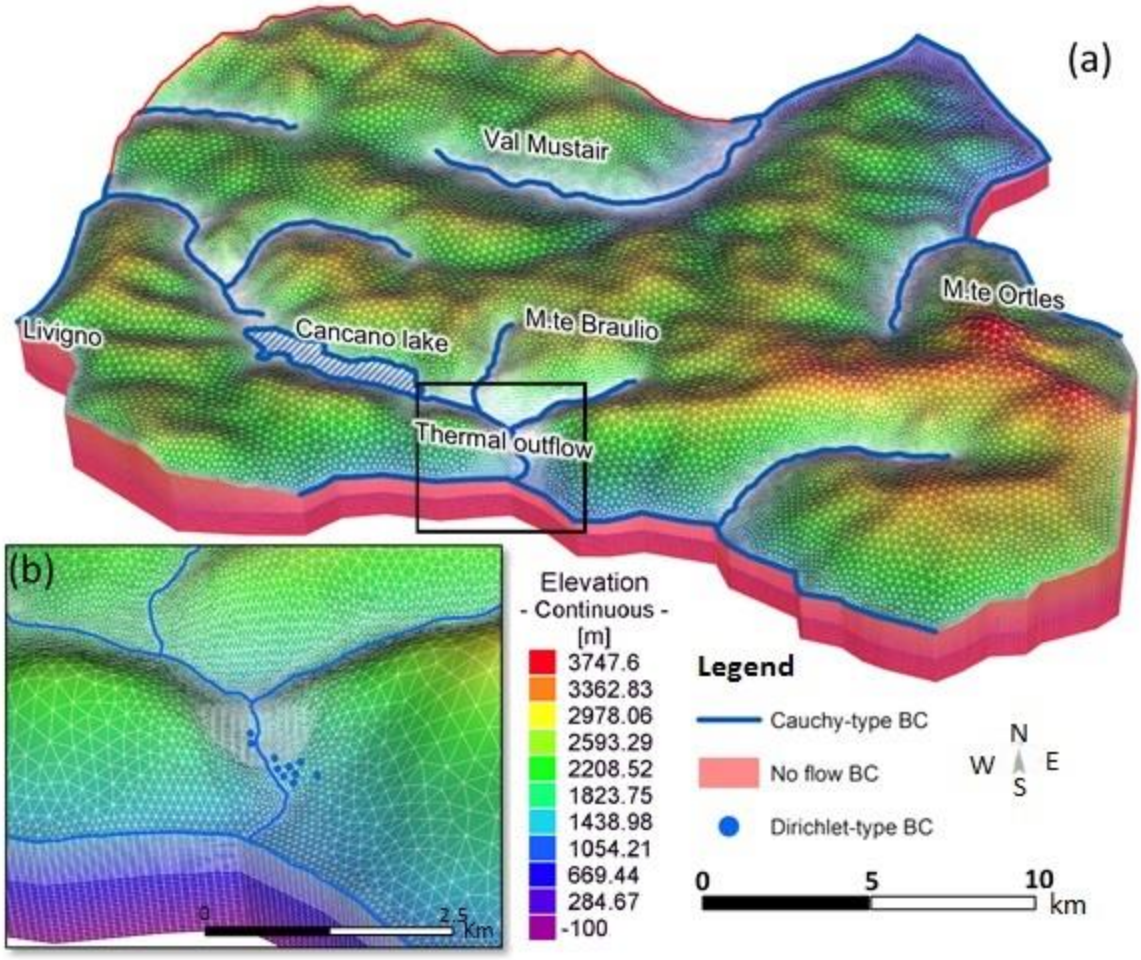


**Figure 5.5: (a)** Three-dimensional hydrodynamic flow model (48 slices with 84,044 triangles for each slice and 4 million prismatic elements), with applied hydraulic boundary conditions. A no-flow boundary condition is set to the bottom of the model (-100 m a.s.l.). **(b)** Enlargement of thermal outflow area as detailed in Fig. 5.1b, with location of thermal springs (blue dots). The 48 slices are visible along the lateral model boundary.

which includes the whole thickness of the low-permeability metamorphic units (-4,500 m a.s.l.), leads to a maximum thickness of ca. 8.5 km (Figure 5.4).

The model surface was discretized into a triangular finite-elements mesh using the software *Midas GTS NX® (2014)*. The mesh quality is very high with only 2.4 % of triangles with obtuse angles (>120°) and 0.1 % of triangles violating the Delaunay's criterion. Mesh refining was applied to ensure good quality simulations: elements size decreases gradually from 300 meters to 30 meters where the largest hydraulic head gradient and water flux dynamics occur, such as near the thermal springs outflow area, lakes and main rivers. This discretization produced a surface mesh made of 42,682 nodes and 84,044 elements (Fig. 5.5 and Fig. 5.6). Finer mesh did not affect the calculated patterns.

The 2D surface mesh was imported into Feflow® using a Matlab® script (*Guide, 1998*). The volume between the topographic surface and the bottom of the model is discretized with 48, for the hydrodynamic model, and 90, for the coupled thermo-hydraulic model, variably thick slices, ranging from 100 meters at the bottom to a minimum of 4 meters near the topographic surface. In total, the 3D meshes consist of more than 4 million prismatic elements for the hydrodynamic flow model and of more than 7.5 million prismatic elements for the coupled thermo-hydraulic model (Fig. 5.5 and Fig. 5.6).

The 3D mesh and reconstructed geological surfaces were imported in FracMan® software (*Dershowitz et al., 1998*) to assign material properties to each 3D element. Using a specific plug-in (DHI-WASY GmbH, ImportMatPorp.dll) the assigned material properties were imported back to Feflow® and linked with the previously created three-dimensional elevation model. In this way, a high quality refined mesh has been attained without structural internal subdivisions and including zones that exhibit different hydraulic and thermal behaviour.

Calculations of both purely hydrodynamic and coupled groundwater flow – heat-transfer processes were performed in Feflow®. All the tested models were calibrated against available measured discharge rates and outflow spring temperatures.

### 5.5.3 Boundary conditions

Groundwater flow boundary conditions were defined based on the geological and hydrogeological conceptual model. A constant head (i.e. Dirichlet type) corresponding to elevation of Bormio thermal springs was imposed at ten superficial nodes (Fig. 5.5). Along the main rivers, lakes and lateral boundaries, a fluid-transfer boundary condition (i.e. Cauchy type) was applied (Fig. 5.5) in order to account for surface-water/groundwater interaction. Such a transfer boundary condition applies a pre-defined reference head, as the value for the boundary condition, combined with a conductance parameter (transfer rate or leakage coefficient), set separately as a material property. In the models, the reference head is assumed equal to elevation and imposed where the water table intersects topography. This is the case for Livigno, Cancano and San Giacomo di Fraele lakes, the main river network (Adda, Adige, Braulio, Viola and Frodolfo rivers) and the bottom of Val Mustair (Rom stream) and Val Venosta (see Figs. 5.1a and 5.5). All the remaining lateral boundaries of the model, coincident with valley bottom and mountain watershed, were considered as no flow boundaries.

In the purely hydrodynamic model, to simulate effective recharge due to snowmelt and rain, an inflow value equal to 40% of mean annual precipitation (i.e. 400 mm/year) was assigned to surface elements belonging to permeable sedimentary units. For areas located above 2,650 m a.s.l. (see Fig. 5.4), where in a typical alpine environment permafrost strongly limits infiltration (*Guglielmin et al., 2001; Boeckli et al., 2011*), the effective recharge was set equal to 0.

Regarding the transient coupled thermo-hydraulic models, a steady-state heat-conductive solution of the problem is used as initial conditions. Fluid-flow boundary conditions are those of the previously described groundwater flow problem. A heat-transfer boundary condition (i.e. Cauchy type), controlled by a heat transmission coefficient, was imposed at all superficial nodes with the exception of those representing thermal springs. This allows discharge temperatures to be different from land surface prescribed temperature. Like the hydraulic equivalent, a heat-transfer boundary condition applies a pre-defined reference temperature, equal to the annual means for different altitude intervals (values ranging from 8 °C to 0 °C)

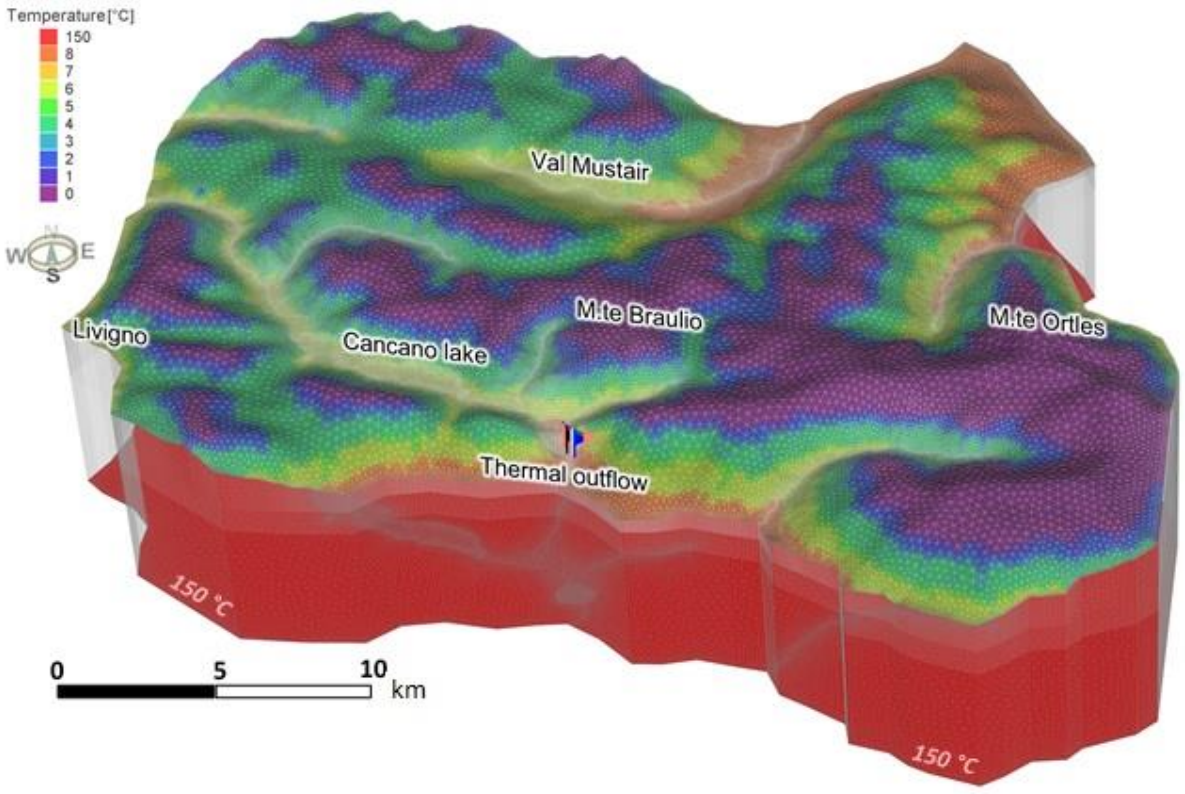


**Figure 5.6:** Three-dimensional coupled hydro-thermal model (90 slices with 84,044 triangles for each slice and 7.5 million prismatic elements), with applied thermal boundary conditions. Reference temperature on ground surface for different elevation intervals (Cauchy type) and fixed temperature of 150 °C (Dirichlet type) at the model bottom (-4,500 m a.s.l.). The 90 slices are visible along the lateral no-heat-flow model boundary.

(Fig. 5.6). Moreover, the lateral boundaries are no flow for both heat and groundwater flow, in particular because no heat is advected across such boundaries, it is assumed that heat conduction is vertical, i.e., no heat crosses.

The coupled thermo-hydraulic simulations, taking into consideration the whole thickness of the conceptual model (ca. 8.5 km), allow to apply a fixed temperature (i.e. Dirichlet type) as boundary condition at the model base (-4,500 meters a.s.l.). Assuming a mean geothermal gradient of 35 °C/km, evaluated for the Central Alps (*Clark et al., 1956; Medici and Rybach, 1995*) a constant temperature of 150 °C was set (Fig. 5.6). This allows the computation of the heat flow through the metamorphic bedrock underlying the major aquifers and facilitates the modelling of basin-scale processes that influence the temperature field over a time interval of less than a million of years (*Lin et al., 2000*).

In the following transient simulations the fluid-flux recharge boundary condition (Neumann type) is set as time-dependent. This allows modelling the gradual reactivation of the subsurface flow, in response to the slow melting of the Last Glacial Maximum (LGM) ice masses, and the presence of permafrost blocking infiltration through the valley side after glacier retreat (*Lebrouc et al., 2013*). Transient infiltration increases from 0% to the calibrated final value, equal to the 40% of annual precipitation (i.e. 400 mm/year), as discussed further in Section '*Thermo-hydraulic model*'. The other hydraulic and thermal boundary conditions were considered constant over time.

## 5.6 HYDRODYNAMIC MODELS

### 5.6.1 Model definition

Groundwater flow simulations represent a preliminary step in the development of the regional thermo-hydraulic numerical model. All the models were run assuming phreatic unconfined aquifer conditions under steady-state regime. Models were calibrated comparing numerical outputs with monitored average flow rates for the thermal springs (i.e. 2400 l/min) and with the mean discharge rate of Rom stream in Val Mustair (i.e. 177,000 $m^3$/day; *Swiss Federal Office of Environment, FOEN, 2017*).

Hydraulic conductivity is the main parameter controlling groundwater flux: a calibration process based on literature data both at global and local scale (*Sonney, 2010; Clerici and*

*Sfratato, 2008*), was carried out to estimate equivalent rock-mass continuum parameters. A clear distinction exists between carbonatic and metamorphic lithologies, these last characterized by a lower estimated hydraulic conductivity. Therefore, a one order of magnitude difference in hydraulic conductivity values was imposed between these units (Fig. 5.7). To the highly fractured deformation band, associated with the Zebrù thrust – Glorenza fault system, has been assigned half an order of magnitude larger hydraulic conductivity with respect to basement units (Table 5.2). Anisotropic hydraulic conductivity is introduced in the vertical direction ($K_z > K_{x,y}$, following *Ofterdinger, 2001*).

The transfer rate parameter, defined as the ratio between the hydraulic conductivity and the thickness of a layer forming the river bed (clogging layer), has been also calibrated. Starting values were defined assuming the same hydraulic conductivity as for the underlying geological unit and a layer thickness of 5 meters.

### 5.6.2 Calibration results

Some parameters (e.g. hydraulic conductivity) strongly influence the model results, while others (e.g. transfer rate) have minor effect on computed outflow rates. Multiple values of both hydraulic conductivity and transfer rate have been tested considering both isotropic and anisotropic conditions.

The transfer rate has a minor control on water table elevation and discharge rates, but controls the interaction between rivers and aquifers. Three orders of magnitude variation in hydraulic conductivities of the clogging layer have been tested. The final calibrated values resulted in a correct hydrologic behaviour, i.e. main rivers and lakes feed the aquifer when they are located above groundwater level and drain it when they are located below the groundwater level (see Fig. 5.7). This calibrated transfer rate avoids the formation of unrealistic "bubble" saturation fronts, observed where rivers are higher than the main water table.

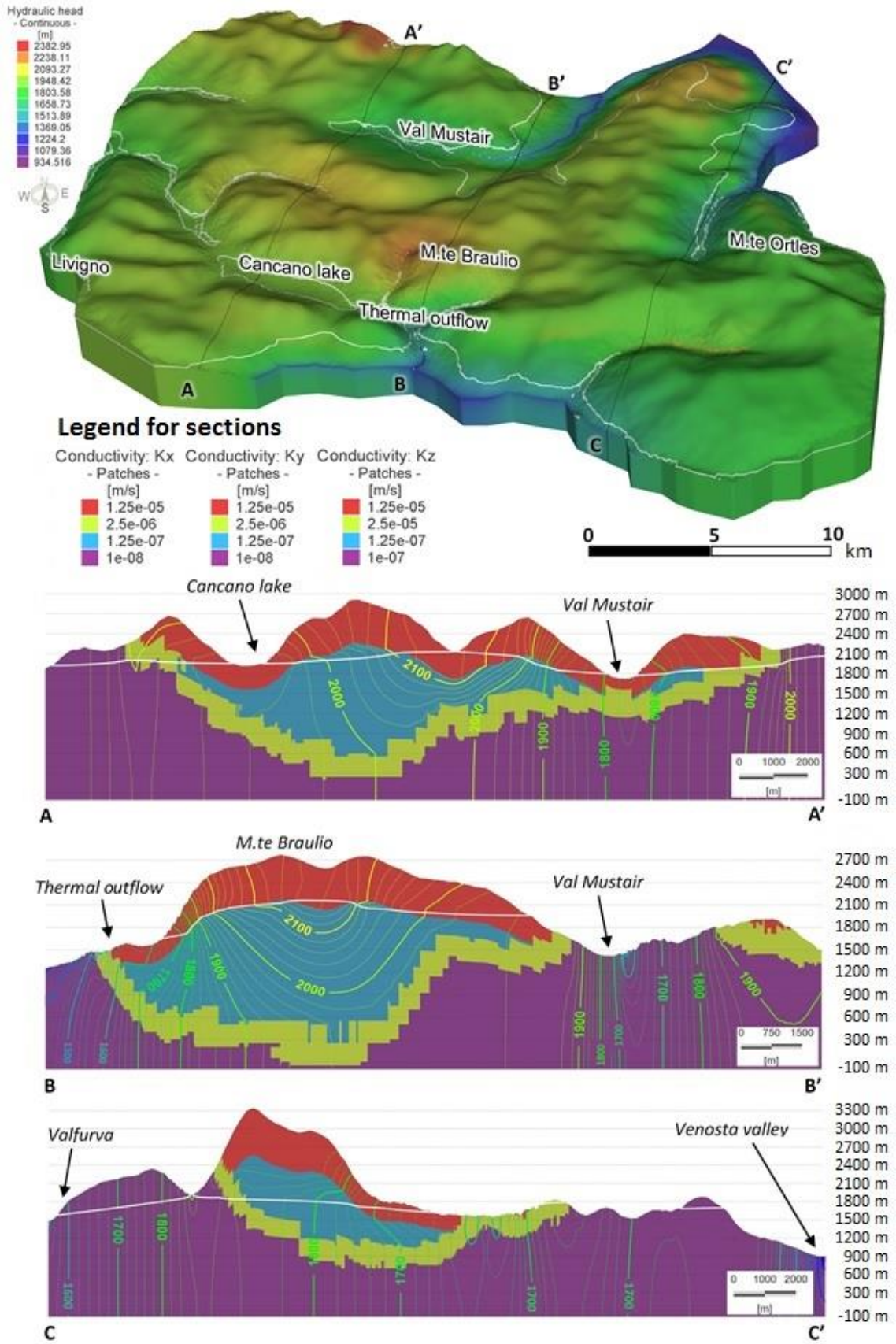


**Figure 5.7:** Hydraulic head distribution and water-table trace on the surface (white line) for the final calibrated hydrodynamic model. Three cross sections coloured according to calibrated hydraulic conductivities values (see Table 5.2 for the complete list of hydraulic properties); hydraulic head isolines are shown. All the cross sections, characterized by double vertical stretching, show a water table (white line) mimicking the topographic surface geometry.

To calibrate the hydraulic conductivity values, a groundwater level map was extracted and edited in a geographic information system (GIS) environment for each simulation, and simulated outflow rates for both thermal springs and Rom stream were compared with the measured values. A range of two orders in magnitude of hydraulic conductivity was tested for each unit. Simulated values ranged from $10^{-7}$ to $10^{-5}$ m/s for the decompressed zone and from $10^{-8}$ to $10^{-6}$ for the deep portions of the dolostone/carbonate reservoir. Hydraulic conductivities from $10^{-6}$ to $10^{-4}$ m/s and from $10^{-9}$ to $10^{-7}$ m/s were used for the Zebrù thrust - Glorenza fault damage zone and for underlying metamorphic units, respectively. Calibrated hydraulic conductivity values (Fig. 5.7) were still consistent with literature data (*Sonney and Vuataz, 2009; Sonney, 2010; Welch and Allen, 2014*). Calculated peak discharges of 2500 l/min and 180,000 $m^3$/day, similar to the monitored ones of 2400 l/min and 177,000 $m^3$/day, were attained at Bormio thermal spring nodes and at the catchment closure of the Rom stream.

The calibrated steady state hydrodynamic model exhibits a realistic hydraulic head distribution typical of the alpine environment where recharge / discharge areas occur in the highland and lowlands, respectively (Fig. 5.7) (*Bodri and Rybach, 1998, Welch and Allen, 2014*). This trend is similar to the one observed in neighbouring areas where excavated tunnels provide additional information regarding deep water pressure distribution (e.g. Fig. 3.19 and Fig. 3.20 in *Ofterdinger, 2001*).

**Table 5.2:** Calibrated values for the hydraulic parameters adopted in the construction of the hydrodynamic numerical model.

| Parameter | Decompressed zone | Deep portion of dolostone/carbonate reservoir | Metamorphic basement | Zebrù thrust – Glorenza fault |
|---|---|---|---|---|
| $K_x = K_y$ [a] (m/s) | $1.25 \times 10^{-5}$ | $1.25 \times 10^{-7}$ | $1 \times 10^{-8}$ | $2.5 \times 10^{-6}$ |
| $K_z$ [b] (m/s) | $1.25 \times 10^{-5}$ | $1.25 \times 10^{-7}$ | $1 \times 10^{-7}$ | $2.5 \times 10^{-5}$ |
| In/Out transfer rate (1/s) | $1.25 \times 10^{-5}$ | $1.25 \times 10^{-8}$ | $1 \times 10^{-8}$ | $2.5 \times 10^{-5}$ |
| In/Out flow on top (mm/yr) | 400 | - | - | 400 |

[a] $K_x$ and $K_y$ represent the hydraulic conductivity in *x* and *y* direction (horizontal plane)

[b] $K_z$ represents the hydraulic conductivity in *z* direction (vertical plane)

## 5.7 HEAT-TRANSFER MODELS

### 5.7.1 Model definition

Following the example of other simulations of heat and fluid transport processes (*Marèchal et al., 1999; Baietto et al., 2008; Gallino et al., 2009; Thiébaud et al., 2010; Dzikowski et al., 2016*), thermal modelling was performed in two steps: firstly, simulations were carried out as a pure heat-conduction problem under steady-state regime; then, the results were taken as initial conditions for a coupled fluid flow and heat transport simulation in both steady and transient regimes.

Hydraulic material properties were assigned from the previously calibrated hydrodynamic model. Initial rock thermal conductivity of 1.33 W/m/K and effective porosity of 0.025 % were assigned to all sedimentary subdomains and values of 2.5 W/m/K and 0.01 % were assigned to the metamorphic units of the model, consistently with literature data (*Robertson, 1988; Sonney and Vuataz, 2009; Sonney, 2010*). The heat transmission coefficient (i.e. transfer rate) was calculated as the heat conductivity of the material divided by the representative element height (*Magri et al., 2015*). Feflow® default values were used for thermal conductivity of water (0.65 W/m/K), heat capacity of solid (2.52 MJ/m$^3$/K) and water (4.2 MJ/m$^3$/K) (Table 5.3).

**Table 5.3:** Calibrated values of thermal material parameters for the four lithologic units of the heat-transfer model. Calibration is performed assuming hydrodynamic parameters as in Table 5.2.

| Parameter | Decompressed zone | Deep portion of dolostone/carbonate reservoir | Metamorphic basement | Zebrù thrust – Glorenza fault |
|---|---|---|---|---|
| Porosity (%) | 0.025 | 0.025 | 0.01 | 0.1 |
| Thermal conductivity of solid (W/m/K) | 1.33 | 1.33 | 2.5 | 1.33 |
| In/Out transfer rate (heat) (J/m$^2$/s/K) | 0.0866 | 0.0866 | 0.1766 | 0.0866 |

### 5.7.2 Purely conductive model

The initial glacial condition, in which the local geothermal gradient was almost undisturbed by groundwater flow, has been modelled as a pure conduction problem under steady-state regime. Thermal boundary conditions and material properties were as presented above. However, because Feflow® does not allow no-flow simulations, a very low and homogeneous value of hydraulic conductivity ($10^{-14}$ m/s) was assigned to all model elements.

As expected, the resulting conductive temperature distribution (Fig. 5.8) is characterized by anomalies in the temperature isosurfaces mainly coinciding with the main valleys or the different thermal properties assigned to model elements. This undisturbed geothermal temperature field has been used as initial internal condition for the following transient simulations.

### 5.7.3 Thermo-hydraulic model

Transient simulations have been performed using the conductive heat flow model temperature distribution as initial conditions, and a starting time equivalent to LGM conditions realized 11,000-12,000 years ago. Similar thermal and timing configurations have been used by other authors (*Maréchal, 1998; Gallino et al., 2009; Thièbaud et al., 2010; Dzikowski et al., 2016*) to simulate the reactivation of infiltration and water circulation, following the regional glacial retreat of LGM ice masses.

Steady-state simulations were performed to determine whether the present day temperature of Bormio thermal waters is compatible with thermal equilibrium between cold infiltrating water and host rocks. At steady-state the simulated temperatures (mean calculated value of 8 °C) at Bormio thermal springs are considerably lower than either the conductive or monitored ones, thus suggesting a thermal disequilibrium (monitored values ranging from 35 to 43 °C; Table 5.1).

Additionally, based on the work of *Deming (1993)*, the time length necessary for the coupled heat/fluid flow system to attain steady state conditions has been calculated. With a model thickness of about 8 km, the system would require 300-600 million years to equilibrate, depending on the chosen parameter setting (porosity and thermal conductivity) used to calculate the thermal diffusivity.

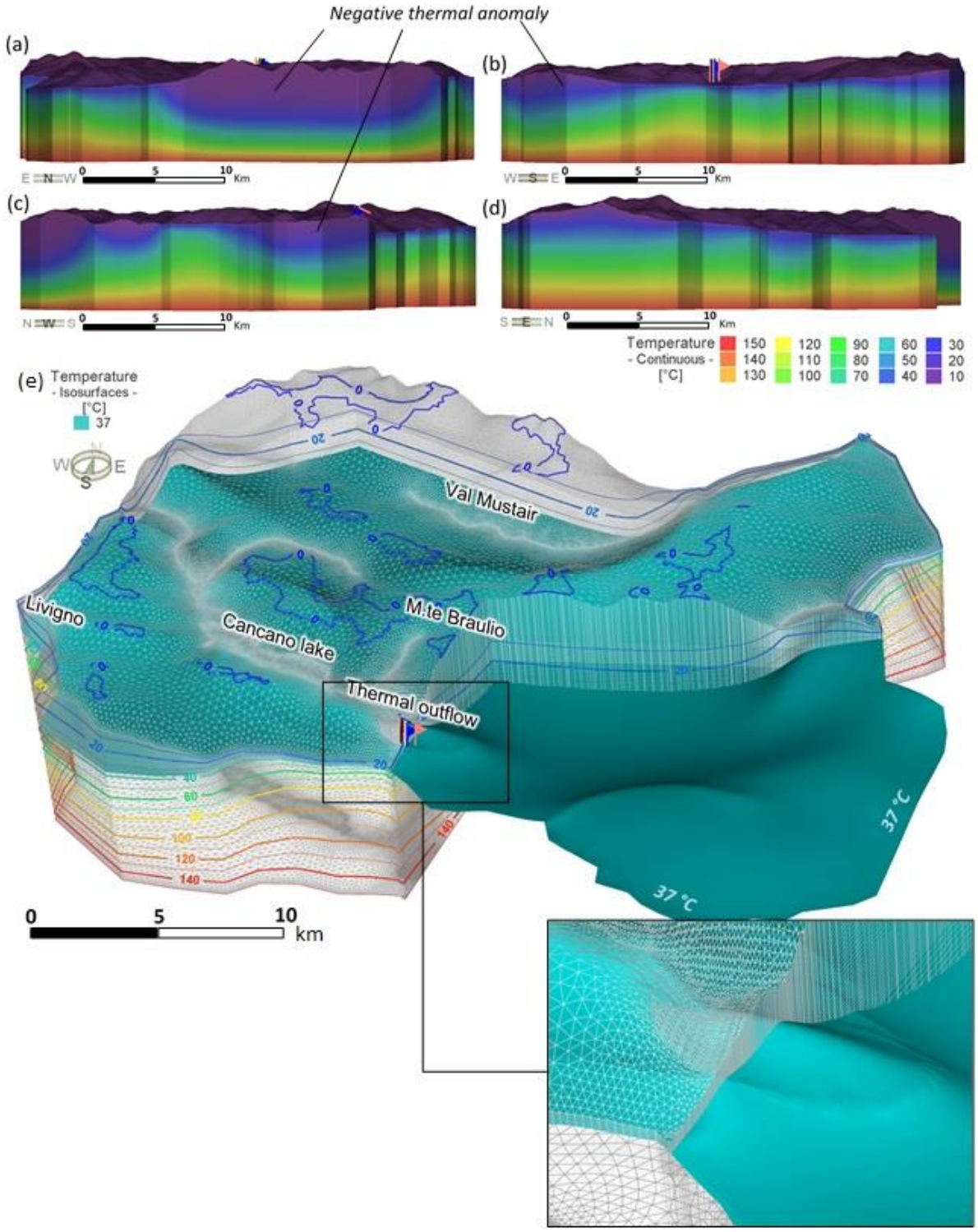


**Figure 5.8: (a)-(d)** Conductive temperature distribution along the sides of the model: **(a)** view from north, **(b)** from south, **(c)** from west and **(d)** from east. **(e)** Perspective view of the model with purely conductive temperature isolines and the 37 °C isosurface (i.e. mean present day thermal springs temperature). Negative thermal anomalies are present below mountain ridges, thus preventing the 37 °C isosurface from reaching the ground surface around the thermal outflow area (see enlargement).

Therefore, these results fully support the hypothesis that long time-scale transient simulations are required to model the thermal evolution of Bormio system between the Last Glacial Maximum (ca. 11-12,000 years B.P.) and the present day.

Computed temperatures at 10 observation points corresponding to Bormio thermal springs (Fig. 5.9) confirm the general long-term cooling evolution of the system. Starting from purely conductive thermal state (Fig. 5.10; 0 yrs), the temperature at Bormio springs increases to a maximum value of about 57 °C, reached after ca. 6,000 years in the simulation, due to the activation of topographically-driven circulation system that drives deep water to the surface along the Zebrù thrust. After this peak, outflow temperature gradually decreases due to increased infiltration of cold water from superficial recharge and snowmelt. The present day average measured value of 37 °C is reached after ca. 13,000 years in the simulation (Fig. 5.10; 13,000 yrs). The model shows a complete cooling of the aquifer after a period of ca. 50,000 years (Fig. 5.10; 50,000 yrs) with an average final simulated temperature of 10 °C. Additional simulations have been performed applying a constant superficial recharge value, all over the

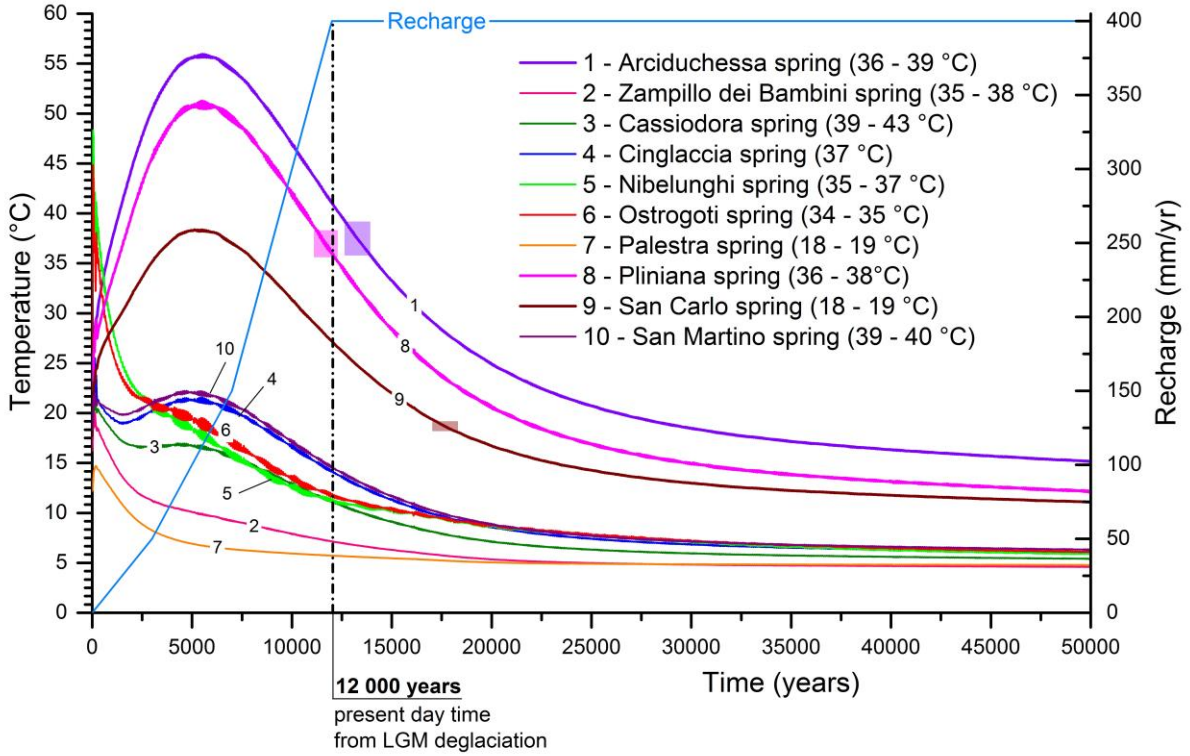


**Figure 5.9:** Time evolution of simulated water discharge temperatures for the coupled hydro-thermal transient model at 10 observation points corresponding to Bormio thermal springs (for location, see Fig. 5.1). Time 0 corresponds to the end of last glaciation (LGM ca. 12,000 years B.P.). The measured temperature ranges for the thermal springs are reported in the legend and as small boxes for the three springs along the model fault trace. The assumed time-dependent recharge applied to the model is shown.

simulation time, and equal to the minimum (5%, i.e. 50 mm/year) and to the maximum (40%, i.e. 400 mm/year) of the transient time-step values (Fig. 5.9).

As the resulting temporal evolution of discharge temperatures does not show a substantial difference from simulation with transient recharge (see Fig. 5.9), it is possible to conclude that Bormio springs temperature evolution is mainly controlled by the thermal and hydraulic property distributions of the model rather than by cold water infiltration rates. However, the adopted time-dependent values (Fig. 5.9) represent the gradual reactivation of subsurface flow, following the melting of LGM ice masses, more realistically.

## 5.8 DISCUSSION

The aim of this study was to simulate the hydrodynamic and thermal behaviour of the complex Bormio alpine fractured system since the LGM. Because of the size (ca. 700 $km^2$) and complexity of the studied area, numerous simplifications have been made in the geometry of the model (e.g. a constant thickness for the damage zone associated with regional Zebrù thrust). Such simplifications, coupled with the loosely constrained hydraulic and thermal parameters, induce some uncertainties in the results. Nevertheless, a calibration process was performed and all the models were tested against available data such as measured river and spring discharge rates and outlet spring temperatures.

As in many other geothermal systems (*Forster and Smith, 1988, 1989; López and Smith, 1995, 1996; Baietto et al., 2008; Dzikowski et al., 2016*), a tectonic structure, in this case the relatively thin and permeable damage zone of the Zebrù thrust – Glorenza fault system (light green in Fig. 5.4 and Fig. 5.7), rapidly transmits groundwater from great depth to the springs. Groundwater flow towards the regional tectonic feature depends on the capability of both the fault zone and the sedimentary rock to transmit fluids, and of the relative contrast in permeability with the basement rocks. The simulated groundwater flows converge to the Adda valley and Bagni Vecchi, the lowest points of the model, where the contact between permeable sedimentary covers and underlying impermeable metamorphic units crops out (Fig. 5.7).

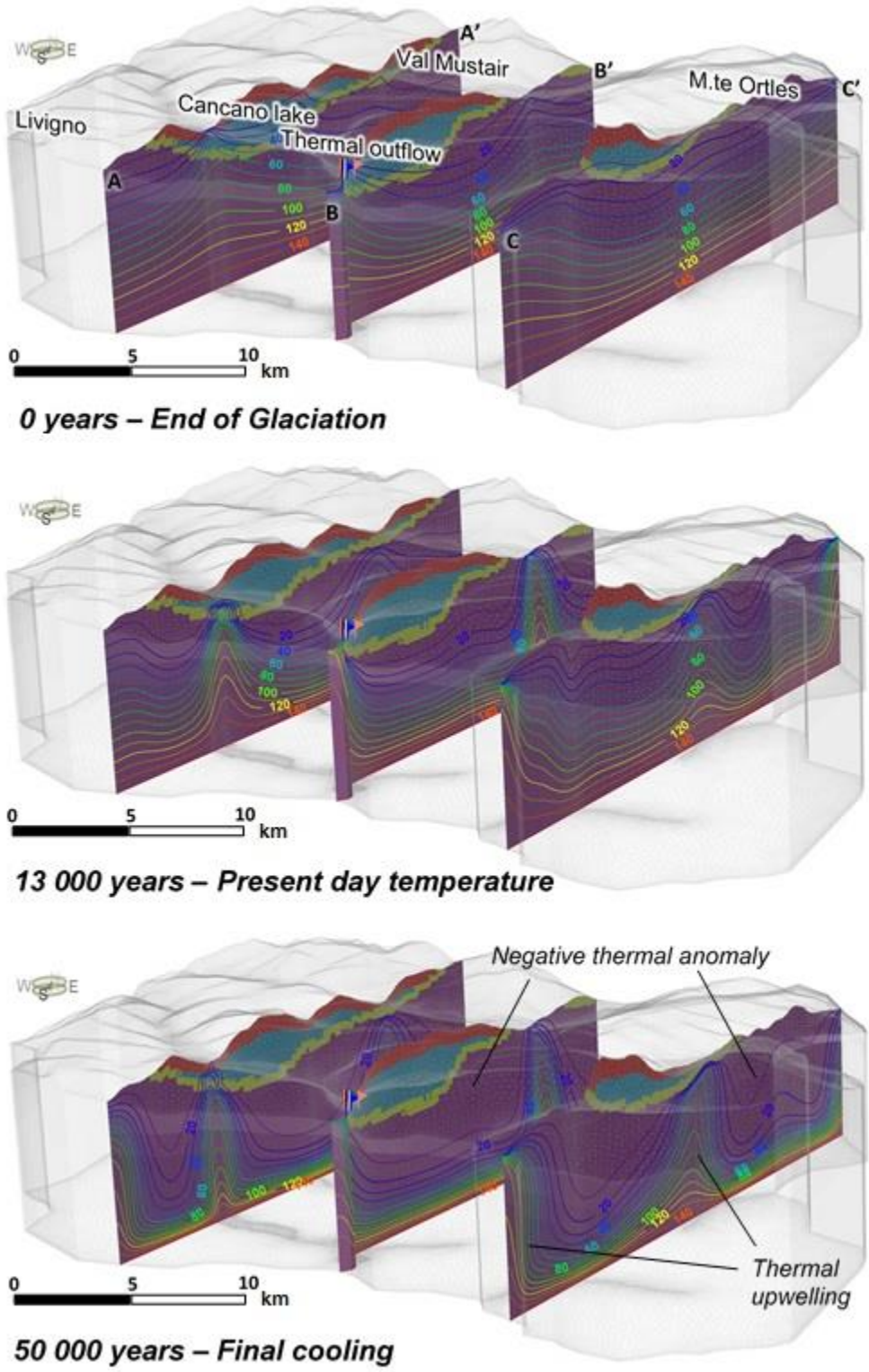


**Figure 5.10:** Evolution with time of water temperature for the coupled-hydro-thermal model. Results are presented at three time steps (0 yrs, 13,000 yrs and 50,000 yrs since LGM) along three cross sections (see traces in Fig. 5.7). Positive (i.e. upwelling) and negative thermal anomalies are shown. Negative anomalies progressively enlarge and deepen with time, while upwelling zones become more evident. Isotherm values are in °C and hydrogeological units are as in Figures 5.4 and 5.7.

The high dip angle of Zebrù thrust (≈ 60°) forces groundwater to upflow and discharge at the observed flow rates (ca. 2400 l/min). Flux-weighted pathlines, providing a visual indication of groundwater flow and relative flux rates, clearly show the role of Zebrù thrust – Glorenza fault system in the regional flow and highlight the areas where cold waters preferentially recharge the system. The forward tracking analysis (Fig. 5.11) shows that thermal hot water originates from a very large area, including the Swiss portion of the model, where meteoric and snowmelt waters infiltrate in the Ortles and S-Charl nappe.

Regarding heat transfer models the system is initially assumed to be dominated by conduction. This is based on the hypothesis that permafrost and glaciers present down to an elevation of ca. 1,000 meters a.s.l. during the last glaciation prevented significant groundwater recharge. The absence of fluid circulation in the steady state/conductive model generates a condition globally warmer than the present day one. At the same time it prevents hot temperatures to be reached at Bormio thermal spring nodes (see Fig. 5.8). Transient coupled hydro-thermal simulations use as starting date the age of significant glacial retreat (LGM) estimated by *Hormes et al. (2008)* around 11,000-12,000 years ago.

The time dependent thermal evolution of the model (Fig. 5.10) shows how groundwater flow affects the thermal gradient in the study area by advective heat flow cooling. The model predicts increasing temperature at the spring nodes till a progressive long term cooling. Topographically-driven advective flow creates a thermal upwelling along the valley talweg (i.e valley floors) and at outflow areas. Negative thermal anomalies (Fig. 5.10) progressively deepen throughout the simulation time below areas where effective recharge (i.e. snowmelt and rain) is assigned (i.e. permeable sedimentary units below the permafrost limit of 2,650 meters a.s.l.).

A similar distribution of positive and negative thermal anomalies has been observed for mountain groundwater flows and thermal regimes (*Forster and Smith, 1988, 1989; Deming, 1993; Bodri and Rybach, 1998; Gallino et al., 2009; Thièbaud et al., 2010; Burns et al., 2015; Dzikowski et al., 2016*). This distribution, observed also in the Bormio model, demonstrates that basal heat flow can be strongly reduced by cold groundwater deepening within mountain systems.

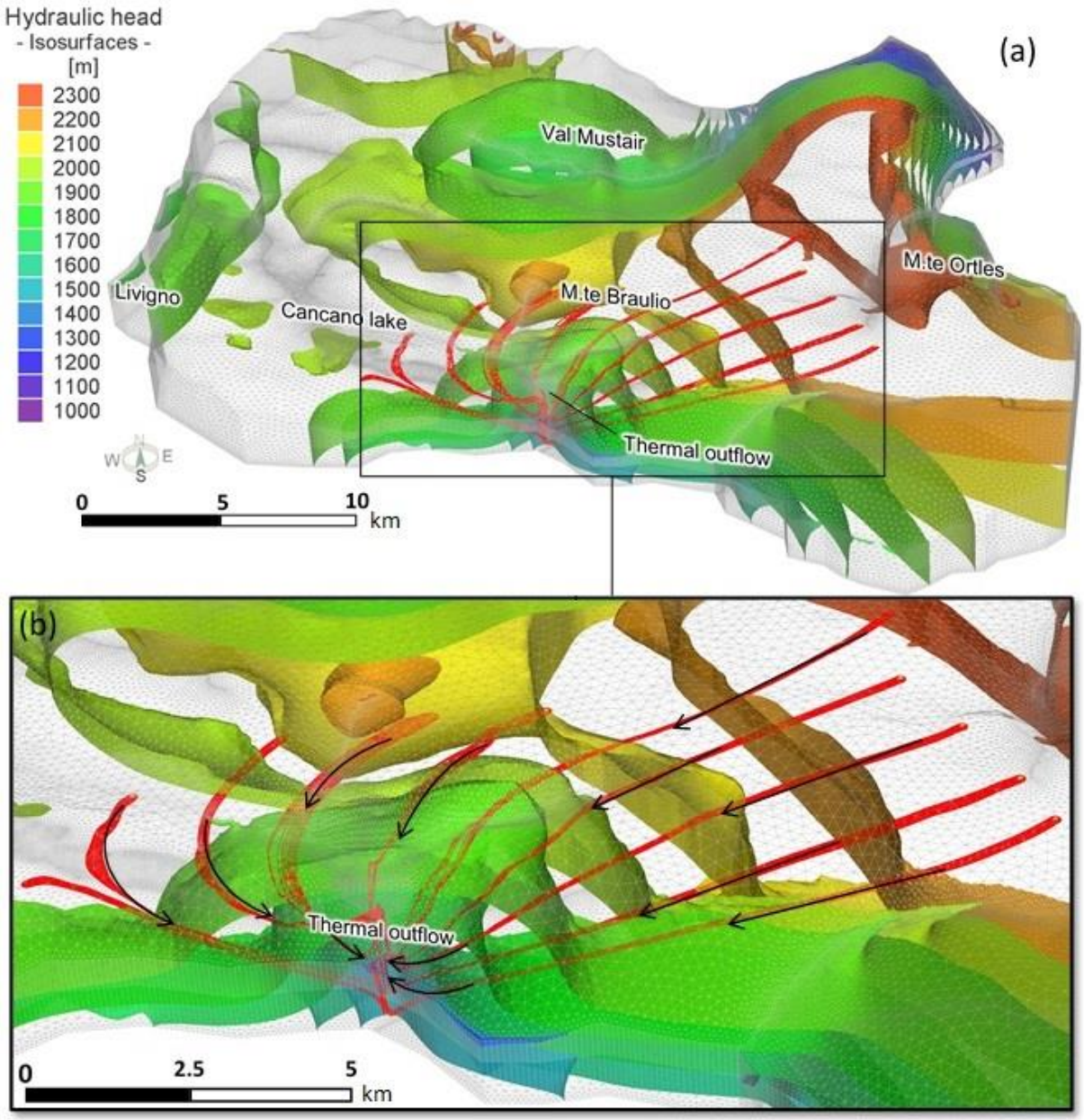


**Figure 5.11:** Flow trajectories for the calibrated hydrodynamic model, showing areas contributing to the Bormio thermal springs: **(a)** Particle tracking from ten selected nodes of the calibrated hydrodynamic model. Thermal hot water originates from a very large area, including the Swiss portion of the model, where meteoric and snowmelt waters infiltrate in the sedimentary nappes (Ortles and S-Charl). Hydraulic head isosurfaces every 100 m are also presented. **(b)** Zoom of the forward tracking analysis in the thermal outflow area. Flow directions are highlighted with black arrows and show the steep upward path followed by rising deep thermal hot water in proximity of Bormio.

The transient thermal analyses show that present day temperatures (i.e. 11,000-12,000 years since LGM) of Bormio thermal waters can only be explained by taking into consideration both progressive heating during deep infiltration and the temporal evolution of the system. As said above, the restored circulation within the aquifer since the end of the last glaciation causes gradual heating of the discharged waters, followed by a progressive cooling. The computed

temperatures approach the recorded present-day values at the spring points around 13,000 years after LGM (see Fig. 5.9). This is observed at three springs (#1, 8 and 9 in Fig. 5.1b and Table 5.1) which fall exactly along the outcropping fault trace in the model. The temperature mismatch for the other springs (Fig. 5.9) is ascribed to the local geometry of the fault zone deformation band, which is clearly simplified in the numerical model, not taking into account splays and other local effects in the vicinity of the ground surface.

As for the role of the Zebrù thrust – Glorenza fault system on fluid flow and heat transfer, the modelling approach allows fluids to enter or leave the fracture zone at any point along its length. Due to the marked difference between calibrated hydraulic and thermal parameters of intact/damaged carbonate and metamorphic lithologies, the contact zone acts as a preferential pathway for hot fluid migration, in particular during initial heating of the model (Fig. 5.10). Perhaps due to the complex three-dimensional structure, the simulations do not show a proper convective circulation established within the fault zone, as found by *Lòpez and Smith (1995)* in their simplified 3D mountain single fault model. Nevertheless, hot ascending plumes show in the modelling results of Figure 5.10, indicating that high-relief surface topography can cause lateral variations in the thermal regime. Figure 5.10 shows a progressive enlargement and deepening of the negative thermal anomalies below the mountain massif and the sharpening of the positive anomalies (i.e. upwelling).

## 5.9 SUMMARY

The influences of groundwater recharge, glaciation and deglaciation, permafrost distribution and hydraulic properties on the development of fluid and heat flow in a typical alpine setting were examined.

The conceptual model was built based on hydrochemical analysis previously performed in the Bormio area. From those preliminary simulations, some typical aquifer conditions can be traced for the Bormio thermal system: 1) water types are dominated by dissolution of the main ion groups Ca–Mg and $SO_4$–$HCO_3$, with seasonal variations for the second end members; 2) dominant oxidizing conditions for the thermal springs; 3) dominant sulphate water type typical of deep and high-temperature processes, suggesting that Bormio thermal waters are not well mixed with shallow waters, with exception of seasonal mixing; 4) low Cl

concentrations, with poor correlations between Cl and other major ions; 5) relatively stable hydrochemical conditions for most of the major ions such as Ca, Mg, K, Na, Cl, $SO_4$; 6) geothermometer results indicate thermal reservoir temperatures of about 50-65°C, reached at the interface between impermeable metamorphic units and more permeable sedimentary covers; 7) circulation times obtained from isotopic data of approximately 5-10 years.

Steady state hydrodynamic simulations are used to define the water table geometry and to calibrate model properties against measured outflow rates at Bormio thermal springs and stream discharge. The model results in a realistic hydraulic head distribution mimicking the mountain massif topography as reported for other alpine environments.

Thermo-hydraulic simulations suggest that an unsteady thermal regime is needed to explain the current spring water temperatures. In particular, the model shows that hydro-thermal flow in the Bormio area mainly occurs along the regional Zebru thrust – Glorenza fault system and that convection plays a minor role compared to topographic advective heat flow. Rainfall infiltration values (40% of the mean annual precipitation), providing the recharge of the system, strongly control Bormio springs outflow rates. The hydraulic and thermal structures of the model constrain the thermal behaviour of the simulations. Positive anomalies evolve with time below the discharge zone and the topographic lows. The modelled time spans 50,000 years since the Last Glacial Maximum. Average monitored spring discharge temperature of 37 °C is reached after ca 13,000 years of simulation (close to the end of the LGM in the area defined at 11,000 to 12,000 yrs BP), while complete cooling of the aquifer occurs within approximately 50,000 years. Thus, contrary to the impression given by human-timescale observations, the Bormio hydrothermal system is not thermally stable.

A large contributing domain, highly elevated relief, complex subsurface structure and high regional heat flow make the Bormio hydrothermal system an interesting case study. The adopted numerical framework proves to be suitable for such complex modelling issue and yields satisfactory hydrothermal results in terms of both flow rate and water temperature. However, rather large uncertainties still exist in the rest of the model domain, mainly due to lack of deep and superficial information.

# 6. THE CASTEL GIORGIO – TORRE ALFINA GEOTHERMAL FIELD

The chapter is largely based on the article of *Volpi et al. (2017)*: *Modeling highly buoyant flows in the Castel Giorgio - Torre Alfina deep geothermal reservoir,* published on on Geofluids Journal.

## 6.1 INTRODUCTION

Dynamic high enthalpy reservoirs are the most worldwide spread and exploited geothermal systems. The high temperatures recorded at the exploitable depths in the range of 1 to 3 km, is usually due to intrusive masses which induce an intense heat-flow, triggering free convection heat transfer mechanisms when a porous aquifer is emplaced above (*Nicholson, 2012*). The occurrence of dynamic high temperature geothermal fields is often tectonically determined, and mainly associated with volcanic active areas or active plate margins. Important examples are the geothermal areas of Yellowstone (*Eaton et al., 1975, Morgan et al., 1977; Lucchitta, 1990*), northern California (*Younker et al., 1982*), the Pannonic Basin (*Ravnik et al., 1995*), and the Rhine Graben (*Werner and Kahle, 1980; Brun et al., 1992; Bellani et al., 2004*). Electricity production is the most important form of utilization of such high temperature geothermal systems (*Kühn, 2004*).

Italy strongly contributes to the development of geothermal power generation. In 1904, the world first electrical power was produced from a geothermal energy source in the Larderello site (Tuscany, central Italy, *Barelli et al., 1995a,b,c, 2000; Batini et al., 2003; Tiwari and Ghosal 2005; Romagnoli et al., 2010; Stober and Bucher, 2013*).

Beyond the world famous Larderello system, fossil and active hydrothermal manifestations are distributed all along the pre-Appennine belt of central Italy, facing the Tyrrhenian coast. This area has undergone to both lithospheric extension and upper mantle doming. Such processes have been active since the Miocene (*Carmignani et al., 1994; Brunet et al., 2000*) and are likely sustained by mass and heat fluxes from the upper mantle. This is suggested by the intense tectonic and volcanic activity associated to extremely high and variable surface heat flux anomalies (*Della Vedova et al., 2001, 2008*). All these processes document a predominant heat transfer mechanism by vertical mass flow, which accumulates large amount of geothermal resources at accessible depths in the upper crust. Two geothermal fields in the area, characterized by heat flow values of up to 1000 $mW/m^2$ (Larderello system) and 600

mW/m$^2$ (Mt. Amiata system) (*Bellani et al., 2004*), are currently exploited for the production of electricity.

Recently, various projects were set up on a regional basis to investigate the geothermal potential of the Italian Tyrrhenian facing areas. Moreover, research and development of new exploitable geothermal fields have been encouraged by the approval of specific decrees of law (i.e. Legislative Decree of 11 February 2010, n. 22, modified by Legislative Decree of 3 March 2011, n. 28 and Article 28 of Decree of Law of 18 October 2012, n. 179).

Among the identified promising areas, the Castel Giorgio - Torre Alfina field (CG-TA, northern Latium, Fig. 6.1) is an example of an early explored and so far not exploited, medium enthalpy geothermal system (*Cataldi and Rendina, 1973; Buonasorte et al., 1988; Colucci and Guandalini, 2014*). Detailed hydro-geothermal data, available for the selected area since early 70s, show that the CG-TA is a potential geothermal reservoir with medium thermal characteristics (120°C - 210°C) whose fluids (pressurized water and gas, mainly $CO_2$) are hosted in a fractured carbonate formation (*Buonasorte et al., 1988, Barberi et al., 1994; Chiarabba et al., 1995; Chiodini et al., 1995; Doveri et al., 2010; Carapezza et al., 2015*). Data from the deepest geothermal drilling in the area (Alfina015 well, max depth -4,826 m a.s.l., see Fig. 6.1 for location) show a highly variable temperature gradient ranging between 0.15 °C/10m and 2.1 °C/10m (*Buonasorte et al., 1991*). Such a strong variation likely indicates the presence of highly convective flow within the reservoir rocks. This finding makes the CG-TA area suitable for future exploitation through a new generation 5 MWe geothermal pilot power plant. Following the guidelines of the above mentioned Italian legislative decrees, this exploitation project is characterized by no gas emission to the atmosphere and total reinjection of the geothermal fluid in the same producing geological formation (i.e. geothermal well doublet system).

Planning of such challenging geothermal field exploitation projects requires an appropriate numerical modelling of the involved heat and fluid transfer processes. These numerical models allow to define well's system design, fracture paths, extraction rates, temperature of injected and produced thermal waters, to interpret hydraulic tests or stimulation processes, and to predict reservoir behaviour during geothermal power production. Therefore, they are

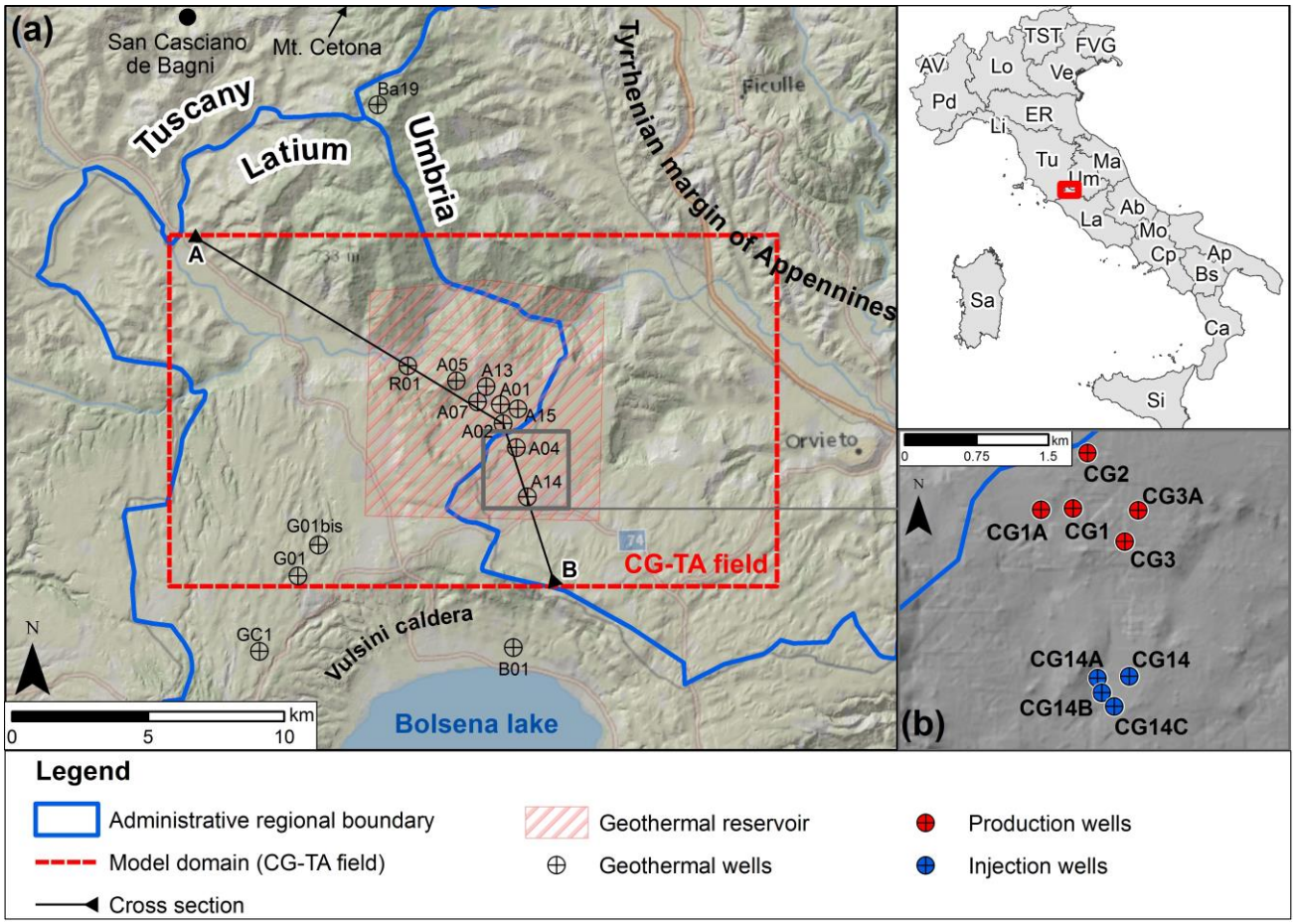


**Figure 6.1: (a)** Geographical setting of the CG-TA geothermal field (red dashed line). The geothermal producing reservoir (red shaded area), the cross section trace A-B, and the existing geothermal wells drilled in the area are shown (where in the labels A stands for Alfina, G for Gradoli, GC for Grotte di Castro, B for Bolsena and Ba for Bagnoregio). **(b)** Enlargement of the SE area of the reservoir with location of the 5 production wells (CG1, CG1A, CG2, CG3 and CG3A) and the 4 injection wells (CG14, CG14A, CG14B and CG14C) used in the simulation of the 5MW field exploitation.

mandatory to optimize the productive capacity and the thermal breakthrough occurrence (*Stober and Bucher, 2013; Li et al., 2016*).

The aim of the present study is to build the first 3D numerical model of the deep, medium-enthalpy CG-TA reservoir to reproduce the highly convective undisturbed present-day natural state of the reservoir. These results, validated against the pressures and temperatures measured in geothermal wells, are afterward used to investigate the feasibility of a geothermal power production configuration (i.e. injection and production wells). The analysis is performed on a hypothetical 50 years operational life cycle adopting a well doublet system at a 1,050 t/h flow rate (*ITW and LKW, 2013*). The finite element open source code OpenGeoSys (*Kolditz et al., 2012*) is used to build the hydro-thermal (HT) model. As additional

numerical constraint, the results are compared against those obtained with the commercial finite element code Feflow® (*Diersch, 2014*).

First, the hydro-geothermal data derived from geophysical investigations and from geothermal wells are described and used to build a conceptual and numerical model of the CG-TA reservoir. Then, the numerical approach based on the OpenGeoSys software is given. Results are obtained both at short (i.e. operational) and long term (i.e. full reservoir recovery) time scale. Besides providing valuable guidelines for future exploitation of the CG-TA deep geothermal reservoir, this study highlights the importance of field data constraints for the interpretation of numerical results of fluid processes in reservoir-scale systems.

## 6.2 RESERVOIR CHARACTERIZATION

### 6.2.1 Regional geological and structural setting

The occurrence of medium- and high-enthalpy geothermal fields in central Italy is localized along the Tyrrhenian margin of the Apennines (i.e. southern Tuscany - Fig. 6.1). Here the geodynamic setting and the magmatic activity produce a huge geothermal anomaly with maximum peaks centred in the Larderello and Mt. Amiata areas, where heat flow values almost double the continental average (*Baldi et al., 1994*).

From a geothermal point of view, southern Tuscany represents the most productive and exploited site of all Italy. Therefore, its complex geological and tectonic setting has been extensively studied by several authors (*Decandia et al., 1998; Liotta et al., 1998; Brogi et al., 2003, 2005; Brogi, 2006*), and many alternative models were proposed to describe the tectonic evolution of the inner Northern Apennine (*Carmignani et al., 1994; Boccaletti et al., 1997; Jolivet et al., 1998; Bonini and Sani, 2002*).

The southern Tuscany is characterized by a shallow Moho discontinuity (20-25 km depth), and a reduced lithosphere thickness due to uprising asthenosphere and the delamination of crustal lithosphere (*Gianelli, 2008*). The present-day structural setting of the Tyrrhenian coast facing regions represents the heritage of two main deformation processes that begun in the Oligocene (i.e. 30 Ma BP) with the Alpine-Apennine orogenesis (*Carminati and Doglioni, 2005*). Firstly a compressive phase resulted in the formation of fold-and-thrust-belts and associated piggy-back basins with NNE-SSW oriented trend (*Buonasorte et al., 1987 and 1995; Petracchini*

*et al., 2015*). Then, a post-collisional extensional tectonics eastward migrating, affected the inner part of the orogenic belt since at least Early Miocene (*Minissale, 1991; Rossetti et al., 1999*). Extension, due to the Tyrrhenian back-arc opening, resulted in the formation of NW–SE tectonic basins and in crustal thinning, with consequent upwelling of magma bodies and increased heat flow (*Della Vedova et al., 2001, 2008; Romagnoli et al., 2010*). Such widespread Late Miocene-Quaternary magmatism was derived from mixing of crustal and mantle sources (*Serri et al., 1993*). Since the Middle Pliocene, southern Tuscany has been affected by rapid surface uplift (*Dallmeyer and Liotta, 1998*), in contrast with the coeval thermal subsidence affecting the nearby northern Tyrrhenian Basin (*Bartole, 1995*).

From late Miocene to late Pliocene, N–S and NW–SE trending normal faults were active in southern Tuscany, bordering several extensional basins (*Pascucci et al., 1999; Montone et al., 2012*) in a non-rotational setting (*Mattei et al., 1996*). Normal faulting within the Apennines and its peri-Thyrrenian foundered thrust belt lead to an increase in vertical permeability, connectivity and fluid mixing in progressively larger and interconnected sectors of the stretched crust (*Ghisetti and Vezzani, 2002*). The continuity of adjacent basins throughout southern Tuscany is interrupted by Quaternary NE–SW strike-slip faults and step-over zones, controlling the magma emplacement in the inner Northern Apennine (*Acocella et al., 2006*).

Due to the interplay of all these phenomena, the geologic and structural settings of the area are quite complex and involve many different lithostratigraphic units. The main and most widespread complexes, from the shallower to the deeper ones (*Nardi et al., 1977; Cosentino et al., 2010; Romagnoli et al., 2010; Colucci and Guandalini 2014;* Fig. 6.2) are, namely:

- *Volcanic complex*: Pliocene-Pleistocene volcanic products found in the north-eastern border of the large volcanic complex of Vulsini caldera (Fig. 6.1). It includes tuff, lavas and pyroclastic rocks, characterized by variable thickness, with a maximum of 200 meters;
- *Neoautochthonous complex*: composed by Miocene to Quaternary deposits, mainly related to marine, lacustrine and to continental environments. It is represented by clays, with limited sand content, conglomerates, marls, evaporates and detrital limestones in a discontinuous layer 50 to 160 meters thick;

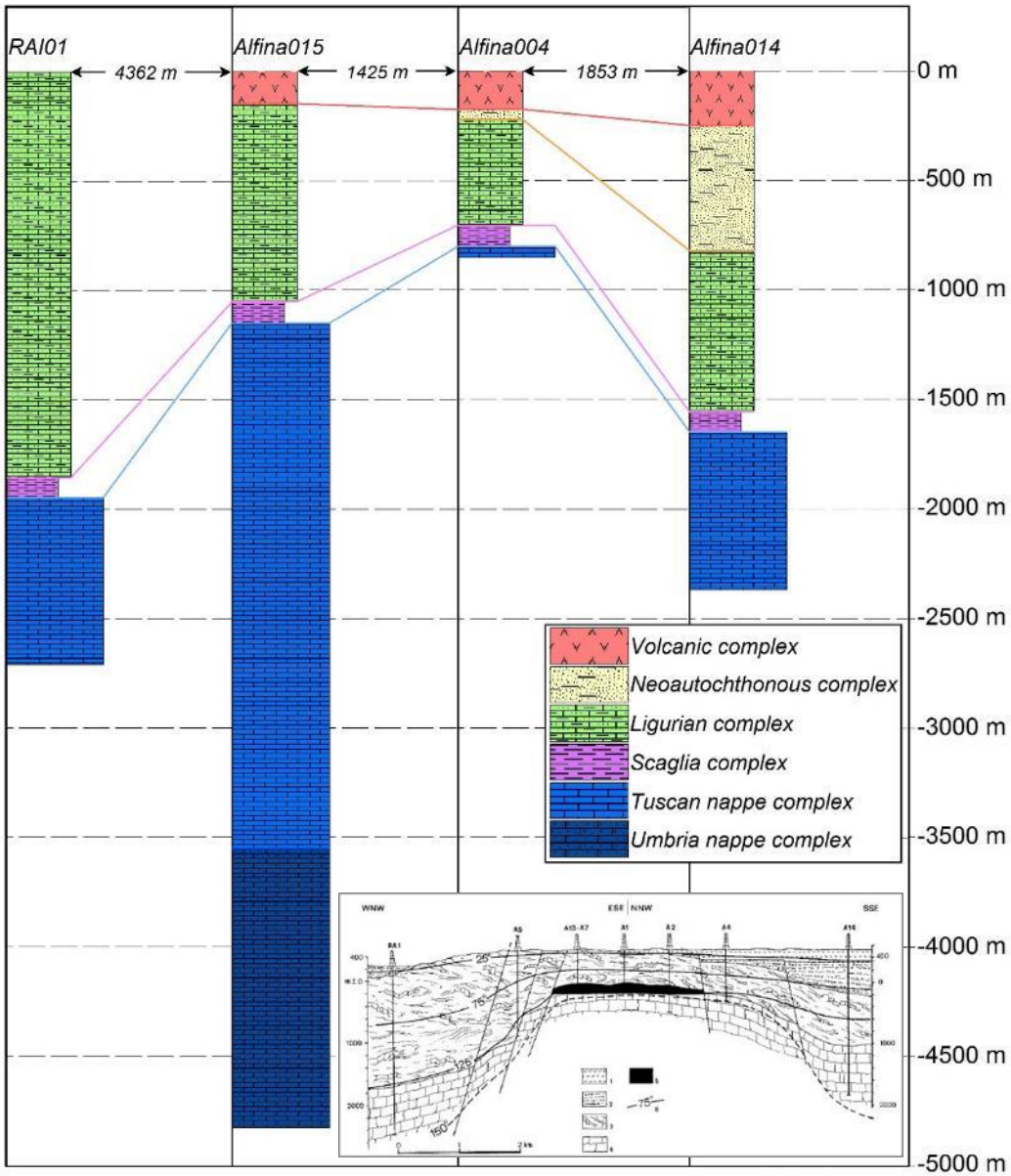


**Figure 6.2:** Stratigraphic columns and correlation section (see trace in Fig. 6.1) compared with the WNW – SSE cross section by *Buonasorte et al. (1988)*. RAI01, Alfina004 and Alfina014 wells belong to the first drilling campaign (1971-1972), while the deepest Alfina015 well was drilled on 1987-1988. The Castel Giorgio – Torre Alfina geothermal reservoir is hosted in a structural high (i.e. horst structure) of fractured Mesozoic limestones belonging to Tuscan and Umbria Nappe complex (light and dark blue units).

- *Ligurian/sub-Ligurian complex*: The genesis is related to the convergence tectonics that caused the closure of the Ligurian-Piedmont Ocean since Late Cretaceous. The main lithologies are Jurassic-Eocene clayey-marly units in flysch facies, sandstones, marly-limestones and ophiolites. They are characterized by a highly variable thickness ranging from 500 to 1,800 meter (RAI01 well, see Fig. 6.1; *Nardi et al., 1977*);

- *Tuscan and Umbria Nappe complex*: represents a sedimentary succession deposited since Triassic to Miocene on the continental paleomargin of the Adria Plate. It is composed by Triassic-Lower Miocene arenaceous and clayey-marly formations, calcareous-siliceous rocks, dolostone and anhydrites. The upper portion of this formation is characterized mainly by marly-limestone and shales, and is referred as the "*Scaglia formation*". The Tuscan and Umbria Nappe carbonatic formation reaches a thickness of about 3,700 meter (Alfina015 well, see Fig. 6.1; *Buonasorte et al., 1991*).

### 6.2.2 The Castel Giorgio - Torre Alfina geothermal field

The CG-TA geothermal field (Fig. 6.1) is located to the north of the Vulsini caldera (*Buonasorte et al., 1988*), at the boundary between the Tuscany, Umbria and Latium regions (central Italy). The Torre Alfina reservoir was extensively explored between the 1970's and the 1990's. We refer to the works of *Cataldi and Rendina (1973)* and of *Buonasorte et al. (1988, 1991)* for the detailed description of the geothermal explorations carried out in the area. These investigations culminated with the drilling of eight geothermal wells, with depths ranging from 563 to 2,710 m, and more recently, with the drilling of a very deep geothermal well (Alfina015 – Fig. 6.2) reaching the depth of 4,826 m.

The integration between stratigraphic borehole logs, geophysical (*Buonasorte et al., 1988; 1991*) and seismic (*Chiarabba et al., 1995*) data identified the CG-TA geothermal reservoir as hosted in a structural high (i.e. horst structure highlighted in the correlation section of Figure 6.2) of fractured Mesozoic limestones, belonging to the Tuscan and Umbria Nappe complex, and marked by positive geothermal and magnetic anomalies (*Vignaroli et al., 2013*). Structural investigations performed in the area by *Buonasorte et al. (1987)* and *Piscopo et al. (2009)* provide a detailed description of the N-S striking post-orogenic extensional faults bounding this horst structure and an analysis of the geometry, orientation, and kinematics of all the other tectonic features occurring in the Torre Alfina geothermal system.

The first geothermal drilling campaign performed in the CG-TA field (1971-1972), was aimed to reach and cross the argillaceous and shaly terrains of the Ligurian and Sub-Ligurian complex. These investigations not only allowed a detailed stratigraphic reconstruction, but also the definition of the basic characteristics of the geothermal reservoir fluids (e.g. pressurized hot water with average temperature of 140°C) and the detection of a gas cap made by 2% of

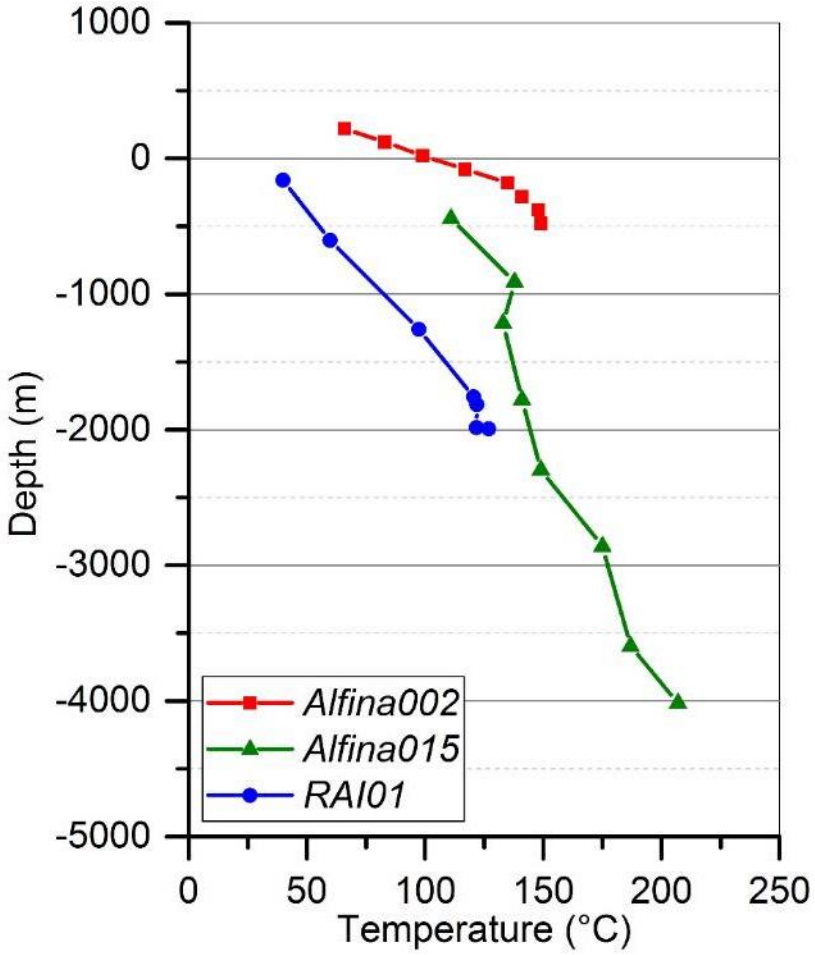


**Figure 6.3:** Temperature vertical profiles along 3 exploration wells according to *Cataldi and Rendina (1973), Buonasorte et al. (1988, 1991)*. Locations of the selected wells are reported in Fig. 6.1. The inversion of the Alfina015 well temperature profile and the values detected at the top and at the bottom of the reservoir (140 °C at -1,050 meters b.g.l. - 207 °C at -4,000 meters b.g.l.), prove the highly convective behaviour of the system.

dissolved $CO_2$. This 100 meter thick cap, recognized only in the central part of the field, was extensively exploited until few years ago for $CO_2$ storage by the well Alfina013 (Fig 6.1).

The target of the more recent campaign (1987-1988) was the deeper and hotter geothermal reservoir, hosted in the metamorphic rocks lying underneath the calcareous formations. Though the exploration did not reach the metamorphic basement, it demonstrated the presence of a single very thick carbonatic reservoir (>3,700 m thick), within which a highly variable temperature gradient of 0.15 °C/10m -0.45°C/10m was recorded (*Buonasorte et al., 1991*). These exploration wells resulted in multiple pressure and temperature vertical profiles

within the geothermal field, three of which are illustrated in Figure 6.3. The available data stands in different depth ranges: Alfina002 well, the shallower one, with measured temperature data reaching -500 m a.s.l.; the second well (RAI01) reached -2,000 m a.s.l., while the last and most recently drilled Alfina015 well provided a full temperature profile up to a depth of -4000 m a.s.l.. The shallower Alfina002 and RAI01 wells, reaching only the top of the reservoir units, registered a linearly increasing temperature with a high geothermal gradient in the range of 1.7–2.1°C/10m (*Buonasorte et al., 1988*). This suggests a mainly conductive heat transfer mechanism associated to the cap rock impermeable units. A similar trend was observed in the shallower portion (up to ca. 1000 m depth) of the deep Alfina015 well (Fig. 6.3). At about 1000 m a knick-point and a thermal inversion are observed along the profile. The geothermal gradient below this depth ranges between 0.15°C/10m and 0.45°C/10m. Such a strong variation, coupled with measured top and bottom nearly constant temperatures of the reservoir fluids (i.e. 140°C and 207°C at 1,050 m and 4,000 m depth, respectively; *Buonasorte et al., 1991*), point toward an intense, large-scale convective flow confined in the area of the buried structural high.

In summary, the CG-TA area is an example of a promising, early explored and yet to be developed geothermal filed. Despite the extremely favourable conditions for exploitation (*Cataldi and Rendina, 1973*), its industrial development was not promoted till 2011. A new geothermal research permit was requested for the Torre Alfina area, aimed to the development of 2 new generation 5 MWe pilot doublet plants, with reduced gas emission (*ITW and LKW, 2013*; *Carapezza et al., 2015*).

## 6.3 CONCEPTUAL MODEL

The spatial extent of the model is fundamental for a reliable simulation of the complex processes involved in a geothermal reservoir. An overly restricted scenario hampers a complete representation of the circulation into the field, whereas a very large one results in a more uncertain geological reconstruction and excessive computational loading. The model area, covering about 293 $km^2$ (Fig. 6.4), is located north of the Vulsini calderas and it is bordered by the Meso-Cenozoic ridge of the Mount Cetona, to the north and by the Bolsena caldera structure, to the south (Fig. 6.1). The extent is large enough for the imposed boundary

conditions not to interfere with the phenomena occurring inside the geothermal field. This is guaranteed by an horizontal distance between lateral model boundaries and the geothermal field of 7.5 km in the E-W direction and of 2.5 km in the N-S direction (Fig. 6.4). Due to the large extent of the geothermal reservoir and its intrinsic geological complexity, a complete review of the existing data and literature was required (*Cataldi and Rendina, 1973; Nardi et al., 1977; Costantini et al., 1984; Buonasorte et al., 1991, 1995; Vignaroli et al., 2013; Carapezza et al., 2015; Colucci and Guandalini, 2014*).

The geological model was based on deep geological cross sections (*Costantini et al., 1984; Nardi et al., 1977; Buonasorte et al., 1988*) and contour line maps of the contact surfaces between geological formations (*Buonasorte et al., 1988; Colucci and Guandalini, 2014*). Major attention was devoted in representing changes inside and outside the geothermal reservoir. The base of the model was located at –4,500 m a.s.l., within fractured limestone reservoir units. The upper limit was defined by a rather flat topography derived from a 20 x 20 meter DEM derived topography. This resulted in a maximum model thickness of about 5 kilometres (from +600 m a.s.l. to -4,500 m a.s.l.; see Fig. 6.4).

The reservoir units are composed, from bottom to top, of evaporites, limestones, marls and radiolarites (Tuscan and Umbria series s.l.; *Costantini et al., 1984*). Such reservoir units are buried by the sealing units, and crop out at San Casciano dei Bagni village. The sealing units consist of an allochthonous flysch-type sequence composed of arenaceous turbidites intercalated with layers of shales, marls, and limestones, overlaid by an ophiolitic sequence (siliceous shales and sandstones including blocks of gabbro and serpentinite) (Ligurian units s.l.; *Carmignani and Lazzarotto, 2004*).

As previously mentioned, the area has undergone a strong post-orogenic deformation phase, resulting in strike-slip and subordinate normal fault systems (with associated fracture network) cutting and dislocating the internal architecture of the reservoir (*Vignaroli et al., 2013*). No anomalous soil $CO_2$ flux was recorded by the detailed investigations performed by *Carapezza et al. (2015)*. This indicates the effectiveness of the impervious behaviour of both the sealing units, which are continuous all over the reservoir area with a thickness of no less than 400 meters, and the fault system connecting the geothermal reservoir with the surface.

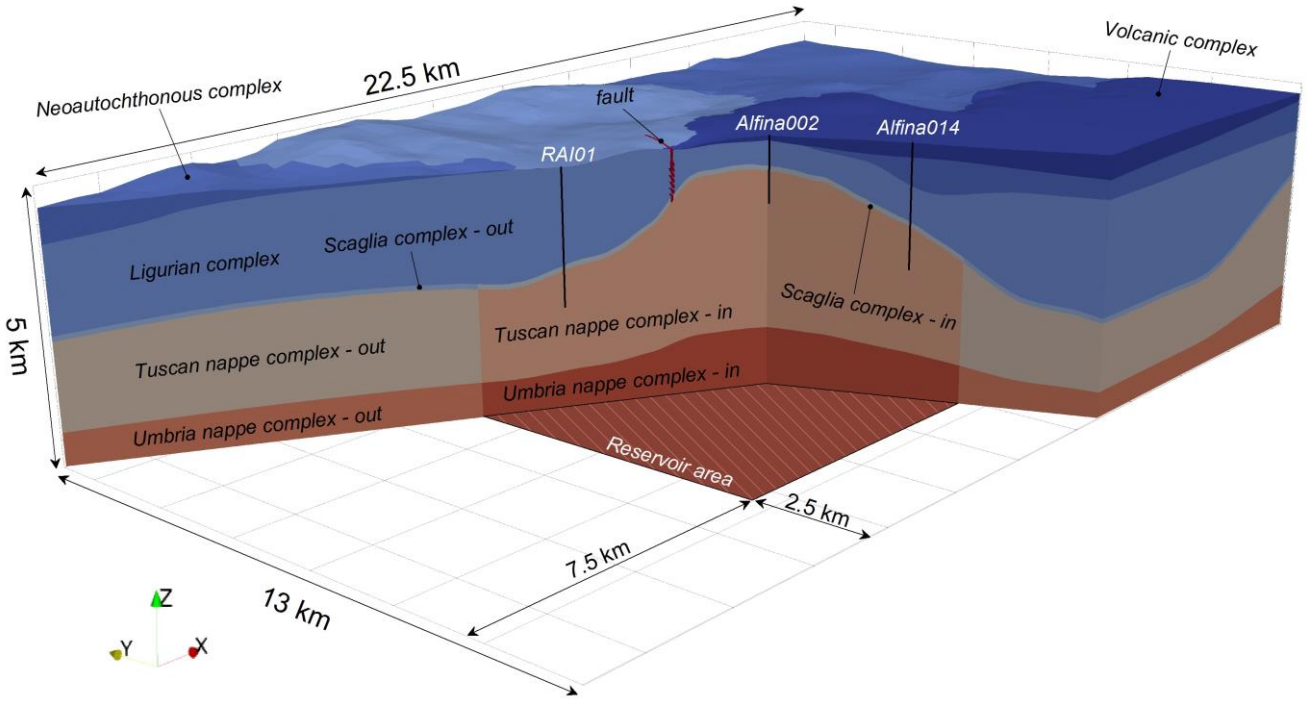


**Figure 6.4:** Three-dimensional geological conceptual model cut along the same WNW – SSE cross section realized by *Buonasorte et al. (1988)* (see Fig. 6.2). The same cross section as in Fig. 6.1 is used to slide the model. Model (ca. 293 km$^2$) internal subdivision shows the seven adopted hydrogeological units, named as reported in Table 6.1. Reservoir units (Scaglia complex, Tuscan nappe complex and Umbria nappe complex) have been distinguished between formations stacked into the geothermal reservoir (unit name – in) and those falling outside the producing area (unit name – out). Distances between reservoir area and lateral model boundaries are shown (7.5 km along E-W direction and 2.5 km along N-S direction).

In summary, the conceptual model consists of seven hydrogeological units (Fig. 6.4), of which the upper three form the sealing cap and the remaining comprise the reservoir. The *Volcanic complex* (1) is the youngest one and it outcrops only in the southern part of the model domain. This formation tends to thin towards the North where it is in contact with the other sealing units, represented by the *Neoautochthonous complex* (2) and the *Ligurian/sub-Ligurian complex* (3). The shallower geothermal reservoir unit is referred as the *Scaglia formation* (4), a tiny layer mainly consisting of argillites. Below this, the fractured limestone rocks of the *Tuscan limestone* formation (5) and the deeper *Umbria limestone* formation (6) are emplaced. The *Scaglia*, *Tuscan* and *Umbria complex* units (# 4, 5 and 6) were additionally subdivided between formations stacked into the proper geothermal reservoir (i.e. the real portion affected by convection phenomena, with an extent of ca. 73 km$^2$), and those falling outside the producing area. The model includes also a NE-SW trending subvertical *fault* (7), with a surface trace of about one kilometre, a vertical extent of 1.5 km and impervious behaviour.

## 6.4 NUMERICAL MODELLING

### 6.4.1 Numerical formulation of the conceptual model

Based on the conceptual model, a refined reservoir-scale three-dimensional thermo-hydraulic (TH) model was built to investigate the different processes involved in the CG-TA geothermal reservoir.

The open-source finite-element simulator OpenGeoSys (OGS, *Kolditz et al., 2012*) was used to solve the differential equations governing density-driven flows. The mathematical and numerical formulation of the problem and the strongly coupled system of equations can be found in *Kolditz et al. (2012)*.

As a flexible non-commercial numerical software code for hydrological and hydrogeological modelling, OGS fully implements all the basic equations governing groundwater flow and heat transport in saturated porous media (e.g. fluid mass conservation, Darcy's law, energy balance equation and Fourier law). Moreover, several equations of state (EOS) have been implemented in the code in order to reproduce temperature and pressure dependent fluid density and viscosity. Here we used the polynomial fittings introduced by *Magri et al. (2015)*, that are valid for a wide range of temperatures ($0 \leq T \leq 350$ °C) and pressures ($p_{sat} \leq p \leq 100$ MPa). Therefore allow for modelling heat transfer in deep geothermal reservoirs where high temperatures and pressures occur.

### 6.4.2 Modelling approach

The model surface (293 $km^2$) was discretized into 17,768 triangular finite elements, satisfying the Delaunay's criterion, by using the GMS software (*EMS-I, 2006*). Mesh refinement was applied to ensure simulation robustness: elements size decreases gradually from 500 meters, at model lateral boundaries, to 10 meters close to the fault zone and around the geothermal wells (Fig. 6.5). We verified that a finer mesh did not affect the calculated patterns.

The 2D surface grid was extruded vertically using a fully unstructured tetrahedral 3D mesh. The total volume of the model was discretized with 35 layers ranging in thickness from 250 meters, at the model bottom, to a minimum of 10 meters, near the topographic surface. In total the 3D mesh consists of 1,720,774 tetrahedral elements (Fig. 6.5) that preserves all outcropping and internal pinching of the geologic formations.

The two modelling challenges are: (i) recreate the present-day, highly convective, unexploited, natural state of the CG-TA geothermal system, and (ii) perform the predictive analysis of the industrial exploitation process of the field. Two scenarios are therefore presented (*Colucci and Guandalini, 2014*). (1) The first one, referred henceforth to as "*Natural state simulation*", reproduces the thermo-hydraulic dynamic conditions of the geothermal reservoir, without extraction or injection of fluid. Pressure and temperature values measured in the three geothermal wells drilled in the area (Fig. 6.3) were used to constrain the numerical results. (2) Once a qualitatively satisfactory match between calculated and observed patterns in these three geothermal wells was obtained, the calculated temperature and pressure fields were used to initialize the second simulation step. The latter includes the operating conditions based on a reasonable configuration of injection and production wells. This scenario, referred as "*Exploitation process simulation*", also assesses the impacts of the exploitation process on the long-term (i.e. up to 10,000 years) natural geothermal flow of the reservoir after the production stage.

The same modelling framework (i.e. boundary conditions, initial conditions, equations of state, spatial and temporal discretization) is applied to the finite element commercial software Feflow®.

### 6.4.3 Boundary conditions

Temperature and pressure boundary conditions are summarized in Figure 6.5. In both scenarios, temperature and pressure distributions at the top were assumed to be time invariant. A fixed value of 15°C (i.e. Dirichlet type), corresponding to the average annual temperature of the area, and an atmospheric pressure value of 1 bar (i.e. Dirichlet type) were set. The implicit assumption is that the groundwater table and the ground surface coincide (*Cataldi and Rendina, 1973; Buonasorte et al., 1988*). Outside the reservoir area, temperature and pressure at the bottom boundary nodes were fixed too (i.e. Dirichlet type). The chosen values were calculated according to the average geothermal and pressure gradients of 0.3°C/10m and 1bar/10m, respectively (Fig. 6.5). On the other hand, given the anomalous geothermal gradient (1.7–2.1 °C/10 m; *Buonasorte et al., 1988*) in the area of the buried structural high, an incoming heat-flux of 0.256 W/m$^2$ (i.e. Neumann type) was applied at the nodes on bottom boundary below the reservoir area (Fig. 6.5).

A no-mass flow condition was imposed over all the lateral boundaries (i.e. adiabatic and impermeable boundaries). As said above, the large distance between the grid boundaries and the reservoir area guarantees that applied boundary conditions do not affect the field behaviour.

The "*Natural state simulation*" was performed to determine the present-day reservoir condition, without any fluid extraction/injection scenarios. To let the system reach the present-day anomalous temperature field, the simulation covers a period of 1 million years. To verify the "*Natural state simulation*", the spatial distribution of the simulated temperature

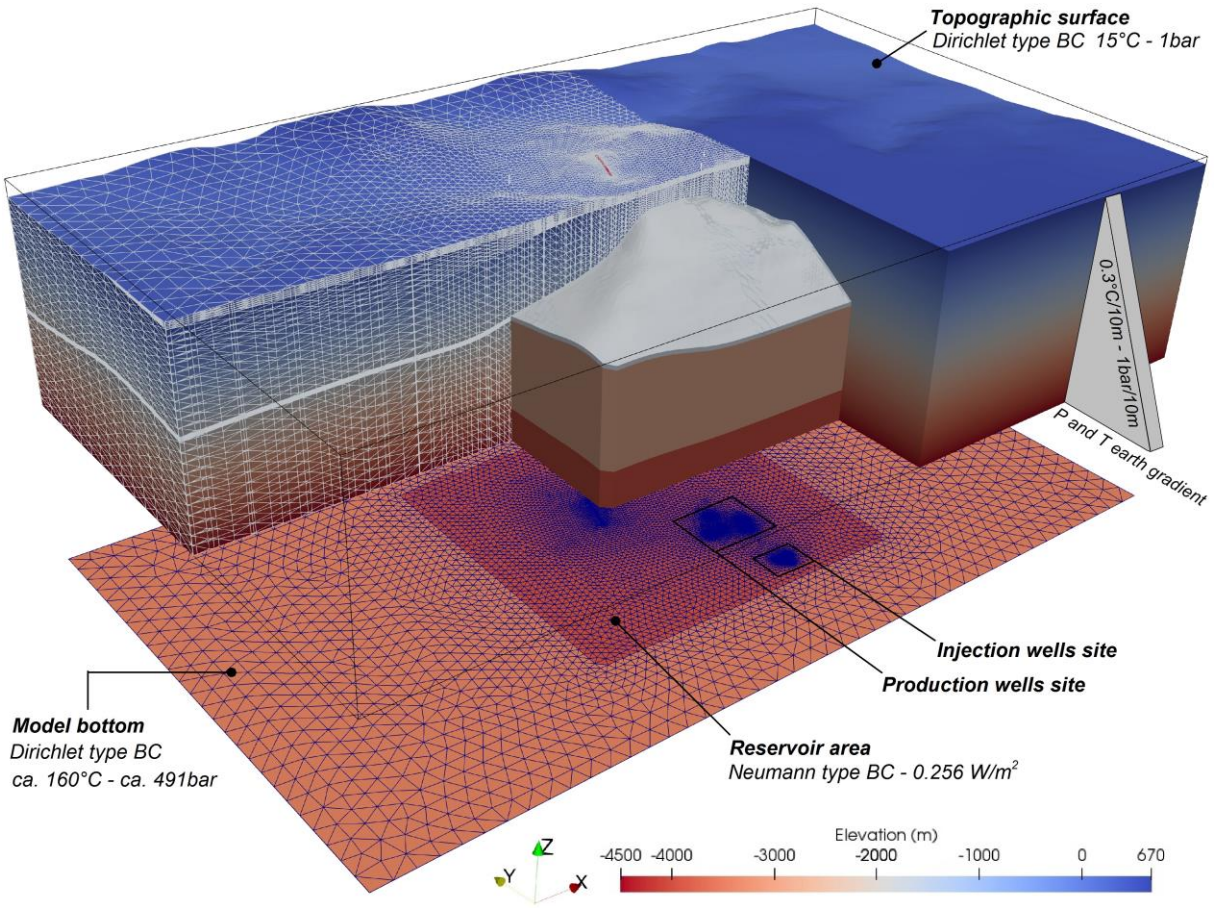


**Figure 6.5:** Three-dimensional thermo-hydraulic model consisting of 35 slices with 17,768 triangles for each slice and 1,720,774 tetrahedral elements. The 35 slices are visible along the left model boundary. Model elevation ranges from 670 to -4500m a.s.l. (see colour bar), while the 2D mesh is exploded below the model. Three-dimensional structure of the reservoir producing units (i.e. Scaglia complex, Tuscan nappe complex and Umbria nappe complex), confined in the area of the buried structural high, is shown in the central portion of the modelled domain (colour scale according to Fig. 6.4). Applied pressure and temperature boundary conditions, at the top and the bottom of the model (i.e. Dirichlet type and Neumann type), as well as the initial condition of the pressure and temperature earth gradients, are shown. A no-flow boundary condition is set to the lateral boundaries of the model. The tested configuration of the production and injection sites (separated horizontally by a distance of ca. 2 km) is highlighted by the refinement in the two-dimensional mesh.

was compared with the measured thermometric vertical profiles in correspondence of 3 geothermal wells (Alfina002, Alfina015 and RAI01; see Fig. 6.1).

To simulate field production and to predict the future system evolution, pressure and temperature boundary conditions remained those applied for the "*Natural state simulation*". A reasonable configuration of 5 production and 4 injection wells, separated horizontally by a distance of ca. 2 km (*Buonasorte et al., 1988*), was inserted in the in the "*Exploitation process simulation*" model (see Fig. 6.1 and Fig. 6.5). A hypothetical 50 year production and injection time span, with a flow rate of 1050 t/h, was chosen following *Buonasorte et al. (1988)*, *Marini et al. (1993)* and *Colucci and Guandalini (2014)*. Starting from this production scenario, a flow rate of 210 t/h for each production well was applied. At each injection well, a constant injection temperature (i.e. Dirichlet type boundary condition) of 80°C and a 262.5 t/h injection rate were applied (*ITW and LKW, 2013*). These boundary conditions, distributed over the nodes of the active length of the production/injection wells (ca. 300 meters discretized with 12 nodes), were set as time-dependent. At the end of the 50 years simulation run, the wells boundary conditions were removed and the simulation ran for an additional 10,000 years to investigate the recovery time and to test the technical sustainability of geothermal power production.

### 6.4.4 Initial conditions

In preparation for the dynamic reservoir simulation, initial reservoir conditions have to be determined. These initial conditions include both the geothermal gradient and the fluid pressure gradient (i.e. when advection/convection is not involved). For this purpose, this initialization phase of the natural state was modelled as a steady state condition without the incoming heat-flux at the bottom of the reservoir. The temperature and pressure boundary conditions and model internal partitioning were set as described above. In this steady state initialization, temperature and pressure effects on fluid density and viscosity were neglected. The values of the petrophysical parameters of the involved litostratigraphic units (Table 6. 1) were derived from available data for the area (*Cataldi and Rendina, 1973; Nardi et al., 1977; Costantini et al., 1984; Buonasorte et al. 1988, 1991, 1995; Cosentino et al., 2010; Giordano et al., 2010; Vignaroli et al., 2013; Carapezza et al., 2015; Colucci and Guandalini, 2014*). Default values for thermal conductivity of water (0.65 W/m/K) and heat capacity of water (4.2

MJ/m$^3$/K) were used. This initialization resulted in a temperature field with values ranging from 15°C to 160°C, at the ground surface and the bottom boundary, respectively (Fig. 6.6a). Fluid pressure ranges from 1 bar, at the ground surface, to 491 bar at the model bottom.

## 6.5 NATURAL STATE SIMULATION

### 6.5.1 Model definition

The natural state simulation aimed to define the present-day, unexploited thermo-fluid dynamic conditions inside the geothermal reservoir including the advective/convective fluid motion. Simulation started by applying initial conditions defined as above. As common practice, the natural state simulations of geothermal fields require a long simulation time so as to attain pressure and temperature stabilization in the reservoir (*Porras et al., 2007; Romagnoli et al., 2010; Llanos et al., 2015; Magri et al., 2015*). Therefore, a 1 Ma simulation time has been chosen, neglecting effects of past climate change or transient effects in the rocks, and representing a generic geologic period. The performed transient simulation adopted a maximum time-step size of 500 years. This time step coincides with the one used to update the fluid density and viscosity values as a function of calculated pressure and temperature. Applied boundary conditions remained the same presented above.

Regarding the assignment of required petrophysical parameters, the reservoir units were distinguished between those falling inside and outside the proper geothermal reservoir (see Fig. 6.4). The latter, were initialized with a value of permeability equal to $1.5*10^{-17}$ m$^2$; while the remaining reservoir units preserved their typical fractured limestone permeability values, derived from the literature works and ranging from $10^{-14}$ to $10^{-15}$ m$^2$ (Table 6. 1). A very low permeability value of $10^{-18}$ m$^2$ adopted for the overlaying sealing units allowed modelling their impervious behaviour. A compressibility value of $10^{-10}$ Pa$^{-1}$, slightly lower compared the one used for the reservoir units (i.e. 1.2–2.5 * $10^{-10}$ Pa$^{-1}$; Table 6. 1), was assigned to these formations. This reduced compressibility allows maintaining the fluid pressure as simulated in the previous stationary system initialization phase, avoiding a fluid pressure rise due to temperature increase. The complete set of applied hydraulic and thermal parameters is given in Table 6. 1.

**Table 6.1:** Hydraulic and thermal parameters of the litostratigraphic units involved in the natural state simulation. Values are taken from literature (*Cataldi and Rendina, 1973; Nardi et al., 1977; Costantini et al., 1984; Buonasorte et al. 1988, 1991, 1995; Cosentino et al., 2010; Giordano et al., 2010; Vignaroli et al., 2013; Carapezza et al., 2015; Colucci and Guandalini, 2014*). For the unit name the added specification *-in* and *-out* are used for formations stacked into (# 4b, 5b and 6b) or outside (# 4a, 5a and 6a) the proper geothermal reservoir, respectively.

| # | Unit | Density | Porosity | Permeability | Compressibility | Th. Conductivity | Specific Heat |
|---|---|---|---|---|---|---|---|
| - | - | $kg/m^3$ | % | $m^2$ | $Pa^{-1}$ | W/m°C | J/kg°C |
| *1* | *Volcanic* | 2200 | 5 | $1*10^{-18}$ | $1*10^{-10}$ | 2 | 1000 |
| *2* | *Neoautochthonous* | 2400 | 30 | $1*10^{-18}$ | $1*10^{-10}$ | 2.4 | 1000 |
| *3* | *Ligurian* | 2400 | 0.55 | $1*10^{-18}$ | $1*10^{-10}$ | 2.4 | 833 |
| *4a* | *Scaglia - out* | 2400 | 1 | $1.5*10^{-17}$ | $1.2*10^{-10}$ | 2.1 | 1000 |
| *4b* | *Scaglia - in* | 2400 | 1 | $1*10^{-15}$ | $1.2*10^{-10}$ | 2.1 | 1000 |
| *5a* | *Tuscan nappe - out* | 2660 | 6 | $1.5*10^{-17}$ | $2.5*10^{-10}$ | 2.4 | 836 |
| *5b* | *Tuscan nappe - in* | 2660 | 6 | $1*10^{-14}$ | $2.5*10^{-10}$ | 2.4 | 836 |
| *6a* | *Umbria nappe - out* | 2660 | 6 | $1.5*10^{-17}$ | $2.5*10^{-10}$ | 2.4 | 836 |
| *6b* | *Umbria nappe - in* | 2660 | 6 | $1.98*10^{-15}$ | $2.5*10^{-10}$ | 2.4 | 836 |
| *7* | *Fault* | 2660 | 1.5 | $1*10^{-18}$ | $1*10^{-10}$ | 2 | 1000 |

### 6.5.2 Results of the natural state simulation

Results of the 3D convective flows are shown in Fig. 6.6 for three different simulation times (i.e. 0, 20,000 and 125,000 years). From the initial conductive temperature field, equal to the average geothermal gradient of 0.3°C/10m (Fig. 6.6a), a very efficient convective circulation develops only into the geothermal reservoir units (# 4b, 5b and 6b, as listed in Table 6. 1). This resulted in a gradual increase of temperature values in this area, while outside the producing units the pressure and temperature fields showed a full correspondence to those obtained at the end of the previous stationary system initialization. Fluid circulates in form of rolls and exhibits multi-cellular convective patterns, which start oscillating after ca. 20,000 years of simulation time (Fig. 6.6b). This implies sharper inherent gradients and continuous creation and disappearance of convective plumes patterns. Within the producing area, three elongated convective cells stretched over the entire geothermal reservoir (Fig. 6.6b). The observed cellular motion consists of multiple central up-flows, with a fluid velocity in the range of 2-$4*10^{-8}$ m/s, and associated lateral down-flows. The strong convective behaviour allows cold

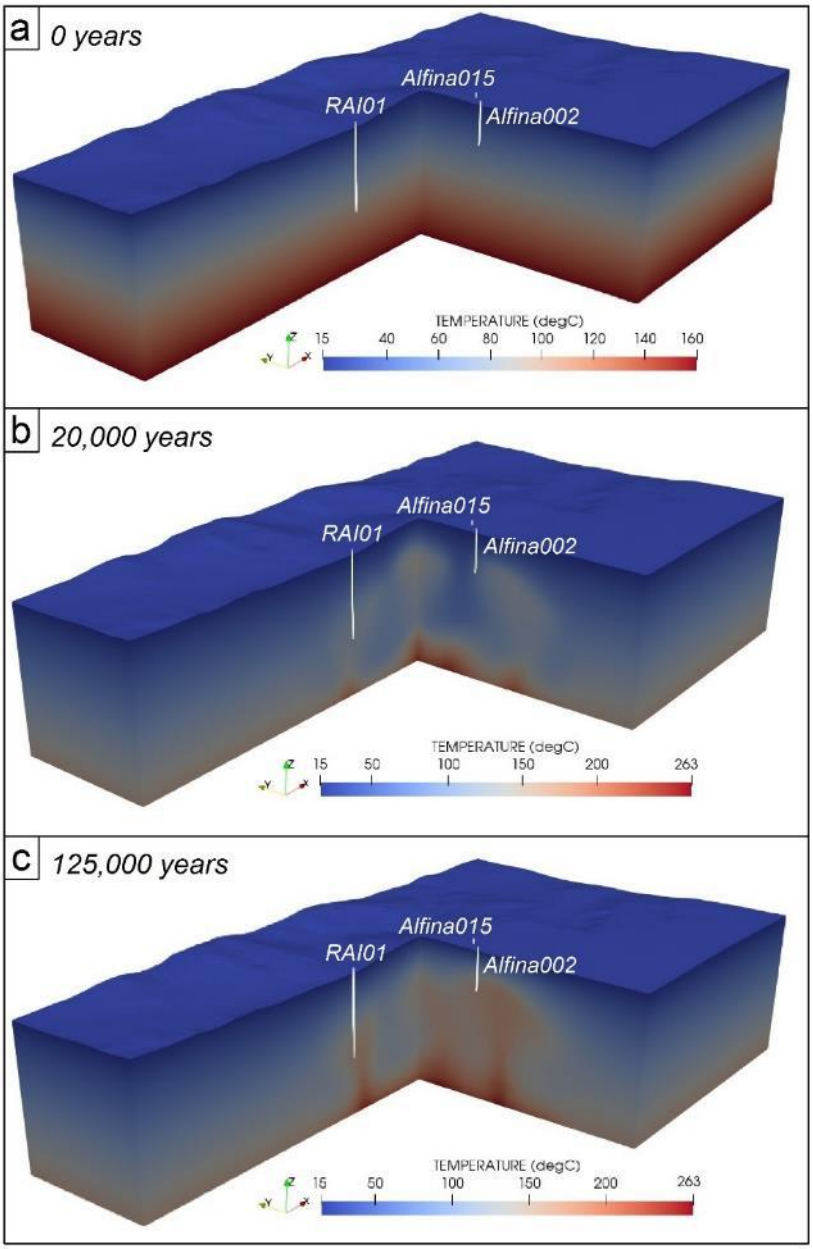


**Figure 6.6:** Temperature field resulting from the transient natural state simulation. The three wells (RAI01, Alfina015 and Alfina002 – see also Fig. 6.1), for which the available temperature logs were used to identify the reservoir present-day thermal state, are shown. Three different simulation times are presented: **(a)** 0 years, initial temperature field equal to the average earth gradient of 0.3°C/10m; **(b)** 20,000 years, beginning of the oscillating multi-cellular convective regime confined in the reservoir units; **(c)** 125,000 years, best fitting time-step resulting in a good match between simulated and real thermometric data for the 3 evaluated wells (see Fig. 6.7).

infiltrating groundwater to reach basement depths where it gets heated before starting its upward migration to the top of the geothermal reservoir. Comparing the results of the natural state simulation along 1D profiles with real surveyed thermal profiles, it is possible to identify the time instant for which the model fits the real reservoir conditions. The identification of

the best fitting simulated temperature profiles was performed through an iterative manual process by comparing computed 1D profiles against temperature profiles at 3 geothermal wells (Alfina002, RAI01 and Alfina015; see Figs. 6.1 and 6.3). The attained best fitting occurs at the 125,000 year simulation time (Fig. 6.6c) for all the three geothermal wells. At that time, the pattern of the three elongated convective cells is highlighted by a sharp difference in temperature between raising and sinking fluids. Velocity of the modelled convective cells raises to ca. $7*10^{-8}$ m/s, while maximum fluid temperature reaches 263°C.

The sigmoidal shape of the temperature profiles suggests the occurrence of the highly convective flow (Fig. 6.7). In fact, all the three simulated profiles exhibit a clear thermal inversion as soon as the reservoir depth is reached (ca. -500 m a.s.l. for the Alfina002 well, ca. -1000 m a.s.l. for the Alfina015 well and ca. -2000 m a.s.l. for the RAI01 well). In the upper 2 km of the temperature profiles (T < 150°C, conductive regime), the difference between simulated and measured values is at maximum 10°C (see Fig. 6.7). A comparison between

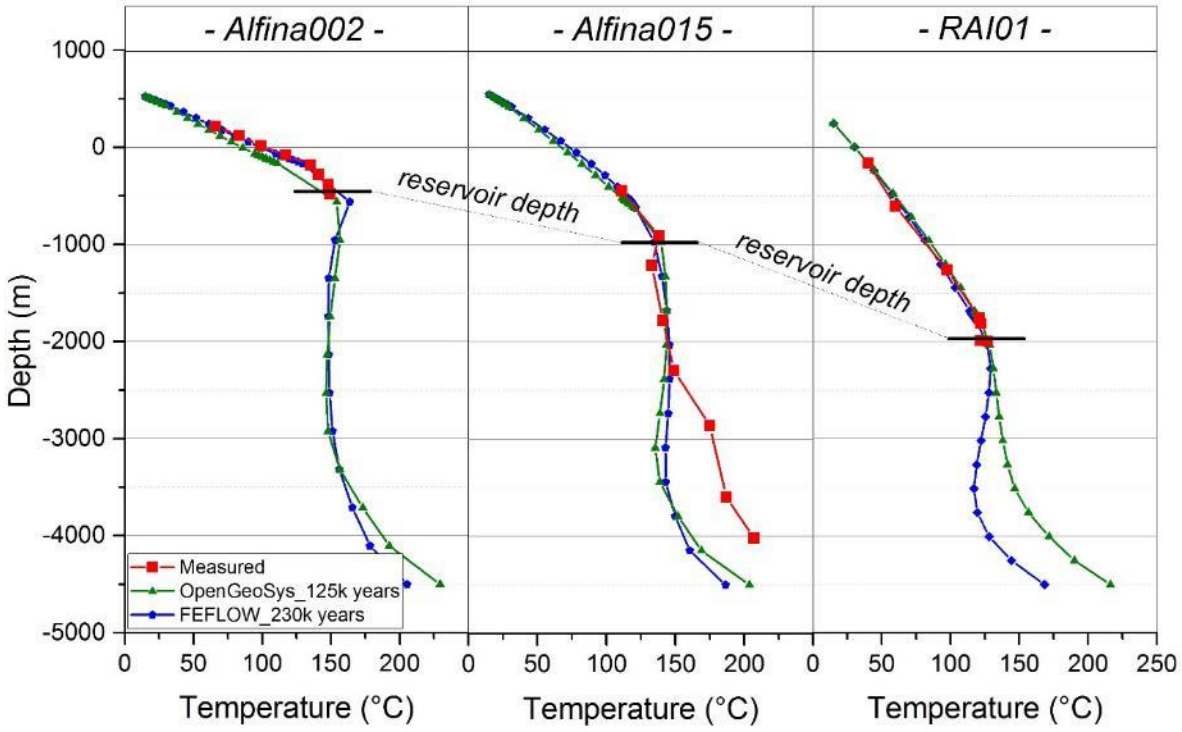


**Figure 6.7:** Results of the natural state simulation. Comparison between best-fitting OpenGeoSys computed temperature profiles (125,000 years of simulation - green curves), best-fitting Feflow® computed temperature profiles (230,000 years of simulation - blue curves) and available real thermometric data (red curves, see Fig. 6.3). Location of the selected wells is reported in Fig. 6.1 and Fig. 6.6. In the plotted thermal logs, the depth of the reservoir top is highlighted. A clear thermal inversion can be seen as soon as the reservoir units are crossed (i.e. -500m a.s.l. for Alfina002 well, -1,050m a.s.l. for Alfina015 well and -2,000m a.s.l. for RAI01 well). This agree with the stepped shape of the measured deep temperature profile of Alfina015 well and supports the hypothesis of a highly convective behaviour of the reservoir.

simulated and measured deep reservoir temperature values (T > 150°C, convective regime) was possible only for the Alfina015 well, representative of almost the entire thickness of the model. The computed profile, in correspondence of the Alfina015 well position, shows a well-developed trend with an almost constant temperature down to about -3,500 m a.s.l.. This can only be associated to the presence of a convective cell. A good fitting of the Alfina015 profile temperature was obtained by slightly shifting the sampling profile location of a few meters so that it hits upward buoyant flow. Feflow® and OGS models exhibit similar temperature-depth profiles in all wells, but at different simulation time (125,000 vs 230,000 year, see discussion). Differences in temperature values are observed at maximum depth, where convection is dominant and controls the thermal evolution of the system (Fig. 6.7).

The computed best-fitting natural state temperature field formed the initial condition for the following dynamic reservoir simulations of the effects induced by the production process.

## 6.6 EXPLOITATION PROCESS SIMULATION

### 6.6.1 Model definition

Once accomplished a satisfactory match for the natural state, a realistic scenario was set up for the future exploitation of the CG-TA geothermal field through a 5 MWe pilot doublet power plant.

To achieve this, the chosen configuration (see Figs. 6.1 and 6.5, *Buonasorte et al., 1988*) of 5 production wells (CG1, CG1A, CG2, CG3, CG3A) and 4 injection wells (CG14, CG14A, CG14B, CG14C) was inserted in the model. The production wells extract the geothermal fluids from the uppermost portion (from -300 to -700 m a.s.l.) of the reservoir units. The extraction depth range depends on the well position relatively to the top of the producing area. The injection of the 80°C fluid, at the above described rate, was designed at a depth ranging between -1,350 and -1,550 m a.s.l.. For both production and injection sites, the well active length was fixed at 300 meters.

Pressure and temperature boundary conditions were those described for the *Exploitation process simulation* (see *Boundary conditions,* Fig. 6.5). Initial conditions, mimicking the present-day distribution of both temperature and pressure field, were imported from the calculated best-fitting time-step (i.e. 125,000 years of simulation time) of the previously

performed *Natural state simulation*. The exploitation time lasted 50 years and total simulation time 10,000 years, so as to evaluate the field long-term effects induced by production process.

### 6.6.2 Field exploitation

The evolution of well pressure over time, computed at a node with depth close to the well bottom, showed that the maximum differences, relatively to the initial pressure field, were reached at the end of the production time (i.e. after 50 years of simulation). In more detail, as shown in Figure 6.8a for wells CG2 and CG3, the production wells realized a depressurization in the 15-17 bar range, at the end of the first year of simulation, and then stabilized to an averaged value of 19 bar at the end of the production time. This pressure variation corresponds to approximately 12-14% of the initial pressure values (from 120 to 150 bar depending on the considered well) in the production wells. At the end of the exploitation of the geothermal field (i.e. after 50 years), no further fluid extraction occurred and the production wells exhibited a fast recovery. The monitored pressures raised back to the initial values in less than 100 years for the whole production site (see Fig. 6.8c for the wells CG2 and CG3).

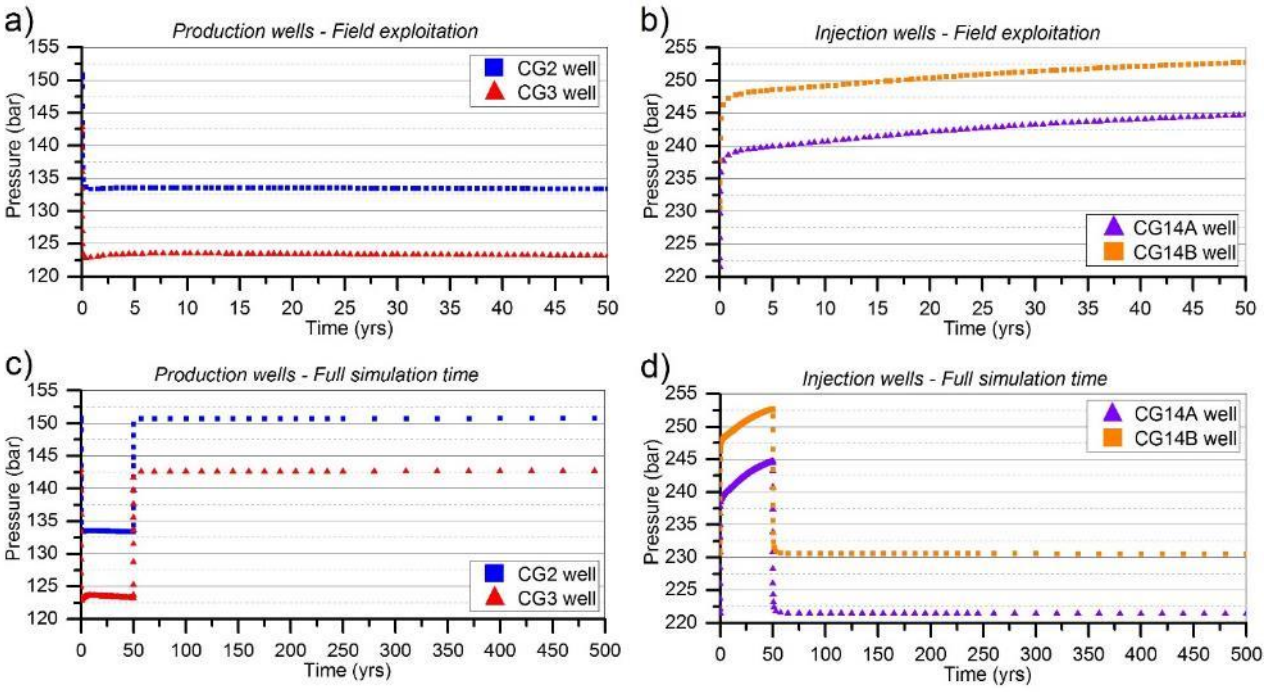


**Figure 6.8:** Evolution of well pressures during the exploitation process simulation at 2 selected production (CG2 and CG3, see Fig. 6.1) and 2 injection (CG14A and CG14B, see Fig. 6.1) wells: **(a)** and **(b)** refer to the 50 years simulation time, and **(c)** and **(d)** to the 10,000 years recovering time. The initial 500 years are shown in the full simulation time plots **(c)** and **(d)** as full recovery is reached. This allows better visualization of the transition between the field exploitation and the quick reestablishment of the initial undisturbed pressures.

On the other hand, at the injection site, injected water resulted in strong overpressures raising quickly in the first years (i.e. around 14-16 bar) to stabilize to an average value of 20 bar after 50 years of simulation (see Fig. 6.8b for wells CG14A and CG14B). These overpressures correspond to approximately 7-10% of the initial pressure field (from 225 to 240 bar, for all the wells) recorded in the injection wells. At the end of the production time, in the same way as for the production wells, pressure values recovered quickly to the initial undisturbed ones (see Fig. 6.8d). Therefore, comparing model pressure distribution at the beginning (Natural state) and at the end of the simulation (i.e. after 10,000 years) no significant variations could be observed.

The evolution of temperature over time for both production and injection wells is plotted in Figure 6.9. During system exploitation, the recorded temperature at the production wells exhibited a progressive increase over time (see Fig. 6.9a for wells CG2 and CG1A). The difference between onset and end of production (i.e. after 50 years) temperatures varies from 2.5°C for CG2 well to a maximum value of 9.5°C for CG1 well. This increase in temperature resulted from the direct extraction of fluids from within a very strong convective system in the inner portion of the reservoir. Hence, from a thermal point of view, this analysis showed no interference effects between injection and production sites.

At the end of the phase of exploitation (Fig. 6.9c), the recorded temperatures at production wells exhibited two different behaviours depending on the position of the well relatively to the generated convective cells. For example, in the CG1A well, the simulated temperature slowly decreased after the first 50 years of simulation time and recovered the initial undisturbed values in about 1,000 years. By contrast, the recorded temperature in the CG2 well, firstly decreased to the initial value and then followed a gently increasing trend (ca. 2°C at the end of 10,000 years simulation, see Fig. 6.9c). To investigate further this behaviour simulation time was extended to 30,000 years (Fig. 6.9e). It turned out that, for wells located close to the convective cell (e.g. CG2 well), the recorded temperature exhibited strong convective oscillations, starting after 5,000 years from end of production, and preventing the

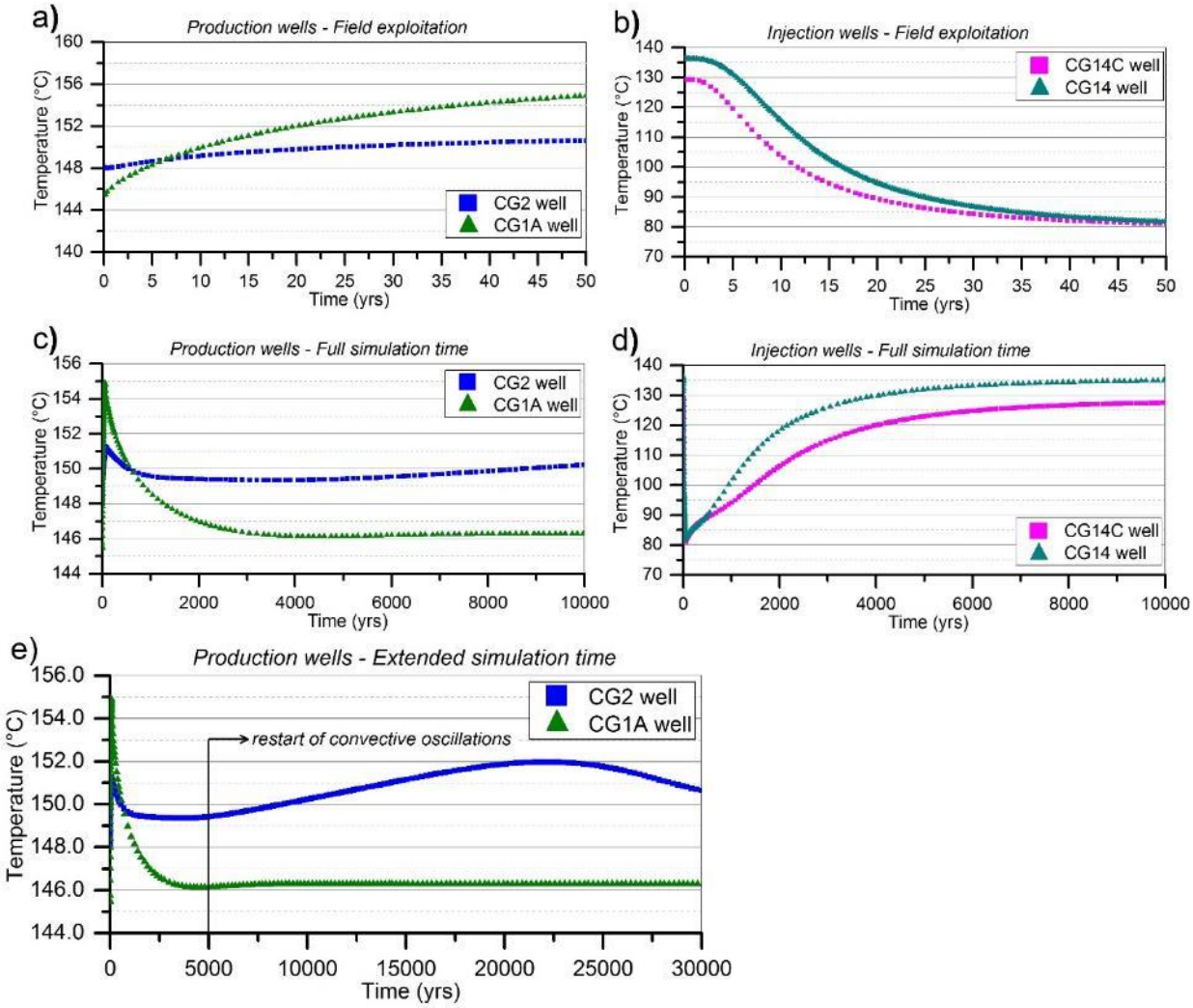


**Figure 6.9:** Evolution of well temperatures during the exploitation process simulation at 2 selected production (CG2 and CG1A, see Fig. 6.1) and 2 injection (CG14 and CG14C, see Fig. 6.1) wells: **(a)** and **(b)** 50 years of exploitation process, and **(c)** and **(d)** the following 10,000 years of recovering. **(e)** Temperature evolution at the production wells (CG2 and CG1A) over the extended simulation time of 30,000 years.

stabilization to the initial temperature values (see Fig. 6.9e). This behaviour was related to the evolution of the convection regime and to the pattern of multiple positive thermal anomalies. Fluid temperature in the injection area slowly decreased over time, reaching the injected value of 80 °C at the end of the production time (see Fig. 6.9b for wells CG14 and CG14C). At the end of exploitation, after 50 years of simulation time, temperatures in the surrounding of the injected wells recovered the initial values after ca. 2,000-3,000 years (see Fig. 6.9c).

To evaluate the thermal response of the CG-TA reservoir to the production process, the influence area of the "cold-water" front was investigated (Fig. 6.10). At the end of the production time, the 80°C isosurface around the four injection wells, covered a subspherical volume with ca. 1 km in diameter (Fig. 6.10b). Therefore, the tested horizontal distance of

about 2 km, between the production and injection sites, fully excluded the hypothesis of a thermal breakthrough.

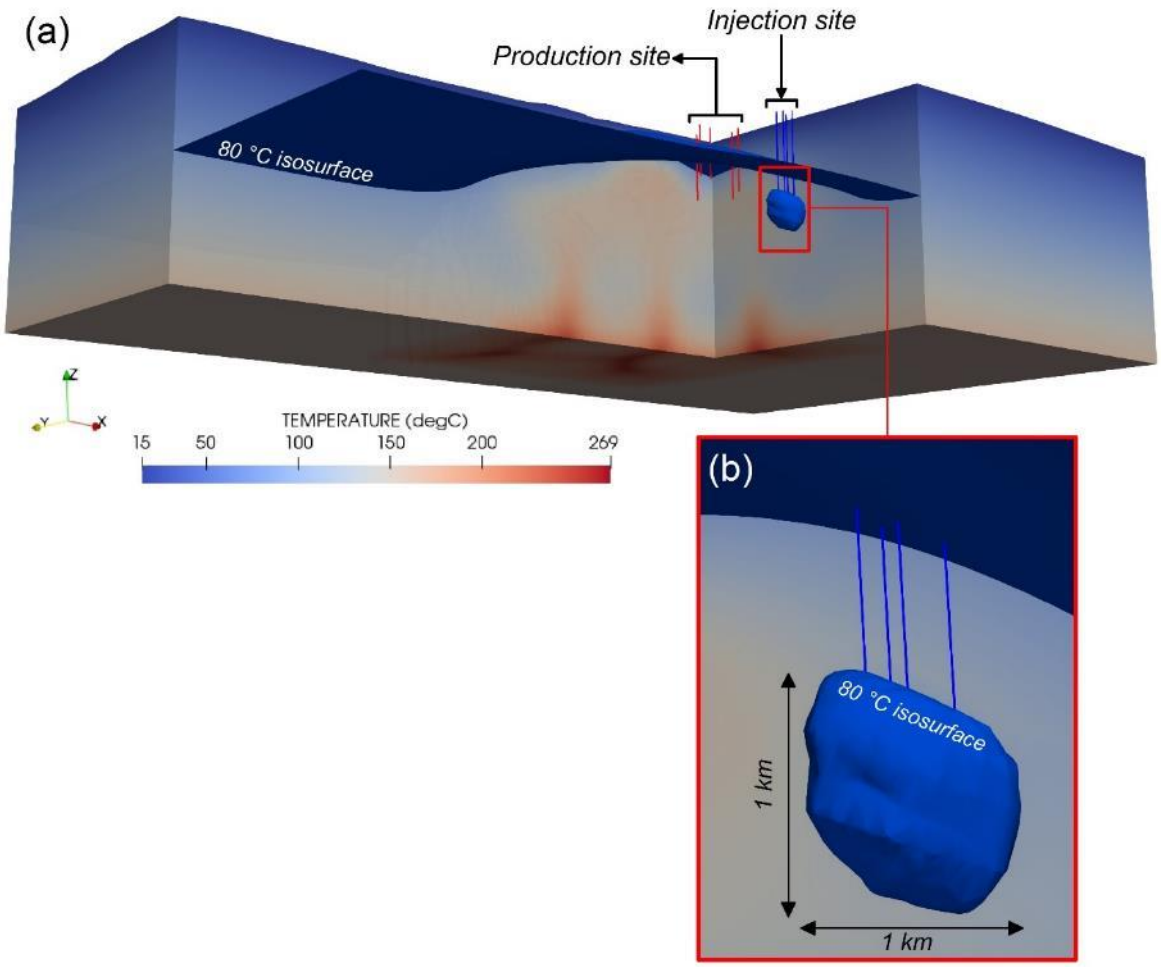


**Figure 6.10: (a)** Perspective view of the temperature field and of the 80°C isosurface (i.e. re-injected fluid temperature) at the end of the 50 years exploitation stage. Location and depth of the production and the injection wells are shown. **(b)** Evaluation of the influence area of the injection wells obtained by representing the 80°C "cold-water" front (i.e. isosurface) around the injection wells at the end of the 50 years field exploitation.

## 6.7 DISCUSSION

Within the present work, an accurate hydro-thermal model was set up to recreate the highly convective behaviour of the CG-TA reservoir and then simulate the exploitation of this undeveloped geothermal field. A general procedure for model calibration was applied (*O'Sullivan, 1985; Bodvarsson et al., 1986; Pruess, 1990a; O'Sullivan et al., 2001; Colucci and*

*Guandalini, 2014*), consisting of a *natural state modelling* followed by an *exploitation process simulation*.

The above described *natural state simulation*, resulted in a good match between simulated (via the OGS code) and measured temperature profiles after ca. 125,000 years of simulation time (see Fig. 6.6c and Fig. 6.7). To analyse the temperature field at the best fitting simulation time (125,000 years, Fig. 6.11), the OGS model was sliced with a vertical plane along the E-W axis and passing through the Alfina015 well (A-A' section in Figures 6.11a, b and c). Two convective plumes were recognized within the reservoir (Fig. 6.11c). Different vertical temperature profiles were extracted along this cross section plane at different relative positions with respect to the convective plumes (i.e. *interplume* or in between the two interacting plumes; *axial* or along the major plume axis; *intersecting* or crossing the upper plume head; *outside* or in a portion not strongly affected by a convecting plume, Fig. 6.11d). An increase in the conductive temperature field of the sealing units (i.e. profile portion above the cap rock/reservoir contact elevation, ranging between -500 and -1,000 m a.s.l. depending on well position) is observed moving toward the axis of the plume (Figures 6.11c and d). Within the reservoir, a thermal inversion characterizes the temperature profiles which cut laterally the main plume (i.e. *interplume*, *intersecting* and *Alfina015* profiles). The sigmoidal shape of the temperature vertical profiles is similar to the one observed in many other convection-dominated geothermal systems, for which comparable analyses were performed (*Della Vedova et al., 2008; Blöcher et al., 2010; Romagnoli et al., 2010; Feather et al., 2013; Fulignati et al., 2014; Ebigbo et al., 2016*).

Multiple horizontal temperature profiles along A-A' (Fig. 6.11e) cross section were extracted at different depths (i.e. -4000, -3000, -2000, -1000, -500, 0 and 300 m a.s.l.). The deepest profiles clearly showed two positive thermal anomalies, with values reaching more than 200°C in correspondence of the plumes axis. The shallower profiles show a progressive merging of the two plumes.

Once determined the unexploited present-day temperature and pressure fields, the computed natural state was used as initial condition to simulate field production and the future system evolution. The highly convective behaviour of the system was suggested by the temperature graphs of the production wells in Figure 6.9a. From these results, we conclude

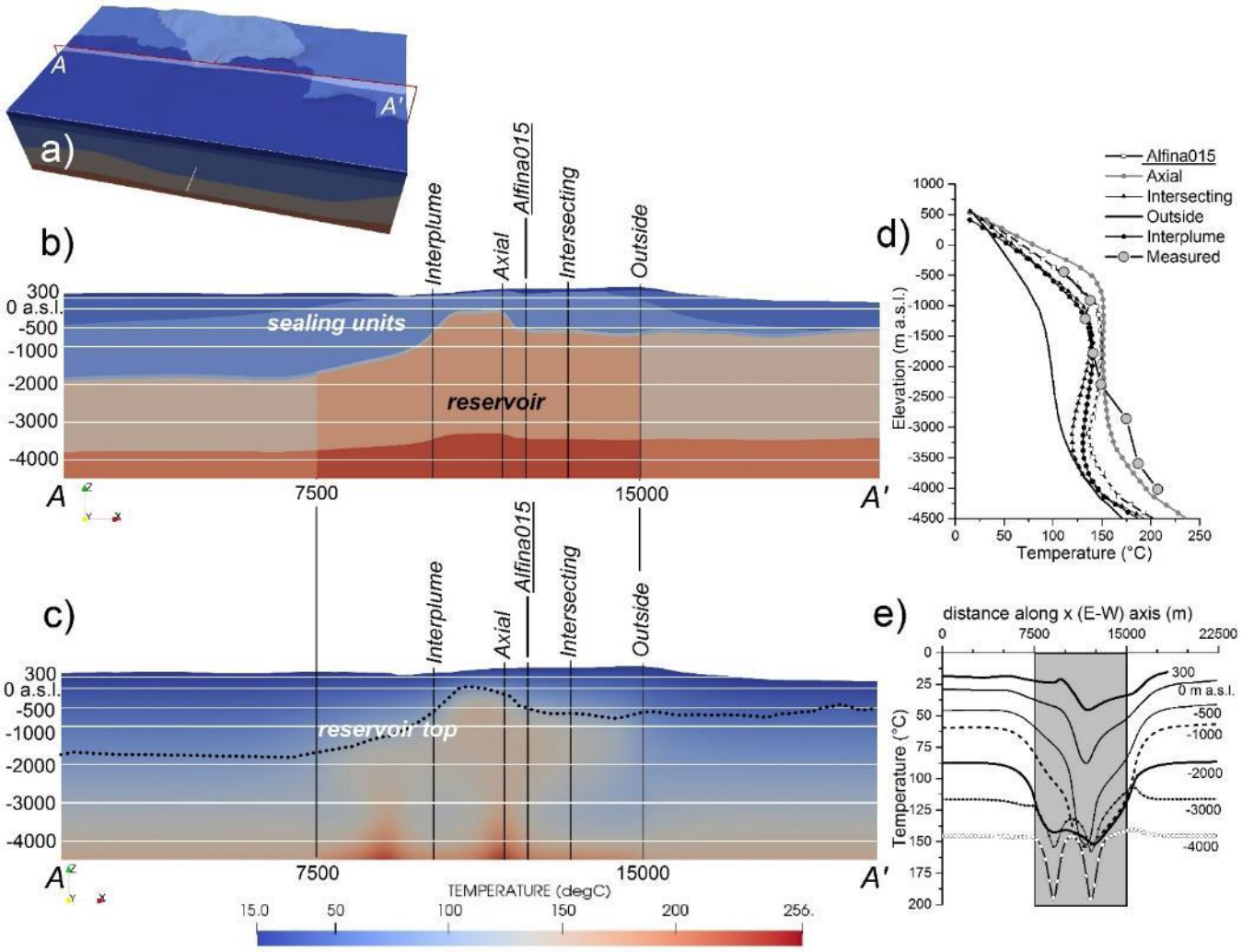


**Figure 6.11:** Analysis of the temperature distribution at the best fitting time as from the OGS model: **(a)** oblique view of the model and the chose sampling plane position; **(b)** cross section of the model with the material limits, the relative position of the reservoir and of the vertical and horizontal sampling profiles; **(c)** temperature field at 125.000 years of simulation time with evidence of the convective plumes developed within the reservoir; **(d)** and **(e)** vertical and horizontal profiles of temperature. Grey box in **(e)** shows the lateral limits of the reservoir.

that the thermal breakthrough was prevented, as testified by the progressive increase in the recorded production site temperatures during the exploitation simulation. Moreover, the exploitation process induced only very small long-term changes with respect to the natural state of the geothermal system. In fact, at the end of the production time (i.e. after 50 years of simulation time), temperature in the production wells located close to the convective cell (e.g. CG2 well) exhibits strong convective oscillations, following the unexploited behaviour modelled in the natural state simulation. Darcy velocity of such convective cells stands in the range of 7.5 - 8.5*$10^{-8}$ m/s, therefore close to the pre-exploitation one.

The performance of the OGS code at modelling the convective flow within the geothermal system has been tested against the Feflow® code. The two codes implemented the same equations of state. OGS and Feflow® results show that the calculated patterns were qualitatively similar (e.g. multi-cellular convective fluid motion, velocities of convective cells) while differences in the calculated values existed (e.g. best fitting time-step in the natural state simulation, absolute pressure and temperature values during exploitation).

Results of the Feflow® and OGS simulation are plotted in Figure 6.7. The iterative manual identification of the best fitting time-step resulted in a good matching between Feflow® simulated and real thermometric data around 230,000 years of simulation time. Even if a quite large time gap characterized the reservoir present-day situation modelled with the two software (i.e. best-fitting at 125,000 years of simulation time for OGS and 230,000 for Feflow®), the simulated vertical profiles perfectly overlapped for the entire depth of Alfina002 and Alfina015 wells. As for the RAI01 well, a good match between the two tested software is observed in the shallower portion of the thermal logs (i.e. cover and impermeable units, conductive pattern). As soon as the reservoir depth is reached (i.e. -2000 m a.s.l.), convection is dominant. As a result, the simulated patterns can highly oscillate leading to larger temperature differences at selected simulation time steps (ca. 50°C at model bottom). At the best fitting simulation time, in the shallower portion of the vertical temperature profiles ($T < 150$ °C) the difference between real measured data and Feflow® simulated values stands in the range of 5°C (see Fig. 6.7). This difference increases in the deeper portion of the temperature logs ($T > 150$ °C) due to the highly convective flow, as previously explained. After 230,000 years of simulation time, Feflow® convective cells exhibited a maximum velocity of ca. $1.36*10^{-7}$ m/s and temperature values reaching 280°C.

Starting from the present-day unexploited temperature and pressure fields, the same production scenario was simulated with Feflow®. Results of pressure and temperature vs. simulation time for both production and injection wells are plotted in Figure 6.12. Feflow® returned a trend very close to the one by OGS, for both pressure and temperature time evolution. It is worth to point out that the gap in the pressure values (~15 bar, Figs. 6.12b and d) is due to the fact that the two codes started from slightly different initial pressure fields, and thus the recovery process stabilizes to these initial undisturbed values.

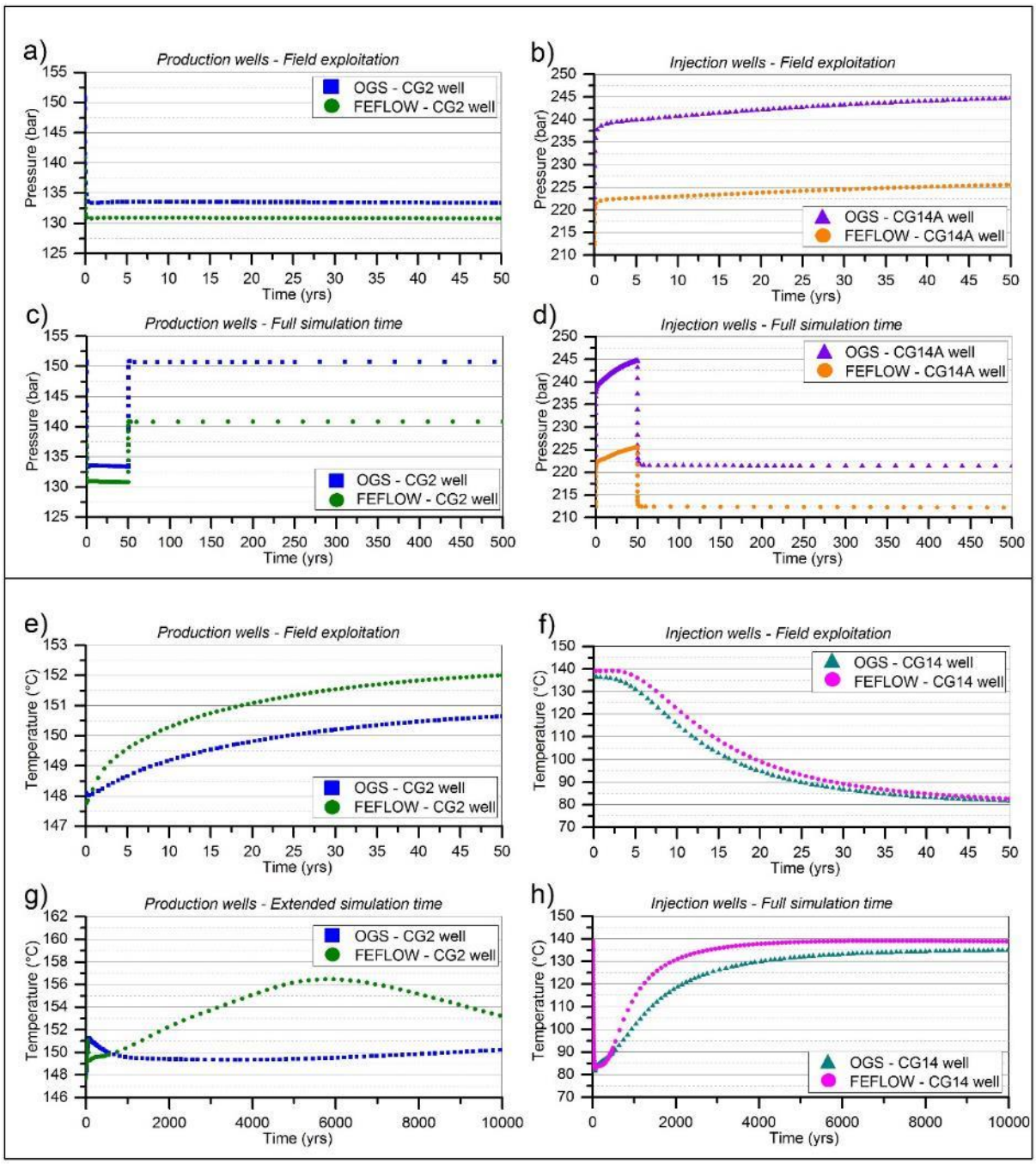


**Figure 6.12:** Comparison between the OpenGeoSys (OGS) and the Feflow® model results **(a)**, **(b)**, **(c)** and **(d)** pressure (CG2 well, see Fig. 6.1 for location), and **(e)**, **(f)**, **(g)** and **(h)** temperature (CG14 well, see Fig. 6.1 for location) evolution in time for both production and injection sites. **(a)**, **(b)**, **(e)** and **(f)** refer to the 50 years field exploitation, while **(c)**, **(d)**, **(g)** and **(h)** to the full simulation time (i.e. 10,000 years). The initial 500 years are shown in the full simulation time plots (c and d) as full recovery is reached.

Furthermore, the applied initial pressure and temperature fields were defined on the natural state condition identified only by the available thermal logs. Therefore, model constrains were only applied to temperature while missing any present-day pressure data. As the two software started from the same initial temperature values identified in the natural state simulation, the time evolution during the field exploitation process is perfectly overlapped (~1°C gap, see Fig. 6.12e). Moreover, at the end of field production, Feflow® exhibits the same convective oscillations in the productive wells as already observed in the OGS results (Fig. 6.12g).
Finally, the areal extent of the 80°C "cold water" front was evaluated in Feflow® as in OGS. The 80°C isosurface propagated away from the injection wells and reached its maximum extent at the end of the production time (i.e. 50 years). Again, a slightly irregular spherical shape, ca. 1 km in diameter, was observed. This confirms that the tested exploitation scenario prevents the thermal breakthrough in the same way as shown by OGS simulation.

## 6.8 SUMMARY

The objectives of this study are to model the origin of the thermal anomaly observed in the CG-TA medium-enthalpy geothermal field, to investigate the feasibility of geothermal exploitation, and to test capabilities of different codes at modelling highly buoyant flows. A fit-for-purpose 3D numerical model of the CG-TA geothermal system was built using the open source OpenGeoSys (OGS) code and the commercial Feflow® code. Following a general procedure for geothermal numerical models calibration, the present-day, highly convective, unexploited (natural) state model preceded the simulation of field production process. Starting from a steady state initialization of the reservoir, a satisfactory *natural state modelling* was achieved with limited differences between measured and computed temperatures. At higher depths, as convection is dominant, strong measured / calculated temperature discrepancies can be observed. The multi-cellular highly convective behaviour (Darcy velocity of $7*10^{-8}$ m/s) of the reservoir was successfully modelled, in agreement with what was inferred by the extensive deep explorations campaigns performed in the area.
Simulation of the *exploitation process* covered a total time interval of 10,000 years with fluid extraction and injection limited to the initial 50 years. Simulations showed that only small changes were induced by the exploitation of the geothermal system (producing well

temperature increase between 2.5 and 9.5°C after 50 years) and no thermal breakthrough occurs. Full recovery occurs in about one thousand years due to the highly convective behaviour of the reservoir. The good agreement between measured and simulated results for the natural state allowed a confident prediction of the reservoir response to future exploitation.

These concluding remarks were also sustained by the qualitatively similar calculated patterns resulting from the Feflow® performed simulation. Even if a time discrepancy in the identification of the present-day natural state occurs between Feflow® and OGS, the convective system behaviour, the fitting between simulated and real thermal data and the reservoir response to the tested exploitation scenario, are fully comparable.

Such models support the understanding of reservoir behaviour and are critical to optimal reservoir management and sustainable utilization. Their reliability could be improved by integrating data from new superficial and deep explorations, and, at the same time, they can support the planning of new investigations, well drilling and the designing of exploitation steps aimed to the usage of geothermal energy in the Caste Giorgio – Torre Alfina area.

# 7. THE TIBERIAN BASIN GEOTHERMAL FIELD

This chapter lays the basis for an article currently in preparation within the framework of a multi-disciplinary project funded by the German Research Foundation (DFG) (grant Ma4450/2-3). The aim of the project is to understand hydrological, hydrochemical and structural features of the Tiberias Basin, particularly the Lower Yarmouk Gorge, at the border between Israel and Jordan. The presented work refers to the hydrogeological aspects of the study area in relation to the presence of widespread thermal springs that could be related to faults or local hydraulic anisotropy.

## 7.1 INTRODUCTION

Deep ground-water flow plays a major role in many geologic processes (*Bredehoeft and Norton, 1990*). Convective high temperature or magmatic hosted reservoirs provide excellent example of the dynamic coupling of large-scale hydrologic systems and the evolution of the Earth's crust (*Garven, 1995; Gvirtzman et al., 1997a*). As consequence of this coupling different system behaviours arise (*Severini and Huntley 1983; Evans et al., 1991; Magri et al., 2015*). Sedimentary basins, hosting a liquid-dominated geothermal anomaly, are subjected to several coexisting forces which drive large-scale ground-water migration (*McKenzie 1978*). They respond to either forced convection (gravity- or pressure driven flow), or free convection (buoyancy- or thermally-driven flow) phenomena *(Chen et al., 1990, Ingebritsen and Sanford, 1999*).

Forced groundwater convection, resulting from a slope in the ground-water table, is a well-known phenomenon observed at large and small basins throughout the world (*Toth, 1978; Deming et al., 1992; Musgrove and Banner, 1993; Person et al., 1996*). Free groundwater convection, arising from the dependence of fluid density on temperature, leads to unstable density stratifications where colder (denser) fluid overlies a warmer (lighter) fluid (*Nield and Bejan, 2006*). Typical pure free convection phenomena can be recognized in correspondence of mid-ocean ridges where strong temperature variations induce sea-water circulation (*Anderson et al., 1979*), and in geothermal systems (e.g. the Perth Basin in Western Australia and Torre Alfina geothermal field in central Italy; *Sheldon et al., 2012; Buonasorte et al., 1991*). The above two mechanisms (i.e. gravity-driven or forced convection flow and buoyancy-driven or free convection flow) may coexist in natural deep groundwater systems, that are named

mixed convective systems (e.g. *Magri et al., 2015*). Mixed convection is invoked as the main process when shallow heat anomaly is coupled with permeable faults or fractures. Early studies of the problem highlighted that the onset of different types of thermal convection require a relatively high permeability in the basin (*Lapwood, 1948*). Therefore, the hydraulic conductivity of the units exerts the major control on groundwater flow, and strongly impacts coupled processes. In this regard, permeable faults provide preferential pathways for mixed convection and for discharge of the regional flow (*McKibbin 1986; Magri et al., 2015*).

Modelling of fractured geothermal aquifers is always a challenge due to the typically limited information describing the fractures geometry, location and properties (*Abbo et al., 2003*). Several 2D and 3D numerical models of faulted basins have been performed in the last 25 years (e.g., *Lopez and Smith, 1995; Ormond et al., 1995; Rabinowicz et al., 1999; Person et al., 2012; Schilling et al., 2013; Kaiser et al., 2013*). These studies reveal the complex flow patterns within the fractured zones and the surrounding aquifers, and highlight the spatial correlation between fracture locations and thermal surface manifestations such as hot springs or fumaroles.

The Tiberian Basin, at the border between Israel, Jordan and Syria (Fig. 7.1a), is a valuable example of large scale groundwater flow coupled to heat transport in a faulted system, where mixed convection phenomena are likely to coexist. Moreover, the shallow heat anomaly characterizing the Northern Israel and Jordan areas, makes that field a potential site for production of electricity through geothermal methods (*Roded et al., 2013*).

The Tiberian Basin is located within in the Jordan Rift Valley (Fig. 7.1a), which includes the lowest land surface elevation on Earth (i.e. the Dead Sea; *Garfunkel, 1981*). This deep base level serves as a discharge area for a gravity-driven ground-water flow systems from surrounding heights. The Jordan Rift valley is constituted by a series of rhomb-shaped pull-apart basins, one of which hosts Lake Tiberias, also known as Lake Kinneret or Sea of Galilee (Fig. 7.1a, *Gvirtzman et al., 1997a; Magri et al., 2016*). This lake represents the main freshwater resource of the Middle East, suppling about 500 million $m^3$ of water per year, or about 30% of the country's annual consumption (*Tahal, 1989*). Therefore, maintaining its water quality is of national interest.

The Lower Yarmuk gorge (LYG, Fig. 7.1b) is a morphological feature within the western margin of the Jordan Rift Valley. The Yarmuk River is deeply incised into Neogene basalts and Eocene and Upper-Cretaceous sedimentary sequences and separates the basalt-covered Golan Heights to the north from the carbonaceous Ajlun Plateau to the south (Fig. 7.1b). As an outstanding phenomenon, around Lake Tiberias, particularly in the Lower Yarmuk Gorge (LYG), thermal waters ascend through fractured Eocene aquicludes forming clusters of hot and saline springs, posing a threat to the future sustainability of the lake freshwater resource (*Starinsky et al., 1979; Bajjali et al., 1997; Bergelson et al., 1999; Abu-Jaber and Ismail, 2003*). Spring clusters (Fig. 7.1b), close to or along the major fault axis, are characterized by widespread temperatures (20 – 60 °C) which indicate that, beside the complex regional flow, also ascending thermal waters control the hydrologic behaviour of the LYG.

The area has been extensively studied and many different data (i.e. hydrogeological data, borehole and chemical analysis on deep and superficial waters, geophysical surveys) have been collected in the past years in both the Israeli and Jordanian territories, providing useful information to characterize this complex system. Several numerical simulations have been performed to assess the deep flow systems, to explain springs behaviour and the anomalous geothermal gradient, to study the heat flow below the Lower Yarmuk gorge and to investigate thermal and salinity effects of pumping from the major aquifers (*Gvirtzman et al., 1997a,b; Rimmer et al., 1999, Hurwitz et al., 2000a,b; Rimmer 2000; Rimmer and Gal 2003; Abbo et al., 2003; Yechieli et al., 2011; Roded et al., 2013; Magri et al., 2015, 2016*). The most recent 2D model from *Magri et al. (2015)* suggested that the LYG hot springs are a mixture of groundwater from the surrounding highlands (topography-driven flow) and thermal fluids ascending along faults (buoyancy-driven flow). However, the two-dimensional limitations of the simulations did not allow to fully capture convective patterns that cross-cut the major flow direction nor those that may develop within the fault plane. Simplified 3D models (*Magri et al., 2016*) inspected the development of different modes of convection, likely responsible of upsurge of thermal water. These simulations showed that crossing flow paths resulted from the coexistence of convection that can develop for example along NE-SW oriented faults within the gorge or in permeable aquifers, and additional flow fields that are induced by the N-S topographic gradients.

The aim of this study is the construction the first regional 3D hydrogeological model of the entire LYG that includes structural features based on actual logs and interpreted seismic lines from both Israeli and Jordanian territories (*Inbar et al., 2018*). The model tests the occurrence of complex transboundary flow paths across faults observed in the idealized 3D model from *Magri et al. (2016)*, phenomena that can characterize any faulted hydrothermal systems and are not strictly related to the LYG. Multiple units, accounting for major aquifers, aquicludes and deep-cutting faults, have been considered. Recharges were implemented based on the numerical representation developed by *Shentzis (1990)* that considers relationships between mean annual rain and topographic elevation.

The regional 3D model reveals that topography-driven N-S and E-W flows strongly control the location of discharge areas while the anomalous spring temperature is not necessarily linked to the presence of fault convection. Local permeability anisotropy due to aquifers folding or facies changes are features sufficient for the rising of hot fluids.

## 7.2 HYDROTHERMAL SETTING OF THE TIBERIAN BASIN

### 7.2.1 Regional hydrogeological and structural setting

The Jordan Rift Valley or Dead Sea Rift Valley (Fig. 7.1) is the deepest terrestrial location on Earth and includes 5.000 $km^2$ with elevations below the sea level. Structurally the Dead Sea Rift is a left-lateral strike-slip transform, with a lateral shift estimated to be 105 km, separating the Sinai-Levant subplate from the Arabian plate (*Gvirtzman et al., 1997a,b*). Along this transform, several en-echelon rhomb-shaped grabens were formed, hosting the two biggest lakes of the Middle East: the freshwater Lake Tiberias and the saline Dead Sea (*Garfunkel, 1981*), with surface water elevations of -210 m a.s.l. and -400 m a.s.l., respectively.

The geological and structural settings of this area have been deeply studied in the last years through subsurface data collected from 20 deep boreholes and from several hundred kilometres of seismic lines carried out during oil exploration in northern Israel (*Ben-Gay and Reznikov, 1997; Klang and Gvirtzman, 1987; and Oil Exploration Investments Ltd. Unpublished reports*). Geological maps and surface columnar sections in northern Israel (*Golani, 1961; Saltzman, 1964; Eliezri, 1965; Michelson et al., 1987; Shaliv, 1991*) were integrated with the

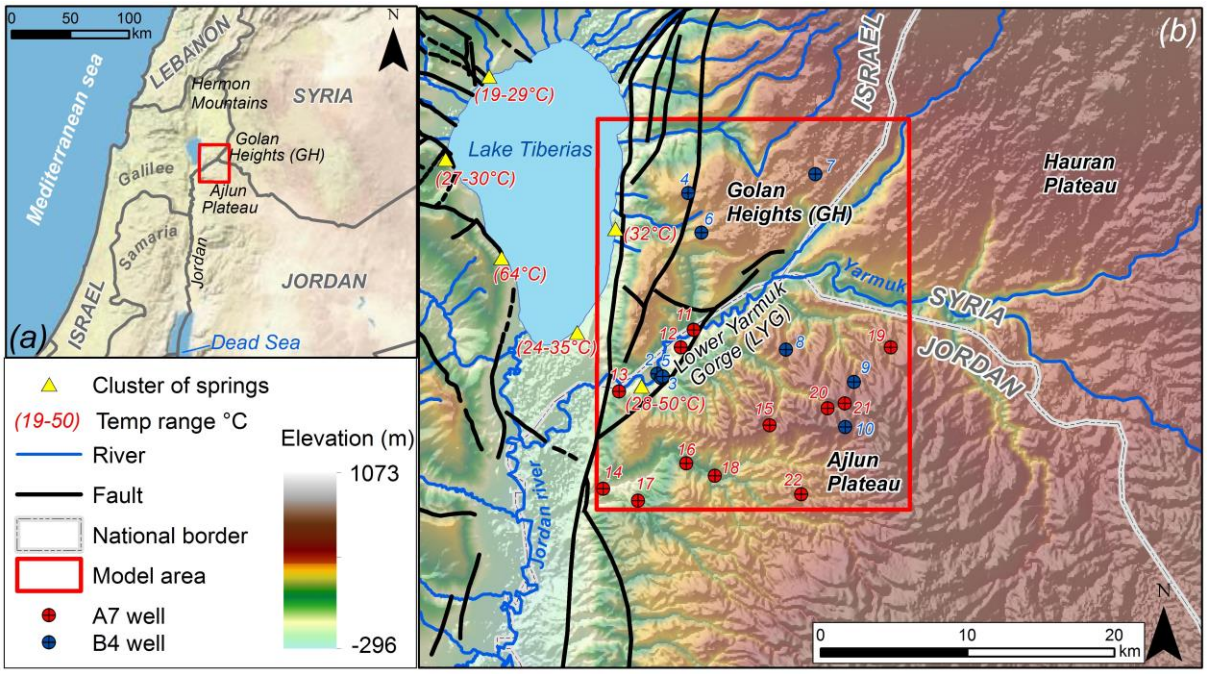


**Figure 7.1: (a)** Geographical setting of the Tiberian Basin (red line), including the main topographic features (i.e. Hermon Mountains, Golan Heights, Ajlun Plateau and Dead Sea) and the administrative national boundaries (gray lines). **(b)** Enlargement of the Tiberian Basin, including the model area (red line), topography, major faults (black lines) (*Inbar et al., 2018*), main rivers (blue lines) and cluster of thermal springs (yellow triangles) occurring all around Lake Tiberias and within Lower Yarmuk Gorge (LYG). Each cluster represents wide areas where different thermal springs are observable and the associated temperature range is highlighted in the brackets. Two sets of wells, drilled in the modelled area and used for the calibration of the numerical model, are also shown. Location of the measurements penetrating the superficial aquifer (#1-10, blue dots, B4 well) and those in the second regional aquifer (#11-22, red dots, A7 well), are presented.

subsurface information to reconstruct the lithostratigrapic sequence of the area. *Saltzman (1964)*, *Meiler (2011)* and *Inbar (2012)* provide a detailed description of the stratigraphy, structure and geo-hydrology of the area, and therefore their assumptions will be used to frame the geological setting of the Tiberian Basin.

On the eastern side of the Lake Tiberias, the Lower Yarmuk Gorge separates the limestone plateau of Ajlun from the basalt-covered limestones of the Golan Heights (GH) (Fig. 7.1). Structurally, the LYG is situated on the southern flank of a WSW-ENE-striking syncline, whose low is covered by the southern Golan (*Shulman et al. 2004; Roded et al., 2013*). The gorge, formed by the River Yarmuk, which approaches from the basaltic Hauran Plateau in Syria, is deeply incised into the Upper Cretaceous/Cenozoic lime- and marlstones and the late Cenozoic basalt cover. The stratigraphy in Golan and Ajlun is similar, although a successive facies change may occur from south to north, due to the changes in the marine deposition environment from proximal to distal.

Above a Permian basement, 2.5 km thick sequence of Triassic Carbonate and marly rocks is emplaced, which structure is to date poorly constrained (*Magri et al., 2016*). A 500 m thick of Jurassic partly karstified limestones and shales represents the base of the deepest of three regional aquifer recognized in the area (*BGR-WAJ, 1993*). Above, the Lower Cretaceous units comprise the 200 m sequence of mostly coarse-grained sandstone, indicating a fluvial deposition system with brief marine ingression (*Saad and Bashish, 1996*). These units have been interpreted as the deepest regional aquifer. Intercalations of limestones and marls are building most of the Upper Cretaceous sequences, from Cenomanian to Campanian units (*Rosenfeld and Hirsch, 2005; Makhlouf et al., 1996*). The latter represents a very thick second regional aquifer confined at the top by the Early Tertiary (Mastrichtian epoch) aquiclude, composed mainly by chalks with some marl and limestone intercalations and forming the LYG floor as well as the base of its shoulders (*Magri et al., 2016*). Above, Tertiary (Eocene epoch) limestones, deposited on a folded terrain and yielding to a thickness of about 200 m (*Flexer, 1964*), are the shallower aquifer in the area. The rift valley is capped by a Miocene–Quaternary sequence that is at least 4 km thick and that consists of evaporites, alluvial deposits, basalt, and a few intrusions of gabbro (*Marcus and Slager, 1985*).

The thick basalt cover at the GH masks over pre-Pliocene faulting. Surface faults were mapped mostly in the western margin of the GH, the majority of them are N-S striking and were considered related to the Dead Sea Rift valley opening (*Michelson, 1982*). In several locations at the northern province of the GH, pre-basalt outcrops reveal faults which curve out of the rift valley, eventually striking SW-NE (*Meiler, 2011*). Similar fault structures are common along the eastern side of the Lake Tiberias from the Bay of Eilat/Aqaba in the south up to the Ajlun Mt. in northern Jordan (*Andrews, 1992*). Aeromagnetic surveys, conducted in northern Jordan at the end of the 90's, were interpreted to show the Dead Sea Rift valley fault and a branching SW-NE lineament, which was identified by field work as a normal fault (*Moh'd, 2000*). Currently, fault patterns are being re-interpreted (*Inbar et al., 2018*) to provide an actual map of major faults within the area.

### 7.2.2 Thermal setting

Through an extensive geothermal survey, made by more than 70 locations only in Israel, a mean basal heat flow value of 40 to 50 mW/m$^2$ has been calculated (*Eckstein, 1976; Eckstein*

*and Simmonsi, 1977; Levitte and Olshina, 1985; Shalev et al., 2008*). Eastward, in Jordan, measured heat fluxes in 18 borehole at depth of several hundred meters, reported a value in the range between 42 and 65 mW/m$^2$ (*Galanis et al., 1986*). All these studies have shown a common gradient of 15-25°C/km for the two neighbouring states. The measured common heat fluxes, in Israel and Jordan, are slightly higher than those measured at the Mediterranean Sea (31 mW/m$^2$; *Erickson et al.,1977*) and definitely lower than those detected at the Red Sea (60–340 mW/m$^2$; *Erickson and Simmons, 1969*), due to the proximity of a relatively young mid-ocean ridge.

Direct heat flow measurements in the GH and in the LYG areas are scarce, mostly since there were very few deep boreholes where a reliable deep conductive basal heat flow may be calculated. Nevertheless, thermal data from groundwater temperature measurements are abundant and used to determine heat flow values. Vast geochemical explorations, have been performed in the Golan–Ajlun area on groundwater at the LYG, aimed to study the geothermal and hydrological system (e.g. *Arad and Bein, 1986; Bajjali et al., 1997; Eckstein, 1976; Levitte and Eckstein, 1978; Mazor et al., 1973, 1980; Starinsky et al., 1979*).

Although the floor of the Lower Yarmuk gorge is built up of Mastrichtian aquiclude (*Arad and Bein, 1986*), thermal springs emerge from it along its northern flank at Hammat Gader (38–51 °C), as well as in Himma (42°C) and Mukheibeh (38°C). The occurrence of these springs is bounded to faults, as suggested by *Siebert et al. (2014)*. Moreover, Meizar boreholes, drilled in the southern Golan flank release artesian groundwater with 41-60°C from the Turonian (Meizar 2) and Santonian (Meizar 3) formations, respectively (Fig. 7.1b). Less heated, the Mukheibeh well (29–46 °C; *Bajjali et al., 1997*), located in the northern flank of the Ajlun, also produce artesian water from the second aquifer. From the Meizar deep wells, located 6–8 km east of the Lake Tiberias in the LYG, geothermal gradients of 46 °C/km were measured, which are about two to three times higher than the average geothermal gradient of the Jordan area. Surprisingly, in contrast with the average heat fluxes of Israel and Jordan, the area around the Lake Tiberias is overall affected by heat flow higher than 60mW/m$^2$, locally reaching 85mW/m$^2$ (*Ben-Avraham et al.,1978; Shalev et al., 2008*).

Departures from regional geothermal gradient have been associated to two phenomena in the work of *Roded et al. (2013)* and *Magri et al. (2015)*: (1) vertical convective effects in

correspondence of zones of large tectonic faults, and especially with junctions of intersecting faults, and (2) heat flow perturbations related to magmatic intrusions although no significant recent volcanic activity took place in that area.

### 7.3 THE CONCEPTUAL MODEL

The spatial extent of the model is fundamental for a reliable simulation of the processes involved in such complex geothermal system. An overly restricted scenario hampers a complete representation of the circulation into the field, whereas a very large one results in a more uncertain geological reconstruction and excessive computational loading. The model area (Fig. 7.1b), covering about 565 $km^2$, lies on the eastern margin of the lower Jordan Rift Valley (i.e. at the border between Israel, Jordan and Syria) and is bordered by the Lake Tiberias only on its W-NW margin. As anomalous heat flux values have been recorded only in the eastward facing side of the Lake Tiberias, particularly along the LYG, the model domain was not extended westward within the Israeli territory. The selected area is diagonally crossed by the Lower Yarmuk Gorge (LYG), which allows the outflow of the Yarmuk drainage basin and flow into the Jordan River, a few kilometres south of Lake Tiberias (Fig. 7.1b). The LYG distinguishes the Golan Heights at North and the Ajlun Plateau to the South, both partially included in the model area. It is supposed that this gorge acts as the mixing zone of two crossing flow pathways: N-S from the Hermon Mountains and from the Ajlun Plateau, and E-W from Jebel al Arab Mountain in Syria (also known as Hauran Plateau or Yarmuk drainage basin).

Due to the large extent of the geothermal reservoir and its intrinsic geological complexity, a complete review of the existing data and literature was required (*Golani, 1961; Saltzman, 1964; Eliezri, 1965; Marcus and Slager, 1985; Klang and Gvirtzman, 1987; Michelson et al., 1987; Shaliv, 1991; BGR-WAJ, 1993; Saad and Bashish, 1996; Makhlouf et al., 1996; Ben-Gay and Reznikov, 1997; Shulman et al., 2004; Rosenfeld and Hirsch, 2005; Meiler, 2011; Inbar, 2012; Roded et al., 2013*). The geological model relies on new 3D interpretations of available well data from both Israeli and Jordan regions. Additional structural constraints are derived from seismic lines in the GH. This complex basin model is the current topic for an article in preparation (*Inbar et al., 2018*). Major attention was devoted in representing model vertical

differentiation in main aquifers and aquitards, as well as the system of 7 normal regional faults (Fig. 7.1b and Fig. 7.2), accounting for the relative displacements of the surrounding aquifers. Different well-established approaches exist to model fractures in porous media (e.g. *Blessent et al., 2014; Vujevic´ et al., 2014*). Here faults are modelled using the Equivalent Porous Media approach (EPM), i.e. permeable units extending from the basement to the top. This choice was dictated by the lack of structural inputs for fault geometry that are required to apply other numerical approaches, such as discrete features (*Magri et al., 2015*). Other authors applied the same approach in their numerical simulation the Tiberian Basin (e.g. *Abbo et al., 2003*), providing satisfactory results. Representing faults as EPM allows the correct computation of conductive thermal buffering along the sides of the fault. Conductive heat transfer from the surrounding rocks to the faults control the onset of thermal convection which is delayed (*Wang et al., 1987; Tournier et al., 2000; Malkovsky and Magri, 2016*). The fault system cut vertically the model in its entire thickness till the top of the impervious Permian basement,

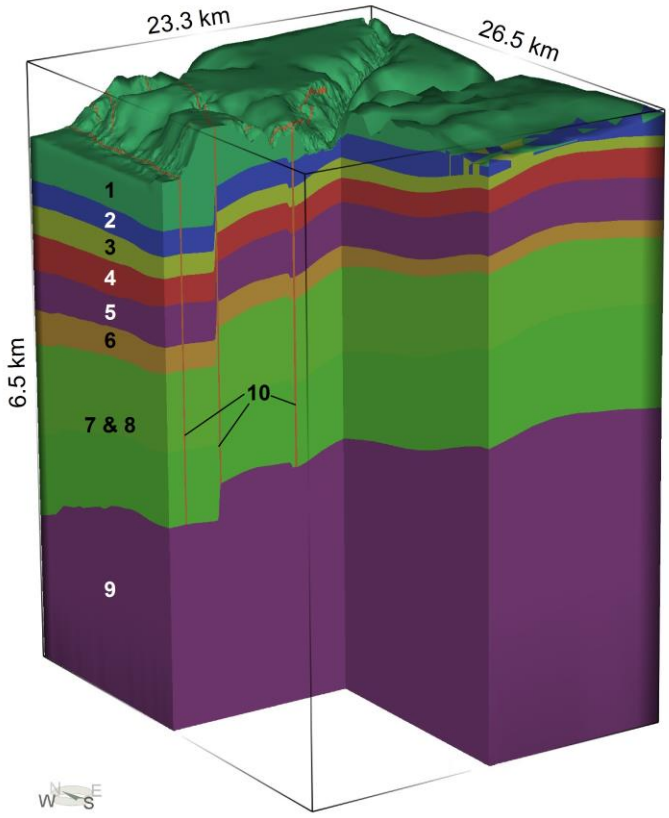


| Age | Epoch | Model zone | Formation sign | Hydrological imprint |
|---|---|---|---|---|
| Quaternary | Pleistocene | 1 | B4 | Superficial aquifer |
| Tertiary | Pliocene | | | |
| | Miocene | | | |
| | Oligocene | | | |
| | Eocene | | | |
| Upper Cretaceous | Mastrichtian | 2 | B3 | Aquiclude |
| | Campanian | 3 | B2 | 2nd Aquifer |
| | Santonian | | B1 | |
| | Turonian | 4 | A7 | 2nd Aquifer |
| | Cenomanian | 5 | A5-A6 | Aquiclude |
| | | | A4 | |
| | | | A3 | |
| | | | A1-A2 | |
| Lower Cretaceous | Albian - Aptian | 6 | K1-K2 | Deepest aquifer |
| Jurassic | - | 7 | Z2 | Aquiclude |
| Triassic | - | 8 | Z1 | Aquiclude |
| Permian | - | 9 | Basement | Aquiclude |
| Fault | - | 10 | Faults | - |

**Figure 7.2:** Three-dimensional geological conceptual model, showing the internal subdivision according to the 10 hydrogeological units. Model extensions are presented (black lines), vertical exaggeration 5:1. The formations constituting the conceptual model are numbered as reported in the associated table (Model Zone column). The table on the right side summarizes the Age and Epoch, together with the Formation Sign and the Hydrological Imprint of all the involved geological units.

which close the model at -6 km a.s.l. The upper limit was defined from a 85 x 85 meter DEM derived topography, including a vast portion with elevations below sea level (Fig. 7.2). This resulted in a maximum model thickness of about 6.5 kilometres (from +580 m a.s.l. to -6,000 m a.s.l.).

The highly fractured rock-mass of the deformation band, associated with the regional normal fault systems, is assumed to constitute a preferred path for deep groundwater circulation as well as a conduit for rapid ascent in the LYG thermal area. This has been suggested by previously geothermal simulations performed in the area (e.g. *Gvirtzman et al., 1997a,b; Roded et al., 2013; Magri et al., 2015, 2016*).

In summary, the conceptual model consists of ten hydrogeological units (Fig. 7.2), that will be here referred using the formation signs adopted from the conceptual model given in *Magri et al. (2015)*. From the bottom, a closing unit named Basement, represent the Permian successions which serve as thermal buffer between bottom heat boundary conditions and the overlying Triassic carbonate units (Z1). Further up the model include the Jurassic limestones (Z2) and the lower regional aquifer made by the Lower Cretaceous conglomerates (K1-K2). Above, early Upper Cretaceous dolostone with interbedded marls (A1 to A6) and Upper Cretaceous limestones (A7) are emplaced, the latter represent the second very thick regional aquifer. The top of this aquifer is located in the Upper Cretaceous formation (B1-B2) dated to Santonian and Campanian epoch. The Early Tertiary marls and chalk (B3) form the aquiclude at the base of the superficial aquifer, made by Tertiary limestones and basalts (B4). The model includes also the system of seven N-S trending normal subvertical Faults (F), with a surface trace ranging from a minimum of 1.5 km to a maximum of more than 21 km, in the case of the structure framing the east margin of the Lake Tiberias (Fig. 7.1).

## 7.4 NUMERICAL MODELLING

A three-dimensional thermo-hydraulic model was built to simulate the deep and complex regional groundwater flow system (Fig. 7.3). The equations governing coupled fluid flow and heat transport processes are solved using the finite element software Feflow® (*Diersch, 2014*). The mathematical formulation has already been explained in previous chapters, and will not

be recalled here. The polynomial fittings of *Magri et al. (2015)* are used to compute variable fluid viscosity and density over the pressure and temperature ranges of the solution domain.

### 7.4.1 Modelling approach

The model surface (565 $km^2$) was discretized into 126,803 high quality triangular finite elements (3.5 % of triangles with obtuse angles (>90°) and 0.4 % of triangles violating the Delaunay's criterion, Fig. 7.3a).

Due to the regional extent of the model domain, mesh refinement was applied to ensure simulation robustness: elements size decreases gradually from 1,500 meters, at model lateral boundaries, to 20 meters close to the fault zone and along the LYG, where water flux and heat transport dynamics occur (Fig. 7.3a). The complex normal fault system is represented as an equivalent porous media of 40 m width, therefore at least 2 elements discretize the fault aperture, accounting for possible buoyant-driven flows within the structure (Fig. 7.3a).

The 2D surface grid was extruded vertically using a fully prismatic 3D mesh (Fig. 7.3b). The total volume of the model was discretized with 26 layers ranging in thickness from 1,500 meters, at the model bottom, to a minimum of less than 50 meters, near the topographic surface. In total the 3D mesh consists of 3,296,878 prismatic elements that preserve the relative displacements between the geological formations.

Based on the conceptual configuration and the three-dimensional mesh presented above, two numerical simulations were run to investigate the different processes involved in the area. Firstly the pure hydrodynamic flow model (no heat transport), then a coupled transient thermo-hydraulic model, which account for possible mixed convective mechanisms confined in the aquifer units or within the fault system.

The steady-state hydrodynamic model was calibrated against available measured groundwater levels recorded in correspondence of 22 well points (see Fig. 7.1 and Table 7.1), both in the superficial (Tertiary units, B4; 10 wells) and second (Upper Cretaceous units, B1-B2/A7; 12 wells) aquifers (*BGR-WAJ, 1993, 1997, 2001*). Steady-state model calibration of hydraulic conductivity was performed by inverse procedure (PEST; *Doherty et al., 1994*). The hydraulic conductivity values found in *Magri et al. (2015)* were used as initial values and adjusted during the calibration.

### 7.4.2 Boundary and initial conditions

Groundwater flow boundary conditions were defined based on the geological and hydrogeological conceptual model. A constant head (i.e. Dirichlet type) corresponding to surface water elevations of -210 m a.s.l. was imposed to the nodes of Lake Tiberias in the upper North-West side of the model (Fig. 7.3a), and extended to the first three slices to account for surface-water/groundwater interaction in the superficial aquifer (B4). The measured groundwater levels resulting from the extensive hydrogeological explorations, performed in both Israeli and Jordan territories (*Arad and Bein, 1986; Bajjali et al., 1997; Eckstein, 1976; Levitte and Eckstein, 1978; Mazor et al., 1973, 1980; Starinsky et al., 1979*), were interpolated in order to obtain a groundwater level map for the B4 aquifer. Resulting values were used as constant head (i.e. Dirichlet type) boundary conditions on the East, West and North model boundaries (Fig. 7.3a), to reproduce the two different N-S and E-W flow

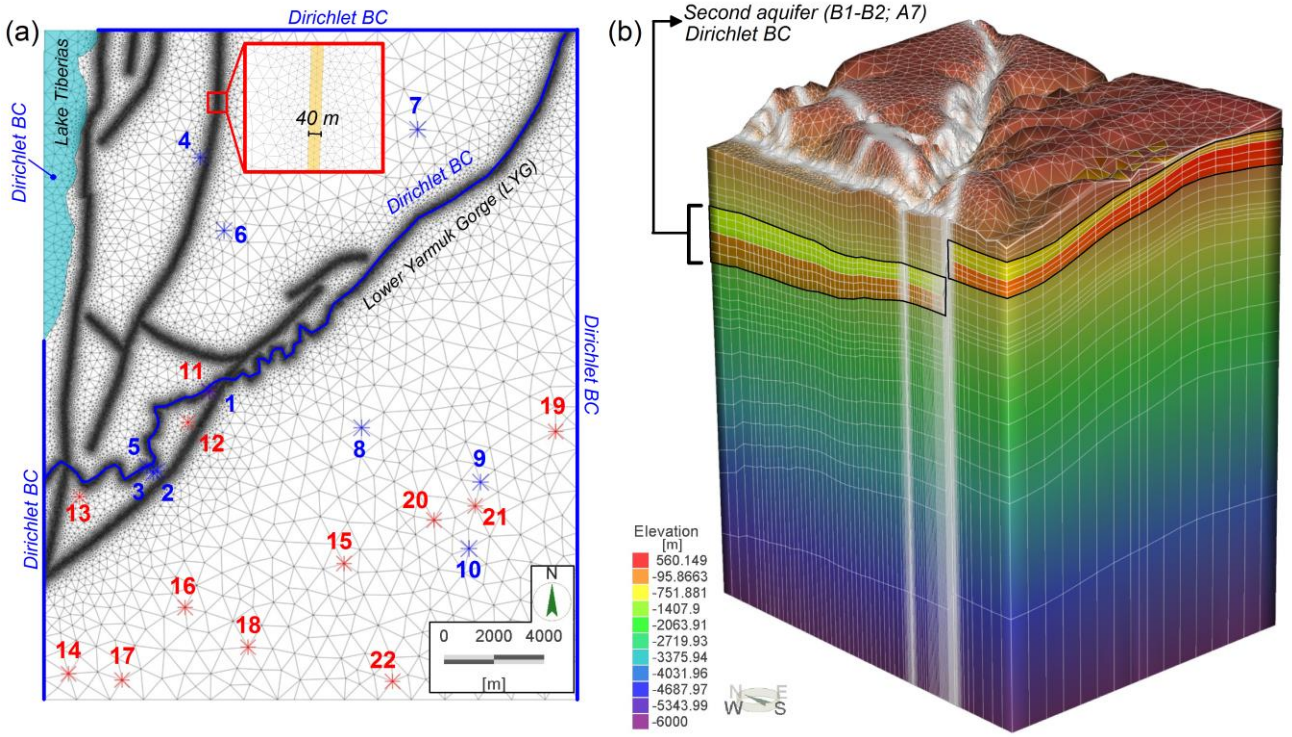


**Figure 7.3: (a)** Model surface (565 km$^2$) discretized into 126,803 high quality triangular finite elements, with mesh refinements around the system of 7 faults and along the Lower Yarmuk Gorge (LYG). Applied hydraulic boundary conditions for the superficial (B4 formation) aquifer, are also shown. Dirichlet type BCs are set along Eastern, Western and Northern model boundaries and in correspondence of the Tiberias Lake. The Lower Yarmuk Gorge (LYG) is highlighted with a blue line, referring to the associated Dirichlet boundary condition. At model surface a Neumann type boundary condition is applied accounting for the recharge of the system. Locations of model wells is presented as in Fig. 7.1: measurements in the superficial aquifer (blue asterisks) and in the second aquifer (red asterisks). Wells are numbered as in Table 7.1. **(b)** Three-dimensional hydraulic model, made by 26 layers and ca. 3.3 million of prismatic elements. Vertical exaggeration 5:1. Model elevation range from 560 to -6,000 m a.s.l. (see color bar). Hydraulic boundary conditions for the second regional aquifer (B1-B2/A7) is highlighted with black lines. A no-flow boundary condition is set all the remaining later boundaries.

**Table 7.1:** Model wells used in calibration process, with station name, belonging aquifer and measured water level (m). Location of the wells is as shown in Figs. 7.1 and 7.3.

| ID_obs | STATION NAME | AQUIFER | MEASURED WATER LEVEL [m a.s.l.] |
|---|---|---|---|
| 1 | Meizar 3 | B4 | -160.00 |
| 2 | Hammat Gader 3 | B4 | -160.00 |
| 3 | Hammat Gader 2 | B4 | -148.00 |
| 4 | Bir Skopia | B4 | 320.00 |
| 5 | Hammat Gader 1 | B4 | -142.00 |
| 6 | Fiq well | B4 | 330.00 |
| 7 | Hital 1 | B4 | 317.00 |
| 8 | SAHAM EXP WSC | B4 | 321.00 |
| 9 | KUFR SOUM EXP. NO 1 | B4 | 348.00 |
| 10 | KUFR SOUM MONITORING | B4 | 376.00 |
| 11 | Meizar 2 | B2-B1; A7 | -160.00 |
| 12 | MUKHEIBA (JRV1) | B2-B1; A7 | -81.10 |
| 13 | MUKHEIBA 5 | B2-B1; A7 | -117.00 |
| 14 | WADI ARAB DAM OBSERVATION 16 A | B2-B1; A7 | -175.00 |
| 15 | MALKA 1/EL SHAIKH | B2-B1; A7 | 17.00 |
| 16 | KUFR ASAD 4 | B2-B1; A7 | -40.80 |
| 17 | WADI AL ARAB NO 8 | B2-B1; A7 | 20.55 |
| 18 | KUFR ASAD EXP | B2-B1; A7 | 53.60 |
| 19 | HARTHA 1 | B2-B1; A7 | 66.00 |
| 20 | IBDER OBSERVATION NO 1 | B2-B1; A7 | 80.00 |
| 21 | KUFR SOUM NO 2 | B2-B1; A7 | 68.00 |
| 22 | FO'ARA EXP | B2-B1; A7 | 95.60 |

pathways in accordance with the previously performed numerical simulations of *Gvirtzman et al. (1997a,b)*, *Roded et al. (2013)* and *Magri et al. (2015, 2016)*. As the Yarmuk river flows along the LYG draining water to the Jordan river, a constant head (i.e. Dirichlet type), 10 meters above surface elevation, was imposed to the nodes of the gorge (Fig. 7.3a) in order to reproduce its artesian conditions.

Similarly to what have been done for the superficial aquifer (B4), an interpolated groundwater level map was created from measured groundwater levels referred to the second aquifer (A7 and B1-B2 formations). Resulting values were assigned as constant head boundary condition to the East, South and West nodes of the involved layers (Fig. 7.3b). All the remaining lateral boundaries of the model were considered as no flow boundaries. In the purely hydrodynamic model, inflow values equal to 70% of mean annual precipitation were assigned to simulate effective recharge. The applied values, ranging from 200 to 350 mm/years, have been derived by the numerical representation developed by *Shentzis (1990)* that considers relationships

between mean annual rain and topographic elevation. These groundwater flow boundary conditions induce a steady state regional flow over the entire domain extension that can be encountered in any basin system, where highlands and lowlands act respectively as recharge and discharge areas (*Toth, 1978*).

Regarding the transient coupled thermo-hydraulic models, a steady-state heat-conductive solution of the problem is used as initial conditions (see Fig. 7.4). Fluid-flow boundary conditions are those of the previously described groundwater flow problem. At the top of the domain, a heat-transfer boundary condition (i.e. Cauchy type), controlled by a heat transmission coefficient and with reference temperature of 20°C, was imposed (Fig. 7.4). Thus, the temperature of the top of the domain is allowed to vary with respect to the convective heat transfer. A constant undisturbed basal geothermal flux (i.e. Neumann type) of 60 mW/m$^2$ is set at the bottom of the model (Fig. 7.4). The lateral boundaries are no flow for both heat and groundwater flow, in particular because no heat is advected across such boundaries, it is assumed that heat conduction is vertical, i.e., no heat crosses.

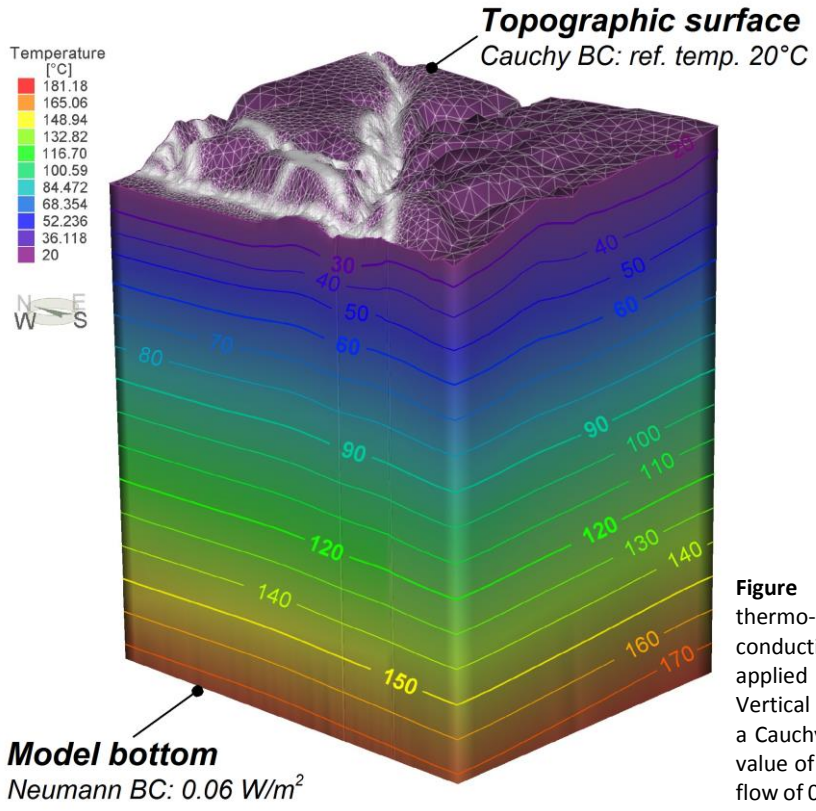


**Figure 7.4:** Three-dimensional coupled thermo-hydraulic model, with initial conductive temperature distribution and applied thermal boundary conditions. Vertical exaggeration 5:1. At model surface a Cauchy type with reference temperature value of 20°C and at model bottom a heat-flow of 0.06 W/m$^2$ (i.e. Neumann type BC) is set.

The initial conditions for head and temperature distributions are derived from steady state simulations of groundwater flow and conductive heat transport, respectively. The initial physical properties of each unit (e.g. hydraulic conductivity, porosity and heat conductivity) are listed in Table 7.2. The assigned values were derived from previous hydrogeological investigations, field studies, lithological descriptions and two-dimensional investigations as detailed *in Magri et al. (2015, 2016)*. Starting from these initial values, hydraulic conductivity of the involved units have been adjusted through the PEST calibration process. Fluid thermal conductivity and heat capacity are constant at reference temperature of 20°C.

## 7.5 RESULTS AND DISCUSSION

### 7.5.1 Hydrodynamic flow model calibration

Groundwater flow simulations represent a preliminary step in the development of a regional coupled thermo-hydraulic numerical model. The hydrodynamic model was run assuming confined saturated aquifer condition under steady-state regime.

Hydraulic conductivity is the main parameter controlling groundwater flux and the initial values were derived from previous studies (*Magri et al., 2015, 2016*). A clear distinction exists between formations constituting the 3 aquifers, the impervious aquicludes and the faults (See Fig. 7.2 and Table 7.2). As pointed out by several authors (*Sonney, 2010; Clerici and Sfratato, 2008*), in such complex systems a calibration process is needed to precisely estimate equivalent rockmass continuum parameters.

The steady-state model was calibrated, through inverse problem using PEST (*Doherty et al., 1994*), on the 22 wells listed in Table 7.1. The first ten control points measure water levels in the superficial aquifer (i.e. B4 formation), while the remaining twelve measurements have been associated to the second regional aquifer (i.e. B1-B2 and A7 formations). Only the hydrogeologic units till the depth of the base of the second regional aquifer (i.e. B4, B3, B1-B2 and A7; see Table 7.2), including the faults, have been considered in the automatic calibration process. Initial hydraulic conductivity values (*Magri et al., 2015*) were considered anisotropic for all model units, except for the aquiclude (i.e. B3 formation) separating the superficial from the second aquifer. In the PEST calibration process, such values are not linked to their initial

**Table 7.2:** Summary of the model conceptualization, including Model zones (as listed in Fig. 7.2), Ages and Hydrological imprint. Initial (from *Magri et al., 2015, 2016*) and calibrated hydraulic parameters applied in the purely hydrodynamic model, are presented together with model thermal parameters used in both steady-state and transient coupled hydro-thermal models. The cells shaded in grey refer to model zones that are not included in the PEST calibration process.

| | | | | | Hydraulic conductivity [m/s] | | | | | Porosity [%] | Thermal conductivity [W/m/K] |
|---|---|---|---|---|---|---|---|---|---|---|---|
| | | | | | Initial values | | Calibrated values | | | | |
| Age | Epoch | Model zone | Formation sign | Hydrological imprint | $k_{x,y}$ | $k_z$ | $k_x$ | $k_y$ | $k_z$ | | |
| Quaternary | Pleistocene | 1 | B4 | Superficial aquifer | 1.00E-06 | 1.00E-06 | 6.83E-08 | 5.61E-08 | 7.37E-07 | 0.06 | 2.1 |
| Tertiary | Pliocene | | | | | | | | | | |
| | Miocene | | | | | | | | | | |
| | Oligocene | | | | | | | | | | |
| | Eocene | | | | | | | | | | |
| Upper Cretaceous | Mastrichtian | 2 | B3 | Aquiclude | 1.00E-07 | 3.00E-08 | 2.29E-09 | 2.54E-09 | 8.15E-09 | 0.0625 | 1.5 |
| | Campanian | 3 | B2 | 2nd Aquifer | 1.00E-05 | 1.00E-05 | 1.82E-06 | 4.81E-06 | 9.23E-08 | 0.08 | 2.24 |
| | Santonian | | B1 | | | | | | | | |
| | Turonian | 4 | A7 | 2nd Aquifer | 4.00E-05 | 4.00E-05 | 8.48E-05 | 1.12E-06 | 3.25E-04 | 0.13 | 2.8 |
| | Cenomanian | 5 | A5-A6 | Aquiclude | 1.00E-10 | 1.00E-10 | 1.00E-10 | 1.00E-10 | 1.00E-10 | 0.04 | 2.5 |
| | | | A4 | | | | | | | | |
| | | | A3 | | | | | | | | |
| | | | A1-A2 | | | | | | | | |
| Lower Cretaceous | Albian - Aptian | 6 | K1-K2 | Deepest aquifer | 7.00E-06 | 7.00E-06 | 7.00E-06 | 7.00E-06 | 7.00E-06 | 0.125 | 2.65 |
| Jurassic | - | 7 | Z2 | Aquiclude | 5.50E-07 | 5.50E-07 | 5.50E-07 | 5.50E-07 | 5.50E-07 | 0.0355 | 2.62 |
| Triassic | - | 8 | Z1 | Aquiclude | 4.00E-07 | 4.00E-07 | 4.00E-07 | 4.00E-07 | 4.00E-07 | 0.0355 | 2.62 |
| Permian | - | 9 | Basement | Aquiclude | 1.00E-10 | 1.00E-10 | 1.00E-10 | 1.00E-10 | 1.00E-10 | 0.01 | 2.5 |
| Fault | - | 10 | Faults | - | 2.70E-06 | 2.70E-06 | 1.28E-05 | 3.54E-07 | 4.04E-08 | 0.2 | 1.1 |

ratio, accounting for anisotropy in both horizontals and vertical directions (see values in Table 7.2). Three degrees of freedom in hydraulic conductivity values are necessary for a reliable calibration process, since, as can be seen from the values in Table 7.1, even inside of the same aquifer, modelled as an homogenous media, the measured hydraulic heads show a strong discrepancy. Scatter plot of the difference between observed and computed groundwater levels is shown in Fig. 7.5., while the resulting calibrated hydraulic conductivity values are listed in Table 7.2 and hydraulic head distributions for the superficial and second regional aquifers are shown in Figure 7.6.

Considering the extent and the complexity of the study area, calibration results indicated a reasonable agreement between simulated and observed hydraulic heads, and calibrated hydraulic conductivity values are consistent with the range of the initial values and with the assumptions made in the construction of the conceptual model. Is worth to point out that, in order to realize a good fitting between the control points in the two aquifers (i.e. B4-superficial and B1-B2/A7-second aquifer), the calibration process results in a very low hydraulic conductivity values for the interposed aquiclude (i.e. B3 units). In fact, for this unit PEST

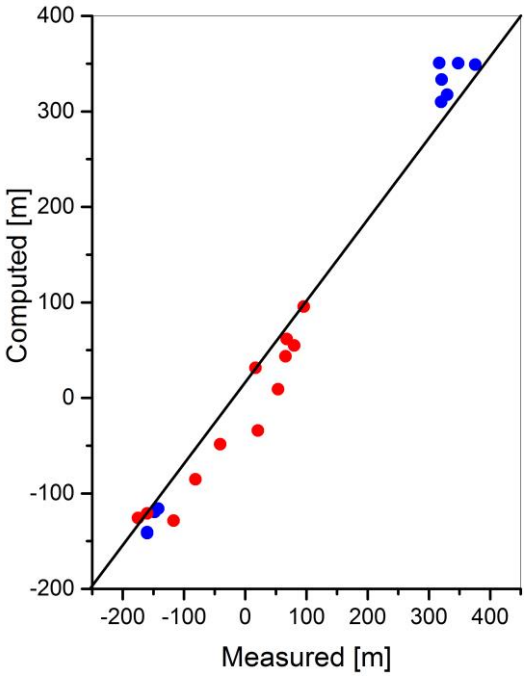


**Figure 7.5:** Scatter plot from PEST calibration process showing the difference between measured and computed hydraulic heads. Points colour refers to the aquifer they belongs, blue dots for the superficial (B4) one and red dots for the second aquifer (B1-B2/A7).

process estimates in both x, y and z directions a parameter value in the range of 2 to 8 x $10^{-9}$ m/s. All the model formations, except for the impervious basement, are crossed by the faults system, which could potentially act as a conduit connecting the superficial and the second aquifer. To avoid this occurrence and keep isolated the two aquifers, the PEST calibration process resulted in a low hydraulic conductivity value for the fault system in vertical direction (i.e. $k_z = 4*10^{-8}$ m/s, see Table 7.2). From the hydraulic head distributions in Figure 7.6b, two different hydraulic systems have been identified in the superficial aquifer (i.e. B4 unit): one in the northern portion of the model domain, the Golan Heights (GH), and one active in the southern side, the Ajlun Plateau. These two hydraulic systems are separated by the SW-NE trending Lower Yarmuk Gorge (LYG). Similarly to what have been observed in the previously performed 2D simulations (*Magri et al., 2015*), the gorge parallel trend of the hydraulic head isolines (Fig. 7.6b) supports the hypothesis that the LYG acts as the mixing zone of the two crossing flow pathways. In the northern GH hydraulic system, beside the N-S groundwater flow, also a strong E-W flow pathway toward the Tiberias Lake, has been recognized. Approaching the lake, this flow is intercepted by the fault system, which may channels the groundwater flow in horizontal directions, due to its higher hydraulic conductivity. The same two hydraulic systems (i.e. below the Golan Heights and the Ajlun Plateau) can be recognized also in the second regional aquifer (Fig. 7.6), even if the impluvium role of the LYG is smoothed with the depth.

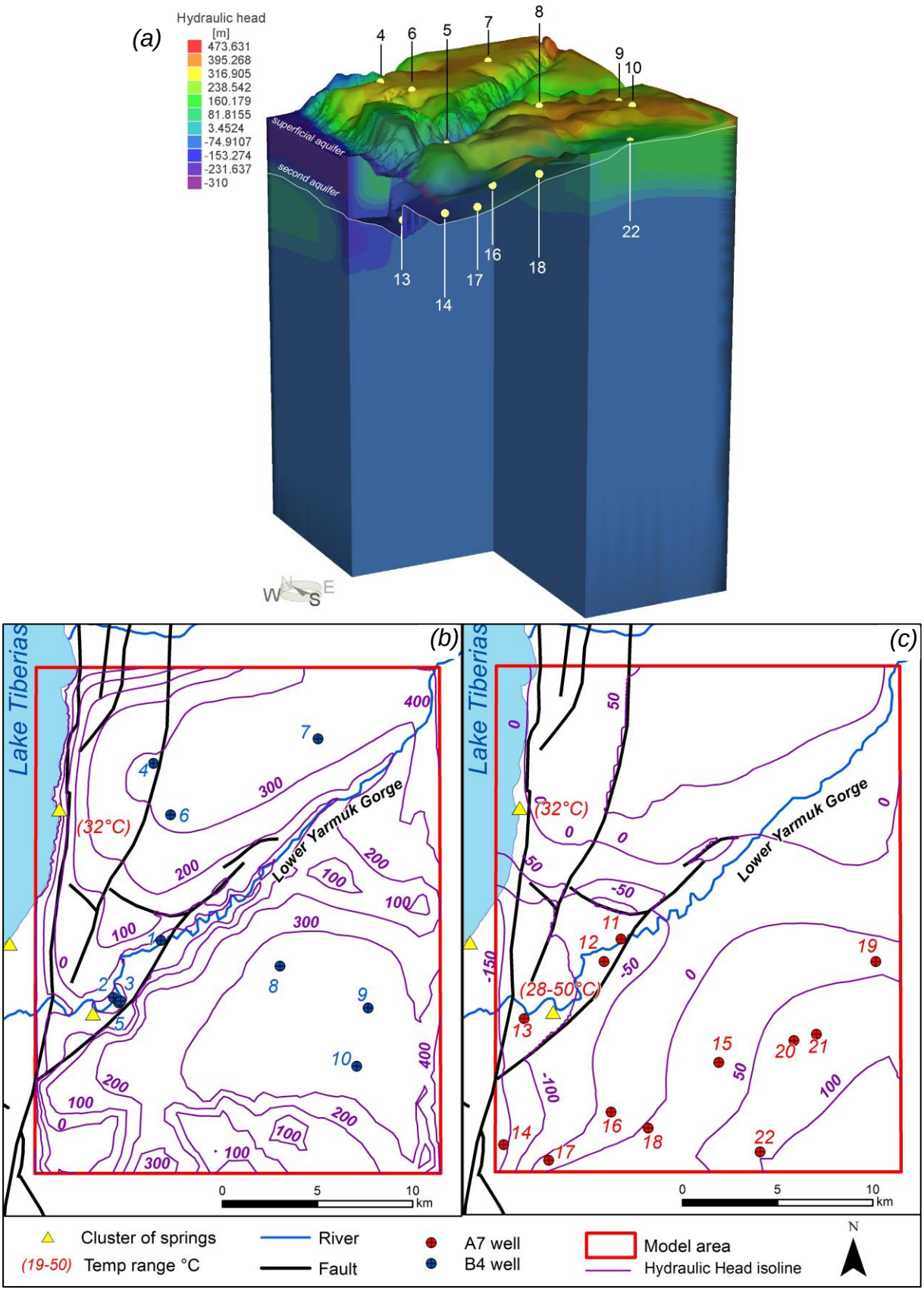


**Figure 7.6: (a)** Three-dimensional calibrated hydraulic head distribution, with location of the well used for PEST calibration process. Vertical exaggeration 5:1. **(b)** Calibrated hydraulic head distribution for the superficial aquifer (B4 formation), isolines (purple) are shown every 100 m; **(c)** calibrated hydraulic head distribution for the second regional aquifer (B1-B2/A7 formations), isolines (purple) are shown every 50 m. Cluster of springs (yellow triangles), together with main rivers (blue lines), faults (black lines) and the location of the wells used for the calibration process.

### 7.5.2 Coupled hydro-thermal results

Transient coupled hydro-thermal simulations have been performed using the conductive heat flow model temperature distribution as initial condition (Fig. 7.4). Accordingly to the previous numerical studies of the area (*Gvirtzman et al., 1997a,b; Roded et al., 2013; Magri et al., 2015, 2016*), no brine transport is computed and fluid density and viscosity are considered dependent on the temperature.

Results of the coupled fluid flow and heat transport process show a vigorous convective regime, as illustrated in Fig. 7.7. The cross-sectional views (*surface 1* and *surface 2* in Figs. 7.7), extracted parallel and perpendicular to the regional flow identified by the pure hydrodynamic model, reveal that fluid convection is confined below the Cenomanian aquiclude (A1-A6 units) with isotropic very low hydraulic conductivity (i.e. $10^{-10}$ m/s). This impervious layer prevents hot waters to reach the surface, neither through the faults system, as they are characterized by a low vertical hydraulic conductivity too (i.e. $k_z = 4*10^{-8}$ m/s, see Table 7.2). However a small increase in temperature can be observed at topographic surface in correspondence of lake Tiberias, the LYG and the surface traces of the faults (Fig. 7.7a). The eastern shore of the Tiberias lake and the LYG correspond to known thermal spring outflow sites, named Gofra (ca. 32 °C) and Hammat Gader (ca. 28–50 °C), respectively (see Figs. 7.1 and 7.7a and Table 7.1). *Siebert et al. (2014)* suggest that the occurrence of these thermal spring clusters is tied strictly to the fault system. This hypothesis is validated by the results of our numerical model too, as the increase in temperature is recorded in correspondence of the fault surface traces (Fig. 7.7a).

Figures 7.7b and 7.8, show that the multicellular convective regimes develop mainly below the LYG and in correspondence of the faults, although not reaching the topographic surface due to the impervious A1-A6 aquiclude. Analysing the flow pathways, in correspondence of four selected nodes (Fig. 7.8), two major independent flow fields can be distinguished: a topography-driven and a buoyancy-driven flow. Firstly, a topographic- or regional-driven flow is recognized in the first and second aquifers (from B4 to A7 units) below the Golan Heights (GH) and the Ajlun Plateau. In the superficial B4 aquifer it is directed mainly towards the deep base levels of Lake Tiberias and Lower Yarmuk Gorge (LYG), serving as a discharge area for the gravity-driven ground-water flow systems from surrounding heights.

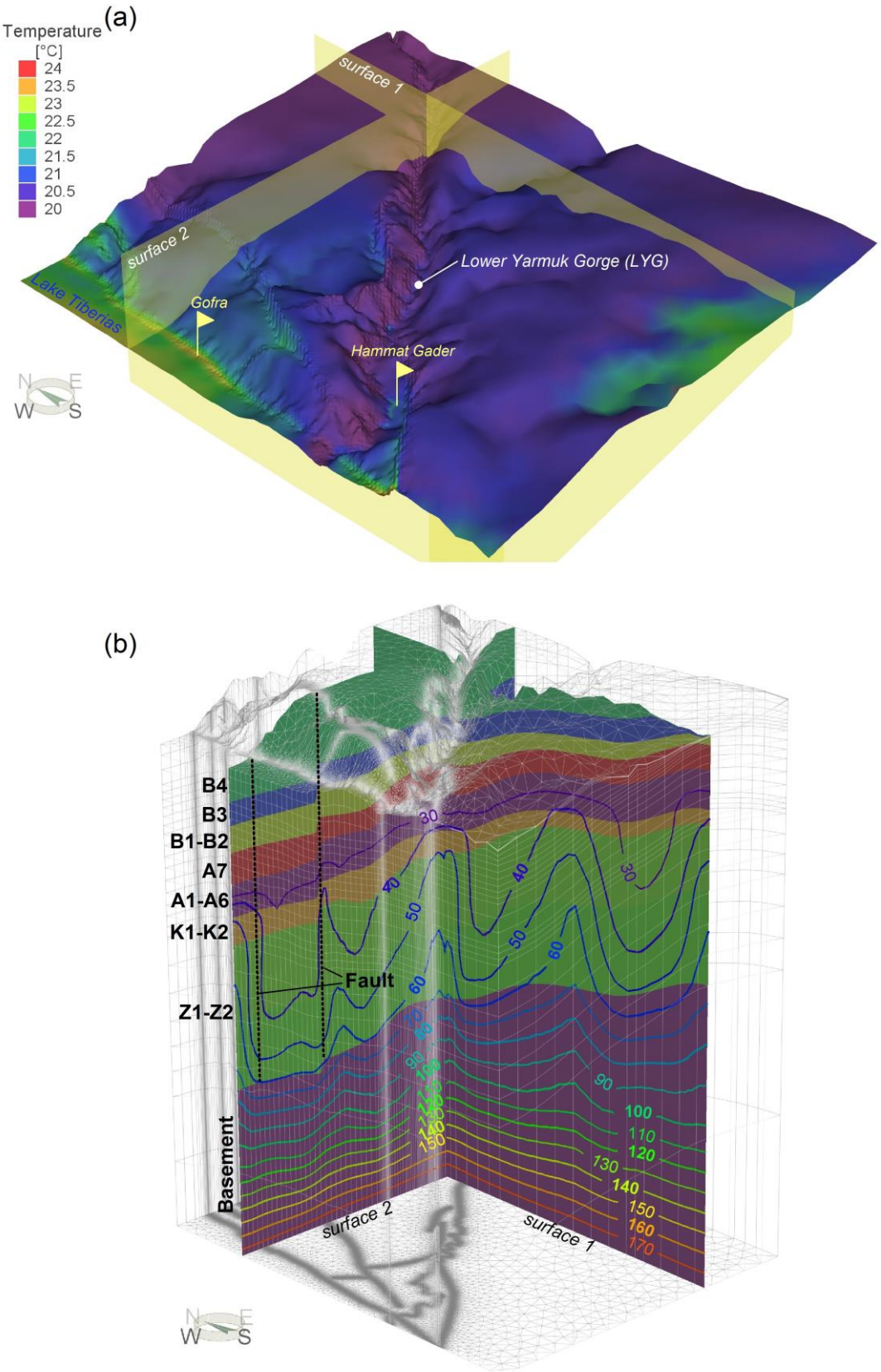


**Figure 7.7: (a)** Temperature distribution of the coupled hydro-thermal model at topographic surface after 1 million of years of simulation. Shaded in yellow the traces of the cross sectional view as in Figure (b) (surface 1 and surface 2). The 2 yellow flags highlight the location of the maximum increase in temperatures, corresponding to the real thermal outflow sites. **(b)** 3D evolution of temperatures in the coupled hydro-thermal model along the two vertical cross sections as in (a) at the end of the transient simulation (i.e. 1 million of years). Vertical exaggeration 5:1. Isoterms values are in °C and hydrogeological units are as in Fig. 7.2.

The effect of topography is smoothed in the second regional aquifer (B1-B2/A7 units), separated from the superficial one by the Maastrichtian aquiclude (B3 unit). As can be seen from Fig. 7.8a, the regional groundwater flow in the second aquifer is mainly E-W and the fault system can be active channelling the flows and extending the time needed to reach model eastern boundary to more than 400 years. Differently a deep-seated highly convective flow is separated from the upper regional flow by the thick Cenomanian aquiclude (A1-A6 units). Multiple squeezed cells develop in the underlying permeable units and buoyant flows induced groundwater motion in a convective-spiral mode. Flow paths in the deepest regional aquifer (i.e. K1-K2 units) have been extracted for the same four points as for the second regional aquifer (Fig. 7.8b). Ascending thermal waters interact with the advective/regional flow, constrained in E-W direction by the boundary conditions, the resulting flow is transversally deviated and undergoes complex helicoidal (spiral-like) patterns (Fig. 7.8b). The coexistence of these flow processes, namely regional and convective flow, results in a mixed convective regime, accordingly the observations of *Magri et al. (2015, 2016)* in their 2D and simplified 3D simulations. The observed mixed convective regime show a long travel time needing more than 25,000 years to reach the model western discharge area (Fig. 7.8b).

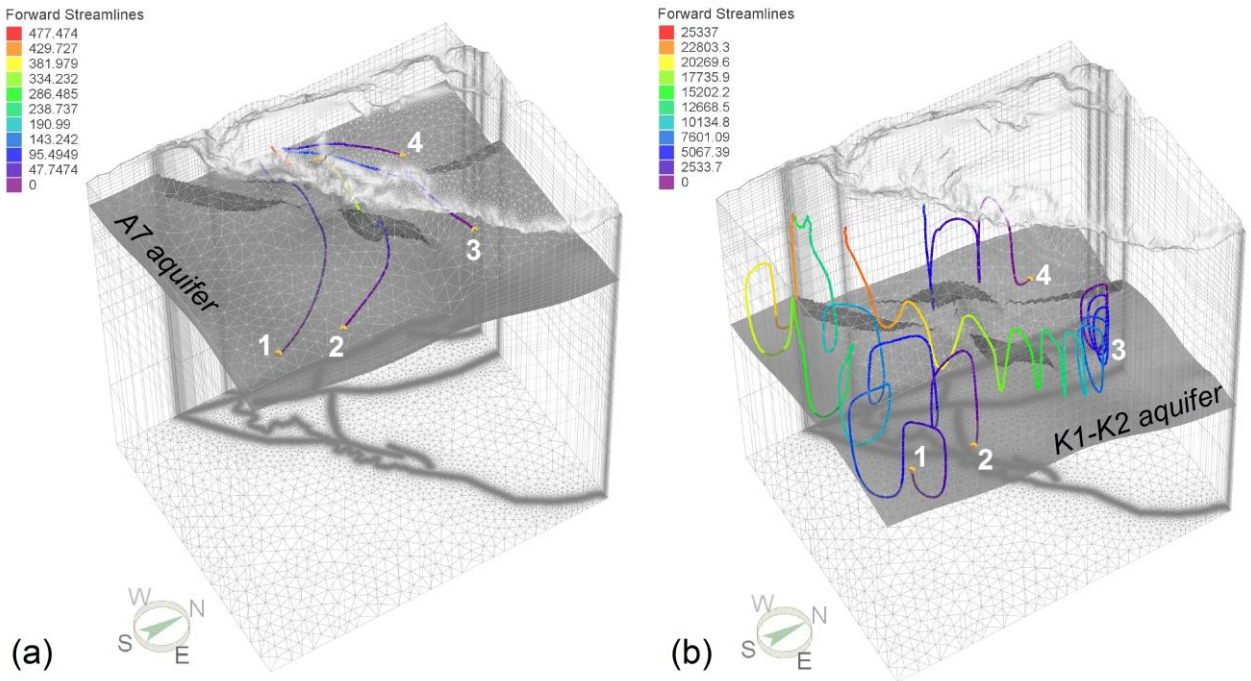


**Figure 7. 8:** Flow trajectories for the coupled hydrothermal model, extracted for 4 selected nodes. Colours of the streamlines depend on the travel time in years. Model vertical exaggeration 5:1. **(a)** Flow paths for the second regional aquifer (A7), representing the regional groundwater flow directed toward the lake Tiberias. **(b)** Flow paths for the same 4 selected nodes in deepest regional aquifer (K1-K1). Helicoidal (spiral-like) pattern represents the mixed convective regime dominating these units.

## 7.6 SUMMARY

This study was aimed to provide useful insights into the possible interactions between deep flow processes in faulted basins, through the construction the first regional 3D hydrogeological model of the entire Tiberian Basin area. The model combines the knowledges acquired from existing geological, hydrogeological and thermal surveys and from previously performed numerical simulations (*Magri et al., 2015, 2016*), with recent structural features based on actual logs and interpreted seismic lines from both Israeli and Jordanian territories (*Inbar et al., 2018*). Using a detailed geological model increases the confidence level for the reproduced geothermal anomalies and the occurrence of complex transboundary flow paths across faults.

Steady-state hydrodynamic simulations are used to calibrate model properties against measured water levels at 22 well points referred to the two main aquifers recognized in the area. Results showed to be extremely sensitive to model hydraulic constraints as superficial recharge of specific aquifer boundary conditions. Nevertheless, a good calibrations was achieved by inverse procedure (PEST) and the alternation of permeable and impervious units, derived from the geological model conceptualization, was preserved. Thermo-hydraulic simulations suggest two different mechanisms of basin-scale groundwater motion influencing the transfer of heat: a topography-driven and a buoyancy-driven flow. The occurrence of these two flow processes is strongly conditioned by the hydraulic properties of the selected formation, as the Mastrichtian (B3) and the Cenomanian (A1-A6) aquicludes isolated the convective domains. The two flow patterns tend to interact only when a permeable horizon is affected by the heat-flow input. In the latter case, realized for example in the deepest regional aquifer (K1-K2), the resulting mixed convective thermal flow is helicoidal and transient. Therefore, from a thermal point of view, these results support the hypothesis of crossing flow paths, resulting from the coexistence of convection, within or without the faults, and additional flow fields that can be induced by topography gradients or by local thermal convection in permeable aquifers below regional aquicludes.

Nevertheless, even if the observed global thermal trend of the area has been simulated, i.e. increase in recorded temperature below the LYG and on the eastern shore of Lake Tiberias, mainly along fault traces, the actual model fail in matching measured spring temperature,

suggesting that faul properties need further calibration calibrated hydraulic model properties prevent thermal water to discharge at the observed temperatures (i.e. 28-50°C range). In this regard, the model presented here should be taken as a reliable starting point for more detailed numerical simulations, focused mainly on the forcing hydraulic parameters (e.g. faults hydraulic conductivities), so as to attain a surface temperature near faulted areas falling within measured ranges. Nevertheless, our results can be considered a satisfactory first attempt to construct a comprehensive regional model of such a complex system, and we argue that a better understanding of the system behaviour has been already achieved through this regional modelling.

# 8. CONCLUDING COMMENTS

## 8.1 SYNTHESIS OF THE STUDIED GEOTHERMAL SYSTEMS

### 8.1.1 The Bormio hydrothermal system

The Bormio hydrothermal system is located in the Upper Valtellina Valley (Central Alps, Italy), within the Penninic and Austro-Alpine sectors of the Alps. This area is an historical Italian thermal site, where ten geothermal springs discharge from dolostones located close to the regional Zebrù thrust - Glorenza fault system. The Bormio area is recognized as a typical alpine low enthalpy geothermal system in normal heat-flow condition. Thermal waters, currently exploited by two thermal establishments, are heated in deep circulation systems and ascend vigorously through permeable regional structures, with temperatures in the 35-40 °C range. The hydraulic and thermal behaviour of this alpine groundwater system was strongly influenced by Quaternary glaciations in terms of permafrost conditions or deposition of impermeable subglacial tills on valley bottom and flanks. In the study area, the effect of the last glaciation was recognized to end around 11,000-12,000 years ago, therefore, this timing was used for the analysis of the model results.

A hydrochemical characterization (major ions and stable isotopes, together with seasonal variations of temperature, electric conductivity and discharge rates) of the discharged thermal waters was used to validate the assumptions formulated in the numerical model. Dominant oxidizing conditions and sulphate water type suggested that Bormio thermal waters are not well mixed with shallow waters. Circulation times, obtained from isotopic data, were in the range of approximately 5-10 years, supporting the hypothesis of a superficial epikarstic and strongly fractured rock mass, accordingly to the field observations. Geothermometers analysis resulted in a thermal reservoir temperatures of about 50-65 °C.

The three-dimensional regional coupled hydrothermal model (ca. 700 $km^2$) was discretized with a highly refined prismatic structured finite-element mesh. Numerical simulations, performed with the commercial code Feflow®, suggested that an unsteady thermal regime is needed to model the reactivation of the system following the end of the Last Glacial Maximum. Results suggested that thermal water flows mainly along damage and shear zones associated to the regional Zebru thrust – Glorenza fault system, and that convection plays a minor role compared to topographic advective heat flow. Results correctly simulated the observed discharge rate of ca. 2,400 L/min and the spring temperatures after ca. 13,000 years

from deglaciation, and showed a complete cooling of the aquifer within a period of approximately 50,000 years. This example gives insights into the influences of deep alpine structures and glaciations on groundwater circulation that control the development of many hydrothermal systems where convective heat flow is subordinated to the regional advective pressure-driven flow.

### 8.1.2 The Castel Giorgio - Torre Alfina geothermal system

The Castel Giorgio - Torre Alfina geothermal reservoir is located in central Italy, at the boundary between the Tuscany, Umbria and Latium regions. From a geothermal point of view, this area (i.e. the Tyrrhenian margin of the Apennines) is one of the most productive and exploited site of whole Italy due to extremely high superficial heat flux anomalies resulting from the intense tectonic and volcanic activity.

The Castel Giorgio - Torre Alfina field is considered a promising, so far not exploited dynamic medium enthalpy reservoir which fluids (pressurized water and gas, mainly $CO_2$) are hosted in a carbonate formation at temperatures ranging between 120 °C - 210 °C. Detailed hydro-geothermal data recognized a strong thermal anomaly associated with a vigorous convective regime. The area has been recently involved in a geothermal exploitation project through a 5 MWe pilot power plant with total reinjection of the fluids in the same producing geological formation.

A three-dimensional reservoir-scale thermo-hydraulic model, covering ca. 293 $km^2$ and discretized into a fully unstructured tetrahedral mesh, was built to sustain this challenging exploitation project. The finite element open-source simulator OpenGeoSys (OGS) was used to reproduce the highly convective undisturbed present-day natural state of the reservoir. Moreover, the commercial finite element Feflow®software was used as additional numerical constraint. The natural state model, calibrated against pressure and temperature data from geothermal wells, resulted in multi-cellular convective patterns that covered the entire geothermal reservoir. Thermal plumes protruded vertically over 3 km at Darcy velocity of about $7*10^{-8}$ m/s. The analysis of the exploitation process demonstrated the sustainability of the planned 50 years production at a flow rate of 1050 t/h. The buoyant circulation within the

geothermal reservoir guaranteed that the tested geothermal doublet distance of 2 km is sufficient to prevent any thermal breakthrough within the estimated operational lifetime.
Results from the two applied software were also compared. OGS and Feflow® returned qualitatively very similar results in terms of convective system behaviour, fitting between simulated and real thermal data and reservoir response to the exploitation scenario. Small differences were identified in predicted peak velocities and temperatures, however these are not affecting the positive final response on possible field exploitation. Model results support the understanding of the Castel Giorgio – Torre Alfina purely convective reservoir, and provide valuable guidelines to the optimal reservoir management and sustainable utilization. These insights can be extended to other dynamic high enthalpy reservoirs worldwide, where pure convective regime is recognized as the dominant heat transfer process, and where an electricity generation exploitation project is planned or currently on-going.

### 8.1.3 Tiberian Basin geothermal field

The Tiberian Basin is located within the Jordan Rift Valley at the border between Israel, Jordan and Syria. Structurally the area is characterized by several en-echelon rhomb-shaped grabens. One of these hosts the Lake Tiberias, the main freshwater resource of the Middle East. On the eastern side of the Lake Tiberias, the Lower Yarmuk Gorge (LYG) allows the outflow of the Yarmuk drainage basin and flows into the Jordan River, a few kilometres south of the lake. On Lake Tiberias shores and along the LYG, thermal waters ascend through fractured aquicludes grouped in clusters of saline and hot springs (temperatures in the range 20 – 60 °C), thus posing a threat to the future sustainability of the lake freshwater resource. Thermal spring clusters are aligned along the regional SW-NE trending normal fault system associated to the Dead Sea Rift opening, suggesting a structural constraint to the thermal outflows.
As the shallow heat anomaly, characterizing the northern Israel and Jordan, makes this field a potential site for production of electricity through geothermal methods, the area was already extensively studied through several 2D and simplified 3D numerical simulations. These works assessed the deep flow system, explained springs behaviour related to the anomalous geothermal gradient, and identified the mixed convection as the dominant heat flow process driving thermal waters below the Lower Yarmuk Gorge.

The first regional 3D hydrothermal model of the entire Tiberian Basin, ca. 565 $km^2$, was then built with the commercial finite element software Feflow®. The model combined the knowledge from existing geological, hydrogeological and thermal surveys, as well as from previously performed numerical simulations. Multiple units, accounting for major aquifers, aquicludes and deep-cutting faults, allowed testing the occurrence of complex transboundary flow paths. Hydrodynamic model results, calibrated against measured water levels at 22 well points referred to the two main aquifers characterizing in the area, showed to be extremely sensitive to model hydraulic constraints, mainly superficial recharge and specific aquifer boundary conditions. Nevertheless, a reasonable agreement between simulated and observed hydraulic heads was achieved, accordingly to the hydraulic model conceptualization. From a thermal point of view, results supported the hypothesis of complex flow paths, derived from the coexistence of free convection, within/without the faults or in permeable aquifers, and additional advective flow fields induced by topography gradients. The mismatch between measured and computed temperatures in correspondence of spring clusters along the LYG and the Tiberias lake shore, was ascribed to the calibrated hydraulic parameters, mainly of the fault system. Further work needs to be done in this regard, using these results as a reliable starting point for more detailed numerical simulations. Nevertheless, this first attempt in regional modelling of such complex system, confirmed the mixed convective behaviour controlling the Tiberian Basin geothermal system evolution and provides useful insights that can be applied in numerical simulations of other convective faulted basins around the world.

## 8.2 CONCLUDING REMARKS ON SIMULATED THERMAL PROCESSES

The thesis concerns the analysis through numerical methods of different fluids related high and low enthalpy geothermal systems. These types of systems are of particular interest because, besides being worldwide widespread, depending on site-specific characteristics they may be suitable for electricity production. Before starting up an exploitation project, assessing the energy potentiality of such systems is strongly recommended due to the high costs involved around geothermal operations. Mathematical models and associated numerical simulations turn out to be helpful tools in this regard. They allow a throughout understanding of the geological-hydrogeological setting, e.g. the system recharge, the hydrological units role

(aquifer-aquiclude distribution), the behaviour of eventually involved structures (faults and fracture network), as well as of the processes responsible for the transfer of heat.

The three modelled systems are grouped by the meteoric origin of the involved fluids, which, in the Bormio and the Tiberian Basin system, discharge at the surface in the form of thermal springs, while in the Castel Giorgio - Torre Alfina field remain confined in the reservoir. On the other hand, the three selected case studies are characterized by substantial differences and a progressively increasing degree of complexity, regarding both the field geological setting and the active thermal regime. In particular, the Bormio hydrothermal system is a typical alpine low enthalpy geothermal field in normal heat-flow condition, where the superficial discharge of thermal waters mainly occurs along the regional Zebru thrust - Glorenza fault system. From modelling results thermal convection plays a minor role compared to topographic advective heat flow. Meteoric waters are heated in deep circulation systems and ascend through the permeable regional fault system with temperatures in the real observed range.

The Castel Giorgio - Torre Alfina geothermal field is an example of promising, medium-enthalpy, fluid-dominated system, for which recently was planned a geothermal exploitation project through a well doublet system. Modelling results fully support field observations: free convection is dominant and a vigorous buoyant circulation, with high Darcy velocities, is confined in the permeable reservoir units. Therefore, the modelled free convective behaviour allows the reservoir to sustain the planned production operational lifetime, with the tested flow rate and production/injection wells configuration preventing thermal breakthrough occurrence.

Lastly, the Tiberian Basin geothermal field, is a valuable example of large-scale groundwater flow coupled to heat transport in a faulted system, and represents the more complicate study case analysed within this thesis. The area has been already extensively studied, also through numerical methods, nevertheless a comprehensive regional 3D numerical model was still missing. This example somehow groups the characteristics of the previous study cases: a complex regional fault system, a shallow thermal anomaly, the upwelling of thermal waters, and an active convective regime, are all characteristics that make this field a potential site for production of electricity through geothermal methods. Modelling results correctly reproduce the coalescence of regional/advective and free convective heat flows, resulting in a helicoidal

and transient mixed convective behaviour, accordingly to what observed in previous 2D simulations. Nevertheless, the applied hydraulic settings (boundary conditions and model properties) prevent the onset of thermal convection along the fault planes, follows that water temperatures in correspondence of surface thermal spring clusters is far from monitored values. In this regard, the first results of this model can be considered as a starting point for further calibration processes aimed to fulfil this mismatch.

## 8.3 CONCLUDING REMARKS ON APPLIED MODELLING APPROACH AND CODES

Developing reliable numerical simulations for geothermal aquifer is not an easy task, mainly due to the complex nature of the geothermal related scientific problems. In the last years, big steps have been done in this direction: advanced computer technologies allows actual modelling of complex processes involved in the coupling between groundwater flow and heat transfer, which was not possible a few years ago. Nevertheless, a clear and standardised modelling approach for geothermal systems has not been accepted worldwide since geothermal systems occur in a variety of geological, physical, chemical and thermodynamic conditions.

An attempt in the direction of establishing a reliable and verified modelling approach for numerical simulations of geothermal aquifers, is proposed within the present work. The same modelling approach was applied for all the three analysed study cases, even though they involve quite different processes in terms of heat transfer phenomena. Firstly, the pure hydrodynamic part of the problem has been separated and solved individually. Depending on site-specific characteristics and data availability, the calibration of the hydrodynamic model has been performed manually (e.g. Bormio and Castel Giorgio – Torre Alfina cases) or through automatic PEST inverse procedure (e.g. Tiberian Basin case). The calibration process, which in hydrodynamic models involves estimation of mainly hydraulic conductivity values, is mandatory to verify if model is producing simulation results that suit to real-world conditions. Calibration was performed against measured spring discharge rates (e.g. Bormio case), measured well pressure profiles (e.g. Castel Giorgio - Torre Alfina case), or measured water levels at well points (e.g. Tiberian Basin). Only when a reasonable calibration of the hydraulic problem has been achieved, the coupled groundwater flow and heat transfer processes can

be simulated together. The coupled hydrothermal models needs to be calibrated for the thermal part itself, usually involving different parameters, such as the thermal conductivity or material porosity. Thermal part of the coupled hydrothermal simulations was calibrated against available thermal data sets, specifically: spring discharge temperatures (e.g. Bormio and Tiberian Basin cases) or measured temperature profiles in real geothermal wells (e.g. Castel Giorgio – Torre Alfina case). This approach turns out to be particularly successful whenever is needed to model separately the advective and the convective regimes, as in the Bormio and Tiberian Basin study cases. Whereas, Castel Giorgio - Torre Alfina case study is a slightly different example, as the model was built to test a geothermal exploitation project in a free convective reservoir. In this case, a specific two steps exploitation focused modelling approach was applied in addition to what previously explained. A "Natural state simulation" reproduced the present-day thermo-hydraulic dynamic conditions of the geothermal reservoir, without extraction or injection of fluid, while the "Exploitation process simulation" assessed the impacts of the exploitation process on the natural geothermal flow of the reservoir, therefore including the well doublet system.

When a fracture aquifer is invoked, as in the case of Bormio and the Tiberian Basin, faults have been modelled using the Equivalent Porous Media approach (EPM), i.e. permeable units extending from the basement to the top. This approach has been widely used for the description of regional flow systems in fractured rocks providing satisfactory results. In this work, such choice was dictated by the lack of structural inputs for fault geometry that are required to apply other numerical approaches, such as the Discrete Fracture Network (DFN).

Various software have been applied to built the models (i.e. Petrel, FracMan, GMS, Matlab, Midas GTS NX) and run the numerical simulations (i.e. Feflow® and OpenGeoSys). These mathematical and numerical codes turn out to be helpful tools in gaining remarkable insights about the three study cases, nevertheless achieved reliable results are tied tightly to a prior thorough framing of the problem. In this regard, any numerical simulation have to be preceded by an accurate study of the selected site. Geological investigations represent the basis of all research programs in the domain of geothermics, and they must be undertaken systematically for every type of geothermal project. Moreover, the occurrence of thermal spring systems is often related to changes in the geological conditions generating hydraulic

contrasts at depth. The more complicated the geological structure is, the longer the time has to be devoted in understanding these structures, because it allows formulating reliable assumptions about the heat and flow systems, needed for the numerical simulations.

Numerical simulations, that in the present work have been performed through two finite element codes: the commercial Feflow® software, applied in all the three study cases, and the open-source OpenGeoSys code, used for the Castel Giorgio – Torre Alfina simulations. This open-source code proved to be a powerful option in terms of results and performances, offering some precious advantages when compared to the well know commercial code Feflow®. These include: a continuous update of the code repository, an active community participating in code debugging and providing new benchmarks for code testing, frequently organized training courses and teaching activities, and ad-hoc compilation of code portions. Therefore, following the guidelines of the OpenGeoSys community to foster test cases with increasing complexity for method development and code comparison, is now planned to repeat the simulations of the Tiberian Basin geothermal field with the OpenGeoSys code. This complex study case, representing a valuable example of large-scale groundwater flow coupled to heat transport in a faulted system, seems the ideal candidate to demonstrate once again the competitiveness of the OpenGeoSys code for solving numerical simulations of hydro-thermal processes in porous and fractured media.

# 9. BIBLIOGRAPHY

Aaheim, H., & Bundschuh, J. (2002). *The value of geothermal energy for developing countries*. Geothermal Energy Resources for Developing Countries, Lisse, Swets&Zeitlinger, 37-51.

Abbo, H., Shavit, U., Markel, D., & Rimmer, A. (2003). *A numerical study on the influence of fractured regions on lake/groundwater interaction; the Lake Kinneret (Sea of Galilee) case*. Journal of hydrology, 283(1), 225-243.

Abu-Jaber, N., & Ismail, M. (2003). *Hydrogeochemical modeling of the shallow groundwater in the northern Jordan Valley*. Environmental Geology, 44(4), 391-399.

Acocella, V., & Funiciello, R. (2006). *Transverse systems along the extensional Tyrrhenian margin of central Italy and their influence on volcanism*. Tectonics, 25(2).

Albu, M., Banks, D., & Nash, H. (1997). *History of mineral and thermal waters. In Mineral and thermal groundwater resources* (pp. 3-20). Springer Netherlands.

Al-Khoury, R. (2011). *Computational modeling of shallow geothermal systems*. CRC Press.

Allegrini, G., Luccioli, F., & Trivella, A. (1992). *Industrial uses of geothermal fluids at Larderello*. Geothermics, 21(5-6), 623-630.

Allis, R. G., & Yusa, Y. (1989). *Fluid flow processes in the Beppu geothermal system, Japan*. Geothermics, 18(5-6), 743-759.

Anderson, R. N., Hobart, M. A., & Langseth, M. G. (1979). *Geothermal convection through oceanic crust and sediments in the Indian Ocean*. Science, 204(4395), 828-832.

Anderson, M. P., Woessner, W. W., & Hunt, R. J. (2015). *Applied groundwater modeling: simulation of flow and advective transport*. Academic press.

Andrews, I. J. (1992). *Cretaceous and Paleogene lithostratigraphy in the subsurface of Jordan*. Ministry of Energy and Mineral Resources.

Antics, M.A. (1997). *Computer simulation of the Oradea geothermal reservoir*. Proceedings of the 22nd Workshop on Geothermal Reservoir Engineering, Stanford University, Stanford, California, 27–29 January 1997, pp. 491–495.

Antics, M., Bertani, R., & Sanner, B. (2013). *Summary of EGC 2013 country update reports on geothermal energy in Europe*. Proceedings of the EGC2013, 3(6).

Antunez, E.U., Bodvarsson, G.S., Walters, M.A. (1994). *Numerical simulation study of the Northwest Geysers geothermal field, a case study of the Coldwater Creek steamfield*. Geothermics 23 (2), 127–141.

Antunez, E.U., Sanyal, S.K., Menzies, A.J., Naka, T., Takeuchi, R., Iwata, S., Saeki, Y., Inoue, T. (1990). *Forecasting well and reservoir behavior using numerical simulation, Uenotai*

*geothermal field, Akita Prefecture, Japan*. Transactions Geothermal Resources Council 14, 1255–1262.

Appelo, C. A. J., & Postma, D. (2004). *Geochemistry, groundwater and pollution*. CRC press.

Arad, A., & Bein, A. (1986). *Saline-versus freshwater contribution to the thermal waters of the northern Jordan Rift Valley, Israel*. Journal of Hydrology, 83(1-2), 49-66.

Arnórsson, S. (2000). *Isotopic and chemical techniques in geothermal exploration, development and use*. International Atomic Energy Agency, 109-111.

Axelsson, G., Bjornsson, G. (1993). *Detailed three-dimensional modeling of the Botn hydrothermal system in N-Iceland.* Proceedings of the 18th Workshop on Geothermal Reservoir Engineering, Stanford University, Stanford, California, 26–28 January 1993, pp. 159–166.

Baietto, A., Cadoppi, P., Martinotti, G., Perello, P., Perrochet, P., & Vuataz, F. D. (2008). *Assessment of thermal circulations in strike-slip fault systems: the Terme di Valdieri case (Italian western Alps)*. Geological Society, London, Special Publications, 299(1), 317-339.

Baldi, P., Bellani, S., Ceccarelli, A., Fiordelisi, A., Squarci, P., & Taffi, L. (1994). *Correlazioni tra le anomalie termiche ed altri elementi geofisici e strutturali della toscana meridionale*. Studi Geologici Camerti, Volume Speciale 1994-1, 139-149.

Baldwin, S. F. (2002). *Renewable energy: progress and prospects*. *Physics Today*, *55*(4), 62.

Barberi, F., Buonasorte, G., Cioni, R., Fiordelisi, A., Foresi, L., Iaccarino, S., Laurenzi, M.A., Sbrana, A., Vernia, L., Villa, I.M. (1994). *Plio-Pleistocene geological evolution of the geothermal area of Tuscany and Latium*. Mem. Descr. Carta Geol. Ital. 49, 77–133.

Barelli, A., Bertani, R., Cappetti, G., Ceccarelli, A. (1995a). *An update on Travale – Radicondoli geothermal field*. In: Proceedings World Geothermal Congress 1995, Florence, Italy, pp. 1581–1586.

Barelli, A., Cappetti, G., Stefani, G. (1995b). *Optimum exploitation strategy at Larderello-Valle Secolo*. In: Proceedings World Geothermal Congress 1995, Florence, Italy, pp. 1779–1783.

Barelli, A., Cappetti, G., Stefani, G. (1995c). *Results of deep drilling in the Larderello–Travale/Radicondoli geothermal area*. In: Proceedings World Geothermal Congress 1995, Florence, Italy, pp. 1275–1278.

Barelli, A., Bertini, G., Buonasorte, G., Cappetti, G., Fiordelisi, A. (2000). *Recent deep exploration results at the margins of the Larderello–Travale geothermal system*. In: Proceedings World Geothermal Congress 2000, Kyushu-Tohoku, Japan, pp. 965–970.

Bartole, R. (1995). *The North Tyrrhenian–Northern Apennines post-collisional system: constraints for a geodynamic model*. Terra Nova, 7(1), 7-30.

Barton, C. A., Zoback, M. D., & Moos, D. (1995). *Fluid flow along potentially active faults in crystalline rock*. Geology, 23(8), 683-686.

Batini, F., Brogi, A., Lazzarotto, A., Liotta, D., Pandeli, E. (2003). *Geological features of the Larderello–Travale and Mt. Amiata geothermal areas (southern Tuscany, Italy)*. Episodes 26, pp. 239–244.

Bear, J. (1972). *Dynamics of Fluids in Porous Media.* Dover Publications New York Google Scholar.

Bear, J. (2012). *Hydraulics of groundwater*. Courier Corporation.

Bear, J., & Bachmat, Y. (1990). *Introduction to Modeling of Transport Phenomena in Porous Media.* Kluwer Academic Publishers Dordrecht Google Scholar.

Bear, J., & Verruijt, A. (1987). *Modelling groundwater flow and pollution*. D. Riedel Publ. Co.

Bear, J., Tsang, C. F., & Marsily, G. D. (1993). *Flow and contaminant transport in fractured rocks*.

Bellani, S., Brogi, A., Lazzarotto, A., Liotta, D., & Ranalli, G. (2004). *Heat flow, deep temperatures and extensional structures in the Larderello Geothermal Field (Italy): constraints on geothermal fluid flow*. Journal of Volcanology and Geothermal Research, 132(1), pp. 15-29.

Ben-Avraham, Z., Hänel, R., & Villinger, H. (1978). *Heat flow through the Dead Sea rift*. Marine Geology, 28(3-4), 253-269.

Ben-Gay, Y., Reznikov, M. (1997). *Multichannel Seismic Survey at the Sea of Galilee*. 733/167/97, Geophysical Institute of Israel.

Benoit, D. (1999). *Conceptual models of the Dixie Valley, Nevada geothermal field*. Transactions-Geothermal Resources Council, 505-512.

Bergelson, G., Nativ, R., & Bein, A. (1999). *Salinization and dilution history of ground water discharging into the Sea of Galilee, the Dead Sea Transform, Israel*. Applied Geochemistry, 14(1), 91-118.

Berra, F. (1994). *Stratigrafia e paleogeografia del Triassico superiore delle falde Ortles e Quattervals (Austroalpino superiore) in Lombardia*. PhD Thesis, Università degli Studi - Milano, Dipartimento di Scienze della Terra.

Bertani, R., Cappetti, G. (1995). *Numerical simulation of the Monteverdi zone (western border of the Larderello geothermal field)*. Proceedings World Geothermal Congress '95, Florence, 18–31 May 1995, pp. 1735–1740.

Bertani, R. (2005a). *World geothermal generation 2001-2005: State of the art*. In Proceedings World Geothermal Congress (Vol. 2005).

Bertani, R. (2005b). *World geothermal power generation in the period 2001–2005*. Geothermics, 34(6), 651-690.

Bertani, R. (2006). *World geothermal power generation 2001–2005.* GRC BulletinMay–June 2006 006, 89–111.

Bertani, R. (2007). *World geothermal generation in 2007*. GHC Bulletin, 7, 19.

Bertani, R. (2010). *Geothermal power generation in the world 2005–2010 update report*. In: Proceedings World Geothermal Congress, Bali, Indonesia, April25–30, 2010.

Bertani, R. (2012). *Geothermal power generation in the world 2005–2010 update report*. Geothermics, 41, 1-29.

Bertani, R. (2016). *Geothermal power generation in the world 2010–2014 update report*. Geothermics, 60, 31-43.

BGR (Deutsche Bundesanstalt für Geowissenschaften und Rohstoffe), WAJ (Water Authority of Jordan) (1993). *Groundwater Resources of Northern Jordan. Structural Features of the Main Hydrogeological Units in Northern Jordan, vol. 3*. BGR-Archive No. 112708, Amman, Jordan.

BGR (Deutsche Bundesanstalt für Geowissenschaften und Rohstoffe), WAJ (Water Authority of Jordan) (1997). *Groundwater Resources of Northern Jordan. Groundwater Modelling. Three Dimensional Groundwater Model of Northern Jordan, vol. 5, part 1*. Amman, Jordan.

BGR (Deutsche Bundesanstalt für Geowissenschaften und Rohstoffe), WAJ (Water Authority of Jordan) (2001). *Groundwater Resources of Northern Jordan. Contributions to the Hydrogeology of Northern Jordan, vol. 4*. Ministry of Water and Irrigation, Amman, Jordan.

Bianchetti, G., Roth, P., Vuataz, F. D., & Vergain, J. (1992). *Deep groundwater circulation in the Alps: Relations between water infiltration, induced seismicity andthermal springs. The case of Val d'Illiez, Wallis, Switzerland*. Eclogae Geologicae Helvetiae, 85(2), 291-305.

Bini, A., Buoncristiani, J.,F., Couterrand, S., Ellwanger, D., Felber, M., Florineth, D., Graf, H.,R., Keller, O., Kelly, M,, Schlüchter, C., Schoeneich, P. (2009). *Switzerland during the Last Maximal 1:500 000*.

Bjørlykke, K., Mo, A., & Palm, E. (1988). *Modelling of thermal convection in sedimentary basins and its relevance to diagenetic reactions*. Marine and Petroleum Geology, 5(4), 338-351.

Blessent, D., Jørgensen, P. R., & Therrien, R. (2014). *Comparing discrete fracture and continuum models to predict contaminant transport in fractured porous media*. Groundwater, 52(1), 84-95.

Blöcher, M. G., Zimmermann, G., Moeck, I., Brandt, W., Hassanzadegan, A., & Magri, F. (2010). *3D numerical modeling of hydrothermal processes during the lifetime of a deep geothermal reservoir.* Geofluids, 10(3), 406-421.

Boccaletti, M., Gianelli, G., & Sani, F. (1997). *Tectonic regime, granite emplacement and crustal structure in the inner zone of the Northern Apennines (Tuscany, Italy): a new hypothesis*. Tectonophysics, 270(1), 127-143.

Bodri, B., & Rybach, L. (1998). *Influence of topographically driven convection on heat flow in the Swiss Alps: a model study*. Tectonophysics, 291(1-4), 19-27.

Bodvarsson, G. S., Pruess, K., Stefansson, V., Steingrimsson, B., Bjornsson, S., Gunnarsson, A., Gunnlaugsson, E. (1986). *Natural state model of the Nesjavellir geothermal field, Iceland* (No. SGP-TR-93-17). Lawrence Berkeley National Laboratory (LBNL), Earth Sciences Division, Berkeley, CA; National Energy Authority of Iceland, Reykjavik, Iceland; Reykjavik Municipal District Heating Service, Reykjavik, Iceland.

Boeckli, L., Brenning, A., Gruber, S., & Noetzli, J. (2011). *A statistical permafrost distribution model for the European Alps.* The Cryosphere Discussions, 5, 1419-1459.

Boldizsar, T. (1964). *Heat flow in the Hungarian basin.* Nature, 202(4939), 1278-1280.

Bonini, M., & Sani, F. (2002). *Extension and compression in the Northern Apennines (Italy) hinterland: Evidence from the late Miocene-Pliocene Siena-Radicofani Basin and relations with basement structures*. Tectonics, 21(3).

Bories, S. A., & Combarnous, M. A. (1973). *Natural convection in a sloping porous layer*. Journal of Fluid Mechanics, 57(1), 63-79.

Bowen, R. (1989). *Geothermal resources*. London and New York: Elsevier Applied Science, Second Edition.

Brassington, R. (2017). *Field hydrogeology*. John Wiley & Sons.

Bredehoeft, J. D., & Norton, D. L. (1990). *Mass and energy transport in a deforming earth's crust*. The role of fluids in crustal processes, 27-41.

Brogi, A. (2006). *Neogene extension in the Northern Apennines (Italy): insights from the southern part of the Mt. Amiata geothermal area*. Geodinamica Acta, 19(1), 33-50.

Brogi, A., Lazzarotto, A., Liotta, D., Ranalli, G. (2003). *Extensional shear zones as imaged by reflection seismic lines: The Larderello geothermal field (central Italy)*. Tectonophysics 363: pp. 127–139.

Brogi, A., Lazzarotto, A., Liotta, D., Ranalli, D., CROP–18 Working Group (2005). *Crustal structures in the geothermal areas of southern Tuscany (Italy): insights from CROP-18 deep seismic reflections lines*. J Volcanol Geotherm Res 148: pp. 60–80.

Brown, D. W., Duchane, D. V., Heiken, G., & Hriscu, V. T. (2012). *Mining the earth's heat: hot dry rock geothermal energy*. Springer Science & Business Media.

Brun, J.P., Gutscher, M.A., DEKORP-ECORS teams, (1992). *Deep crustal structure of the Rhine Graben from DEKORS- ECORS seismic reflection data: A summary*. Tectonophysics 208, pp. 139-147.

Brunet, C., Monié, P., Jolivet, L., Cadet, J. P. (2000). *Migration of compression and extension in the Tyrrhenian Sea, insights from 40Ar/39Ar ages on micas along a transect from Corsica to Tuscany*. Tectonophysics 321: pp. 127–155.

Bundschuh, J. (2010). *Introduction to the numerical modeling of groundwater and geothermal systems: fundamentals of mass, energy and solute transport in poroelastic rocks*. CRC Press.

Bundschuh, J., Alvarado, G. E., Rodriguez, J. A., Roldán, A. R., Palma, J. C., Zuñíga, A., Reyes, E., Castillo, G. & Salgado, R. M. (2002). *Resources and policy of geothermal energy in the Central America. Geothermal energy for developing countries*. AA Balkema, Leiden, The Netherlands, pp. 313-364.

Bundschuh, J., & Alvarado, G. E. (Eds.). (2007). *Central America: Geology, resources and hazards (2 Volumes).* Balkema Publisher, Lisse, The Netherlands, pp. 869–894

Bundschuh, J., & Coviello, M. (2002). *Geothermal energy: capacity building and technology dissemination. Geothermal energy for developing countries*. Balkema Publisher, Lisse, The Netherlands, 77-90.

Buonasorte, G., Fiordelisi, A., Pandeli, E., Rossi, U., Sollevanti, F. (1987). *Stratigraphic correlations and structural setting of the pre-neoautochthonous sedimentary sequences of Northern Latium*. Periodico di Mineralogia, 56, pp. 111-122.

Buonasorte, G., Cataldi, R., Ceccarelli, A., Costantini, A., d'Offizi, S., Lazzarotto, A., & Bertrami, R. (1988). *Ricerca ed esplorazione nell'area geotermica di Torre Alfina (Lazio-Umbria)*. Bollettino della Società Geologica Italiana, 107(2), 265-337.

Buonasorte, G., Pandeli, E., Fiordelisi, A. (1991). *The Alfina 15 Well; deep geological data from northern Latium (Torre Alfina geothermal area)*. Bollettino della Società Geologica Italiana, 110(3-4), pp. 823-831.

Buonasorte, G., Cameli, G. M., Fiordelisi, A., Parotto, M., Perticone, I. (1995). *Results of geothermal exploration in Central Italy (Latium-Campania)*. In *Proceedings of the World Geothermal Congress, Florence, Italy*, pp. 18-31.

Burgassi, P. D. (1999). *Historical outline of geothermal technology in the Larderello region to the middle of the 20th century*. Stories from a Heated Earth, 195-219.

Burns, E. R., Williams, C. F., Ingebritsen, S. E., Voss, C. I., Spane, F. A., & DeAngelo, J. (2015). *Understanding heat and groundwater flow through continental flood basalt provinces: insights gained from alternative models of permeability/depth relationships for the Columbia Plateau, USA.* Geofluids, 15(1-2), 120-138.

Caine, J. S., Evans, J. P., & Forster, C. B. (1996). *Fault zone architecture and permeability structure*. Geology, 24(11), 1025-1028.

Calmbach, L. (1997). *AquaChem computer code-version 3.7*. 42. Waterloo, Ontario, Canada N2L, 3L3.

Caltagirone, J. P. (1975). *Thermoconvective instabilities in a horizontal porous layer*. Journal of Fluid Mechanics, 72(2), 269-287.

Caputo, M. (1999). *Diffusion of fluids in porous media with memory*. Geothermics, 28(1), 113-130.

Carapezza, M. L., Ranaldi, M., Gattuso, A., Pagliuca, N. M., & Tarchini, L. (2015). *The sealing capacity of the cap rock above the Torre Alfina geothermal reservoir (Central Italy) revealed by soil $CO_2$ flux investigations*. Journal of volcanology and geothermal research, 291, 25-34.

Carmignani, L., Decandia, F.A., Fantozzi, P.L., Lazzarotto, A., Liotta, D., Meccheri, M., (1994). *Tertiary extensional tectonics in Tuscany (Northern Apennines, Italy).* Tectonophysics 238, pp. 295-315.

Carmignani, L., Lazzarotto, A. (2004). *Carta geologica della Toscana / geological Map of Tuscany (Italy) 1: 250000.* Regione Toscana, Direzione delle Politiche Territoriali e Ambientali-Servizio geologico.

Carminati, E., Doglioni, C. (2005). *Mediterranean tectonics*. *Encyclopedia of geology*, *2*, pp. 135-146.

Carslaw, H. S., Jaeger, J. C. (1959). *Heat in solids* (Vol. 1). Clarendon Press, Oxford, pp. 342.

Cataldi, R. (1999). *The year zero of geothermics*. Stories from a Heated Earth, 7-17.

Cataldi, R., & Rendina, M. (1973). *Recent discovery of a new geothermal field in Italy: Alfina. Geothermics*, *2*(3), 106-116.

Cataldi, R., & Burgassi, P. D. (1999). *Flowering and decline of thermal bathing and other uses of natural heat in the Mediterranean area, from the birth of Rome to the end of the first millennium.* Stories from a heated earth. Our geothermal heritage. GRC & IGA, Sacramento, Ca, 147-163.

Cataldi, R., Hodgson, S. F., & Lund, J. W. (1999). *Stories from a heated earth: our geothermal heritage (Vol. 19)*. Geothermal Resources Council.

Chandrasekharam, D., & Bundschuh, J. (2002). *Geothermal energy resources for developing countries.* CRC Press.

Chandrasekharam, D., & Bundschuh, J. (2008). *Low-enthalpy geothermal resources for power generation (Vol. 172).* Leiden: CRC Press.

Change, C. (2007). *Synthesis Report.* Contribution of Working Groups I, II and III to the Fourth Assessment Report of the Intergovernmental Panel on Climate Change.

Chapman, D. S., & Pollack, H. N. (1975). *Global heat flow: a new look*. Earth and Planetary Science Letters, 28(1), 23-32.

Chapron, E. (1999). *Controles climatiques et sismo-tectonique de la sedimentation lacustre dans l'avant-pays alpin (Lac Du Bourget, Leman) durant la quaternaire recent*. PhD Thesis, Université de Lille 1, Villeneuve-d'Ascq, France (Université de soutenance).

Charléty, J., Cuenot, N., Dorbath, L., Dorbath, C., Haessler, H., & Frogneux, M. (2007). *Large earthquakes during hydraulic stimulations at the geothermal site of Soultz-sous-Forêts.* International Journal of Rock Mechanics and Mining Sciences, 44(8), 1091-1105.

Chen, W., Ghaith, A., Park, A., & Ortoleva, P. (1990). *Diagenesis through coupled processes: modeling approach, self-organization, and implications for exploration*.

Chiarabba, C., Amato, A., Fiordelisi, A., (1995). *Upper crustal tomographic images of the Amiata–Vulsini geothermal region, central Italy.* J. Geophys. Res. 100, 4053–4066.

Chiodini, G., Frondini, F., Ponziani, F., (1995). *Deep structures and carbon dioxide degassing in Central Italy.* Geothermics 24, 81–94.

Clark, S. P., & Niblett, E. R. (1956). *Terrestrial heat flow in the Swiss Alps*. Geophysical Journal International, 7(s4), 176-195.

Clerici, A., & Sfratato, F. (2008). *Stima della conducibilità idraulica in ammassi rocciosi.* Italian J Eng Geol Environ, 1, 67-76.

Colucci and Guandalini (2014). *Modelli geologici e simulazione numerica di sistemi geotermici*. Rapporto di Ricerca di Sistema. http://doc.rse-web.it/doc/doc-sfoglia/15000985-316054/15000985-316054.html

Conti, P. (1994). *La falda Austroalpina dell'Ortles e l'evoluzione tettonica delle Dolomiti dell'Engadina (Svizzera-Italia) (con 17 tavole).* Mem. Descr. Carta Geol d'It 53, p 104.

Cosentino, D., Cipollari, P., Marsili, P., Scrocca, D. (2010). *Geology of the central Apennines: a regional review.* Journal of the Virtual Explorer. 36, paper 12.

Costantini, A., Ghezzo, C., Lazzarotto, A. (1984). *Carta geologica dell'area geotermica di Torre Alfina (prov. di Siena--Viterbo--Terni).* Ente Nazionale per l'Energia Elettrica (ENEL), Unità Nazionale Geotermica – Pisa. Cartografia S.EL.C.A., Firenze.

Craig, H. (1963). *The isotopic geochemistry of water and carbon in geothermal areas.* In Nuclear geology on geothermal areas, Spoleto Conference Proceedings, 1963 (pp. 17-53).

Craig, H. (1966). *Isotopic composition and origin of the Red Sea and Salton Sea geothermal brines.* Science, 154(3756), 1544-1548.

Cruchet, M. (1985). *Influence de la decompression sur le comportement hydrogeologique des massifs cristallins en basse Maurienne (Savoie, France).* Géologie Alpine, 61, 65-73.

Cruse, T. A., & Rizzo, F. J. (Eds.). (1975). *Boundary-integral Equation Method: Computational Applications in Applied Mechanics.* Presented at 1975 Applied Mechanics Conference, the Rensselaer Polytechnic Institute, Troy, New York, June 23-25, 1975 (Vol. 11). American Society of Mechanical Engineers.

Dallmeyer, R. D., & Liotta, D. (1998). *Extension, uplift of rocks and cooling ages in thinned crustal provinces: the Larderello geothermal area (inner Northern Apennines, Italy)*. Geological Magazine, 135(2), 193-202.

Davies, G. F. (1980). *Thermal histories of convective Earth models and constraints on radiogenic heat production in the Earth*. Journal of Geophysical Research: Solid Earth, 85(B5), 2517-2530.

Davies, J. H. (2013). *Global map of solid Earth surface heat flow*. Geochemistry, Geophysics, Geosystems, 14(10), 4608-4622.

De Caro, M., Crosta, G. B., Frattini, P., Perico, R., and Volpi, G. (2017). *Hydrofacies reconstruction of glaciofluvial aquifers and groundwater flow modelling in a densely urbanized area under changing climatic conditions.* Hydrol. Earth Syst. Sci. Discuss., https://doi.org/10.5194/hess-2017-555, in review.

Decandia, F. A., Lazzarotto, A., Liotta, D., Cernobori, L., Nicolich, R. (1998). *The CROP 03 traverse: insights on post-collisional evolution of Northern Apennines.* Mem. Soc. Geol. It, 52, pp. 427-439.

Della Vedova, B., Bellani, S., Pellis, G., Squarci, P. (2001). *Deep temperatures and surface heat flow distribution.* In: Vai GB, Martini IP (eds) Anatomy of an orogen: the Apennines and adjacent Mediterranean basins. Kluwer, Dordrecht, pp 65–76.

Della Vedova, B., Vecellio, C., Bellani, S., & Tinivella, U. (2008). *Thermal modelling of the Larderello geothermal field (Tuscany, Italy).* International Journal of Earth Sciences, 97(2), 317-332.

Deming, D. (1993). *Regional permeability estimates from investigations of coupled heat and groundwater flow, North Slope of Alaska*. Journal of Geophysical Research: Solid Earth, 98(B9), 16271-16286.

Deming, D., Sass, J. H., Lachenbruch, A. H., & de Rito, R. F. (1992). *Heat flow and subsurface temperature as evidence for basin-scale ground-water flow, North Slope of Alaska*. Geological Society of America Bulletin, 104(5), 528-542.

Dershowitz, W., Lee, G., Geier, J., Foxford, T., La Pointe, P., Thomas, A. (1998). *FracMan: interactive discrete fracture data analysis, geometric modeling, and exploration simulation*. User documentation, Seattle, WA, Golder Associates Inc.

Dickson, M. H., & Fanelli, M. (2013). *Geothermal energy: utilization and technology*. Routledge.

Diersch, H. J. (2014). *FEFLOW Finite Element Modeling of Flow, Mass and Heat Transport in Porous and Fractured Media*. Springer-Verlag Berlin Heidelberg, ISBN 978-3-642-38738-8.

Dietrich, P., Helmig, R., Sauter, M., Hötzl, H., Köngeter, J., & Teutsch, G. (2005). *Flow and transport in fractured porous media.* Springer Science & Business Media.

Diodato, D. M. (1994). *A compendium of fracture flow models*. Work sponsored by US Department of Defense, United States Army, Europe, Combat Maneuver Training Center, Hohenfels, Germany.

Doherty, J. (1994). *PEST: a unique computer program for model-independent parameter optimisation.* Water Down Under 94: Groundwater/Surface Hydrology Common Interest Papers; Preprints of Papers, 551.

Doveri, M., Lelli, M., Marini, L., Raco, B., (2010). *Revision, calibration and application of the volumemethod to evaluate the geothermal potential of some recent volcanic areas of Latium, Italy.* Geothermics 39, 260–269.

Drever, J. I. (1997). *The Geochemistry of Natural Waters: Surface and Groundwater Environments.* Prentice Hall. Eaglewood Cliffs, New Jersy, USA.

Durand-Delga, M., Pandeli, E., & Bertani, G. (2001). *Le champ géothermique de Larderello (Toscane, Italie): situation géologique, utilisations industrielles, rôle de la famille De Larderel*. Géologie Alpine 77, 9–21.

Dzikowski, M., Josnin, J. Y., & Roche, N. (2016). *Thermal influence of an Alpine deep hydrothermal fault on the surrounding rocks.* Groundwater, 54(1), 55-65.

Eaton, G. P., Christiansen, R. L., Iyer, H. M., Pitt, A. M., Mabey, D. R., Blank, H. R., Zietz, I., Gettings, M. E. (1975). *Magma beneath Yellowstone National Park*. Science 188, pp. 787-796.

Ebigbo, A., Niederau, J., Marquart, G., Dini, I., Thorwart, M., Rabbel, W., Pechnig, R., Bertani, R., Clauser, C. (2016). *Influence of depth, temperature, and structure of a crustal heat source on the geothermal reservoirs of Tuscany: numerical modelling and sensitivity study. Geothermal Energy*, *4*(1), 5.

Eckstein, Y. (1976). *The measurements and interpretation of terrestrial heat flow in Israel*. Ph.D. thesis, Jerusalem, Israel, Hebrew University, 170 p.

Eckstein, Y., & Simmonsi, G. (1977). *Measurement and interpretation of terrestrial heat flow in Israel.* Geothermics, 6(3-4), 117-142.

Eliezri, I. Z. (1965). *The geology of the Beit-Jann region (Galilee, Israel).* Israel Journal of Earth Sciences, 14(2), 51.

Ellis, A. J., & Mahon, W. A. J. (1964). *Natural hydrothermal systems and experimental hot-water/rock interactions.* Geochimica et Cosmochimica Acta, 28(8), 1323-1357.

Ellis, A. J., & Mahon, W. A. J. (1967). *Natural hydrothermal systems and experimental hot water/rock interactions (Part II).* Geochimica et Cosmochimica Acta, 31(4), 519-538.

EMS-I, (2006). *Groundwater Modeling System 6.0*. Environmental Modeling Systems, Inc., South Jordan, UT.
http://www.aquaveo.com/software/gms-groundwater-modeling-system-introduction. Cited Oct. 2017.

Energy Information Administration (2001). *Office of Integrated Analysis and Forecasting, International Energy Outlook 2001,* DOE/EIA-0484, US Department of Energy, Washington DC (http://www.eia.doe.gov/oiaf/ieo/index.html, last access 27.09.2017).

Erickson, A. J., and Simmons, G. (1969). *Thermal measurements in the Red Sea hot brines pool*. In Degens, E. T., and Ross, D. A. eds., Hot brines and recent heavy metal deposits in the Red Sea: Berlin, Germany, Springer, p. 114–121.

Erickson, A. J., Simmons, G., & Ryan, W. B. F. (1977). *Review of heat flow data from the Mediterranean and Aegean seas.* In: Structural history of the Mediterranean Basins (Symp. Split 1976), Ed Technip, Paris (pp. 263-280).

Ernstson, K., & Kirsch, R. (2006). *Groundwater geophysics - A tool for hydrogeology*.

Eugster, V. H. (1971). *Beitrag zur Tektonik des südöstlichen Graubündens (Gebiet zwischen Landwasser und Ortler).* Eclogae geologicae Helvetiae 64.1, p 133-147.

Evans, D. G., & Nunn, J. A. (1989). *Free thermohaline convection in sediments surrounding a salt column.* Journal of Geophysical Research: Solid Earth, 94(B9), 12413-12422.

Evans, D. G., Nunn, J. A., & Hanor, J. S. (1991). *Mechanisms driving groundwater flow near salt domes.* Geophysical Research Letters, 18(5), 927-930.

Evans, D. G., & Raffensperger, J. P. (1992). *On the stream function for variable‐density groundwater flow.* Water Resources Research, 28(8), 2141-2145.

Evans, J. P., Forster, C. B., & Goddard, J. V. (1997). *Permeability of fault-related rocks, and implications for hydraulic structure of fault zones.* Journal of structural Geology, 19(11), 1393-1404.

Feather, B. M., Malate, R. C. M. (2013). *Numerical modeling of the Mita geothermal field, Cerro Blanco, Guatemala.* In Proceedings of the Thirty-Eighth Workshop on Geothermal Reservoir Engineering, Stanford University, Stanford, CA, February, pp. 11-13.

Fish, J., & Belytschko, T. (2007). *A first course in finite elements.*

Fischedick M, Langniß O, Nitsch J (2000). *After the getting off – future course of renewable energies.* S. Hirzel Verlag, Stuttgart Leipzig (in German).

Flexer, A. (1964). *The Paleogeography of the Senonian and Maestrichtian in Northern Israel.* PhD Thesis, Hebrew University, Jerusalem, 157 pp.

Foglio CARG 1:50,000 (2009). *Cartografia geologica ufficiale Foglio CARG 1:50,000 N. 024, Bormio.*

Forster, C., & Smith, L. (1988). *Groundwater flow systems in mountainous terrain: 2. Controlling factors.* Water Resources Research, 24(7), 1011-1023.

Forster, C., & Smith, L. (1989). *The influence of groundwater flow on thermal regimes in mountainous terrain: a model study.* Journal of Geophysical Research: Solid Earth, 94(B7), 9439-9451.

Fouillac, C., & Michard, G. (1981). *Sodium/lithium ratio in water applied to geothermometry of geothermal reservoirs.* Geothermics, 10(1), 55-70.

Fournier R.O. (1977). *Chemical geothermometers and mixing models for geothermal systems.* Geothermics, 5, 1, 41-50.

Fournier, R. O. (1981). *Application of water geochemistry to geothermal exploration and reservoir engineering*. Chap. 4. Geothermal System, Principles and Case Histories, 109-143.

Fournier, R. O. (1999). *Hydrothermal processes related to movement of fluid from plastic into brittle rock in the magmatic-epithermal environment*. Economic Geology, 94(8), 1193-1211.

Freeston, D. H. (1996*). Direct uses of geothermal energy 1995*. Geothermics, 25(2), 189-214.

Fridleifson, I., B. (1999). *Historical aspects of geothermal utilization in Iceland*. In: Cataldi R, Hodgson SF, Lund JW (eds). Stories from a heated Earth. Geothermal Resources Council, Davis California USA, pp 307-319.

Froitzheim, N., & Manatschal, G. (1996). *Kinematics of Jurassic rifting, mantle exhumation, and passive-margin formation in the Austroalpine and Penninic nappes (eastern Switzerland).* Geological society of America bulletin, 108(9), 1120-1133.

Froitzheim, N., Conti, P. T., & Van Daalen, M. (1997). *Late Cretaceous, synorogenic, low-angle normal faulting along the Schlinig fault (Switzerland, Italy, Austria) and its significance for the tectonics of the Eastern Alps.* Tectonophysics, 280(3), 267-293.

Froitzheim, N., Plasienka, D., Schuster, R. (2008). *Alpine tectonics of the Alps and Western Carpathians.* Geol. Cent. Eur. 2, 1141–1232.

Fulignati, P., Marianelli, P., Sbrana, A., & Ciani, V. (2014). *3D geothermal modelling of the Mount Amiata hydrothermal system in Italy*. Energies, 7(11), 7434-7453.

Galanis, S. P., Sass, J. H., Munroe, R. J., & Abu-Ajamieh, M. (1986). *Heat flow at Zerqa Ma'in and Zara and a geothermal reconnaissance of Jordan (No. 86-631).* US Geological Survey.

Gallino, S. (2007). *Hydrogéologie, géochimie et modélisation hydrodynamique-thermique d'un système thermo-minéral associé un contact structural alpin (Aix-les-Bains-Savoie).* PhD Thesis, Université de Savoie, France, 338 pp.

Gallino, S., Josnin, J. Y., Dzikowski, M., Cornaton, F., & Gasquet, D. (2009). *The influence of paleoclimatic events on the functioning of an alpine thermal system (France): the contribution of hydrodynamic–thermal modeling.* Hydrogeology journal, 17(8), 1887.

Garfunkel, Z. (1981). *Internal structure of the Dead Sea leaky transform (rift) in relation to plate kinematics.* Tectonophysics, 80(1-4), 81-108.

Garven, G. (1995). *Continental-scale groundwater flow and geologic processes*. Annual Review of Earth and Planetary Sciences, 23(1), 89-117.

Geologische Karte der Schweiz 1:500,000 (2005). Geologische Bearbeitung durch: Institut für Geologie, Universität Bern, und Bundesamt für Wasser und Geologie.ISBN: 3-906723-39-9.

Ghisetti, F., & Vezzani, L. (2002). *Normal faulting, transcrustal permeability and seismogenesis in the Apennines (Italy).* Tectonophysics, 348(1), 155-168.

Gianelli, G. (2008). *A comparative analysis of the geothermal fields of Larderello and Mt. Amiata, Italy.* Geothermal energy research trends. Nova Science, New York, 59-85.

Giardini, D. (2009). *Geothermal quake risks must be faced*. Nature, 462(7275), 848.

Giggenbach, W. F. (1988). *Geothermal solute equilibria. derivation of Na-K-Mg-Ca geoindicators.* Geochimica et cosmochimica acta, 52(12), 2749-2765.

Giggenbach, W. F. (1992). *Isotopic shifts in waters from geothermal and volcanic systems along convergent plate boundaries and their origin.* Earth and planetary science letters, 113(4), 495-510.

Giggenbach, W. F. (1997). *The origin and evolution of fluids in magmatic-hydrothermal systems.* Geochemistry of hydrothermal ore deposits, 737-796.

Gibert, J. P., & Jaudin, F. (1999). *Using geothermal waters in France: The district heating system of Chaudes-Aigues from the Middle Ages.* Stories from a heated Earth, R. Cataldi, SF Hodgson, JW Lund (eds.), Geothermal Resources Council, Davis, CA/USA, 287-306.

Giordano, G., De Benedetti, A. A., Diana, A., Diano, G., Gaudioso, F., Marasco, F., Miceli, M., Mollo, S., Cas, R. A. F., Funiciello, R. (2006). *The Colli Albani mafic caldera (Roma, Italy): stratigraphy, structure and petrology.* J. Volcanol. Geotherm. Res. 155, pp. 49–80.

Gleeson, T., & Manning, A. H. (2008). *Regional groundwater flow in mountainous terrain: Three‐dimensional simulations of topographic and hydrogeologic controls*. Water Resources Research, 44(10).

Golani, U. (1961). *On the Cenomanian-Turonian lithostratigraphy of central Galilee*. Bull. Res. Counc. Israel, 10G, 116-146.

Grant, M. A. (1982). *Geothermal reservoir engineering.* John Wiley & Sons, Ltd.

Guglielmin, M., Cannone, N., & Dramis, F. (2001). *Permafrost–glacial evolution during the Holocene in the Italian Central Alps.* Permafrost and Periglacial Processes, 12(1), 111-124.

Guide MUS, (1998). *The mathworks,* Inc., Natick, MA, 5, p 333.

Gvirtzman, H., Garven, G., & Gvirtzman, G. (1997a). *Hydrogeological modeling of the saline hot springs at the Sea of Galilee, Israel.* Water Resources Research, 33(5), 913-926.

Gvirtzman, H., Garven, G., & Gvirtzman, G. (1997b). *Thermal anomalies associated with forced and free ground-water convection in the Dead Sea rift valley.* Geological Society of America Bulletin, 109(9), 1167-1176.

Haar, L., Gallagher, J. S., & Kell, G. S. (1984). *NBS/NRC Steam Tables*. Hemisphere, Washington, DC, Google Scholar.

Haas, J. L. (1971). *The effect of salinity on the maximum thermal gradient of a hydrothermal system at hydrostatic pressure.* Economic Geology, 66(6), 940-946.

Hayba, D. O., & Ingebritsen, S. E. (1997). *Multiphase groundwater flow near cooling plutons.* Journal of Geophysical Research: Solid Earth, 102(B6), 12235-12252.

Hanano, M. (1992a). *Reservoir engineering studies of the Matsukawa geothermal field, Japan.* Transactions Geothermal Resources Council 16, 643–650.

Hanano, M. (1992b). *Simulation study of the Matsukawa geothermal reservoir: natural state and its response to exploitation.* Journal of Energy Resources Technology 114, 309–314.

Hanor, J. S. (1987). *Kilometre-scale thermohaline overturn of pore waters in the Louisiana Gulf Coast.* Nature, 327(6122), 501-503.

Häring, M. O., Schanz, U., Ladner, F., & Dyer, B. C. (2008). *Characterisation of the Basel 1 enhanced geothermal system.* Geothermics, 37(5), 469-495.

Harris, D. C. (2010). *Quantitative chemical analysis.* Macmillan.

Haselwimmer, C., Prakash, A., & Holdmann, G. (2013). *Quantifying the heat flux and outflow rate of hot springs using airborne thermal imagery: Case study from Pilgrim Hot Springs, Alaska.* Remote sensing of environment, 136, 37-46.

Heiken, G. (1982). *Geology of geothermal systems*. In: Edwards LM, Chilingar GV, Rieke III HH, Fertl WH (eds) Handbook of Geothermal Energy, Gulf Publishing Company, Houston, pp 177-217

Heise, W., Bibby, H. M., Caldwell, T. G., Bannister, S. C., Ogawa, Y., Takakura, S., & Uchida, T. (2007). *Melt distribution beneath a young continental rift: the Taupo Volcanic Zone, New Zealand.* Geophysical Research Letters, 34(14).

Hem, J. D. (1985). *Study and interpretation of the chemical characteristics of natural water (Vol. 2254).* Department of the Interior, US Geological Survey.

Henley, R. W. (1985). *The geothermal framework of epithermal deposits.* Reviews in Economic Geology, 2, 1-24.

Henley, R. W., & Ellis, A. J. (1983). *Geothermal systems ancient and modern: a geochemical review.* Earth-science reviews, 19(1), 1-50.

Henley, R. W., Barton, P. B., Truesdell, A. H., & Whitney, J. A. (1984). *Fluid-mineral equilibria in hydrothermal systems (Vol. 1).* El Paso, TX: Society of Economic Geologists.

Henley, R. W., & Adams, D. P. M. (1992). *Strike-slip fault reactivation as a control on epithermal vein-style gold mineralization.* Geology, 20(5), 443-446.

Hickman, S., Sibson, R., & Bruhn, R. (1995). *Introduction to special section: Mechanical involvement of fluids in faulting.* Journal of Geophysical Research: Solid Earth, 100(B7), 12831-12840.

Hill, M. C., & Tiedeman, C. R. (2006). *Effective groundwater model calibration: with analysis of data, sensitivities, predictions, and uncertainty.* John Wiley & Sons.

Hirschberg, S., Wiemer, S., & Burgherr, P. (2014). *Energy from the Earth: Deep Geothermal as a Resource for the Future? (Vol. 62).* vdf Hochschulverlag AG.

Hochstein, M. P. (1990). *Classification and assessment of geothermal resources. Small geothermal resources: A guide to development and utilization*. UNITAR, New York, 31-57.

Hormes, A., Ivy-Ochs, S., Kubik, P. W., Ferreli, L., & Michetti, A. M. (2008). *$^{10}$Be exposure ages of a rock avalanche and a late glacial moraine in Alta Valtellina, Italian Alps.* Quaternary International, 190(1), 136-145.

Horton, C. W., & Rogers Jr, F. T. (1945). *Convection currents in a porous medium*. Journal of Applied Physics, 16(6), 367-370.

Hurwitz, S., Stanislavsky, E., Lyakhovsky, V., & Gvirtzman, H. (2000a). *Transient groundwater-lake interactions in a continental rift: Sea of Galilee, Israel.* Geological Society of America Bulletin, 112(11), 1694-1702.

Hurwitz, S., Lyakhovsky, V., & Gvirtzman, H. (2000b). *Transient salt transport modeling of shallow brine beneath a freshwater lake, the Sea of Galilee, Israel.* Water resources research, 36(1), 101-107.

IAEA - International Atomic Energy Agency (2005). *Isotopic Composition of Precipitation in the Mediterranean Basin in Relation to Air Circulation Patterns and Climate.* IAEA-TECDOC-1453. IAEA, Vienna, pp. 223.

Inbar, N. (2012). *The Evaporitic Subsurface Body of Kinnarot Basin – Stratigraphy, Structure, Geohydrology.* Ph.D Thesis, Tel Aviv University, 131 pp.

Inbar, N., Rosenthal, E., Magri, F., Siebert, C., Moeller, P., & Flexer, A. (2018). *Faulting patterns determining groundwater flow paths in the Lower Yarmouk Gorge.* In preparation.

Ingebritsen, S. E., & Sanford, W. E. (1999). *Groundwater in geologic processes*. Cambridge University Press.

ITW & LKW Geotermia Italia S.p.A. (2013). *Impianto pilota geotermico Castel Giorgio (TR). Progetto definitivo e programma lavori.* http://www.va.minambiente.it/it-IT/Oggetti/Documentazione/1373/1855?Testo=Progetto%20e%20Programma%20Lavori&pagina=1#form-cercaDocumentazione

Ivy-Ochs, S., Kerschner, H., Reuther, A., Maisch, M., Sailer, R., Schaefer, J., Kubik, P., W., Synal, H., A. & Schlüchter, C. (2006). *The timing of glacier advances in the northern European Alps based on surface exposure dating with cosmogenic $^{10}$Be, $^{26}$Al, $^{36}$Cl, and $^{21}$Ne.* Geological Society of America Special Papers, 415, 43-60.

Ivy‐Ochs, S., Kerschner, H., Reuther, A., Preusser, F., Heine, K., Maisch, M., Kubik, P., W. & Schlüchter, C. (2008). *Chronology of the last glacial cycle in the European Alps.* Journal of Quaternary Science, 23(6‐7), 559-573.

Jamier, D. (1975). *Etude de la fissuration, de l'hydrologie et de la géochimie des eaux profondes des massifs de l'Arpille et du Mont Blanc.* PhD thesis, Univesity of Lausanne.

Jaupart, C., Labrosse, S., & Mareschal, J. C. (2007). *7.06—Temperatures, heat and energy in the mantle of the earth. Treatise on geophysics*, *7*, 223-270.

Ji-Yang, W. (1995). *23. Historical Aspects of Geothermal Waters in China.*

Jolivet, L., Faccenna, C., Goffé, B., Mattei, M., Rossetti, F., Brunet, C. & Parra, T. (1998). *Midcrustal shear zones in postorogenic extension: example from the northern Tyrrhenian Sea.* Journal of Geophysical Research: Solid Earth, 103(B6), 12123-12160.

Kaiser, B. O., Cacace, M., & Scheck-Wenderoth, M. (2013). *Quaternary channels within the Northeast German Basin and their relevance on double diffusive convective transport processes: Constraints from 3-D thermohaline numerical simulations.* Geochemistry, Geophysics, Geosystems, 14(8), 3156-3175.

Kappelmeyer, O., & Haenel, R. (1974). *Geothermics with special reference to application.* Berlin Gebrueder Borntraeger Geoexploration Monographs Series, 4.

Katsikadelis, J. T. (2002). *Boundary elements: theory and applications.* Elsevier.

Kinzelbach, W. (1987). *Numerische Methoden zur Modellierung des Transports von Schadstoffen im Grundwasser (Vol. 21).* München: Oldenbourg.

Klang, A., and Gvirtzman, G. (1987). *Structural contour map of the top Judea or Talme Yafe surface,Western Galilee and Mt. Carmel, the coastal plain and the continental shelf: Israel, Oil Exploration (Investments) Ltd., scale: 1:50,000, 1 sheet.*

Kohl, T., Signorelli, S., & Rybach, L. (2001). *Three-dimensional (3-D) thermal investigation below high Alpine topography*. Physics of the Earth and Planetary Interiors, 126(3), 195-210.

Kolditz, O., Bauer, S., Bilke, L., Böttcher, N., Delfs, J. O., Fischer, T. & Park, C. H. (2012). *OpenGeoSys: an open-source initiative for numerical simulation of thermo-hydro-mechanical/chemical (THM/C) processes in porous media.* Environmental Earth Sciences, 67(2), 589-599.

Krásný, J., & Sharp, J. M. (2007). *Groundwater in Fractured Rocks: IAH Selected Paper Series (Vol. 9).* CRC Press.

Kresic, N. (2006). *Hydrogeology and groundwater modeling.* CRC press.

Kühn, M. (2004). *Reactive flow modeling of hydrothermal systems.* Berlin, Heidelberg, New York: LNES 103, Springer-Verlag.

Labrosse, S. (2002). *Hotspots, mantle plumes and core heat loss.* Earth and Planetary Science Letters, 199(1), 147-156.

Langmuir, D. (1997). *Aqueous Environmental Chemistry: Upper Addle River.*

Lapwood, E. R. (1948). *Convection of a fluid in a porous medium.* In Mathematical Proceedings of the Cambridge Philosophical Society (Vol. 44, No. 4, pp. 508-521). Cambridge University Press.

Le Lous, M. (2017). *Transferts de pression, de masse et d'énergie au sein des systèmes aquifères grandes profondeurs: application à la géothermie haute énergie.* PhD thesis, Univesity of Bordeaux 3.

Lebrouc, V., Schwartz, S., Baillet, L., Jongmans, D., & Gamond, J. F. (2013). *Modeling permafrost extension in a rock slope since the Last Glacial Maximum: Application to the large Séchilienne landslide (French Alps).* Geomorphology, 198, 189-200.

Ledru, P., & Frottier, G. F. (2010). *Geothermal Energy Systems: Exploration. Development, and Utilization.* Wiley-VCH.

Levitte, D., & Eckstein, Y. (1978). *Correlation between the silica concentration and the orifice temperature in the warm springs along the Jordan-Dead Sea Rift Valley.* Geothermics, 7(1), 1-8.

Levitte, D., & Olshina, A. (1985). *Isotherm and geothermal gradient maps of Israel.* Geological Survey of Israel.

Li, T., Shiozawa, S., & McClure, M. W. (2016). *Thermal breakthrough calculations to optimize design of a multiple-stage Enhanced Geothermal System.* Geothermics, 64, 455-465.

Lin, G., Nunn, J. A., & Deming, D. (2000). *Thermal buffering of sedimentary basins by basement rocks: implications arising from numerical simulations.* Petroleum Geoscience, 6(4), 299-307.

Lindal, B. (1973). *Industrial and other applications of geothermal energy.* Geothermal Energy, UNESCO, Paris, 135-148.

Liotta, D., Cernobori, L., Nicolich, R. (1998). *Restricted rifting and its coexistence with compressional structures: results from the CROP 3 traverse (Northern Apennines, Italy). TERRA NOVA-OXFORD-*, *10*, pp. 16-20.

Llanos, E. M., Zarrouk, S. J., Hogarth, R. A. (2015). *Numerical model of the Habanero geothermal reservoir, Australia.* Geothermics, 53, pp. 308-319.

Longinelli, A., & Selmo, E. (2003). *Isotopic composition of precipitation in Italy: a first overall map.* Journal of Hydrology, 270(1), 75-88.

López, D. L., & Smith, L. (1995). *Fluid flow in fault zones: analysis of the interplay of convective circulation and topographically driven groundwater flow.* Water Resources Research, 31(6), 1489-1503.

López, D. L., & Smith, L. (1996). *Fluid flow in fault zones: influence of hydraulic anisotropy and heterogeneity on the fluid flow and heat transfer regime.* Water Resources Research, 32(10), 3227-3235.

Lucchitta, I. (1990). *Role of heat and detachment in continental extension as viewed from the eastern Basin and Range Province in Arizona.* Tectonophysics 174, pp. 77-114.

Lund, J. W., & Freeston, D. H. (2001). *World-wide direct uses of geothermal energy 2000.* Geothermics, 30(1), 29-68.

Lund, J. W., & Boyd, T. L. (2016). *Direct utilization of geothermal energy 2015 worldwide review.* Geothermics, 60, 66-93.

Luzzini, F. (2012). *L'industria principesca. Piero Ginori Conti e l'impianto geotermico di Larderello.* Acque Sotterr.(Ital. J. Groundw.), 3, 97-98.

Magri, F., Bayer, U., Maiwald, U., Otto, R., & Thomsen, C. (2009*). Impact of transition zones, variable fluid viscosity and anthropogenic activities on coupled fluid‐transport processes in a shallow salt‐dome environment.* Geofluids, 9(3), 182-194.

Magri, F., Inbar, N., Siebert, C., Rosenthal, E., Guttman, J., & Möller, P. (2015). *Transient simulations of large-scale hydrogeological processes causing temperature and salinity anomalies in the Tiberias Basin.* Journal of Hydrology, 520, 342-355.

Magri, F., Möller, S., Inbar, N., Möller, P., Raggad, M., Rödiger, T. & Siebert, C. (2016). *2D and 3D coexisting modes of thermal convection in fractured hydrothermal systems-Implications for transboundary flow in the Lower Yarmouk Gorge.* Marine and Petroleum Geology, 78, 750-758.

Mahon, W. A. J. (1967). *Natural hydrothermal systems and reaction of hot water with sedimentary rocks.* New Zealand Journal of Science, 10(1), 206.

Majer, E. L., Baria, R., Stark, M., Oates, S., Bommer, J., Smith, B., & Asanuma, H. (2007). *Induced seismicity associated with enhanced geothermal systems*. Geothermics, 36(3), 185-222.

Makhlouf, I., Hiayri, A., & Azzam, H. A. (1996). *Surface and subsurface lithostratigraphic relationships of the Cretaceous Ajlun Group in Jordan.* Hashemite Kingdom of Jordan, Natural Resources Authority, Geology Directorate, Subsurface Geology Division.

Malkovsky, V. I., & Magri, F. (2016). *Thermal convection of temperature-dependent viscous fluids within three-dimensional faulted geothermal systems: Estimation from linear and numerical analyses.* Water Resources Research, 52(4), 2855-2867.

Manzella, A. (1999). *Geophysical methods in geothermal exploration.* Unpublished Lecture notes of International Institute for Geothermal Research, Pisa, Italy.

Marcus, E., & Slager, J. (1985). *The sedimentary-magmatic sequence of the Zemah 1 well (Jordan-Dead Sea Rift, Israel) and its emplacement in time and space.* Israel journal of earth-sciences, 34(1), 1-10.

Maréchal, J. C. (1998). *Les circulations d'eau dans les massifs cristallins alpins et leurs relations avec les ouvrages souterrains.* PhD thesis, No. 1769, Ecole Polytechnique Fédérale de Lausanne, Lausanne, Switzerland, p 174 – 296.

Maréchal, J. C., Perrochet, P., & Tacher, L. (1999). *Long-term simulations of thermal and hydraulic characteristics in a mountain massif: The Mont Blanc case study, French and Italian Alps.* Hydrogeology Journal, 7(4), 341-354.

Marini, L., Franceschini, F., Ghigliotti, M., Guidi, M., Merla, A. (1993). *Valutazione del potenziale geotermico nazionale.* ENEA-Geotermica Italiana Report for the Ministero dell'Industria, del Commercio e dell'Artigianato.

Mattei, M., Kissel, C., & Funiciello, R. (1996). *No tectonic rotation of the Tuscan Tyrrhenian margin (Italy) since late Messinian.* Journal of Geophysical Research: Solid Earth, 101(B2), 2835-2845.

Mazor, E. (2003). *Chemical and isotopic groundwater hydrology (Vol. 98).* CRC Press.

Mazor, E., Kaufman, A., & Carmi, I. (1973). *Hammat Gader (Israel): Geochemistry of a mixed thermal spring complex.* Journal of Hydrology, 18(3-4), 289-303.

Mazor, E., Levitte, D., Truesdell, A. H., Healy, J., & Nissenbaum, A. (1980). *Mixing models and ionic geothermometers applied to warm (up to 60° C) springs: Jordan Rift Valley, Israel.* Journal of Hydrology, 45(1-2), 1-19.

McKenna, J. R., & Blackwell, D. D. (2004). *Numerical modeling of transient Basin and Range extensional geothermal systems.* Geothermics, 33(4), 457-476.

McKenzie, D. (1978). *Some remarks on the development of sedimentary basins.* Earth and Planetary science letters, 40(1), 25-32.

McKibbin, R. (1986). *Heat transfer in a vertically-layered porous medium heated from below.* Transport in Porous Media, 1(4), 361-370.

McKibbin, R., & O'Sullivan, M. J. (1981). *Heat transfer in a layered porous medium heated from below.* Journal of fluid mechanics, 111, 141-173.

Medici, F., & Rybach, L. (1995). *Geothermal map of Switzerland 1995: heat flow density (No. 30).* Commission Suisse de géophysique.

Medina, A., & Carrera, J. (1996). *Coupled estimation of flow and solute transport parameters.* Water Resources Research, 32(10), 3063-3076.

Meiler, M. (2011). *The deep geological structure of the Golan Heights and the evolution of the adjacent Dead Sea fault system.* Tel Aviv University.

Mercer, J. W. (1991). *Common mistakes in model applications.* In Symposium on Ground Water (pp. 1-6). ASCE.

Mercer, J. W., & Faust, C. R. (1979). *A review of numerical simulation of hydrothermal systems/Examen de la simulation numérique des systèmes hydrothermiques.* Hydrological Sciences Journal, 24(3), 335-343.

Mercer, W. J., & Faust, R. C. (1981). *Ground-water modelling.* National water well association, (NWWA), Worthington, OH.

Michelson, H. (1982). *Geological Survey of the Golan Heights (with Some Remarks on Exploration for Hydrocarbons).* Water Planning for Israel Rep., Tel Aviv, pp. 48.

Michelson, H., Flexer, A., & Erez, Z. (1987). *A comparison of the eastern and western sides of the Sea of Galilee and its implication on the tectonics of the northern Jordan Rift Valley.* Tectonophysics, 141(1-3), 125-134.

Midas GTS NX, (2014). *Analysis Reference.* South Korea: Midas Information Technology Co, Ltd.

Mignan, A., Landtwing, D., Kästli, P., Mena, B., & Wiemer, S. (2015). *Induced seismicity risk analysis of the 2006 Basel, Switzerland, enhanced geothermal system project: Influence of uncertainties on risk mitigation.* Geothermics, 53, 133-146.

Minissale, A. (1991). *Thermal springs in Italy: their relation to recent tectonics.* Applied geochemistry, 6(2), 201-212.

Moeck, I. S. (2014). *Catalog of geothermal play types based on geologic controls.* Renewable and Sustainable Energy Reviews, 37, 867-882.

Moh'd, B. K. (2000). *The Geology of Irbid and Ash Shuna Ash Shamaliyya (Waqqas): Map Sheets No. 3154-II and 3154-III.* Hashemite Kingdom of Jordan, Natural Resources Authority, Geology Directorate, Geological Mapping Division.

Mongillo, M. A. (1992). *Remote sensing techniques for geothermal investigation and monitoring in New Zealand*.PhD thesis, ResearchSpace, Auckland.

Montanelli, I. (1969). *Storia di Roma: 753 B.C.-476 A.D.* In Storia d'Italia. Riuoli Edit., Milan.

Montone, P., Mariucci, M. T., & Pierdominici, S. (2012). *The Italian present‐day stress map.* Geophysical Journal International, 189(2), 705-716.

Moore, J. E. (2011*). Field hydrogeology: a guide for site investigations and report preparation.* CRC Press.

Morgan, P., Blackwell, D. D., Spalord, R. E. (1977). *Heat flow measurements in Yellowstone Lake and thermal structure of the Yellowstone caldera.* J. Geophys. Res. 82, pp. 3719-3732.

Muffler, L. J. P. (1979*). Assessment of geothermal resources of the United States, 1978 (No. USGS-CIRC-790).* Geological Survey, Reston, VA (USA). Geologic Div..

Muffler, L. J. P. (1985). *Geothermal energy and geothermal resources of hydrothermal convection systems.* Energy For ourselves and our prosperity. Prentice Hall, Englewood Cliffs, 188-207.

Musgrove, M., & Banner, J. L. (1993). *Regional ground-water mixing and the origin of saline fluids: Midcontinent, United States.* SCIENCE-NEW YORK THEN WASHINGTON-, 259, 1877-1877.

Narasimhan, T. N., & Witherspoon, P. A. (1976). *An integrated finite difference method for analyzing fluid flow in porous media.* Water Resources Research, 12(1), 57-64.

Nardi, L. D., Pieretti, G., Rendina, M. (1977). *Stratigrafia dei terreni perforati dai sondaggi ENEL nell'area geotermica di Torre Alfina.* Bollettino della Societa Geologica Italiana, 96(3), pp. 403-422.

National Research Council (1996). *Rock fractures and fluid flow: contemporary understanding and applications.* National Academies Press.

Nield, D. A. (1968*). Onset of thermohaline convection in a porous medium.* Water Resources Research, 4(3), 553-560.

Nield, D. A. & Bejan, A. (2006). *Convection in porous media (Vol. 3).* New York: springer.

Nicholson, K. (1993). *Geothermal Fluids – Chemistry and Exploration Techniques.* Springer Verlag, Berlin

Nicholson, K. (2012). *Geothermal fluids: chemistry and exploration techniques.* Springer Science & Business Media.

Norton, D., & Knight, J. (1977). *Transport phenomena in hydrothermal systems: cooling plutons.* Am. J. Sci.;(United States), 277.

Ofterdinger, U. S. (2001). *Ground water flow systems in the Rotondo granite, Central Alps (Switzerland).* PhD thesis, Naturwissenschaften ETH Zürich, Nr. 14108, p 38-70.

Ormond, A., Boulègue, J., & Genthon, P. (1995). *A thermoconvective interpretation of heat flow data in the area of Ocean Drilling Program Leg 116 in a distal part of the Bengal Fan.* Journal of Geophysical Research: Solid Earth, 100(B5), 8083-8095.

O'Sullivan, M.J. (1985). *Geothermal reservoir simulation.* Energy Research 9, pp. 313–332.

O'Sullivan, M.J., Barnett, B.G., Razali, M.Y. (1990). *Numerical simulation of the Kamojang geothermal field, Indonesia.* Transactions Geothermal Resources Council 14, 1317–1324.

O'Sullivan, M. J., Pruess, K., & Lippmann, M. J. (2001). *State of the art of geothermal reservoir simulation.* Geothermics, 30(4), 395-429.

Özgüler, M. E., & Kasap, A. (1999). *The geothermal history of Anatolia, Turkey. Stories from a Heated Earth.* Sacramento: Geothermal Resources Council, International Geothermal Association.

Pan, J. B., Lee, C. C., Lee, C. H., Yeh, H. F., & Lin, H. I. (2010). *Application of fracture network model with crack permeability tensor on flow and transport in fractured rock.* Engineering Geology, 116(1), 166-177.

Parry, W. T. (1998). *Fault-fluid compositions from fluid-inclusion observations and solubilities of fracture-sealing minerals.* Tectonophysics, 290(1), 1-26.

Pascucci, V., Merlini, S., & Martini, I. P. (1999). *Seismic stratigraphy of the Miocene-Pleistocene sedimentary basins of the Northern Tyrrhenian Sea and western Tuscany (Italy).* Basin Research, 11(4), 337-356.

Pastorelli, S., Marini, L., & Hunziker, J. C. (1999). *Water chemistry and isotope composition oftheAcquarossa thermal system, Ticino, Switzerland.* Geothermics, 28(1), 75-93.

Pena Reyes, F. A., Crosta, G. B., Frattini, P., Basiricò, S., & Della Pergola, R. (2015). *Hydrogeochemical overview and natural arsenic occurrence in groundwater from alpine springs (upper Valtellina, Northern Italy).* Journal of Hydrology, 529, 1530-1549.

Perello, P., Marini, L., Martinotti, G., & Hunziker, J. C. (2001). *The thermal circuits of the Argentera Massif (Western Alps, Italy): an example of low-enthalpy geothermal resources controlled by Neogene alpine tectonics.* Eclogae Geologicae Helvetiae, 94(1), 75-94.

Person, M., Raffensperger, J. P., Ge, S., & Garven, G. (1996). *Basin‐scale hydrogeologic modeling.* Reviews of Geophysics, 34(1), 61-87.

Person, M., Hofstra, A., Sweetkind, D., Stone, W., Cohen, D., Gable, C. W., & Banerjee, A. (2012). *Analytical and numerical models of hydrothermal fluid flow at fault intersections.* Geofluids, 12(4), 312-326.

Petracchini, L., Scrocca, D., Spagnesi, S., Minelli, F. (2015). *3D geological modeling to support the assessment of conventional and unconventional geothermal resources in the Latium region (Central Italy).* In World Geothermal Congress, pp. 19-25.

Pham, M., Menzies, A.J. (1993). *Results from a field-wide numerical model of The Geysers geothermal field.* Transactions Geothermal Resources Council 17, 259–265.

Pham, M., Menzies, A.J., Sanyal, S.K., Lima, E., Shimada, K., Juarez, J., Cuevas, A. (1996). *Numerical modeling of the high-temperature geothermal system of Amatitlan, Guatemala.* Transactions Geothermal Resources Council 20, 833–838.

Pham, M., Klein, C., Sanyal, S., Xu, T., & Pruess, K. (2001). *Reducing cost and environmental impact of geothermal power through modeling of chemical processes in the reservoir.* In proceedings of 26th Workshop on Geothermal Reservoir Engineering, Stanford University.

Phillips, O. M. (1991). *Flow and reactions in permeable rocks.* Cambridge University Press.

Pirajno, F. (1992). *Hydrothermal mineral deposits – Principles and fundamental concepts for the exploration geologist.* Springer Verlag, Berlin Heidelberg New York.

Piscopo, D., Gattiglio, M., Sacchi, E., Destefanis, E. (2009). *Tectonically-related fluid circulation in the San Casciano dei Bagni-Sarteano area (M. Cetona ridge-Southern Tuscany): a coupled structural and geochemical investigation.* Bollettino della Societa Geologica Italiana, 128(2), pp. 575-586.

Poeter, E. P., & Hill, M. C. (1999). *UCODE, a computer code for universal inverse modeling.* Computers & Geosciences, 25(4), 457-462.

Pollack, H. N., Hurter, S. J., & Johnson, J. R. (1993). *Heat flow from the Earth's interior: analysis of the global data set.* Reviews of Geophysics, 31(3), 267-280.

Porras, E. A., Tanaka, T., Fujii, H., Itoi, R. (2007). *Numerical modeling of the Momotombo geothermal system, Nicaragua.* Geothermics, 36(4), pp. 304-329.

Pozzi, R. (1965). *Schema tettonico dell'alta Valtellina da Livigno al Gruppo dell'Ortles (con carta geologica e carta tettonica).* Eclogae Geologicae Helvetiae 58(1), 21–38.

Pozzi, R., Bollettinari, G., Clerici, A. (1990). *Studio geomorfologico e geologico applicato dell'Alta Valtellina: alto bacino dell'Adda con chiusura a Tirano.* Azienda energetica municipale.

Pruess, K., Wang, J. S. Y., & Tsang, Y. W. (1990a). *On thermohydrologic conditions near high‐level nuclear wastes emplaced in partially saturated fractured tuff: 1. simulation studies with explicit consideration of fracture effects.* Water Resources Research, 26(6), 1235-1248.

Pruess, K., Wang, J. S. Y., & Tsang, Y. W. (1990b). *On thermohydrologic conditions near high‐level nuclear wastes emplaced in partially saturated fractured tuff: 2. Effective continuum approximation.* Water Resources Research, 26(6), 1249-1261.

Pruess, K. (2002). *Mathematical modeling of fluid flow and heat transfer in geothermal systems – an introduction in five lectures.* Geothermal Training Programme, Report 3, LBNL-51295.

Pruess, K., & Spycher, N. (2006). *Proceedings of TOUGHSymposium 2006.* Lawrence Berkeley National Laboratory, Berkeley,CA.

Rabinowicz, M., Sempéré, J. C., & Genthon, P. (1999). *Thermal convection in a vertical permeable slot: Implications for hydrothermal circulation along mid‐ocean ridges.* Journal of Geophysical Research: Solid Earth, 104(B12), 29275-29292.

Raffensperger, J. P., & Garven, G. (1995a). *The formation of unconformity-type uranium ore deposits; 2, Coupled hydrochemical modeling.* American Journal of Science, 295(6), 639-696.

Raffensperger, J. P., & Garven, G. (1995b). *The formation of unconformity-type uranium ore deposits; 1, Coupled groundwater flow and heat transport modeling.* American Journal of Science, 295(5), 581-636.

Raffensperger, J. P., & Vlassopoulos, D. (1999). *The potential for free and mixed convection in sedimentary basins.* Hydrogeology Journal, 7(6), 505-520.

Raven, K. G. (1977). *Preliminary evaluation of structural and groundwater conditions in underground mines and excavations.* Report of Activities, Geological Survey of Canada, Ottawa, 39-42.

Ravnik, D., Rajver, D., Polijak, M., Zivcic, M. (1995). *Overview of the geothermal field of Slovenia in the area between the Alps, the Dinarides and the Pannonian basin.* Tectonophysics 250, pp. 135-149.

Repsold, H. (1989). *Well logging in groundwater development (Vol. 9).* Heise.

Rimmer, A. (2000). *The influence of lake level on the discharge of the Kinneret saline springs.* Advances in limnology. Stuttgart, (55), 55-67.

Rimmer, A., Hurwitz, S., & Gvirtzman, H. (1999). *Spatial and temporal characteristics of saline springs: Sea of Galilee, Israel.* GroundWater, 37(5), 663-673.

Rimmer, A., & Gal, G. (2003). *Estimating the saline springs component in the solute and water balance of Lake Kinneret, Israel.* Journal of hydrology, 284(1), 228-243.

Roberts, P. H., Jones, C. A., & Calderwood, A. R. (2003). Energy fluxes and ohmic dissipation in the Earth's core. Earth's core and lower mantle, 100-129.

Robertson, E. C. (1988). *Thermal properties of rocks (No. 88-441).* US Geological Survey.

Roded, R., Shalev, E., & Katoshevski, D. (2013). *Basal heat-flow and hydrothermal regime at the Golan–Ajloun hydrological basins.* Journal of Hydrology, 476, 200-211.

Romagnoli, P., Arias, A., Barelli, A., Cei, M., & Casini, M. (2010). *An updated numerical model of the Larderello–Travale geothermal system, Italy. Geothermics*, *39*(4), 292-313.

Romijn, E. (Ed.). (1985). *Geothermics, thermal-mineral waters and hydrogeology*. Theophrastus Publications.

Rosenfeld, A., & Hirsch, F. (2005). *The cretaceous of Israel.* Geological Framework of the Levant, 2, 393-436.

Rossetti, F., Faccenna, C., Jolivet, L., Funiciello, R., Tecce, F.., Brune.t, C. (1999*). Syn- versus post-orogenic extension: The case study of Giglio Island (Northern Tyrrhenian Sea, Italy).* Tectonophysics 304, pp. 71-93.

Rybach, L. (1976). *Radioactive heat production in rocks and its relation to other petrophysical parameters.* Pure and Applied Geophysics, 114(2), 309-317.

Rybach, L. (1995). *Thermal waters in deep Alpine tunnels.* Geothermics, 24(5-6), 631-637.

Rybach, L., Eugster, W., Griesser, J. C. (1987). *Die geothermischen Verhältnisse in der Nordschweiz.* Eclogae Geologicae Helvetiae 80 (2), 531–534.

Saad, L. A., & Bashish, M. (1996). *Surface and Subsurface Lithostratigraphic Relationships of the Kurnub Sandstone Group in Jordan.* Hashemite Kingdom of Jordan, Natural Resources Authority, Geology Directorate, Subsurface Geology Division.

Sachse, A., Rink, K., He, W., & Kolditz, O. (2015). *OpenGeoSys-Tutorial: computational hydrology I: groundwater flow modeling.* Springer.

Saltzman, U. (1964). *The Geology of Tabcha-Hukok-Migdal region.* P.N. 374, Tahal, Tel Aviv, (in Hebrew).

Sanyal, S. K. (2005). *Classification of geothermal systems–a possible scheme.* In Thirtieth Workshop on Geothermal Reservoir Engineering, Stanford University, Stanford, California (pp. 85-88).

Santilano, A., Manzella, A., Gianelli, G., Donato, A., Gola, G., Nardini, I. & Botteghi, S. (2015). *Convective, intrusive geothermal plays: what about tectonics?.* Geothermal Energy Science, 3(1), 51-59.

Santilano, A. (2017). *Deep geothermal exploration by means of electromagnetic methods: New insights from the Larderello geothermal field (Italy).* PhD thesis, Politecnico di Torino.

Sauty, J. P. (1980). *An analysis of hydrodispersive transfer in aquifers. Water Resources Research, 16*(1), pp. 145–158.

Schilling, O., Sheldon, H. A., Reid, L. B., & Corbel, S. (2013). *Hydrothermal models of the Perth metropolitan area, Western Australia: implications for geothermal energy.* Hydrogeology Journal, 21(3), 605-621.

Scholz, C. H., Anders, M. H. (1994). *The permeability of faults.* The Mechanical Involvement of Fluids in Faulting, editors S. Hickman, R. Sibson, and R. Bruhn, US Geological Survey-Red Book LXIII, OF Report, 94-228.

Sclater, J., Jaupart, C., & Galson, D. (1980). *The heat flow through oceanic and continental crust and the heat loss of the Earth.* Reviews of Geophysics, 18(1), 269-311.

Scotti, R., Brardinoni, F., & Crosta, G. (2014). *Post-LIA glacier changes along a latitudinal transect in the Central Italian Alps.* The Cryosphere, 8(6), 2235-2252.

Scotti, R., Crosta, G. B., & Villa, A. (2017). *Destabilisation of Creeping Permafrost: The Plator Rock Glacier Case Study (Central Italian Alps).* Permafrost and Periglacial Processes, 28(1), 224-236.

Sekioka, M. (1999). *Japanese geothermal waters throughout history.* In: Cataldi R, Hodgson SF, Lund JW (eds) Stories from a heated Earth. Geothermal Resources Council, Davis California USA, pp 393-405.

Serri, G., Innocenti, F., & Manetti, P. (1993). *Geochemical and petrological evidence of the subduction of delaminated Adriatic continental lithosphere in the genesis of the Neogene-Quaternary magmatism of central Italy.* Tectonophysics, 223(1-2), 117-147.

Seton, M., Müller, R. D., Zahirovic, S., Gaina, C., Torsvik, T., Shephard, G. & Chandler, M. (2012). *Global continental and ocean basin reconstructions since 200Ma.* Earth-Science Reviews, 113(3), 212-270.

Severini, A. P., & Huntley, D. (1983). *Heat Convection in Warm Springs Valley, Virginia.* Groundwater, 21(6), 726-732.

Severne, C. M. (1999). *28. Traditional Use of Geothermal Resources by New Zealand Maori.* Stories from a heated earth: our geothermal heritage, 19, 435.

Shalev, E., Levitte, D., Gabay, R., & Zemach, E. (2008). *Assessment of geothermal resources in Israel.* Geological Survey of Israel.

Shaliv, G. (1991). *Stages in the tectonic and volcanic history of the Neogene basin in the Lower Galilee and the valleys.* Rep. GSI/11, 91, 94.

Sheldon, H. A., Florio, B., Trefry, M. G., Reid, L. B., Ricard, L. P., & Ghori, K. A. R. (2012). *The potential for convection and implications for geothermal energy in the Perth Basin, Western Australia.* Hydrogeology Journal, 1-18.

Shentzis, I. D. (1990). *Mathematical models for long-term prediction of mountainous river runoff: methods, information and results.* Hydrological Sciences Journal, 35(5), 487-500.

Shulman, H., Reshef, M., & Ben-Avraham, Z. (2004). *The structure of the Golan Heights and its tectonic linkage to the Dead Sea Transform and the Palmyrides folding.* Israel Journal of Earth Sciences, 53.

Sibson, R. H. (1987). *Earthquake rupturing as a mineralizing agent in hydrothermal systems.* Geology, 15(8), 701-704.

Sibson, R. H. (1994). *Crustal stress, faulting and fluid flow.* Geological Society, London, Special Publications, 78(1), 69-84.

Sibson, R. H. (2001). *Seismogenic framework for hydrothermal transport and ore deposition.* Reviews in Economic Geology, 14, 25-50.

Siebert, C., Möller, P., Geyer, S., Kraushaar, S., Dulski, P., Guttman, J. & Rödiger, T. (2014). *Thermal waters in the Lower Yarmouk Gorge and their relation to surrounding aquifers.* Chemie der Erde-Geochemistry, 74(3), 425-441.

Singhal, B. B. S., & Gupta, R. P. (1999). *Fractures and discontinuities.* In Applied Hydrogeology of Fractured Rocks (pp. 13-35). Springer Netherlands.

Singhal, B. B. S., & Gupta, R. P. (2010). *Applied hydrogeology of fractured rocks.* Springer Science & Business Media.

Slack, K. (2009). *Geothermal resources and climate emissions.* Geothermal Energy Association, Washington,DC. Draft Report for Public Review.

Smith, D. A. (1980). *Sealing and nonsealing faults in Louisiana Gulf Coast salt basin.* AAPG Bulletin, 64(2), 145-172.

Smith, G. D. (1985). *Numerical solution of partial differential equations: finite difference methods.* Oxford university press.

Smith, M. C. (1983). *A history of hot dry rock geothermal energy systems.* Journal of Volcanology and Geothermal Research, 15(1-3), 1-20.

Smith, L., Forster, C. B., & Evans, J. P. (1990). *Interaction between fault zones, fluid flow and heat transfer at the basin scale.*

Solomon, S. (Ed.). (2007). *Climate change 2007-the physical science basis: Working group I contribution to the fourth assessment report of the IPCC (Vol. 4).* Cambridge University Press.

Sonney, R. (2010). *Groundwater Flow, Heat and Mass Transport in Geothermal Systems of a Central Alpine Massif: The Cases of Lavey-les-Bains, Saint-Gervais-les-Bains, and Val D'Illiez.* PhD thesis, faculty of Sciences of the University of Neuchâtel, p 111 – 130.

Sonney, R., & Vuataz, F. D. (2007). *BDFGeotherm: the database of geothermal fluids in Switzerland.* In Proc. European Geothermal Congress.

Sonney, R., & Vuataz, F. D. (2008). *Properties of geothermal fluids in Switzerland: a new interactive database.* Geothermics, 37(5), 496-509.

Sonney, R., & Vuataz, F. D. (2009). *Numerical modelling of Alpine deep flow systems: a management and prediction tool for an exploited geothermal reservoir (Lavey-les-Bains, Switzerland).* Hydrogeology journal, 17(3), 601-616.

Sonney, R., & Vuataz, F. D. (2010). *Validation of chemical and isotopic geothermometers from low temperature deep fluids of northern Switzerland.* In Proceedings World Geothermal Congress (Vol. 14, No. 1423, pp. 1-12). International Geothermal Association.

Starinsky, A., Katz, A., & Levitte, D. (1979). *Temperature-composition-depth relationship in Rift Valley hot springs: Hammat Gader, northern Israel.* Chemical Geology, 27(3), 233-244.

Stober, I., & Bucher, K. (2013). *Geothermal energy.* Germany: Springer-Verlag Berlin Heidelberg. doi, 10, 978-3.

Sutton, F. M., & McNabb, A. (1977). *Boiling curves at Broadlands geothermal field, New Zealand.* NzJ Sci, 20, 333-337.

Svalova, V. (1999). 21. *Geothermal Legends through History in Russia and the Former USSR: A Bridge to the Past.* Stories from a heated earth: our geothermal heritage, 19, 337.

Swiss Federal Office of Environment, FOEN (2017). *Rom - Müstair Current situation: Discharge and water level.* http://www.hydrodaten.admin.ch/en/2617.html, accessed Jan 2017.

Tahal (1989). *Hydrogeological and Hydrometeorological Model of the Yarmouk Basin.* Water Planning for Israel Rep. 01/89/62, Tel Aviv, pp. 53 (in Hebrew).

Terakawa, T., Miller, S. A., & Deichmann, N. (2012). *High fluid pressure and triggered earthquakes in the enhanced geothermal system in Basel, Switzerland*. Journal of Geophysical Research: Solid Earth, 117(B7).

Thiébaud, E. (2008). *Fonctionnement d'un système hydrothermal associé à un contact tectonique alpin (La Léchère, Savoie). Apports de l'hydrogéologie, de la géochimie et de la modélisation hydrodynamique–thermique en vue de la gestion de la resource.* PhD Thesis, Université de Savoie, France, p 306 – 330.

Thiebaud, E., Gallino, S., Dzikowski, M., & Gasquet, D. (2010). *The influence of glaciations on the dynamics of mountain hydrothermal systems: numerical modeling of the La Léchère system (Savoie, France).* Bulletin de la Société Géologique de France, 181(4), 295-304.

Thomas, R. P. (1986). *Heat-flow mapping at The Geysers geothermal field (No. DOE/SF/11721-T1).* California Dept. of Conservation, Sacramento (USA). Div. of Oil and Gas.

Tiwari, G. N., & Ghosal, M. K. (2005). *Renewable energy resources: basic principles and applications.* Alpha Science Int'l Ltd.

Tóth, J. (1963). *A theoretical analysis of groundwater flow in small drainage basins.* Journal of geophysical research, 68(16), 4795-4812.

Tóth, J. (1978). *Gravity‐induced cross‐formational flow of formation fluids, red earth region, Alberta, Canada: Analysis, patterns, and evolution.* Water Resources Research, 14(5), 805-843.

Toth, A., & Bobok, E. (2016). *Flow and Heat Transfer in Geothermal Systems: Basic Equations for Describing and Modeling Geothermal Phenomena and Technologies*. Elsevier.

Tournier, C., Genthon, P., & Rabinowicz, M. (2000). *The onset of natural convection in vertical fault planes: consequences for the thermal regime in crystalline basementsand for heat recovery experiments.* Geophysical Journal International, 140(3), 500-508.

Truesdell, A. H., & Hulston, J. R. (1980). *Isotopic evidence on environments of geothermal systems.* In Handbook of environmental isotope geochemistry. Vol. 1.

UNEP: *Vital Water Graphics.* United Nations Environmental Programme, UNEP, Nairobi, Kenya, http://www.unep.org/dewa/assessments/ecosystems/water/vitalwater/ (accessed November 2017)

Varet J., Beutin P., Lajouanie B., Laplaige P., Lemale J., Desplan A., Horel Y., Le Bel L. and Castello M. (2004). *La géothermie - les enjeux des géosciences.* Technical report, Agence de l'Environnement et de la Maîtrise de l'Énergie (ADEME) Bureau de Recherches Géologiques et Minières (BRGM).

Vignaroli, G., Pinton, A., De Benedetti, A. A., Giordano, G., Rossetti, F., Soligo, M., Berardi, G. (2013). *Structural compartmentalisation of a geothermal system, the Torre Alfina field (central Italy).* Tectonophysics, 608, pp. 482-498.

Volpi, G., Riva, F., Pena Reyes, F. A., Basiricò, S., Penna, D. (2016). *Geochemical characterization of the Bormio hydrothermal system (central Italian Alps).* Rend Online Soc Geol It 41(2016):99–102. doi:10.3301/ROL.2016.103.

Volpi, G., Magri, F., Frattini, P., Crosta, G. B., & Riva, F. (2017). *Groundwater-driven temperature changes at thermal springs in response to recent glaciation: Bormio hydrothermal system, Central Italian Alps.* Hydrogeology Journal, 1-18.

Vuataz, F. D. (1983). *Hydrology, geochemistry and geothermal aspects of the thermal waters from Switzerland and adjacent alpine regions.* Journal of volcanology and geothermal research, 19(1-2), 73-97.

Vujević, K., Graf, T., Simmons, C. T., & Werner, A. D. (2014). *Impact of fracture network geometry on free convective flow patterns.* Advances in Water Resources, 71, 65-80.

Wang, M., Kassoy, D. R., & Weidman, P. D. (1987*). Onset of convection in a vertical slab of saturated porous media between two impermeable conducting blocks.* International journal of heat and mass transfer, 30(7), 1331-1341.

WASY-GmbH (ed). (2002). *FEFLOW Finite-element Subsurface Flow and Transport Simulation System, User's Manual/Reference manual/White Papers. Release 5.2.* WASY, Berlin.

Watson, A. (2013). *Geothermal engineering: fundamentals and applications.* Springer-Verlag New York.

Weight, W. D., & Sonderegger, J. L. (2001). *Manual of applied field hydrogeology.* McGraw-Hill.

Weisstein, E. W. (2002*). CRC concise encyclopedia of mathematics.* CRC press.

Welch, L. A., & Allen, D. M. (2012). *Consistency of groundwater flow patterns in mountainous topography: Implications for valley bottom water replenishment and for defining groundwater flow boundaries.* Water Resources Research, 48(5).

Welch, L. A., & Allen, D. M. (2014*). Hydraulic conductivity characteristics in mountains and implications for conceptualizing bedrock groundwater flow.* Hydrogeology Journal, 22(5), 1003-1026.

Werner, D., Kahle, H.G. (1980). *A geophysical study of the Rhinegraben, kinematics and geothermics.* Geophys. J. R. Astron. Soc. 62, pp. 617-629.

White, D. E. (1992). *The Beowawe geysers, Nevada, before geothermal development (No. 1998).* USGPO; Book and Open-File Report Sales, US Geological Survey [distributor],.

Williams, D. L., & Von Herzen, R. P. (1974). *Heat loss from the Earth: new estimate.* Geology, 2(7), 327-328.

Wolski, P. (1998*). Remote sensing, land use and hydrotopes in Western Province, Zambia.* Elements of a groundwater study. Physics and Chemistry of the Earth, 23(4), 479-484.

Wood, J. R., & Hewett, T. A. (1982*). Fluid convection and mass transfer in porous sandstones-A theoretical model.* Geochimica et Cosmochimica Acta, 46(10), 1707-1713.

Yeamans, F. (1983). *Basin and range geothermal hydrology: an empirical approach.* Geothermal Resources Council Special Report, 13, 159-175.

Yechieli, Y., Shaliv, G., Wallman, S., Kessler, A., Rozenzpet, M., Berger, D., Bein, A., (2011). *Three Dimensional Model for the Kalanit Basin (Fuliya and Tabgha Basin).* GSI Project Report GSI/38/2011, 101 pp. (in Hebrew).

Younker, L.W., Kasameyer, P.W., Tewhey, J.D. (1982). *Geological, geophysical, and thermal characteristics of the Salton Sea Geothermal field, California.* J. Volcanol. Geotherm. Res. 12, pp. 221-258.

Yourownpower: *GRED III Geothermal exploration project.*
http://www.yourownpower.com/GREDIII/ (accessed October 2017).

Zhao, C., Mühlhaus, H. B., & Hobbs, B. E. (1997). *Finite element analysis of steady‐state natural convection problems in fluid‐saturated porous media heated from below.* International Journal for Numerical and Analytical Methods in Geomechanics, 21(12), 863-881.

Zhao, C., Hobbs, B. E., & Mühlhaus, H. B. (1998a). *Finite element modelling of temperature gradient driven rock alteration and mineralization in porous rock masses.* Computer Methods in Applied Mechanics and Engineering, 165(1-4), 175-187.

Zhao, C., Hobbs, B. E., & Mühlhaus, H. B. (1998b). *Analysis of pore-fluid pressure gradient and effective vertical-stress gradient distribution in layered hydrodynamic systems.* Geophysical Journal International, 134(2), 519-526.

Zhao, C., Hobbs, B. E., & Mühlhaus, H. B. (1999a). *Theoretical and numerical analyses of convective instability in porous media with upward throughflow.* International Journal for Numerical and Analytical Methods in Geomechanics, 23(7), 629-646.

Zhao, C., Hobbs, B. E., Mühlhaus, H. B., & Ord, A. (1999b). *Finite element analysis of flow patterns near geological lenses in hydrodynamic and hydrothermal systems.* Geophysical Journal International, 138(1), 146-158.

Zhao, C., Hobbs, B. E., & Mühlhaus, H. B. (2000). *Finite element analysis of heat transfer and mineralization in layered hydrothermal systems with upward throughflow.* Computer methods in applied mechanics and engineering, 186(1), 49-64.

Zhao, C., Hobbs, B. E., Mühlhaus, H. B., Ord, A., & Lin, G. (2001). *Finite element modelling of three‐dimensional convection problems in fluid‐saturated porous media heated from below.* International Journal for Numerical Methods in Biomedical Engineering, 17(2), 101-114.

Zhao, C., Hobbs, B. E., & Ord, A. (2008). *Convective and advective heat transfer in geological systems.* Springer Science & Business Media.

Zienkiewicz, O.C. and Taylor, R.L. (1991). *The finite element method (2 Volumes).* McGraw Hill, New York, NY.

Zienkiewicz, O. C., & Taylor, R. L. (2000). *The finite element method: Vol. 1: The basis.* Butterworth-heinemann.